Open Quantum Dynamics of Mesoscopic Bose-Einstein Condensates

By

Joel Frederick Corney, BSc.(Hons)

A thesis submitted to the University of Queensland
for the degree of Doctor of Philosophy
Department of physics
September 1999

Except where acknowledged in the customary manner, the material presented in this thesis is, to the best of my knowledge and belief, original and has not been submitted in whole or in part for a degree in any university.

Joel Frederick Corney

The heavens are telling the glory of God;
and the firmament proclaims his handiwork.
Day to day pours forth speech,
and night to night declares knowledge.
There is no speech, nor are there words;
their voice is not heard;
yet their voice goes out through all the earth,
and their words to the end of the world.
- from the 19th Psalm

Acknowledgements

My thanks must first go to my Ph.D. supervisors Profs. Gerard Milburn and Peter Drummond. I am much obliged to you both for providing me with such challenging and rewarding research opportunities; for sharing with me your passion for science and deep insight into physics; and for your patience. It has been my privilege to learn from you.

Completing a Ph.D. is much less daunting when one is able to call upon the counsel of those who have gone before. So for advice, encouragement and stimulation, I thank Drs. Howard Wiseman, Karen Kheruntsyan, He Bi Sun, Ariel Liebman and Michael Gagen. (Howard, your thesis was invaluable.) My thanks also to Ian Mortimer, as well as Drs. Bill Munro, Hao He and John Breslin, for aid with computing resources and numerical simulations. For the lively physics discussions, considered opinions and mutual commiserations, I am indebted to my roommates Damian Pope, Greg Collecutt and David Harris. I am conscious also of the many others in the department who have assisted me in innumerable ways, and who contribute to making the place such a stimulating and pleasant environment to do physics.

From outside of U.Q., I give special thanks to Dr. Weiping Zhang, for both the privilege of collaborating with you and for your hospitality during my (all too brief) visit to Macquarie University.

On a more personal note, I would like to express appreciation to my wife Vivienne, for her support, understanding and tolerance, particularly when I was writing up. Thanks too for proofreading my thesis so thoroughly - I'm sure any errors remaining are the ones I made after you read it! Lastly, I thank my parents, who taught me the value of curiosity and learning (not many households could boast of so many sets of encyclopaedias!). I hope you will continue to gently admonish me when my thinking is unscientific.

List of Publications

This thesis is based in part upon the following refereed publications:

1. Milburn, G. J., Harris, D., Corney, J., Wright, E., and Walls, D. F. Quantum dynamics of an atomic Bose-Einstein condensate. In *Atom Optics: Proceedings of SPIE 2995* (Washington, 1997), M. G. Prentiss and W. D. Phillips, Eds., The International Society for Optical Engineers, p. 232.

2. Milburn, G. J., Corney, J. F., Wright, E. M., and Walls, D. F. Quantum dynamics of an atomic Bose-Einstein condensate in a double-well potential. *Physical Review* **A 55**, 6 (June 1997), 4318–4324.

3. Corney, J. F., Drummond, P. D., and Liebman, A. Quantum noise limits to terabaud communications. *Optics Communications* **140** (Aug. 1 1997), 211–215.

4. Corney, J. F., and Milburn, G. J. Homodyne measurements on a Bose-Einstein condensate. *Physical Review* **A 58**, 3 (Sept. 1998), 2399–2406.

5. Corney, J. F., Milburn, G. J., and Zhang, W. Weak force detection using a double Bose-Einstein condensate. *Physical Review* **A 59**, 6 (June 1999), 4630–4635.

6. Drummond, P. D., and Corney, J. F. Quantum dynamics of evaporatively cooled Bose-Einstein condensates. *Physical Review* **A 60**, 4 (Oct. 1999), R2661–R2664.

7. Drummond, P. D., and Corney, J. F. Quantum noise in optical fibers I: stochastic equations. *Journal of the Optical Society of America* **B**, to appear.

8. Corney, J. F., and Drummond, P. D. Quantum noise in optical fibers II: Raman jitter in soliton communications. *Journal of the Optical Society of America* **B**, to appear.

Abstract

The properties of an atomic Bose-Einstein condensate in a double-well potential are investigated through a two-mode analysis. An analytic solution for the semiclassical tunnelling and self-trapping dynamics is compared with numerical simulations of the quantum dynamics, which exhibit collapses and revivals for a closed system. A continuous non-destructive measurement technique to monitor the Josephson tunnelling oscillations is presented, in which the condensate in one well dispersively shifts the phase of a coherent probe beam in proportion to atom-number. The evolution of the resulting homodyne photocurrent and Bloch Q distributions shows that oscillations develop even when the initial state possesses phase symmetry. The conditional dynamics of the condensate which result from measurement back-action also appear in certain semiclassical formulations. The homodyne measurement technique is incorporated into a proposed weak-force detector. A maximally entangled initial state, which is the ground state for a double condensate with strong attractive atomic interactions, enables a high-precision measurement.

The dynamics of quantum many-body multimode systems of interacting bosons are simulated using phase-space methods. The use of the Wigner technique predicts novel noise effects in fibre solitons. The positive-P representation is used to simulate the formation of mesoscopic Bose-Einstein condensates via evaporative cooling in three dimensional atom traps. The results indicate highly non-classical behaviour near the critical point, and provide evidence for the spontaneous formation of vortices. Comparisons with corresponding mean-field calculations reveal large differences between the semiclassical and fully quantum results. Finally, the possibility of future progress with alternative phase-space methods is considered.

Contents

List of Figures

List of Tables

List of Abbreviations and Symbols

This list includes some of the more important mathematical symbols used.

FP	Fokker-Planck
GP	Gross-Pitaevskii
QMC	quantum Monte Carlo
RF	radio-frequency
a_0	s-wave scattering length
$\hat{a}^\dagger$, $\hat{a}$	creation and annihilation operators for an optical mode
a_1, a_2	normalised positive-P phase-space variables
α	coherent amplitude of an optical mode
$\mathcal{C}$	phase-space confinement parameter
c	speed of light in a vacuum ($299\,792\,458\text{ms}^{-1}$)
$\hat{c}^\dagger$, $\hat{c}$	atomic creation and annihilation operators for the local modes
χ	coupling strength between a light field and the condensate
$\overline{D^{\cdots}}$	diffusion matrix in the FP equation for $\cdots$
Δ	frequency shift induced by a weak force
$\mathcal{D}_{\ldots}$	second-order (and higher) differential operator
$\mathcal{F}(\omega)$	fluorescence function for the Raman gain in optical fibres
G	Wigner function
G_2	normally ordered second-order correlation function
Γ	homodyne measurement strength
$\Gamma_{\ldots}(\mathbf{r})$	absorption profile
$\hat{H}_2$	two-mode Hamiltonian
$\hbar$	Planck's constant ($1.054\,572\,66 \times 10^{-34}\text{Js}$)
h_R	Raman gain in an optical fibre

$\Im\{\cdots\}$	imaginary part of $\cdots$
$\hat{J}_x$, $\hat{J}_y$, $\hat{J}_z$	angular momentum operators
k_B	Boltzmann's constant ($1.380\,658 \times 10^{-23}\mathrm{JK}^{-1}$)
κ	atom collision strength
$\mathcal{L}_{\cdots}$	first-order differential operator
$\big\lvert\mu\big\rangle$	atomic coherent state, or Bloch state
$\big\langle n(k)\big\rangle$	observed momentum distribution
$n(k)$	single-trajectory momentum distribution
$\big\langle n(j)\big\rangle$	angular momentum distribution
N	number of condensed atoms
Ω	tunnelling frequency
P	Glauber-Sudarshan P function
$Pr\{\cdots\}$	probability of $\cdots$
$\hat{\Psi}$	photon-field annihilation operator
Φ_N	condensate mean field
$\hat{\psi}^\dagger$, $\hat{\psi}$	bosonic many-body creation and annihilation operators for atoms
$\big\lvert\Psi\big\rangle$	system ket vector
$\big\lvert\tilde{\Psi}\big\rangle$	unnormalised system ket vector
$\big\lvert\Psi_c\big\rangle$	conditional system ket vector
$\pm q_0$	positions of well minima
Q	quantum optics Q function
$Q(\mu)$	atomic Q function
$\Re\{\cdots\}$	real part of $\cdots$
ρ	ground-state spatial density distribution
$\hat{\rho}$	density operator for the condensate
$\hat{\rho}_c$	conditional density operator for the condensate
Θ	normalised atom collision strength ($\kappa N/\Omega$)
U_0	two-body interaction strength
u_1, u_2	local ground-state modes of the double-well potential
$V_{\cdots}(\mathbf{r})$	trapping potential
W, dW	Wiener process and increment

Chapter 1

Condensation 'without forces'

> The theory is pretty, but is there some truth in it?
> - *A. Einstein*[1].

1.1 An historical introduction

What is now known as Bose-Einstein condensation was predicted by Albert Einstein in 1924[139]. Einstein's contribution to statistical mechanics was but a brief interlude in his life as a physicist, but this alone, without relativity or his contributions to the early quantum theory would have guaranteed him fame, at least in scientific circles. Before any quantum theory had been fully developed, Einstein was investigating the quantum statistical properties of massive particles. He generalised the work of Bose, who had only dealt with the statistical properties of photons, and in the process predicted a new, quantum state of matter.

In deriving an equilibrium distribution of radiation, Bose had treated light as a quantum gas[2] of photons[14]. Einstein reasoned that if quanta of light could be treated in this way, then so could particles of matter, and derived the properties of a quantum gas of 'molecules'. This was the beginning of quantum statistical mechanics.

Among Einstein's predictions was that below a certain temperature, part of the gas must condense into the quantum state of lowest energy, thus creating a macroscopic occupation of a single quantum state[54]. For some years, the existence of this phenomenon was treated with some skepticism, with Einstein himself wondering if the effect could be

[1] From a letter to Ehrenfest in December 1924, quoted on page 432 of [139].

[2] A quantum gas in the sense that its constituent particles are indistinguishable.

real[3]. Even if the theory was correct, this special kind of condensation was thought not to exist in nature or be possible in the laboratory, because the required temperature was so low that interatomic forces would cause the gas to condense into a solid.

The concept of Bose-Einstein condensation gained credence after it was invoked as the underlying principle of superfluidity in liquid helium, and later superconductivity in metals. However, in both of these systems, the interparticle interactions are so strong as to mask any pure condensation effects. Einstein had suggested hydrogen as a candidate in which condensation may occur. In 1959, spin-polarised hydrogen was predicted to remain gaseous down to zero temperature[80]. The 1980s saw the development of trapping and cooling techniques required to produce ultracold samples of hydrogen gas. This was adapted to heavier alkali-metal gases in this decade, leading to the production of the first[4] Bose-Einstein condensate in 1995[3, 16, 35], some 70 years after Einstein's first prediction of the phenomenon.

1.2 Underlying themes

Bose-Einstein condensation cannot occur, even in theory, for all particles: not all particles possess the symmetric wavefunction that gives rise to Bose-Einstein statistics, a fact realised in the two years following Einstein's work[3]. Any particle may be classed into one of two groups, according to the intrinsic angular momentum that it possesses: fermions, with half-integer values of spin, and bosons, with integer spin. The former includes quarks, electrons and protons, while the latter encompasses photons and composite particles (such as atoms and billiard balls) that contain an even number of fermions[5]. This classification of particles was introduced by Dirac in 1927, to remove confusion over the applicability of Pauli's exclusion principle. Fermions obey this principle, which says that no more than one particle can exist in any one quantum state. Bosons, on the other hand, are not so constrained. Two or more may exist in the same state, and are thus capable of the quantum degeneracy necessary for Bose-Einstein condensation.

[3] See chapter 23 of [139] and the references contained therein.

[4] Atomic interactions are still play a role, so these condensates are not exactly the 'ideal' condensate predicted by Einstein. They are, however, significantly closer to it than the traditional condensed matter systems.

[5] Conversely, composite particles composed of an odd number of fermions are themselves fermions; for example, a proton consists of three quarks.

How is this quantum degeneracy induced? What conditions will force massive particles into the same state so that they become indistinguishable? The answer lies in Heisenberg's uncertainty principle[6], a fundamental principle underlying all of quantum mechanics. This principle states that there is associated with all physical systems an irreducible uncertainty, such that there is a limit to the precision with which two complementary quantities may both be known. For example, in terms of the uncertainty of the position Δx and momentum Δp of a particle, the uncertainty principle states that

$$\Delta p \Delta x \geq \frac{\hbar}{2}, \tag{1.1}$$

where $\hbar$ is related to Planck's constant by $h = 2\pi\hbar$. Thus the more definite is a particle's momentum, the more uncertain is its position. This gives rise to the wave nature of quantum mechanics, since a particle's state is now probabilistic, encapsulated by a wavefunction. The uncertainty in position is reflected in the spread of the wavefunction.

For two particles to be in the same state, their wavefunctions must overlap and become indistinguishable. The spatial spread of the wavefunction is characterised by the de Broglie wavelength, which for particles in thermal equilibrium is

$$\lambda_{\text{th}} = \frac{h}{\sqrt{3mk_BT}}, \tag{1.2}$$

where k_B is Boltzmann's constant, m is the mass of the particles and T is the temperature of the gas. Thus particles with a smaller mass have a larger position spread, which is why hydrogen was considered for many years to be the most promising candidate with which to achieve condensation.

Quantum degeneracy in a gas occurs when the de Broglie wavelength becomes larger than the interparticle spacing. This gives a critical temperature T_c for the onset of Bose-Einstein condensation which increases with density of the gas. Hence the gas must be tightly confined while it is cooled so that a relatively high density is maintained. It is not then surprising that the two main enemies of successful condensation are heating effects and unwanted interactions between particles. Interparticle collisions may produce excessive atom loss from traps as well as causing atoms to stick together. This is detrimental as the atoms must remain delocalised to avoid forming into a solid.

However, certain interactions, namely elastic collisions, are needed to mediate the energy distribution (thermalisation) described by Bose-Einstein statistics. The large effective

[6] Also introduced in 1927, a very important year for quantum mechanics!

cross-section for elastic collisions in alkali metals is a major reason that condensation was achieved first in Rubidium rather than in the lighter element of hydrogen.

1.3 Thesis rationale

The Bose-Einstein condensate is truly a quantum object, even though it may be macroscopic in size, in the sense that it is a consequence of quantum statistics and it is essentially a matter-wave. However the characteristic of behaving as a wave is not it in itself a quantum property. Even though classically matter is usually described as particulate, a description entirely in terms of waves is still a classical description. What makes an object quantum is the marriage of both particle-like and wave-like properties.

In this thesis, we will be studying the condensate primarily as a *quantum* field, meaning that the discrete nature of the field is taken into account, as opposed to a semiclassical description in which the continuous or deterministic limit is taken. The Bose-Einstein condensate in atomic gases is a transient (metastable) state of matter, produced through a dynamical evaporation process. Thus the true nature of the condensate is revealed through its evolution in time, so the focus of this thesis is on calculations of *dynamics*. The quantum features are most pronounced in condensates with relatively few numbers of atoms. Such *mesoscopic* condensates are not truly microscopic, since they can be imaged with visible light, and are not macroscopic since they contain many fewer particles ($\ll 10^{23}$) than 'everyday' objects. The mesoscopic regime allows quantum mechanical calculations in the time domain, which become intractable for larger systems without invoking semiclassical approximations. Finally the condensate does not exist in isolation: it forms by interacting with a reservoir of thermal atoms and it suffers from atom losses and from fluctuations in the trapping fields. Also any measurements will couple it to the environment. Thus a realistic treatment of condensation and subsequent condensate dynamics must model the condensate as an *open* system.

1.4 Thesis structure

The work presented in this thesis falls neatly into two parts: the first dealing with two-mode dynamics and the second studying multimode systems. The two-mode work is grounded in a particular model of the condensate in a double-well potential. This is

introduced in Ch. 2 along with an analysis of various semiclassical and quantum properties of the double condensate, not all of which is directly built upon by later chapters; an acceptable route to take is through Sec. 2.1 then the beginning of Sec. 2.3 before proceeding to the later chapters. Chapter 3 introduces a nondestructive measurement technique for the condensate, which is utilised in Ch. 5 in a scheme for measuring weak forces. Chapter 4 summarises different ways to extend the study of the open dynamics begun in Ch. 3 and in doing so provides a link to the phase-space techniques used in the second part of the thesis.

The underlying equations of dilute atomic condensates are similar to those governing the nonlinear propagation of light in optical fibres. Chapter 6 discusses this system as one to which the quantum-optical phase-space methods have been successfully applied; Ch. 7 provides the application to Bose-Einstein condensates. Throughout this thesis some results from stochastic calculus are used, and these are summarised in the first appendix. Appendix B supplements the final chapter.

The order of the chapters is deliberate, but the reader is most welcome to begin in any section. Where a section builds on another, I have given the cross-references. Because this thesis touches several distinct fields, summaries of topical work is provided in particular sections rather than in one large literature review for the whole thesis. I trust that I have provided enough signposts for you to find your way.

Part I

Quantum dynamics of monitored Bose-Einstein condensates

Chapter 2

Properties of an atomic Bose condensate in a double-well potential

This chapter introduces the model of the condensate that will be used throughout the first half of this thesis. We will overview some of the semiclassical and quantum properties of the double-well condensate in isolation, before considering coupling to the environment in Sec. 2.3.4. Dynamical properties, including Josephson tunnelling and macroscopic self-trapping, will be analysed, as well as equilibrium properties, such as the transition temperature, energy eigenstates and spatial correlations.

2.1 Condensate model

We consider a dilute gas of atoms moving in a symmetric double-well tapping potential. This is described by the normally-ordered many-body Hamiltonian[72]:

$$\hat{H}(t) = \int d^3\mathbf{r} \left[\frac{\hbar^2}{2m} \nabla\hat{\psi}^\dagger \cdot \nabla\hat{\psi} + V\hat{\psi}^\dagger\hat{\psi} + \frac{U_0}{2}\hat{\psi}^\dagger\hat{\psi}^\dagger\hat{\psi}\hat{\psi} \right], \tag{2.1}$$

where m is the atomic mass, $U_0 = 4\pi\hbar^2 a_0/m$ measures the strength of the two-body interaction, and a_0 is the s-wave scattering length. The binary hard-sphere collision model used here to describe interparticle interactions presupposes that all relevant distance scales are larger then $a_0 \sim 1nm$. The Heisenberg picture field operators, $\hat{\psi}(\mathbf{r}, t)$ and $\hat{\psi}^\dagger(\mathbf{r}, t)$, annihilate and create atoms at position $\mathbf{r}$ and commute at equal times according to

$$\left[\hat{\psi}(\mathbf{r}), \hat{\psi}^\dagger(\mathbf{r}')\right] = \delta^3(\mathbf{r} - \mathbf{r}'). \tag{2.2}$$

In terms of these operators, the total atom number operator is

$$\hat{N} = \int d^3\mathbf{r}\hat{\psi}^\dagger(t,\mathbf{r}),\hat{\psi}(t,\mathbf{r}). \tag{2.3}$$

The trapping potential is a double-well potential in which the interwell coupling occurs along the x-axis:

$$V(\mathbf{r}) = b\left(x^2 - q_0^2\right)^2 + \frac{1}{2}m\omega_t^2(y^2+z^2), \tag{2.4}$$

where ω_t is the trap frequency in the $y-z$ plane and where b gives the strength of the confinement in the x direction. This potential has elliptic fixed points at $\mathbf{r}_1 = +q_0\mathbf{x}$, $\mathbf{r}_2 = -q_0\mathbf{x}$, at which the linearised motion is harmonic with frequency $\omega_0 = q_0(8b/m)^{1/2}$. For simplicity, we set $\omega_t = \omega_0$ and scale the length by $r_0 = \sqrt{\hbar/2m\omega_0}$, which is the position uncertainty in a harmonic oscillator ground state. The barrier height is then given by $B = (\hbar\omega_0/8)(q_0/r_0)^2$.

A full analysis of the quantum dynamics resulting from the many-body Hamiltonian Eq. (2.1) is not tractable, however considerable insight can be gained within a two-mode approximation or with a semiclassical picture. For a suitable choice of B, the two lowest single-particle energy eigenstates will lie beneath the barrier, with the third eigenstate separated by a relatively large energy gap. We will assume that the atoms interact sufficiently weakly such that, near zero temperature, they have condensed into the two lowest single-particle states. This enables a treatment of the many-body problem with a two-mode approximation, as Fig. 2.1 illustrates. The resulting model is sufficiently simple to enable an analytic solution to be found for the semiclassical equations, and to permit a tractable numerical comparison of the semiclassical description with the full quantum dynamics. We will first derive the two-mode Hamiltonian before discussing the semiclassical dynamics in Sec. 2.2.

We can expand the potential around each minimum into local harmonic potentials:

$$V(\mathbf{r}) = \tilde{V}^{(2)}(\mathbf{r}-\mathbf{r}_j) + \ \ldots \quad , \tag{2.5}$$

where $j = 1, 2$ and

$$\tilde{V}^{(2)}(\mathbf{r}) = 4bq_0^2|\mathbf{r}|^2. \tag{2.6}$$

The local-mode solutions of the individual wells $u_j(\mathbf{r})$ are then

$$u_j(\mathbf{r}) = \frac{-(-1)^j}{(2\pi r_0^2)^{\frac{3}{4}}} e^{-\frac{1}{4}(x-q_0)^2+y^2+z^2)/r_0^2} \tag{2.7}$$

Figure 2.1: *Two-mode approximation for a condensate in a double-well potential.*

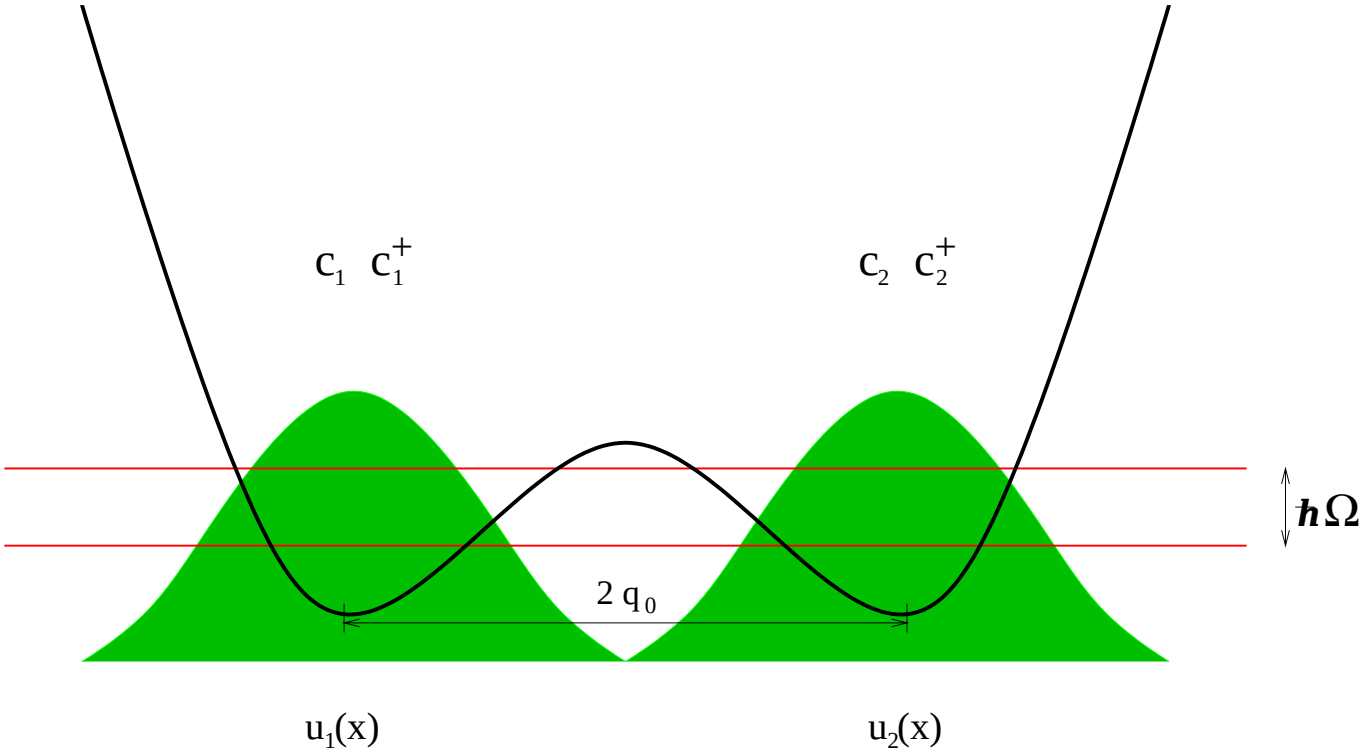

with energy E_0. They are approximately orthogonal with a correction to the orthogonality given by the overlap between the modes of opposite wells:

$$\begin{aligned} \int d^3\mathbf{r} u_j^*(\mathbf{r}) u_k(\mathbf{r}) &= \delta_{j,k} + (1-\delta_{j,k}) e^{-\frac{1}{2}q_0^2/r_0^2} \\ &= \delta_{j,k} + (1-\delta_{j,k})\epsilon, \quad j,k = 1,2. \end{aligned} \tag{2.8}$$

The energy eigenstates of the global double-well potential may then be approximated as linear combinations

$$u_\pm(\mathbf{r}) \approx \frac{1}{\sqrt{2}} \left[u_1(\mathbf{r}) \pm u_2(\mathbf{r}) \right], \tag{2.9}$$

with corresponding eigenvalues $E_\pm = E_0 \pm \mathcal{R}$, and

$$\mathcal{R} = \int d^3\mathbf{r} u_1^*(\mathbf{r}) [V(\mathbf{r}) - \tilde{V}^{(2)}(\mathbf{r} - \mathbf{r}_1)] u_2(\mathbf{r}). \tag{2.10}$$

The matrix element $\mathcal{R}$, which is of order ϵ^1, describes the coupling between the local modes. The tunnelling frequency, Ω, between the two minima is then given by the energy level splitting of these two lowest states:

$$\Omega = \frac{2\mathcal{R}}{\hbar} = \frac{3}{8}\omega_0 \frac{q_0^2}{r_0^2} e^{\frac{1}{2}q_0^2/r_0^2}. \tag{2.11}$$

In the two-mode approximation, we expand the field operators in terms of the local modes and introduce the Heisenberg picture annihilation and creation operators

$$\hat{c}_j(t) = \int d^3\mathbf{r} u_j^*(\mathbf{r})\hat{\psi}(\mathbf{r},t) \tag{2.12}$$

so that $[\hat{c}_j, \hat{c}_k^\dagger] \approx \delta_{jk}$. The validity of this expansion is ensured when the overlap is small:

$$\frac{\mathcal{R}}{E_0} = \frac{\Omega}{\omega_0} \ll 1. \tag{2.13}$$

The ratio of the separation of the minima of the global potential $V(\mathbf{r})$ to the position uncertainty in the states $u_j(\mathbf{r})$ can be as small as $2q_0/r_0 = 6$ (as in some of the simulations presented in this thesis), and yet still satisfy this condition. The many-body Hamiltonian then reduces to the following two-mode approximation:

$$\hat{H}_{2a}(t) \;=\; E_0(\hat{c}_1^\dagger\hat{c}_1 + \hat{c}_2^\dagger\hat{c}_2) + \frac{\hbar\Omega}{2}(\hat{c}_1\hat{c}_2^\dagger + \hat{c}_1^\dagger\hat{c}_2) + \hbar\kappa\left((\hat{c}_1^\dagger)^2\hat{c}_1^2 + (\hat{c}_2^\dagger)^2\hat{c}_2^2\right), \tag{2.14}$$

where $\kappa = U_0/2\hbar V_{\text{eff}}$, and $V_{\text{eff}}^{-1} = \int d^3\mathbf{r}|u_0(\mathbf{r})|^4$ is the effective mode volume of each well. Here we have retained only the self-interaction contribution to the nonlinearity, as the cross-interaction contributions are of order ϵ^2.

The two-mode approximation is valid when many-body interactions produce only small modifications of the ground state properties of the individual potentials. This is true when

$$\hbar\omega_0 = \frac{\hbar^2}{2mr_0^2} \gg \frac{N|U_0|}{V_{\text{eff}}}. \tag{2.15}$$

Using $V_{\text{eff}} \approx 8\pi^{3/2}r_0^3$ for this case, we obtain the following condition on the number of atoms:

$$N \ll \frac{r_0}{|a_0|}. \tag{2.16}$$

If we choose values of $r_0 = 5\ \mu m$ and $a_0 = 5\ nm$, then $N = 100$ satisfies this criterion. Thus the two-mode approximation is valid for small number of atoms compared to current experiments with $N = 10^3 \leftrightarrow 10^6$.

In studying the semiclassical and quantum dynamics of the two-mode condensate, we will only be concerned with the case where $\kappa > 0$, corresponding to repulsive interaction between atoms. A negative κ is also possible, although gasses with this attractive interaction are rarely used in experiments. Because we have chosen to study condensates in spatially separated wells, the nonlinear cross-interaction between the condensates is negligible. However, one may also study overlapping two-species condensates, as is common in the literature, where such terms are important.

2.2 Semiclassical dynamics

We begin the semiclassical analysis with the mean-field approximation. For this we employ the Hartree approximation [185] for a fixed number of atoms N, and write the atomic state vector as

$$|\Psi_N(t)\rangle = \frac{1}{\sqrt{N!}}\left[\int d^3\mathbf{r}\Phi_N(\mathbf{r},t)\hat{\psi}^\dagger(\mathbf{r},0)\right]^N|0\rangle, \tag{2.17}$$

where $|0\rangle$ is the vacuum. The self-consistent Gross-Pitaevskii (GP) equation[1] for the condensate wave function $\Phi_N(\mathbf{r},t)$ follows from the Schrödinger equation $i\hbar|\dot{\Psi}_N(t)\rangle = \hat{H}(0)|\Psi_N(t)\rangle$, and is given by [106, 154, 185]

$$i\hbar\frac{\partial\Phi_N}{\partial t} = \left[-\frac{\hbar^2}{2m}\nabla^2 + V(\mathbf{r}) + NU_0|\Phi_N|^2\right]\Phi_N. \tag{2.18}$$

For a particular choice of the global potential $V(\mathbf{r})$, Eq. (2.18) can be solved numerically for a given initial condition. We will assume a factorised solution $\Phi_N(\mathbf{r},t) = \phi_N(x,t)\Phi_N(y,z,t)$ and only consider the nonharmonic motion in the x-direction. The resulting equation is

$$i\hbar\frac{\partial\phi_N}{\partial t} = \left[-\frac{\hbar^2}{2m}\frac{\partial^2}{\partial x^2} + V(x) + NU_0|\phi_N|^2\right]\phi_N. \tag{2.19}$$

Before proceeding to a numerical solution of this equation we will first derive an approximate two-mode model for which the Gross-Pitaevskii equation is analytically solvable.

2.2.1 Two-mode semiclassical analysis

Deriving the equations of motion

We begin by expanding the mean field ϕ_N in terms of the local modes as follows

$$\phi_N(x,t) = \mathbf{u}(x)\cdot\mathbf{A}(t), \tag{2.20}$$

where

$$\begin{aligned}\mathbf{u}(x) &= (u_1(x), u_2(x)) \\ &= (2\pi r_0^2)^{-\frac{1}{4}}\left(e^{-(x-q_0)^2/4r_0^2}, -e^{-(x+q_0)^2/4r_0^2}\right) \qquad (2.21)\\ \mathbf{A}(t) &= (A_1(t), A_2(t))\,. \qquad (2.22)\end{aligned}$$

[1] Also known as the nonlinear Schrödinger equation

Using this expansion, Eq. (2.19) becomes,

$$i\hbar\mathbf{u}(x)\cdot\dot{\mathbf{A}}(t) \simeq \left(V(x)-\overline{V}^{(2)}(x)+NU_0\left(u_1^2(x)|A_1(t)|^2+u_2^2(x)|A_2(t)|^2\right)\right)\mathbf{u}(x)\cdot\mathbf{A}(t), \tag{2.23}$$

where cross-interaction terms have been neglected in the nonlinear term and where

$$\begin{aligned}\overline{V}^{(2)}(x)\mathbf{u}(x) &= \frac{\hbar^2}{2m}\frac{\partial^2}{\partial x^2}\mathbf{u}(x)\\ &= \frac{m\omega_0^2}{2}\mathrm{diag}\left((x-q_0)^2-2r_0^2,(x+q_0)^2-2r_0^2\right)\mathbf{u}(x).\end{aligned} \tag{2.24}$$

After a little algebraic manipulation and an integration over x, we get the following equation for the linear evolution of $\mathbf{A}$:

$$i\hbar\dot{\mathbf{A}} = \begin{pmatrix} \frac{R_{11}-S_{12}R_{21}}{1-S_{12}S_{21}} & \frac{R_{12}-S_{12}R_{22}}{1-S_{12}S_{21}} \\ \\ \frac{R_{21}-S_{21}R_{11}}{1-S_{21}S_{21}} & \frac{R_{22}-S_{21}R_{12}}{1-S_{21}S_{21}} \end{pmatrix}\mathbf{A}, \tag{2.25}$$

where

$$R_{jj} = \int(V-V_{jj}^{(2)})u_j^2dx \simeq \frac{3\hbar\omega_0 r_0^2}{16q_0^2}+\frac{\hbar\omega_0}{2} \tag{2.26a}$$

$$R_{ij} = \int(V-V_{jj}^{(2)})u_iu_jdx \simeq \frac{\hbar\Omega}{2} \tag{2.26b}$$

$$S_{ij} = \int u_iu_jdx = e^{-q_0^2/2r_0^2} = \epsilon \tag{2.26c}$$

for $i \neq j$. If the overlap between the local mode functions is sufficiently small, i.e. $(q_0/r_0)^2 \gg 1$, then $|R_{jj}| \gg |S_{ij}R_{ji}|$ and $|R_{ij}| \gg |S_{ij}R_{jj}|$. This leads to the following approximate equations of motion:

$$\begin{aligned}i\hbar\dot{\mathbf{A}} &= \begin{pmatrix} R_{11} & R_{12} \\ R_{21} & R_{22} \end{pmatrix}\mathbf{A}\\ &= \begin{pmatrix} \frac{\hbar\nu}{2} & \frac{\hbar\Omega}{2} \\ \frac{\hbar\Omega}{2} & \frac{\hbar\nu}{2} \end{pmatrix}\mathbf{A},\end{aligned} \tag{2.27}$$

where $\nu = 3\omega_0 r_0^2/(8q_0^2)+\omega_0$.

Similar considerations of the nonlinear terms lead to the full equations of motion:

$$i\hbar\dot{\mathbf{A}} = \begin{pmatrix} \frac{\hbar\nu}{2}+\frac{NU_0|A_{11}|^2}{V_{\mathrm{eff}}} & \frac{\hbar\Omega}{2} \\ \frac{\hbar\Omega}{2} & \frac{\hbar\nu}{2}+\frac{NU_0|A_{22}|^2}{V_{\mathrm{eff}}} \end{pmatrix}\mathbf{A}. \tag{2.28}$$

Using $\vec{M} = \begin{pmatrix} 0 & 1 \\ 1 & 0 \end{pmatrix}$, Eq. (2.28) can be written in the form

$$i\dot{\mathbf{A}} = \frac{\nu}{2}\mathbf{A} + \frac{\Omega}{2}\vec{M}\mathbf{A} + 2N\kappa\mathrm{diag}(|A_{11}|^2 + |A_{22}|^2)\mathbf{A}, \tag{2.29}$$

This is the discrete self-trapping equation considered in [10], which describes a system of coupled anharmonic oscillators. Finally if we let $b_j = e^{i\nu t/2}A_j$, we get the semiclassical equations of motion:

$$\dot{b}_1 = \frac{-i\Omega}{2}b_2 - 2i\kappa N|b_1|^2 b_1 \tag{2.30a}$$

$$\dot{b}_2 = \frac{-i\Omega}{2}b_1 - 2i\kappa N|b_1|^2 b_2. \tag{2.30b}$$

These equations share the same form with the Heisenberg equations of motion for the annihilation and creation operators, $\hat{c}_j$ and $\hat{c}_j^\dagger$.

The total particle number constraint $|b_1|^2 + |b_2|^2 = 1$ provides a constant of the motion, which enables us to rewrite Eq. (2.30) in terms of three real variables, x, y, z defined by

$$x = \frac{1}{2}(|b_2|^2 - |b_1|^2) \tag{2.31a}$$

$$y = -\frac{i}{2}(b_1^* b_2 - b_2^* b_1) \tag{2.31b}$$

$$z = \frac{1}{2}(b_1^* b_2 + b_1 b_2^*). \tag{2.31c}$$

The equations of motion then become

$$\dot{x} = -\Omega y \tag{2.32a}$$

$$\dot{y} = \Omega x - 4\kappa N z x \tag{2.32b}$$

$$\dot{z} = 4\kappa N y x, \tag{2.32c}$$

which trace out motion on the surface of a sphere defined by

$$\frac{1}{4} = x^2 + y^2 + z^2. \tag{2.33}$$

Analytic solution

The semiclassical equations for the first order moments (Eq. (2.32)) can be analysed by finding the constants of the motion. If Eq. (2.32a) is substituted into Eq. (2.32c) and the result integrated, we get another constant of the motion:

$$C_1 = z + \frac{2\kappa N}{\Omega}x^2 = z_0 + \frac{2\kappa N}{\Omega}x_0^2. \tag{2.34}$$

This describes a parabolic surface in three-dimensional space. The intersection of this surface and that of the sphere described by Eq. (2.33) is the line (parametrised by s):

$$(x, y, z) = \left(s, z_0 + 2\Theta\left(x_0^2 - s^2\right), \pm\sqrt{\frac{1}{4} - (z_0 + 2\Theta x_0^2)^2 + (8\Theta^2 x_0^2 + 4\Theta z_0 - 1)s^2 - 4\Theta^2 s^4} \right), \tag{2.35}$$

which describes the trajectories of the system for the initial conditions $x(0) = x_0$ and $z(0) = z_0$. The constant $\Theta = \kappa N/\Omega$ is the normalised multiparticle interaction strength. Using these two constants of motion, the set of equations also reduces to the following first-order nonlinear differential equation:

$$\dot{x} = \pm\sqrt{\alpha + \beta x^2 - \gamma x^4}, \tag{2.36}$$

where $\alpha = \Omega^2(\frac{1}{4} - C_1^2)$, $\beta = \Omega(4\kappa N C_1 - \Omega)$ and $\gamma = 4\kappa^2 N^2$. This equation corresponds to that of a particle moving in the quartic potential $V_1(x) = \frac{1}{4}\gamma x^4 - \frac{1}{2}\beta x^2$. When $\beta > 0$, $V_1(x)$ is a double-well potential with minima at $x_\pm = \pm\sqrt{\beta/(2\gamma)}$ separated by a barrier of height $V_B = \frac{1}{8}\beta^2/\gamma$.

A solution to Eq. (2.36) can be written down exactly in terms of the Jacobi elliptic functions. To see this, we can rewrite Eq. (2.36) as

$$\int_0^t dt' = \int_{x_0}^{x} \frac{dx'}{\pm\sqrt{\gamma(x'^2 - A)(B - x'^2)}}, \tag{2.37}$$

where the constants A and B are

$$A = \frac{\beta - \sqrt{\beta^2 + 4\alpha\gamma}}{2\gamma} \tag{2.38a}$$

$$B = \frac{\beta + \sqrt{\beta^2 + 4\alpha\gamma}}{2\gamma}. \tag{2.38b}$$

The form of the solution depends upon the values of A and B, which in turn depend on the initial conditions and on the parameter Θ. The problem is greatly simplified if the initial conditions are chosen first. We are interested in what happens to the Josephson tunnelling effect when the atom interactions are present, so we will look at two cases in which the initial conditions lead to full tunnelling oscillations in the atom-number difference x. In the first case, $x_0 = z_0 = 0$ and $y_0 = 1/2$, which means that the atoms are initially distributed equally across both wells but with maximum tunnelling momentum. In the absence of collisions, all the atoms will move to one well and then the other. The

Figure 2.2: *The Θ dependence of (a) the period and (b) the amplitude of the semiclassical solutions of the double-well system. The dashed line in the plots corresponds to all the atoms starting in one well ($x_0 = \frac{1}{2}$, $z_0 = 0$), while the continuous line corresponds to the atoms being initially distributed equally between the wells but with maximum tunnelling momentum ($x_0 = 0$, $z_0 = 0$). In (a), the period is scaled by $T_0 = 2\pi/\Omega$, and in (b) an amplitude of 0.5 corresponds to full tunnelling oscillations. The critical value of Θ is $\Theta_c = 1$.*

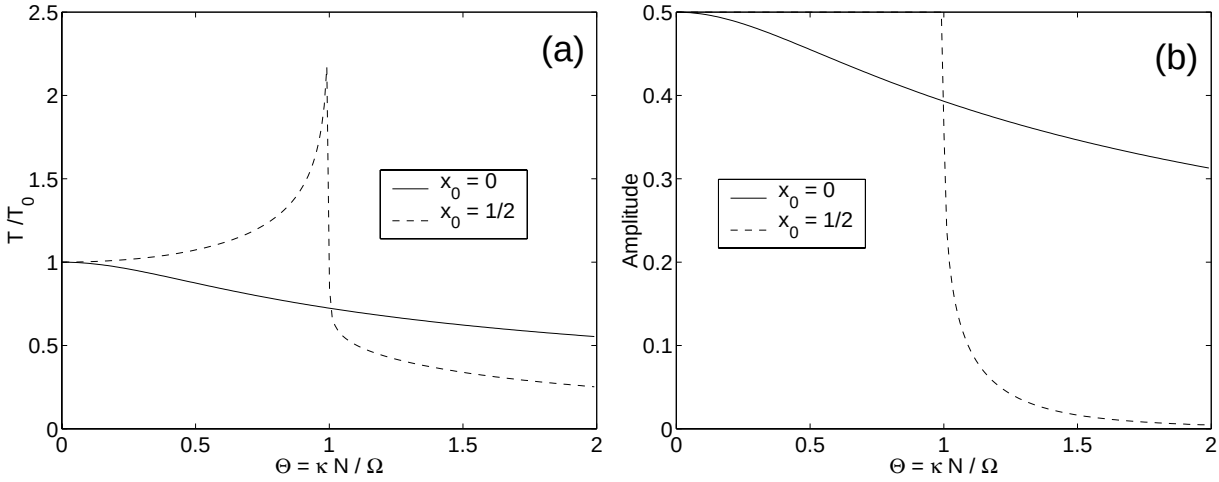

constants in Eq. (2.37) reduce to $A = -\frac{1}{8}(\sqrt{1+4\Theta^2}+1)/\Theta \leq 0$ and $B = \frac{1}{8}(\sqrt{1+4\Theta^2}-1)/\Theta \geq 0$, and so the solution in terms of elliptic functions is

$$x(t) = \sqrt{\frac{\sqrt{4\Theta^2+1}-1}{8\Theta^2}}\left(\mathrm{cn}(\Omega(4\Theta^2+1)^{\frac{1}{4}}t - K(k); k(\Theta)) - 1\right) \tag{2.39a}$$

$$k(\Theta) = \sqrt{\frac{1}{2} - \frac{1}{2\sqrt{4\Theta^2+1}}}. \tag{2.39b}$$

This solution is always oscillatory with a period $4K(k)/(\Omega(4\Theta^2+1)^{1/4})$, where $K(k)$ is the complete elliptic integral of the first kind. In the limit of weak atom interactions ($\Theta \ll 1$), $k \to 0$, and the elliptic function reduces to a cosine with frequency Ω and amplitude $\frac{1}{2}$. This corresponds to full tunnelling oscillations. The modulus k increases with Θ, which decreases both the period and the amplitude. When the collisions dominate, i.e. $\Theta \gg 1$, $k \to \frac{1}{\sqrt{2}}$ and so the period approaches $4K(\frac{1}{\sqrt{2}})/(\Omega\sqrt{2\Theta})$ and the amplitude goes to zero. Figure 2.2 illustrates the dependence of the period and amplitude on Θ.

In the second case, the systems starts with all the atoms in one well, i.e. $y_0 = z_0 = 0$ and $x_0 = \frac{1}{2}$. In this case, the constants in Eq. (2.37) become $A = \frac{1}{4}(1 - 1/\Theta^2)$ and $B = \frac{1}{4} \geq 0$. The sign of A depends on the value of Θ, and so we must distinguish between

the two cases. For $\Theta \leq 1$, $A < 0$ and the solution to Eq. (2.37) becomes

$$x(t) = \frac{1}{2}\mathrm{cn}(\Omega t;\Theta)). \tag{2.40}$$

Once again, this reduces to ordinary sinusoidal oscillations when $\Theta \ll 1$, as shown in Fig. 2.3(a). As Θ increases, the amplitude of the oscillations does not diminish, but the period $4K(k)/\Omega$ increases and the waveform becomes more anharmonic (see Fig. 2.3(b)). As the critical value of $\Theta_c = 1$ is reached, the period becomes infinite, the solution asymptotically decays to zero (Fig. 2.3(c)).

Above the critical value, in other words $A > 0$, the solution is

$$x(t) = \frac{1}{2}\mathrm{dn}(\Omega\Theta t; k(\Theta)) \tag{2.41a}$$

$$k(\Theta) = 1 - \sqrt{1 - \frac{1}{\Theta^2}}. \tag{2.41b}$$

So above the critical value, the solution is again periodic, with period $2K(k)/(\Omega\Theta)$, but with diminishing peak-to-peak amplitude: $1 - \sqrt{1-k^2}$ (Fig. 2.3(d)). When $\Theta \gg 1$, the condensate remains trapped in one well. Figure 2.2 illustrates the Θ dependence of the period and amplitude.

Fixed points

The fixed points of the system provide an insight into the dynamics of the system for general initial conditions. The fixed points are

$$(x_\infty, y_\infty, z_\infty)_1 = (0, 0, \frac{1}{2}) \tag{2.42a}$$

$$(x_\infty, y_\infty, z_\infty)_2 = (0, 0, -\frac{1}{2}) \tag{2.42b}$$

$$(x_\infty, y_\infty, z_\infty)_3 = \frac{1}{4}(\sqrt{4\Theta^2 - 1}, 0, 1)\Theta \tag{2.42c}$$

$$(x_\infty, y_\infty, z_\infty)_4 = \frac{1}{4}(-\sqrt{4\Theta^2 - 1}, 0, 1)\Theta. \tag{2.42d}$$

The stability of these points can be calculated by expanding $x = x_\infty + \xi/\Omega$ and $y = y_\infty + \psi/\Omega$, which leads to the linearised equation for $\mathbf{X} = (\xi, \psi)'$:

$$\dot{\mathbf{X}} = \begin{pmatrix} 0 & -1 \\ 1 - 4\Theta z_\infty + \frac{4\Theta x_\infty^2}{z_\infty} & \frac{4\Theta x_\infty y_\infty}{z_\infty} \end{pmatrix} \mathbf{X}. \tag{2.43}$$

Figure 2.3: *The semiclassical evolution of $x(t)$ for different values of the parameter $\Theta = \kappa N/\Omega$. In (a) $\Theta = 0.0$, in (b) $\Theta = 0.9$, in (c) $\Theta = 1.0$, and in (d) $\Theta = 1.1$. The dashed line corresponds to all the atoms starting in one well ($x_0 = \frac{1}{2}$, $z_0 = 0$), while the continuous line corresponds to the atoms being initially distributed equally between the wells but with maximum tunnelling momentum ($x_0 = 0$, $z_0 = 0$). The critical value of Θ is $\Theta_c = 1$.*

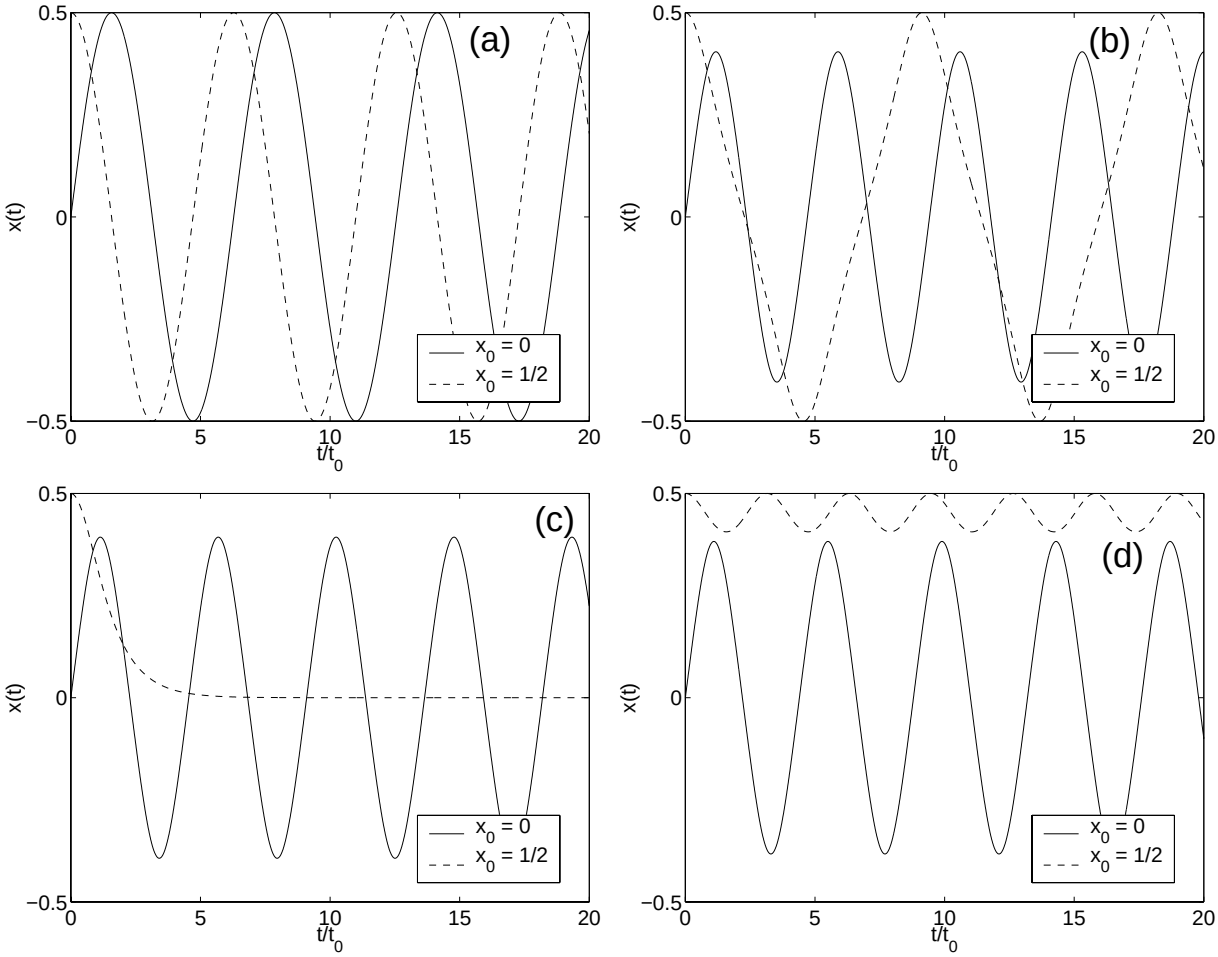

Figure 2.4: *Bifurcation diagrams for fixed points of the semiclassical system, showing the* Θ *dependence of (a)* z_∞ *and (b)* x_∞*. The continuous line corresponds to elliptic fixed points while the dashed line corresponds to the saddle fixed points. A pitchfork bifurcation occurs at* $\Theta = \frac{1}{2}$*.*

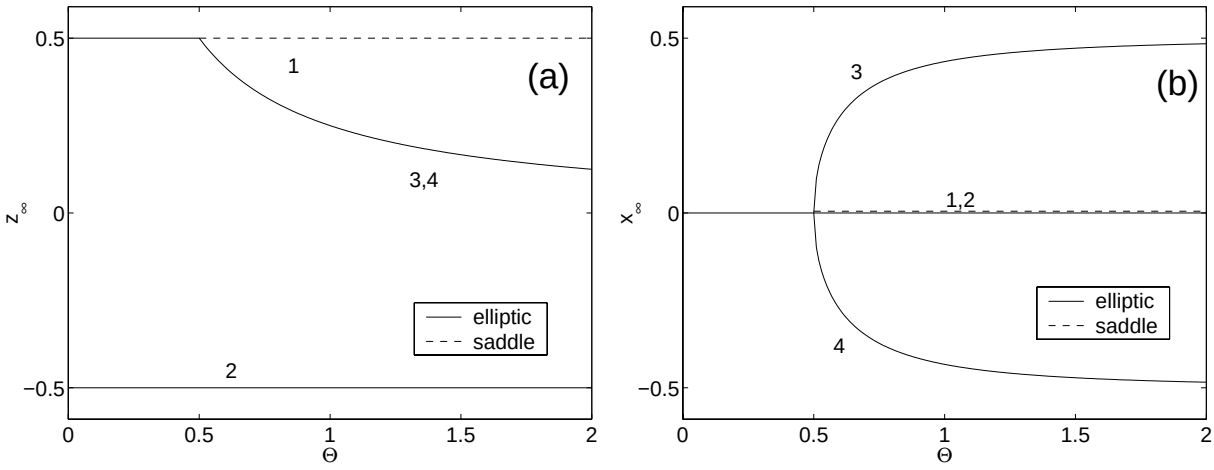

The resultant eigenvalues for each fixed point are:

$$\lambda_1 = \pm\sqrt{2\Theta - 1} \tag{2.44a}$$

$$\lambda_2 = \pm i\sqrt{2\Theta + 1} \tag{2.44b}$$

$$\lambda_{3,4} = \pm i\sqrt{4\Theta^2 - 1} \tag{2.44c}$$

Thus we have a pitchfork bifurcation at $\Theta = \frac{1}{2}$. For $\Theta < \frac{1}{2}$, there are two elliptic points at the top and bottom of the Bloch sphere. Above the bifurcation, i.e. $\Theta > \frac{1}{2}$, the elliptic point at the top of the sphere turns into a saddle point, and two elliptic points split off from the north pole and move towards the equator at $x = \pm\frac{1}{2}$. All of this is illustrated in the bifurcation diagrams in Fig. 2.4.

Phase-space portraits

We can analyse the motion away from the fixed points by plotting the phase-space portraits. This is most easily done by using polar co-ordinates $(\theta, \phi) = (\arccos 2z, \arctan y/x)$, so that $x = \frac{1}{2}\cos\phi\sin\theta$, $y = \frac{1}{2}\sin\phi\sin\theta$ and $z = \frac{1}{2}\cos\theta$. The equations of motion in polar co-ordinates become:

$$\dot{\theta} = -\kappa N \sin 2\phi \sin\theta \tag{2.45a}$$

$$\dot{\phi} = \Omega - \kappa N\,(1 + \cos 2\phi)\cos\theta. \tag{2.45b}$$

In these variables, regular Josephson tunnelling is described by the contours of constant ϕ. Numerical integration of these equations gave the phase portraits shown in Fig. 2.5. In these plots, the north pole corresponds to the bottom edge of the window, the south pole to the top edge, the point $x = -\frac{1}{2}$ to the centre of the plot and the point $x = \frac{1}{2}$ to the midpoint of the vertical edges.

Now the bifurcation point $\Theta = \frac{1}{2}$ is not the same as the critical point $\Theta_c = 1$. When $\Theta < \frac{1}{2}$, all trajectories in phase space orbit around the sphere approximately parallel to the equator, as shown in Fig. 2.5(a), and this corresponds to regular tunnelling. When $\Theta > \frac{1}{2}$, trajectories in the lower portion of the sphere still execute tunnelling oscillations, but in the upper portion of the sphere, the motion is trapped on either the right or the left half of the sphere in orbits around the two new elliptic fixed points (Fig. 2.5(b)). The separatrices of the saddle point at the top of the sphere bound the two types of orbits (Fig. 2.5(d)). The critical point is then merely when a trajectory starting at $x = \pm\frac{1}{2}$ lies on the separatrix (Figs. 2.5(c&d)). Above the critical point, this trajectory will travel around the new elliptic point, in orbits of decreasing size as the elliptic point moves closer to $x = \pm\frac{1}{2}$ (Fig. 2.5(e)). Even for $\Theta > 1$, there will still be trajectories that can cross from one side of the sphere to the other in tunnelling oscillations. A trajectory that starts at $x_0 = 0$, will always be able to do this (see Fig. 2.5(e)). This is consistent with the dynamics shown in Fig. 2.3.

2.2.2 The Gross-Pitaevskii equation

We now turn to the full numerical solution of the Gross-Pitaevskii (GP) equation (Eq. (2.18)) for the double-well system. Rewriting the GP equation using normalised variables facilitates the numerical computation:

$$i\frac{\partial u(z,\tau)}{\partial \tau} = \left[-\frac{1}{2}\frac{\partial^2}{\partial z^2} + \frac{z^4}{32z_0^2} - \frac{z^2}{16} + \frac{z_0^2}{32} + K|u(z,\tau)|^2\right] u(z,\tau), \tag{2.46}$$

where $\tau = t/t_0$, $z = x/r_0$, $z_0 = q_0/r_0$ and $u = \sqrt{r_0}\Phi_N$. The scaling constants are $t_0 = 1/(2\omega_0)$ and $r_0 = \sqrt{\hbar t_0/m} = \sqrt{\hbar/(2m\omega_0)}$. The coefficient of the nonlinear term is $K = 2\sqrt{\pi}\kappa N/\omega_0 = 8\sqrt{\pi^3}\Theta t_0/T_0$, where T_0 is the period of the tunnelling oscillations. To generate numerical solutions from this scaled GP equation, a split-step Fourier semi-implicit method was used. The details of this algorithm may be found in the second half of this thesis. The code was adapted from the Multi-Dimensional Simulator program of

Figure 2.5: *The phase portrait of semiclassical dynamics in the double-well system plotted in polar co-ordinates, for different values of the parameter* $\Theta = \kappa N/\Omega$. *In (a)* $\Theta = 0.250$, *in (b)* $\Theta = 0.505$, *in (c) and (d)* $\Theta = 1.00$, *and in (e)* $\Theta = 5.00$. *In these coordinates,* $x = \frac{1}{2}\cos\phi\sin\theta$, $y = \frac{1}{2}\sin\phi\sin\theta$ *and* $z = \frac{1}{2}\cos\theta$. *Maximum occupation of each well corresponds to* $(\theta, \phi) = (\pi/2, 2n\pi)$ *and* $(\theta, \phi) = (\pi/2, \pi)$, *for* $n = 0, 1$.

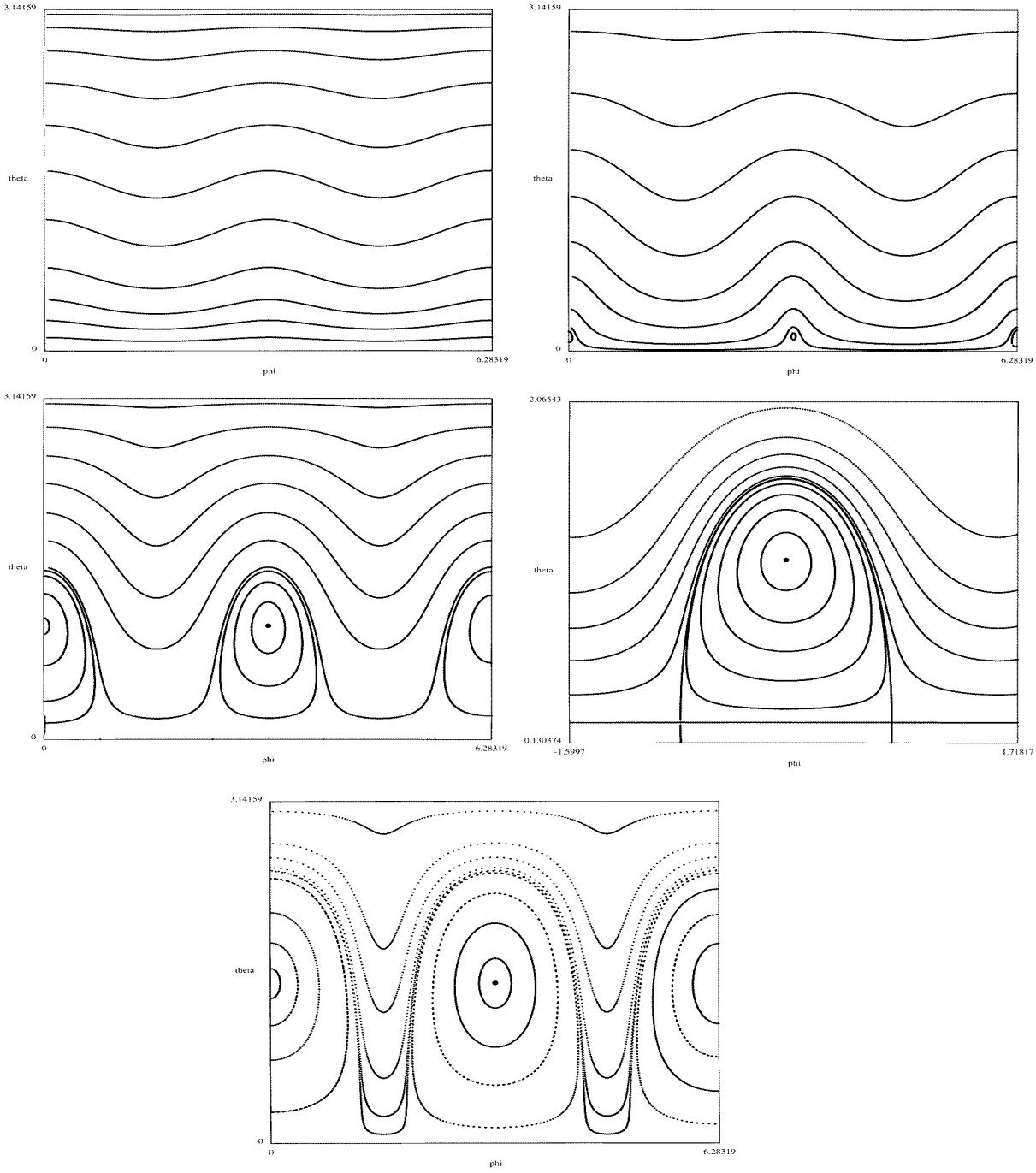

Figure 2.6: *The mean-field ground state for a potential with minima at $x = \pm 4r_0$. The continuous line is the ground-state wave function for the double-well potential calculated from the GP equation. The dashed line is the ground-state mode of the quadratic approximation to the potential at $x = q_0$. The dotted line shows the shape of the quartic potential. The scaling of the vertical axis is arbitrary.*

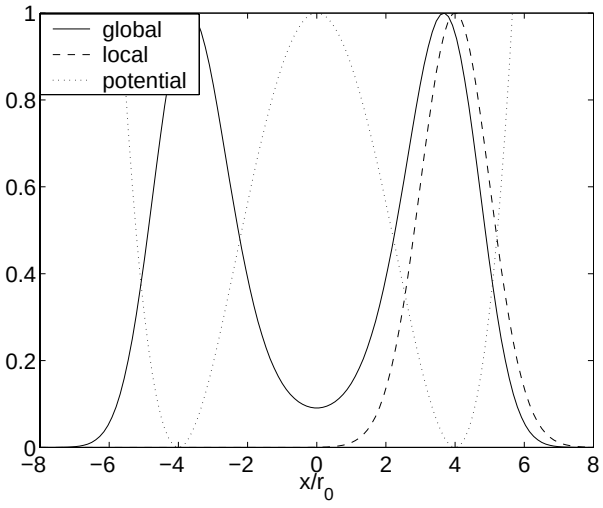

Drummond[49, 176][2]

If we simulate Eq. (2.46), for a potential with minima at $z = \pm z_0 = \pm 4$ and with $K = 0$, we see that there are high frequency oscillations superimposed on the regular tunnelling motion, as shown in Figs. 2.7(a) and 2.8(a). The high frequency components are even larger in amplitude in the $z_0 = \pm 3$ case (Figs. 2.7(e) and 2.8(e)). The reason for these components is revealed in Fig. 2.6. This figure shows the ground-state wave function of the double-well potential, which is calculated by evolving the GP equation in imaginary time. For double wells with a ratio of $z_0 = q_0/r_0$ near these values, the global wave function cannot be expanded in terms of the ground-state modes of the local quadratic potential. The presence of the other well has an effect on the local mode that cannot be neglected, due to the relatively large overlap between the two local modes. The most striking effect that can be seen is that the appropriate local modes have been translated toward the origin: In the $z_0 = 4$ potential, the peak of the wave function is located at $z = 3.65$. Some improvement can be made if we choose a Gaussian centred at $z = 3.65$ to be the initial state. This suppresses all but one of the higher frequencies, as Figs. 2.7(b) and 2.8(b) show. Not all of this extraneous motion disappears because the shape of the most appropriate local wave functions has also changed, and does not fit to symmetric

[2]See Sec. 7.4 for a brief description of the algorithm

Table 2.1: *Calculations of the tunnelling period T_0/t_0, based on different choices of z_0', with comments on the significance of each choice. The tunnelling frequency is calculated from* $\Omega = \frac{3}{8}\omega_0 {z_0'}^2 \exp(-\frac{1}{2}{z_0'}^2)$.

${z_0'}^3$	$T_0/t_0 = 4\pi\omega_0/\Omega$	Comments
4.00	6.24×10^3	Position of well minimum
3.65	1.97×10^3	Maximum of local mode
3.40	938	Minimises high frequency components
3.21	562	Corresponds to observed tunnelling period
3.11	439	Calculated from critical value of Θ

Gaussians. If the position of the initial distribution is reduced further to $z = 3.4$, then the unwanted oscillations are reduced to a minimum (Figs. 2.7(c) and 2.8(c)), although there are now several contributing frequencies.

The question arises how to calculate the tunnelling frequency Ω, which depends on the overlap of the local wave functions. If the local modes are no longer centred at the minima of the trapping potential, then the calculation of Ω based on z_0 would no longer be accurate. Could the calculation be done assuming the same form for Ω but with z_0 replaced by z_0', chosen to be the centre of the initial distribution that gives the cleanest Josephson oscillations? In fact the observed period corresponds to a value of $z_0' = 3.21$, which is smaller again, evidently because the local potentials are now asymmetric, and skewed towards the origin. Starting at this value does not give the cleanest oscillations, as shown in Figs. 2.7(d) and 2.8(d). The different results for the calculation of the tunnelling period are summarised in the Table 2.1.

What remains of the self-trapping effect for strong atom interactions in these GP simulations? Figures 2.9 and 2.10 show the evolution of atom density and the mean position calculated from this, for different collisional strengths, for a $z_0 = 4.0$ trapping potential and an initial distribution centred at $z = 3.65$. The tunnelling dynamics exhibit the qualitative predictions of the two-mode analysis. There is a critical value of the nonlinearity ($0.1015 < K_c < 0.1020$) which marks the boundary between two distinct types of behaviour. Below the critical value (Figs. 2.9(a-c) and 2.10(a-c)), we see full Josephson tunnelling oscillations, with the oscillations becoming slower and more anharmonic as K increases towards the critical value. Tunnelling is inhibited above the critical value, with

Figure 2.7: *Evolution of the mean position of a condensate in a double-well potential with minima at $x = \pm 4r_0$ (in (a) to (d)) and $x = \pm 3r_0$ (in (e) and (f)), calculated from the GP equation. The high frequency components present in the tunnelling waveform for different initial conditions can be seen. The initial distribution is centred at $4.00z_0$ in (a), $3.65z_0$ in (b), $3.40z_0$ in (c), $3.21z_0$ in (d), $3.00z_0$ in (e), and $2.30z_0$ in (f).*

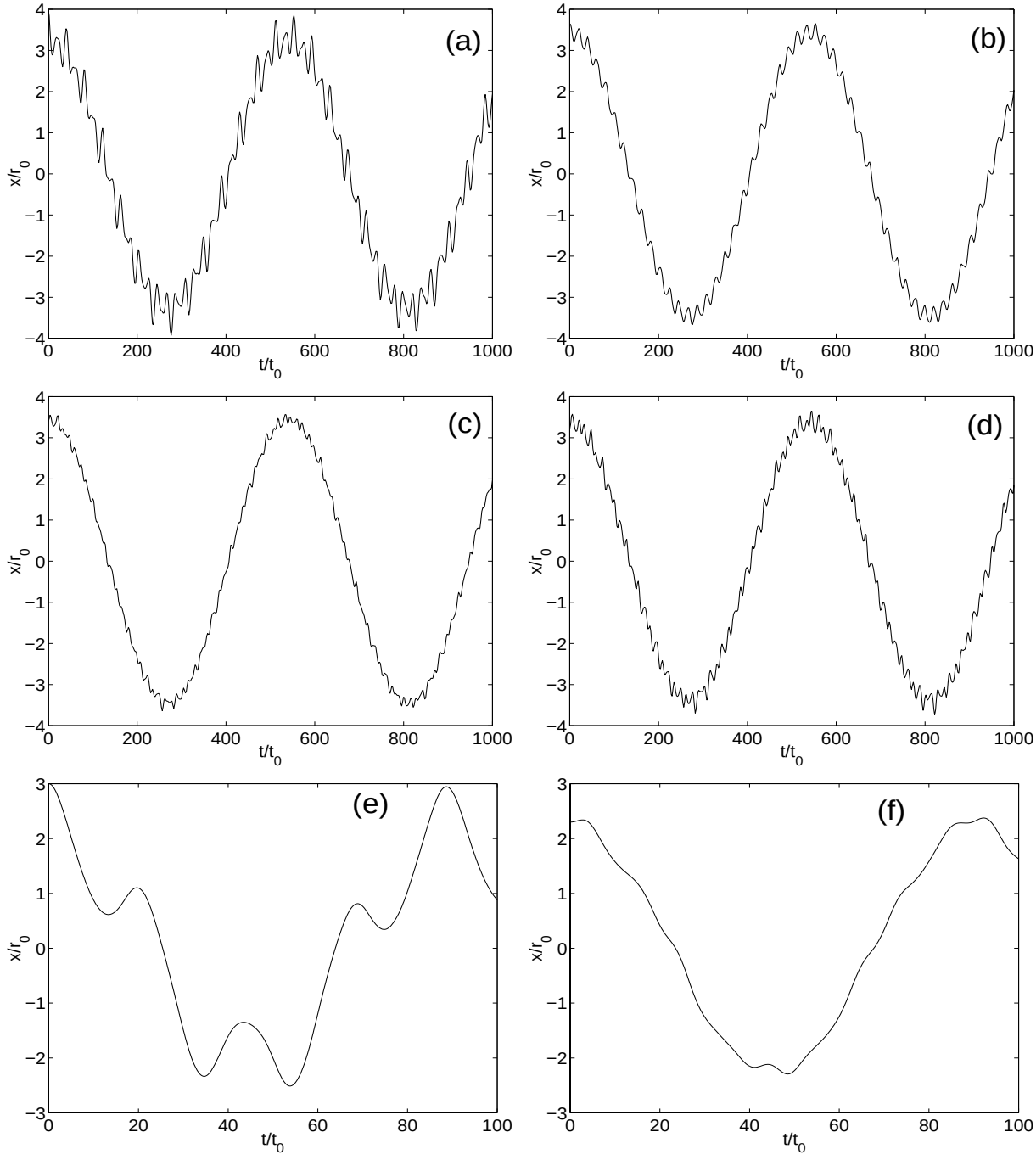

Figure 2.8: *Spectrum of the tunnelling oscillations of a condensate in a double-well potential with minima at $x = \pm 4r_0$ (in (a) to (d)) and $x = \pm 3r_0$ (in (e) and (f)), calculated from the GP equation. The high frequency components present in the tunnelling waveform for different initial conditions can be seen. The initial distribution is centred at $4.00z_0$ in (a), $3.65z_0$ in (b), $3.40z_0$ in (c), $3.21z_0$ in (d), $3.00z_0$ in (e), and $2.30z_0$ in (f).*

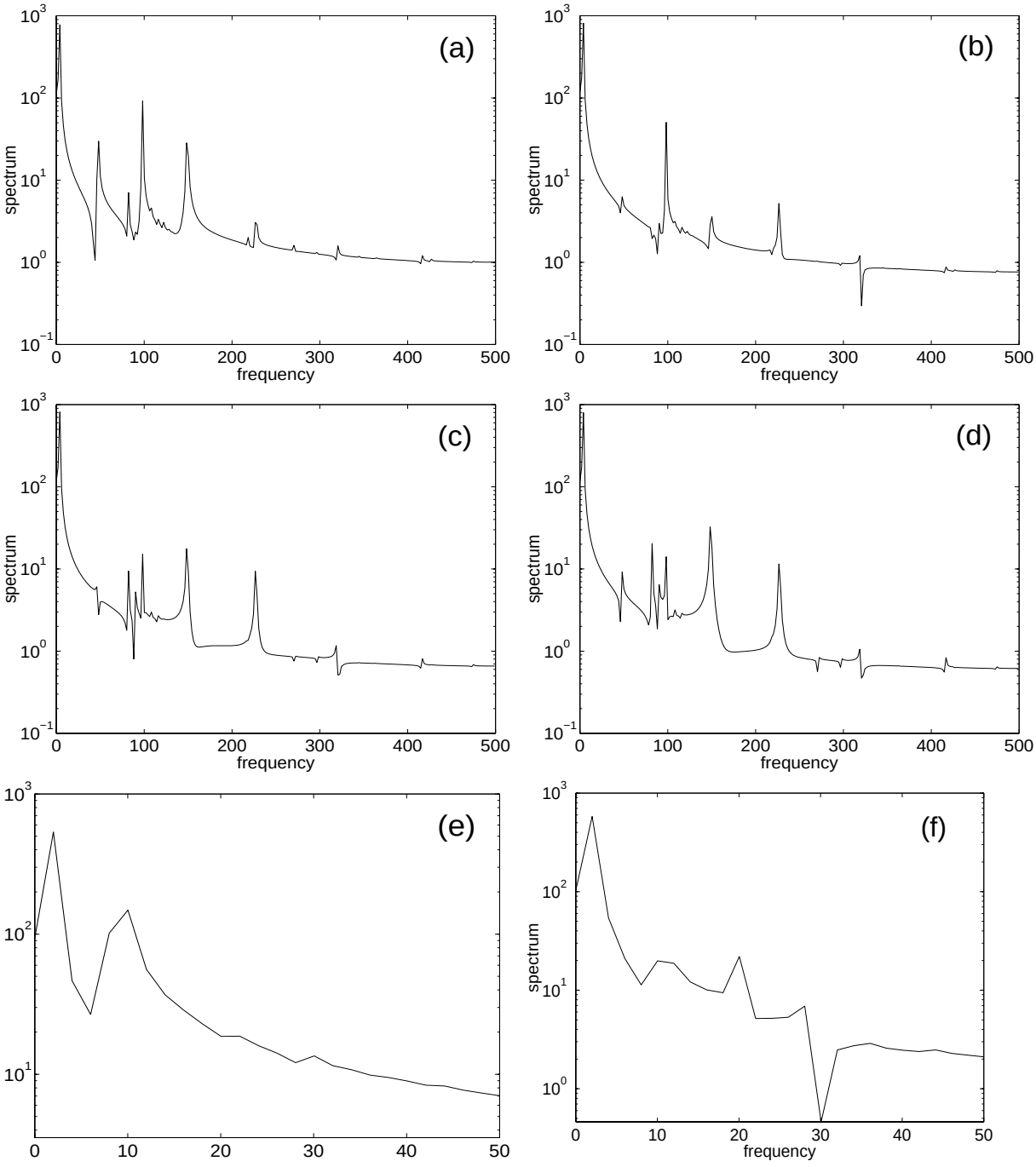

Figure 2.9: *Evolution of the atom density of a condensate in a double-well potential with minima at $x = \pm 4r_0$, calculated from the GP equation with different strengths of the nonlinear atom interactions, both above and below the critical value. In (a) $K = 0.0000$, in (b) $K = 0.1000$, in (c) $K = 0.1015$, in (d) $K = 0.1020$, in (e) $K = 0.1500$, and in (f) $K = 0.5000$. Note that (a), (e) and (f) extend for only half the time as (b) to (d).*

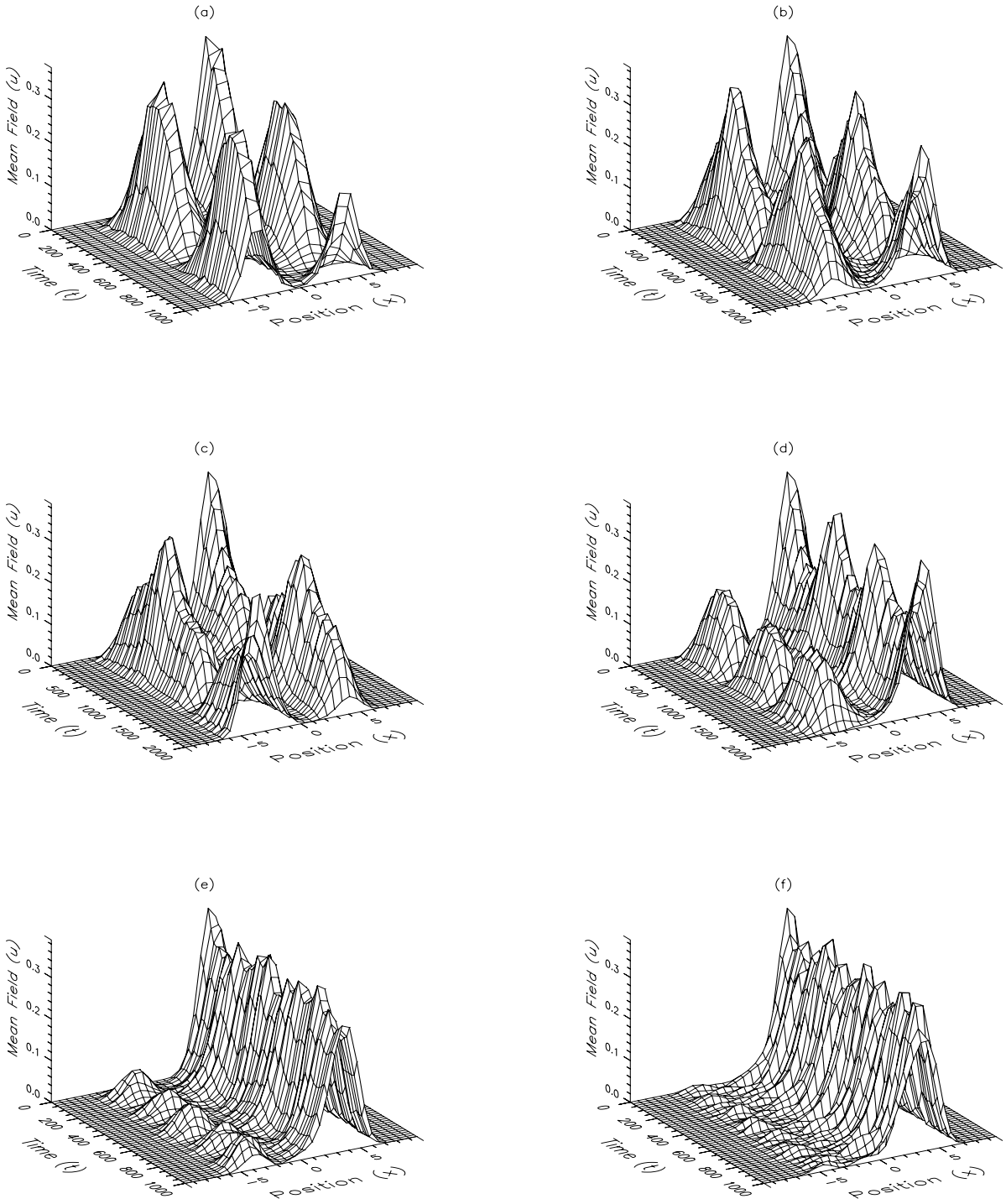

Figure 2.10: *Tunnelling oscillations of a condensate in a double-well potential with minima at* $x = \pm 4r_0$*, calculated from the GP equation with different strengths of the nonlinear atom interactions, both above and below the critical value. In (a)* $K = 0.0000$*, in (b)* $K = 0.1000$*, in (c)* $K = 0.1015$*, in (d)* $K = 0.1020$*, in (e)* $K = 0.1500$*, and in (f)* $K = 0.5000$*. Note that (a), (e) and (f) extend for only half the time as (b) to (d).*

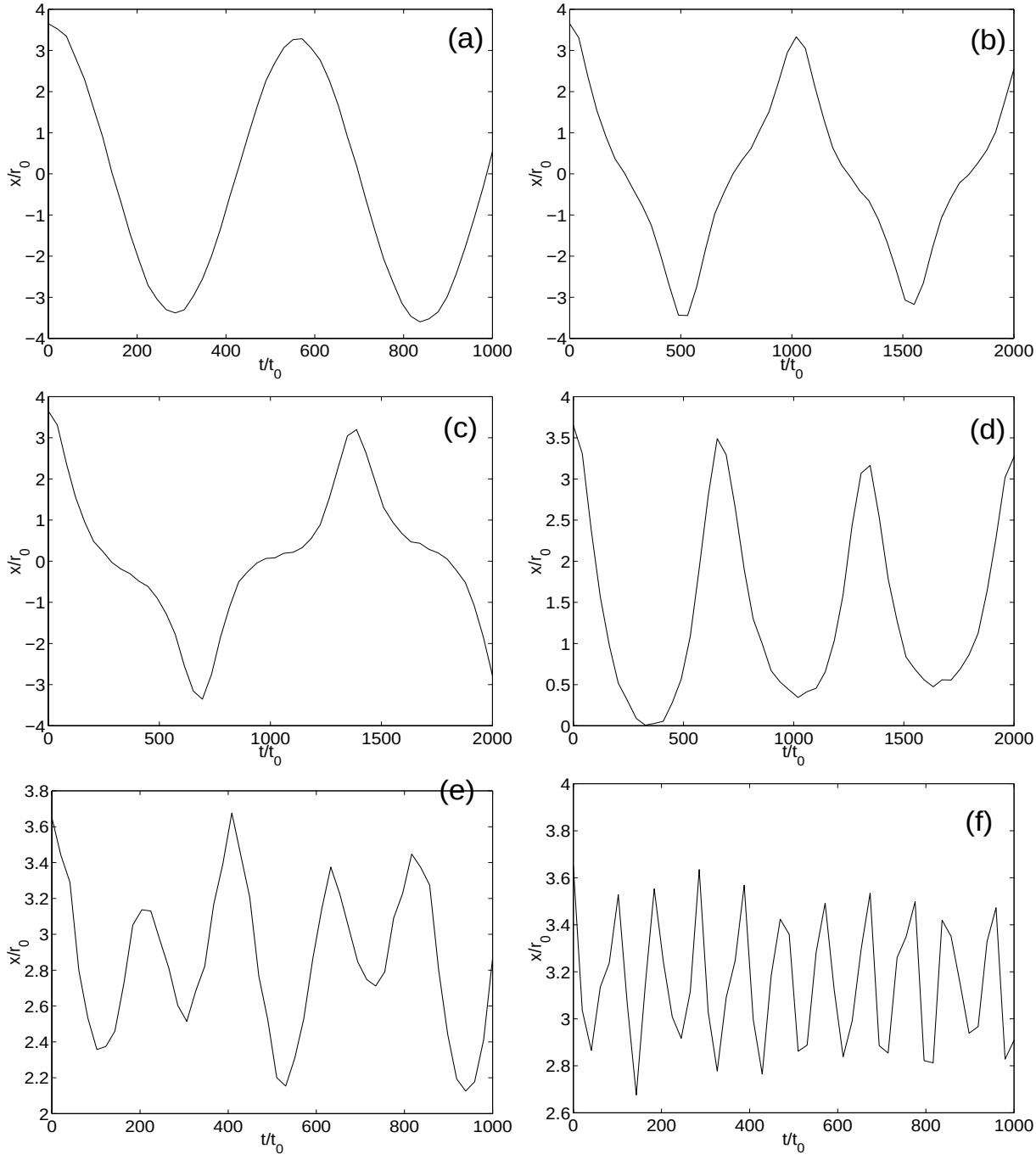

small oscillations that decrease in period and amplitude as K increases further (Figs. 2.9(d-f) and 2.10(d-f)). Both types of behaviour are consistent with the description in terms of Jacobi elliptic functions predicted from the two-mode analysis. What is not predicted correctly is just what this critical value is: the self-trapping effect occurs for larger nonlinearities than that predicted from the two-mode analysis. If we assume that at the critical value $\Omega = \kappa N$, then we get a smaller period T_0 (and hence z_0') than the observed value, and different from any other value discussed above. See Table 2.1 for the comparison with other calculations of tunnelling period. This is yet another consequence of the large overlap between the two local modes.

In summary, the main features of the semiclassical two-mode description survive in the full Gross-Pitaevskii treatment. An adjustment of the tunnelling frequency Ω and the critical ratio Θ allows the two-mode treatment to correctly predict behaviour even in closely spaced wells. These adjustments would be unnecessary for trapping potentials with a large separation, in which case the unwanted oscillations should not appear. But the tunnelling period increases exponentially with the well separation $2z_0$, which makes the numerical integration quite demanding on computer time, especially when the nonlinearity in Eq. (2.46) is large.

2.3 Quantum dynamics

Because of the conservation of total particle number, the two-mode Hamiltonian (Eq. (2.14)) translates into an angular momentum model which allows us to represent the quantum dynamics on the surface of a Bloch sphere. To see this, we can remove the first term in Eq. (2.14) by transforming to an interaction picture, resulting in the Hamiltonian

$$\hat{H}_{2b} = \frac{\hbar\Omega}{2}(\hat{c}_1\hat{c}_2^\dagger + \hat{c}_1^\dagger\hat{c}_2) + \hbar\kappa((\hat{c}_1^\dagger)^2\hat{c}_1^2 + (\hat{c}_2^\dagger)^2\hat{c}_2^2). \tag{2.47}$$

Introducing the angular momentum operators, which are similar to the transformations in the semiclassical case (Eq. 2.31):

$$\hat{J}_z = \frac{1}{2}(\hat{c}_1^\dagger\hat{c}_2 + \hat{c}_2^\dagger\hat{c}_1), \tag{2.48a}$$

$$\hat{J}_x = \frac{1}{2}(\hat{c}_2^\dagger\hat{c}_2 - \hat{c}_1^\dagger\hat{c}_1), \tag{2.48b}$$

$$\hat{J}_y = \frac{i}{2}(\hat{c}_2^\dagger\hat{c}_1 - \hat{c}_1^\dagger\hat{c}_2), \tag{2.48c}$$

and setting $\hat{c}_1^\dagger \hat{c}_1 + \hat{c}_2^\dagger \hat{c}_2 = \hat{N} = N$, we arrive at

$$\hat{H}_2 = \hbar\Omega \hat{J}_z + 2\hbar\kappa \hat{J}_x^2. \tag{2.49}$$

Here we have neglected terms proportional to N and N^2 since they merely correspond to a shift in the energy scale. The Casimir invariant is

$$\hat{J}^2 = \frac{\hat{N}}{2}\left(\frac{\hat{N}}{2} + 1\right). \tag{2.50}$$

This is analogous to an angular momentum model with total angular momentum given by $j = \frac{1}{2}N$. The semiclassical equations (Eq. (2.32)) are then obtained by taking average values of the Heisenberg equations of motion for the components of angular momentum and factorising with the identification $\langle \hat{J}_\mu \rangle / N = \mu$ where $\mu \in \{x, y, z\}$.

The angular momentum operators have a simple physical interpretation. The operator $\hat{J}_z$ corresponds to the particle occupation number difference between the single-particle energy eigenstates. For example the maximal weight eigenstate $|j, j\rangle_z$ corresponds to all the particles occupying the highest single-particle energy eigenstate, $u_+(x)$. The operator $\hat{J}_x$ gives the particle number difference between the localised states of each well. In fact, the x-component of the position operator in the field representation is

$$\hat{x} = \frac{2q_0}{N}\hat{J}_x. \tag{2.51}$$

Thus the maximal and minimal weight eigenstates of $\hat{J}_x$ correspond to the localisation of all the particles in one well or the other. Lastly, $\hat{J}_y$ corresponds to the tunnelling momentum, proportional to the rate of change of $\hat{x}$.

In [125] the full quantum dynamics was solved and the results compared with the semiclassical solutions in the two mode approximation. For this calculation, the quantum state was represented as a vector in the eigenbasis of $\hat{J}_z$, and the Hamiltonian as a matrix in the same basis. The Hamiltonian matrix was then exponentiated (through a truncated power series) to form the unitary evolution matrix, which was applied to the initial state to evolve it in time. The initial state here is $\big|j, j\big\rangle_x$, corresponding to all the atoms in one well. The quantum results reveal that the semiclassical oscillations are modified by a periodic collapse and revival envelope, as shown in Fig. 2.11. For the small condensates considered here ($N = 100$ and $N = 400$), the collapse occurs after only a few oscillations. However, in the limit of large N, the semiclassical approximation becomes good for longer

Figure 2.11: *Collapses and revivals in the tunnelling oscillations of condensates containing 100 atoms (continuous line) and 400 atoms (dashed line). In (a), the atom collisions are below the critical strength (with $\Theta = 0.9$), and in (b), the atom collisions are above the critical strength (with $\Theta = 2.0$). The time axis has been scaled by $t_0 = 1/\Omega$.*

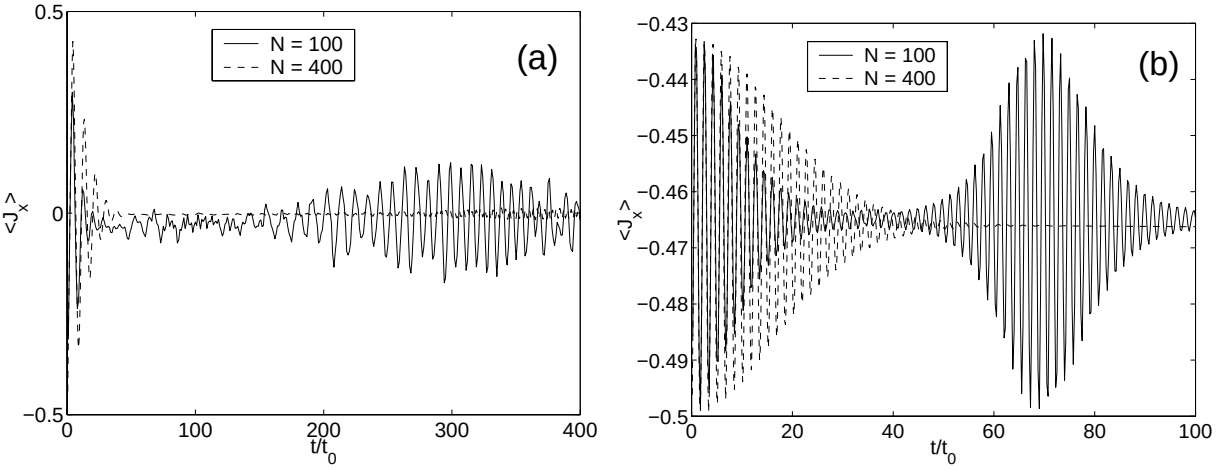

and longer times. We now focus on some other quantum features of the system for small N.

2.3.1 Energy eigenstates

The dynamics governed by the two-mode Hamiltonian (Eq. (2.49)) can be characterised in terms of the competition between quantum tunnelling and atom-interaction effects, described by the first and second terms in the Hamiltonian respectively. The normalised interaction strength $\Theta = \kappa N/\Omega$, introduced in Sec. 2.2.1, specifies the relative strength of the interaction term over the tunnelling term. When the interaction strength is small ($\Theta \ll 1$), the first terms dominate, in which case the energy eigenstates are close to the eigenstates of $\hat{J}_z$. The ground state will be near the lowest weight eigenstate $\left|j, -j\right\rangle_z$, which is just the single-particle ground state of the double-well potential. The higher eigenvalues will be separated by integer multiples of $\hbar\Omega$ above this lowest energy.

If the strength of the atomic collisions is increased, the self-interaction energy will contribute more to the total energy and will thereby alter the eigenstates of the Hamiltonian. The lowest energy states will be the ones which tend to minimise the average square atom density ($(N_1^2 + N_2^2)/V_{\text{eff}}^2$), subject to the average density (N/V_{eff}) being constant. For very strong interactions ($\Theta \gg 1$), the second, nonlinear term in the Hamiltonian dominates,

and so the eigenstates of the Hamiltonian should be close the $\hat{J}_x^2$ eigenstates. The ground state will then be close to the zero weight state $\big|j,0\big\rangle_x$, with all other states being doubly degenerate. This ground state corresponds to an equal number of atoms in each well, and hence a minimum in the local atom density.

Figure 2.12 shows the energy eigenvalues of the scaled Hamiltonian

$$\overline{\hat{H}}_2 = \frac{\hat{H}_2}{\hbar\Omega} = \hat{J}_z + 2\frac{\Theta}{N}\hat{J}_x^2, \tag{2.52}$$

for different values of the scaled interaction strength Θ. In Fig. 2.12(a), where $\Theta = 0.5$, the low-lying part of the spectrum is dominated by the eigenstates of $\hat{J}_z$, with a characteristic linear increase of the energy with the integer m labeling the sequence of states. In both Figs. 2.12(b) and 2.12(c) (with $\Theta = 2$ and $\Theta = 20$ respectively), the upper part of the spectrum is modified by the presence of the $\hat{J}_x^2$ term, which produces the doublet structure. For a very large interaction strength, such as $\Theta = 100$ as in Fig. 2.12(d), the eigenstates approach the doubly degenerate $\hat{J}_x^2$ eigenstates, with the energy increasing quadratically with the integer m labeling of eigenstates. The result for a larger condensate (400 atoms) with $\Theta = 2$ is shown in Fig. 2.13. This shows a similar division of the spectrum into a linear lower half and an quadratic upper half.

When Θ is neither in the limit of being very small or very large, approximate expressions for the ground state can be written down using perturbation theory. For example, when $\Theta > 1$, the corrections to the ground state and its corresponding energy can be found as follows. The Hamiltonian is separated into unperturbing and perturbing parts: $\hat{H}_2 = \hat{H}^{(0)} + \hat{V}$, where $\hat{H}^{(0)} = 2\kappa\hat{J}_x^2$ and $\hat{V} = \Omega\hat{J}_z$. Then the ground state and energy are written as expansions which go to first order in $\hat{V}$:

$$\big|E_0^{(1)}\big\rangle = \big|E_0^{(0)}\big\rangle + \Delta\big|E_0^{(0)}\big\rangle \tag{2.53a}$$

$$E_0^{(1)} = E_0^{(0)} + \Delta E_0^{(0)}, \tag{2.53b}$$

where $\big|E_0^{(0)}\big\rangle$ is the eigenvector of $\hat{H}^{(0)}$ with eigenvalue $E_0^{(0)}$. Substituting these expansions in to the eigenvalue equation and equating terms of like order in $\hat{V}$ gives

$$(\hat{H} - E_0^{(0)})\Delta\big|E_0^{(0)}\big\rangle = (\Delta E_0^{(0)} - \hat{V})\big|E_0^{(0)}\big\rangle. \tag{2.54}$$

Using the orthonormality of the $\big|E_m^{(0)}\big\rangle$ and assuming that $\Delta\big|E_0^{(0)}\big\rangle$ is orthogonal to $\big|E_0^{(0)}\big\rangle$, we can substitute the expansion

$$\Delta\big|E_0^{(0)}\big\rangle = \sum_{m\neq 0} B_m\big|E_m^{(0)}\big\rangle \tag{2.55}$$

Figure 2.12: *Energy spectra, scaled by $\hbar\Omega$, for $N = 100$ and different values of the atom-interaction strength. In (a) $\Theta = 0.5$, in (b) $\Theta = 2$, in (c) $\Theta = 20$, and in (d) $\Theta = 100$.*

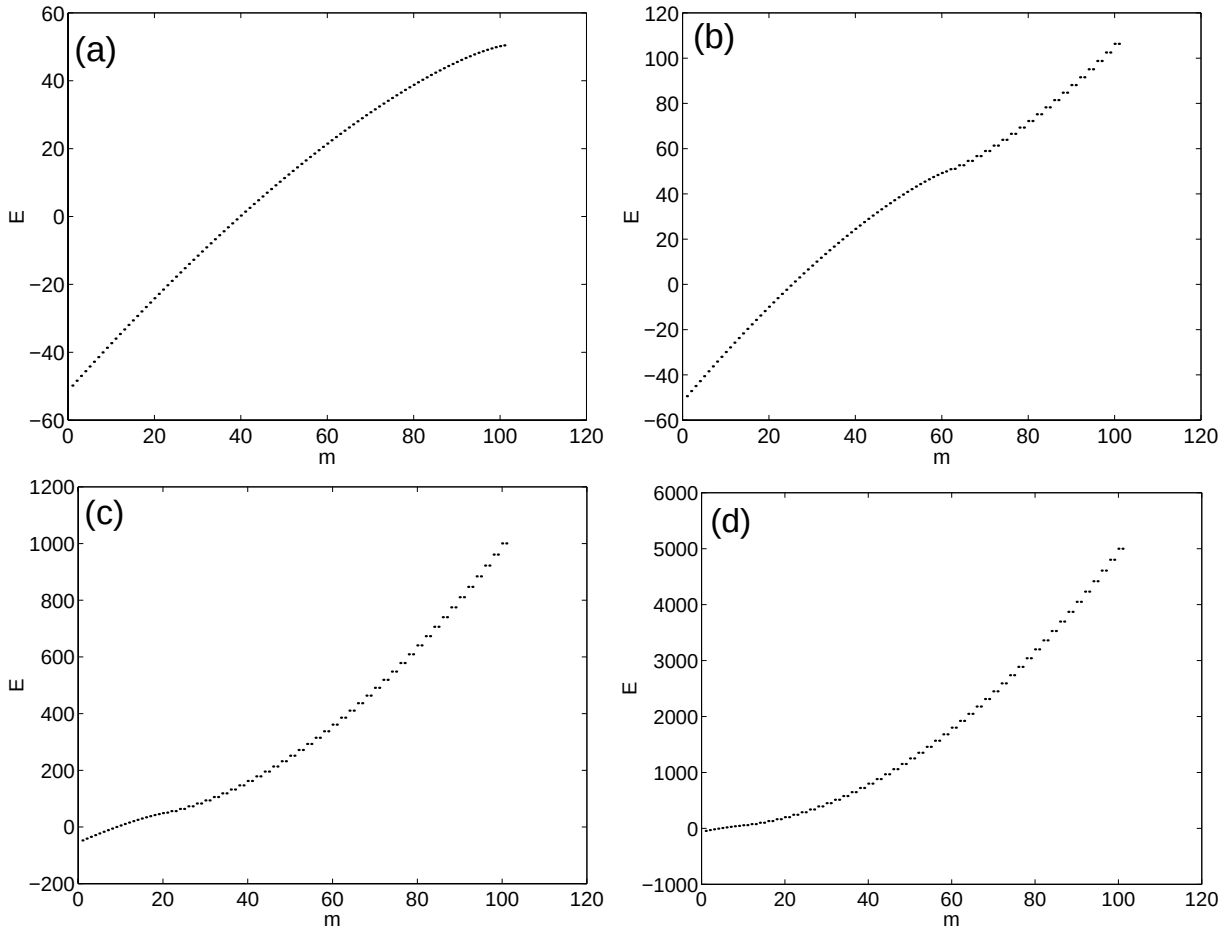

Figure 2.13: *Energy spectrum, scaled by $\hbar\Omega$, for $N = 400$ and $\Theta = 2$.*

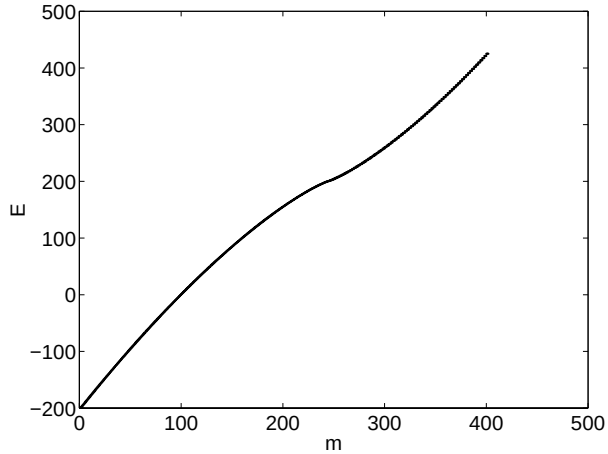

into Eq. (2.54) to obtain the following expression for the ground-state correction:

$$\Delta\big|E_0^{(0)}\big\rangle = \sum_{m\neq 0} \frac{\big\langle E_m^{(0)}\big|\hat{V}\big|E_0^{(0)}\big\rangle}{E_0^{(0)} - E_m^{(0)}}\big|E_m^{(0)}\big\rangle. \tag{2.56}$$

The energy corresponding to this ground state is

$$\big\langle E_0^{(1)}\big|\hat{H}_0 + \hat{V}\big|E_0^{(1)}\big\rangle \simeq E_0^{(0)} + \big\langle E_0^{(0)}\big|\hat{V}\big|E_0^{(0)}\big\rangle - \sum_{m\neq 0} \frac{3E_0^{(0)} + E_m^{(0)}}{\left(E_0^{(0)} - E_m^{(0)}\right)^2}\left|\big\langle E_m^{(0)}\big|\hat{V}\big|E_0^{(0)}\big\rangle\right|^2, \tag{2.57}$$

where terms higher than second order have been neglected.

For the double-well system, $E_m^{(0)} = 2\kappa m^2$, $\big\langle E_0^{(0)}\big|\hat{V}\big|E_0^{(0)}\big\rangle = 0$ and the other matrix elements can be calculated using ${}_x\big\langle j, m\pm 1\big|\hat{J}_z\big|j,m\big\rangle_x = \mp\frac{i}{2}\sqrt{j(j+1) - m(m\pm 1)}$. It follows that the correction to the ground state due to V is:

$$\begin{aligned}\Delta\big|E_0^{(0)}\big\rangle &= \sum_{m\neq m0} \frac{\big\langle E_m^{(0)}\big|\hat{V}\big|E_0^{(0)}\big\rangle}{-E_m^{(0)}}\big|E_m^{(0)}\big\rangle \\ &= \frac{i\Omega\sqrt{j(j+1)}}{4\kappa}\left(\big|j,1\big\rangle_x - \big|j,-1\big\rangle_x\right),\end{aligned} \tag{2.58}$$

which is just an odd superposition of the next highest (degenerate) eigenstates of $\hat{J}_x^2$. Thus the perturbed eigenstate is

$$\big|E_0^{(1)}\big\rangle = \big|E_0^{(0)}\big\rangle + \Delta\big|E_0^{(0)}\big\rangle = \frac{\big|j,0\big\rangle_x + \frac{i\Omega\sqrt{j(j+1)}}{4\kappa}\left(\big|j,1\big\rangle_x - \big|j,-1\big\rangle_x\right)}{\sqrt{1 + \frac{j(j+1)\Omega^2}{8\kappa^2}}}, \tag{2.59}$$

and the corresponding energy is

$$\begin{aligned}E_0^{(1)} &= \sum_{m\neq 0} \frac{\left|\big\langle E_m^{(0)}\big|\hat{V}\big|E_0^{(0)}\big\rangle\right|^2}{-E_m^{(0)}} \\ &= -\frac{\Omega^2 j(j+1)}{4\kappa}.\end{aligned} \tag{2.60}$$

This same perturbed eigenstate can also be calculated by forming a trial state from an odd superposition like

$$\big|E_0^{(1)}\big\rangle = \big|j,0\big\rangle_x + \lambda\left(\big|j,1\big\rangle_x - \big|j,-1\big\rangle_x\right) \tag{2.61}$$

and finding the λ which minimises the energy $E_0^{(1)}$.

The second-order correction to the ground state is

$$\begin{aligned} \left|E_0^{(2)}\right\rangle &= \sum_{m\neq 0}\sum_{k\neq 0} \frac{\left\langle E_m^{(0)}\right|\hat{V}\left|E_k^{(0)}\right\rangle\left\langle E_k^{(0)}\right|\hat{V}\left|E_0^{(0)}\right\rangle}{\left(E_0^{(0)}-E_m^{(0)}\right)\left(E_0^{(0)}-E_k^{(0)}\right)}\left|E_m^{(0)}\right\rangle \\ &= \frac{-\Omega^2\sqrt{j(j+1)}\sqrt{j(j+1)-2}}{64\kappa}\left(\left|j,2\right\rangle_x+\left|j,-2\right\rangle_x\right), \end{aligned} \tag{2.62}$$

which is an even superposition.

2.3.2 Transition temperature

One characteristic quantity of an ensemble of bosons is the transition temperature T_c. This is the temperature at which a macroscopic occupation of the ground state develops, and can be calculated by studying how the condensate fraction N_0/N varies with temperature. In the thermodynamic limit, the temperature at which the condensed fraction first appears is sharply defined, but in a system of a finite number of particles, the transition is smoother[100].

The two-mode model provides a good illustration of this. Let us consider a grand canonical ensemble of weakly interacting atoms, with the populations of the energy levels E_i obeying the Bose-Einstein distribution:

$$N(E_i) = \frac{ze^{-\beta(E_i-E_0)}}{1-ze^{-\beta(E_i-E_0)}}, \tag{2.63}$$

where the fugacity z is defined in terms of the chemical potential μ as $z=\exp(\beta\mu)$. The temperature dependence enters through $\beta = 1/(k_BT)$. The condensate fraction can be calculated from the fugacity: $N_0 = z/(1-z)$, which in turn can be calculated from the total number constraint:

$$N = \sum_{i=0}^{N} N(E_i) = \sum_{l=1}^{\infty} z^l \sum_{i=0}^{N} e^{-l\beta(E_i-E_0)}. \tag{2.64}$$

From this equation, the condensate fraction can be calculated numerically using the energy eigenvalues found in the previous section.

We consider first the two limiting cases in which the spectrum can be written down in analytic form. When the atom interactions are negligible (i.e. $\Theta \ll 1$), the energy eigenvalues will be the $E_i - E_0 = i\hbar\Omega$. This is similar to the one-dimensional harmonic oscillator considered by Ketterle and van Druten[100], except that the spectrum now has

an upper bound. Equation (2.64) becomes

$$N = \frac{z}{1-z} + \sum_{l=1}^{\infty} z^l e^{-l\beta\hbar\Omega} \frac{1 - e^{-lN\beta\hbar\Omega}}{1 - e^{-l\beta\hbar\Omega}}. \tag{2.65}$$

A high temperature approximation, in which $\beta\hbar\Omega \ll 1$, gives the approximate result[4]:

$$N = \frac{z}{1-z} + \frac{k_B T}{\hbar\Omega} \ln\left(\frac{1 - ze^{-(N+\frac{1}{2})\hbar\Omega/(k_B T)}}{1 - z(1 - \hbar\Omega/(2k_B T))}\right). \tag{2.66}$$

The critical temperature T_c can be determined as the minimum temperature that satisfies the above equation when $N_0 = 0$. This is easily done by taking $z \to 1$, to give

$$N = \frac{k_B T_c}{\hbar\Omega} \ln\left(\frac{1 - e^{-(N+\frac{1}{2})\hbar\Omega/(k_B T)}}{\hbar\Omega/(2k_B T_c)}\right), \tag{2.67}$$

and a condensate fraction when $T < T_c$ of

$$\frac{N_0}{N} = 1 - \frac{T \ln\left(2k_B T(1 - e^{(N+\frac{1}{2})\hbar\Omega/k_B T})/(\hbar\Omega)\right)}{T_c \ln\left(2k_B T_c(1 - e^{(N+\frac{1}{2})\hbar\Omega/k_B T_c})/(\hbar\Omega)\right)}. \tag{2.68}$$

The critical temperature for the bounded spectrum, as specified in Eq. (2.67), is larger than that of the corresponding unbounded spectrum. Intuitively, this is because of the restricted number of noncondensate modes in the system, which would force a nonzero population into the ground state when the temperature is still high.

For the other limiting case, when $\Theta \gg 1$, the collision term is dominant and so the spectrum is doubly degenerate and quadratic: $E_i = 2\hbar\kappa i^2$. The condensate fraction and critical temperature are then determined by

$$N = \frac{z}{1-z} + 2\sum_{l=1}^{\infty} z^l \sum_{i=1}^{N/2} e^{2li^2\beta\hbar\kappa}, \tag{2.69}$$

which would need to be solved numerically.

The condensate fraction as a function of temperature is shown in Fig. 2.14 for $N = 100$ atoms and in Fig. 2.15 for an $N = 400$ condensate. The exact calculations involved solving Eq. (2.64) with the spectra calculated in Sec. 2.3.1. The critical temperature T_c was calculated with the same method as Eq. (2.67), but with the exact spectra. The approximate calculation for the $\Theta = 0$ case is from Eqs. (2.67) and (2.68).

Figures 2.14(a-d) are all quite similar. The calculated critical temperature T_c does not correspond to the condensate fraction being equal to zero. Rather, there is an exponential

[4]The approximation $e^{-\epsilon}/(1 - e^{-\epsilon}) \simeq e^{-\epsilon/2}/\epsilon$ is used, which is correct to second order in ϵ.

Figure 2.14: *The condensate fraction versus temperature (scaled by $\hbar\Omega/k_B$) for $N = 100$ and different values of the atom-interaction strength. In (a) $\Theta = 0$, in (b) $\Theta = 0.5$, in (c) $\Theta = 2$, in (d) $\Theta = 20$, in (e) $\Theta = 100$ and in (f) $\Theta = 500$.*

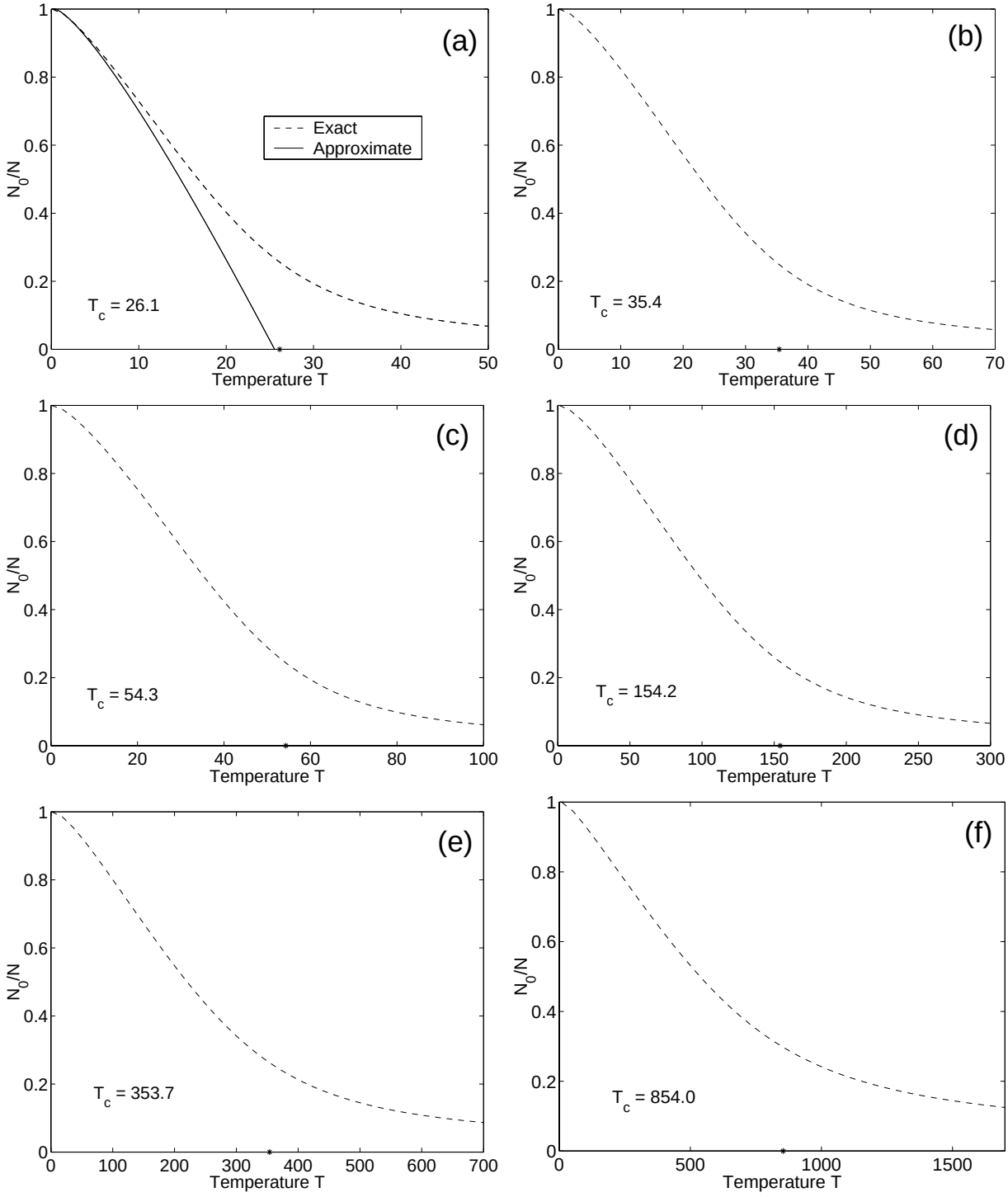

Figure 2.15: *Condensate fraction versus temperature (scaled by $\hbar\Omega/k_B$) for $N = 400$ and different values of the atom-interaction strength. In (a) $\Theta = 0$ and in (b) $\Theta = 100$.*

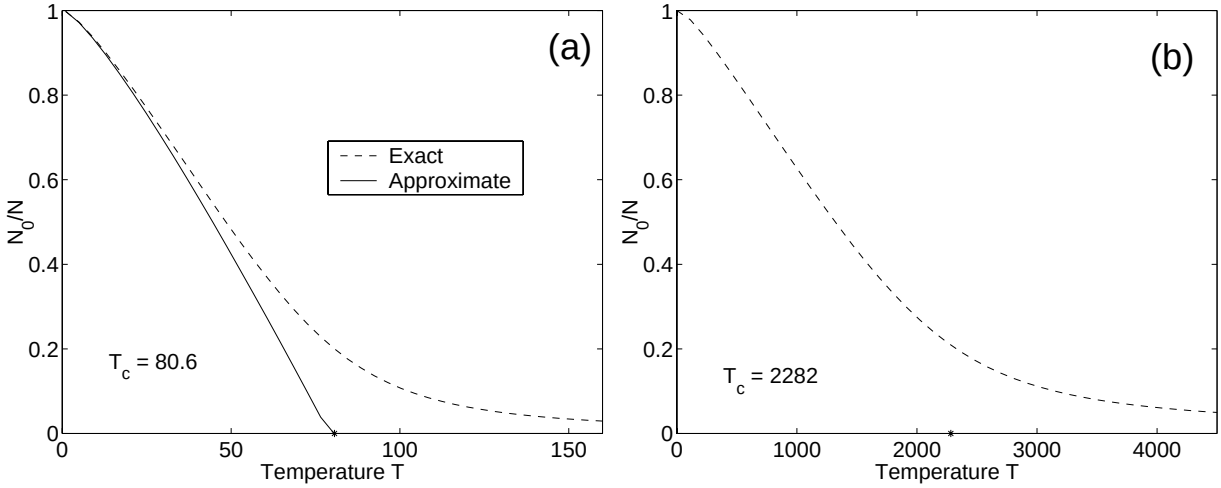

high-temperature tail to the graph, with the critical point corresponding to a condensate fraction of $N_0/N \simeq 0.25$. Because the analytic calculation of condensate fraction in Fig. 2.14(a) assumes that $N_0/N \to 0$ at $T = T_c$, it makes a poor fit to the exact result for this small number of atoms. For very large self-interactions (Figs. 2.14(e&f)), N_0/N decreases at a slower rate (when the temperature axis has been scaled by T_c), making the value of N_0/N at T_c even larger.

For the larger condensate (Fig. 2.15), the high temperature tail is smaller, and so the approximate calculation provides a better fit, except near the critical region. Once again, strong atom interactions decrease the rate at which this tail falls away, perhaps because the more strongly interacting atoms have a thermalising effect that aids the growth of the condensate at higher temperatures. However, we should keep in mind that, for strongly interacting atoms, the validity of the Bose-Einstein distribution function (Eq. (2.63)) is not guaranteed.

2.3.3 Coherence properties of the ground state

The 'density function' of the ground state of the condensate affords some insight into first-order coherence effects, and is defined in terms of the many-body boson operators as

$$\rho(x,t) \quad = \quad \left\langle \hat{\psi}^\dagger(x,t)\hat{\psi}(x,t) \right\rangle . \tag{2.70}$$

For the two-mode model, this becomes

$$\rho(x,t) = \Big\langle \frac{N}{2} - \hat{J}_x(t) \Big\rangle |u_1(x)|^2 + \left\langle \frac{N}{2} + \hat{J}_x(t) \right\rangle |u_2(x)|^2 - 2\big\langle \hat{J}_z(t) \big\rangle u_1(x) u_2(x), \quad (2.71)$$

where the u_i are the local modes for each well, as defined in Eq. (2.7). Now ρ can be calculated analytically from the ground state in the two limiting cases of the collisional strength. To facilitate the discussion, we will use the single-particle normalised interaction strength $\overline{\kappa} = \kappa/\Omega$, which differs by a factor of N from the multiparticle normalised interaction strength Θ introduced in the Sec. 2.2.1. For the $\big|j,-j\big\rangle_z$ ground state, the density function factorises into

$$\rho^a(x,t) = N|\phi(x)|^2; \qquad \phi(x) = \frac{(u_1(x) - u_2(x))}{\sqrt{2}}, \quad (2.72)$$

where $\phi(x)$ is the single-particle ground state of the global potential. Because this can be factorised into the square of a single macroscopic wave-function, it possesses full first-order coherence and can be characterised by a single long-range order parameter. For the strongly interacting case, the ground state $\big|j,0\big\rangle_x$ leads to

$$\rho^b(x,t) = \frac{N}{2}\left(u_1(x)^2 + u_2(x)^2\right), \quad (2.73)$$

which is just the sum of the density functions for each of the local modes. Both of these cases are illustrated in Fig. 2.16, for a double-well potential in which the two minima are at $q_0 \pm 3x_0$. The feature that distinguishes the two extremes is the presence or absence of the interference fringe in the centre between the two wells, whose presence reduces the density function at this point. Its size is a maximum for the tunnelling dominated ground state (when $\overline{\kappa} \ll 1$) and is zero when the $\overline{\kappa} \gg 1$. In general, its relative size is proportional to the moment $|\big\langle \Psi_0 \big| \hat{J}_z \big| \Psi_0 \big\rangle|/N^2$, where $\big|\Psi_0\big\rangle$ is the ground state. Figure 2.17(a) shows that $\big\langle \Psi_0 \big| \hat{J}_z \big| \Psi_0 \big\rangle/N$ changes little as N varies, and therefore the size of the interference term varies approximately inversely with the size of the condensate, becoming negligible for large N. Figure 2.17(b) reveals how the interference term varies with $\overline{\kappa}$ in between the two extremes. There appears to be a threshold value of $\overline{\kappa}$, above which the interference term is close to zero.

Second-order coherence features are indicated by the normally-ordered second-order correlation function:

$$G_2(x_1,x_2,t) = \big\langle \hat{\psi}^\dagger(x_1)\hat{\psi}^\dagger(x_2)\hat{\psi}(x_2)\hat{\psi}(x_1) \big\rangle. \quad (2.74)$$

Figure 2.16: *The ground-state spatial density distribution* $\rho = \langle \hat{\psi}^\dagger(x)\hat{\psi}(x)\rangle$, *scaled by the peak value. The continuous line is for* $\overline{\kappa} \ll 1$ *and the dashed line is for* $\overline{\kappa} \gg 1$.

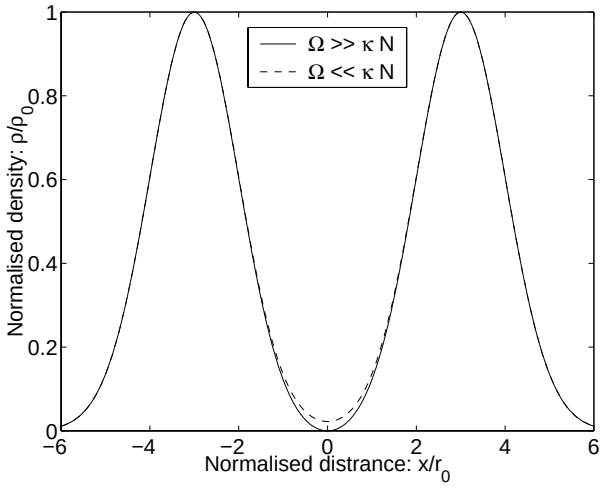

Figure 2.17: *Plots of the moment* $\langle \hat{J}_z \rangle / N$ *calculated for the ground state. In (a), the number of atoms* N *in the condensate is varied and* $\overline{\kappa}$ *is held constant, while (b) shows how* $\langle \hat{J}_z \rangle$ *varies with* $\overline{\kappa}$ *for constant* N.

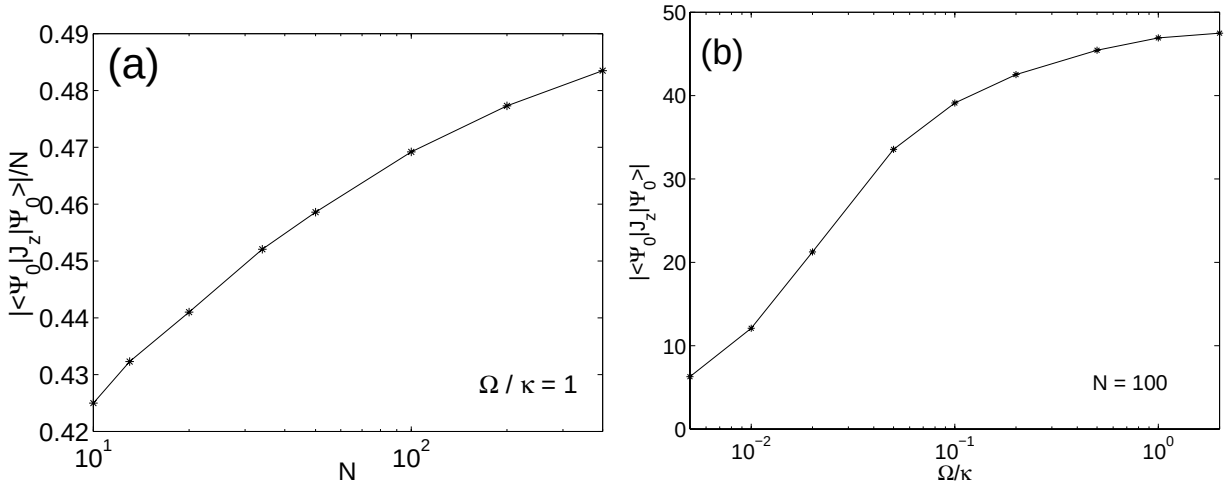

This is just the joint probability distribution to detect an atom at x_1 and x_2 which has been considered by [95]. For the double-well system, this becomes

$$\begin{aligned}
G_2(x_1,x_2,t) &= \left\langle \frac{N^2}{4} - \hat{J}_x^2 \right\rangle u_1^2(x_1)u_2^2(x_2) \\
&+ \left\langle (N-1)\hat{J}_z - \hat{J}_x\hat{J}_z - \hat{J}_x\hat{J}_z \right\rangle u_1^2(x_1)u_1(x_2)u_2(x_2) \\
&\quad + \left\langle (N-1)\hat{J}_z + \hat{J}_x\hat{J}_z + \hat{J}_x\hat{J}_z \right\rangle u_1(x_1)u_2(x_1)u_2^2(x_2) \\
&+ \left\langle \frac{N}{2}\left(\frac{N}{2}-1\right) + \hat{J}_x(\hat{J}_x+1-N) \right\rangle u_1^2(x_1)u_1^2(x_2) \\
&\quad + \left\langle \frac{N}{2}\left(\frac{N}{2}-1\right) + \hat{J}_x(\hat{J}_x-1+N) \right\rangle u_2^2(x_1)u_2^2(x_2) \\
&\quad\quad + \left\langle 4\hat{J}_z^2 - N \right\rangle u_1(x_1)u_1(x_2)u_2(x_1)u_2(x_2) \\
&+ \left\langle (N-1)\hat{J}_z - \hat{J}_x\hat{J}_z - \hat{J}_x\hat{J}_z \right\rangle u_1(x_1)u_1^2(x_2)u_2(x_1) \\
&\quad + \left\langle (N-1)\hat{J}_z + \hat{J}_x\hat{J}_z + \hat{J}_x\hat{J}_z \right\rangle u_1(x_2)u_2^2(x_1)u_2(x_2) \\
&+ \left\langle \frac{N^2}{4} - \hat{J}_x^2 \right\rangle u_1^2(x_2)u_2^2(x_1). \qquad (2.75)
\end{aligned}$$

We will look at the case where the atoms considered come from different wells, i.e. $x_1 < 0$ and $x_2 > 0$, which means that $u_i(x_{3-i}) \ll u_j(x_j)$, for $i,j = 1,2$. The lines in Eq. (2.75) have been arranged in order of size, from zeroth order terms to fourth order terms. For a condensate in the ground state for either of the limiting cases ($\overline{\kappa} \ll 1$ or $\overline{\kappa} \gg 1$), $\langle \hat{J}_x \rangle = \langle \hat{J}_x\hat{J}_z \rangle = \langle \hat{J}_z\hat{J}_x \rangle = 0$, and so Eq. (2.75) becomes

$$\begin{aligned}
G_2(x_1,x_2,t) &= \left\langle \frac{N^2}{4} - \hat{J}_x^2 \right\rangle u_1^2(x_1)u_2^2(x_2) \\
&+ \left\langle (N-1)\hat{J}_z \right\rangle \left(u_1^2(x_1)u_1(x_2)u_2(x_2) + u_1(x_1)u_2(x_1)u_2^2(x_2)\right) \\
&+ \left\langle \frac{N}{2}\left(\frac{N}{2}-1\right) + \hat{J}_x^2 \right\rangle \left(u_1^2(x_1)u_1^2(x_2) + u_2^2(x_1)u_2^2(x_2)\right) \\
&\quad + \left\langle 4\hat{J}_z^2 - N \right\rangle u_1(x_1)u_1(x_2)u_2(x_1)u_2(x_2) \\
&+ \left\langle (N-1)\hat{J}_z \right\rangle \left(u_1(x_1)u_1^2(x_2)u_2(x_1) + u_1(x_2)u_2^2(x_1)u_2(x_2)\right) \\
&+ \left\langle \frac{N^2}{4} - \hat{J}_x^2 \right\rangle u_1^2(x_2)u_2^2(x_1). \qquad (2.76)
\end{aligned}$$

The 'first order' term on the second line of Eq. (2.76) indicates the size of the interference fringes and scales as $\langle \hat{J}_z \rangle / N$ relative to the peak value, the same as with the density function. (See Fig. 2.17 for how this term varies with N and $\overline{\kappa}$.) This term disappears when $\overline{\kappa} \gg 1$ and approaches a maximum when $\overline{\kappa} \ll 1$. In the latter case, the correlation

Figure 2.18: *The spatial second-order correlation function* $G_2(x) = \langle \hat{\psi}^\dagger(x)\hat{\psi}^\dagger(-x)\hat{\psi}(-x)\hat{\psi}(x)\rangle$, *scaled by the peak value, for* $N = 100$. *The continuous line is for* $\overline{\kappa} \ll 1$ *and the dashed line is for* $\overline{\kappa} \gg 1$.

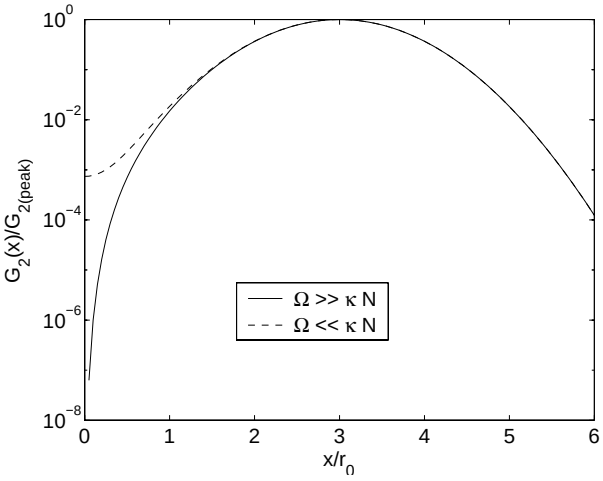

function again factorises:

$$G_2^a(x_1, x_2) = \frac{N}{4}(N-1)\phi^2(x_1)\phi^2(x_2), \tag{2.77}$$

indicating second order coherence. The strong-interaction limit does not lead to this full factorisation, but once again gives a correlation function which involves the sum of the local density functions for each well:

$$G_2^b(x_1, x_2) = \frac{N}{2}\left(\frac{N}{2} - 1\right)\Big(\Big(u_1^2(x_1) + u_2^2(x_1)\Big)\Big(u_1^2(x_2) + u_2^2(x_2)\Big) + 2u_1(x_1)u_2(x_1)u_1(x_2)u_2(x_2)\Big) + \frac{N}{2}\Big(u_1(x_1)u_2(x_2) + u_2(x_1)u_1(x_2)\Big)^2. \tag{2.78}$$

This can be simplified if we set $x_1 = x = -x_2$:

$$G_2^b(x) = \frac{N^2}{4}\left(u_1^2(x) + u_2^2(x)\right) + \frac{N}{2}(N-1)u_1(x)^2u_2(x)^2, \tag{2.79}$$

which is plotted in Fig. 2.18, along with $G_2^a(x)$. As this figure indicates, the difference is very small.

2.3.4 A condensate in a noisy potential

We conclude this chapter, and give a taste of what is to come, by opening up the double-well system to the environment. We will look at how a noisy trapping potential affects the quantum and semiclassical dynamics of the condensate. The decoherence introduced

by coupling the system to the environment may inhibit tunnelling, or suppress quantum revivals after a collapse.

A trapping potential with fluctuating well depths can be modelled by adding a fluctuating linear term:

$$V_r(x,t) = b(x^2 - q_0^2)^2 + \hbar\eta(t)x, \tag{2.80}$$

where $\eta(t)$ is a real stochastic process with a zero mean and a white spectrum:

$$\big\langle \eta(t)\eta(t')\big\rangle = \frac{\gamma}{2q_0^2}\delta(t-t'). \tag{2.81}$$

The constant γ gives the variance of the well-depth difference $\Delta V(t)$:

$$\sigma^2(\Delta V) = \int_{t-T}^{t+T} \big\langle \Delta V(t)\Delta V(t')\big\rangle dt'/2T = \gamma/T. \tag{2.82}$$

By rewriting $\hat{x} = 2q_0\hat{J}_x/N$, the two-mode Hamiltonian becomes

$$\hat{H}_r = \hbar\Omega\hat{J}_z + 2\hbar\kappa\hat{J}_x^2 + \frac{\sqrt{2\gamma}\hbar}{N}\frac{dW}{dt}\hat{J}_x, \tag{2.83}$$

where $dW(t)$ is the Wiener increment[5]. The Hamiltonian in Eq. (2.83) can generate stochastic evolution equations, which are to be interpreted in the Stratonovich sense[5]. For mathematical convenience, we will use the Ito calculus[5], in which case the master equation is

$$d\hat{\rho} = -\frac{i}{\hbar}\left[\hat{H}_r, \hat{\rho}\right] - \frac{\gamma}{N^2}\left[\hat{J}_x, \left[\hat{J}_x, \hat{\rho}\right]\right]. \tag{2.84}$$

When averaged over all realisations of the noise, the master equation simply becomes

$$d\hat{\rho}_e = -i\left[\Omega\hat{J}_z + 2\kappa\hat{J}_x^2, \hat{\rho}_e\right] - \frac{\gamma}{N^2}\left[\hat{J}_x, \left[\hat{J}_x, \hat{\rho}_e\right]\right]. \tag{2.85}$$

This equation governs the mean behaviour of all operators[6]. The equivalent semiclassical equations of motion become

$$\dot{x} = -\Omega y \tag{2.86a}$$

$$\dot{y} = \Omega x - 4\kappa N z x - \frac{\gamma}{N^2}y \tag{2.86b}$$

$$\dot{z} = 4\kappa N y x - \frac{\gamma}{N^2}z. \tag{2.86c}$$

[5]Appendix A summarises the properties of the Wiener process and overviews the two ways (Ito and Stratonovich) in which stochastic calculus may be implemented. Gardiner's book [61] makes for excellent background reading on this topic.

[6]i.e. the expectation-*operator* behaviour calculated from the stochastic ensemble, as opposed to the expectation-*value* behaviour calculated from the quantum ensemble.

Thus the dynamics are no longer constrained to the Bloch sphere, due to the diffusive spread of individual trajectories over the surface of the sphere. The tunnelling oscillations in x and y will be damped at the rate $\frac{1}{2}\gamma/N^2$.

The master equation for the mean operators (Eq. (2.85)) is not unique to the particular stochastic realisation we have used to derive it. In fact, we may also regard Eq. (2.85) as the mean behaviour of a 'jump' stochastic process, which allows a simple calculation of the mean-operator evolution. In this realisation, discrete 'detection events' (due to the $\hat{J}_x\hat{\rho}_e\hat{J}_x$ term) are separated by periods of continuous evolution (due to the $\hat{J}_x^2\hat{\rho}_e + \hat{\rho}_e\hat{J}_x^2$). We then interpret individual stochastic trajectories as the evolution conditioned on past detection events. For a pure initial state, the conditional master equation for this realisation leads the stochastic Schrödinger equation[179]:

$$d\big|\Psi_c(t)\big\rangle = \left[dN(t)\left(\frac{\hat{J}_x}{\sqrt{\langle\hat{J}_x^2\rangle}} - 1\right) + dt\left(\frac{\gamma}{N^2}\left(\big\langle\hat{J}_x^2\big\rangle_c - \hat{J}_x^2\right) - i\left(\Omega\hat{J}_z + 2\kappa\hat{J}_x^2\right)\right)\right]\big|\Psi_c(t)\big\rangle, \tag{2.87}$$

where the random variable $dN(t) \in \{0, 1\}$ takes on the expectation value

$$E\left[dN(t)\right] = \frac{2\gamma}{N^2}\big\langle\hat{J}_x^2\big\rangle_c dt. \tag{2.88}$$

This expectation value is the probability that a measurement event will occur in time dt, in which case $dN = 1$. Otherwise $dN = 0$. This means that if a detection occurs, the system ket jumps to

$$\big|\widetilde{\Psi}'_c(t)\big\rangle = \hat{J}_x\big|\Psi_c(t)\big\rangle, \tag{2.89}$$

where the tilde denotes an unnormalised ket. In between jumps, the system evolves non-unitarily to

$$\big|\widetilde{\Psi}_c(t+\Delta t)\big\rangle = e^{-i\hat{H}'t/\hbar}\big|\Psi_c(t)\big\rangle, \tag{2.90}$$

where $\hat{H}' = \hat{H}_2 - i\frac{1}{2}\gamma\hbar/N^2\hat{J}_x^2$.

Figure 2.19 shows the conditional and unconditional evolution of the of $\big\langle\hat{J}_x\big\rangle$ in the absence of atomic collisions for two different values of γ. When $\gamma = 10\Omega$ (Fig. 2.19(a)), $\big\langle\hat{J}_x\big\rangle$ executes full tunnelling oscillations, although at $t = 100$, the amplitude in the unconditional evolution has decayed by 5%. This agrees with the semiclassical equations (Eq.

Figure 2.19: *Conditional (continuous line) and unconditional (dashed line) evolution of a 100-atom condensate in a noisy double-well potential, in the absence of collisions. The unconditional evolution is calculated from 100 trajectories. In (a), $\gamma/\Omega = 10$ and in (b), $\gamma/\Omega = 100$. The time axis has been scaled by $t_0 = 1/\Omega$.*

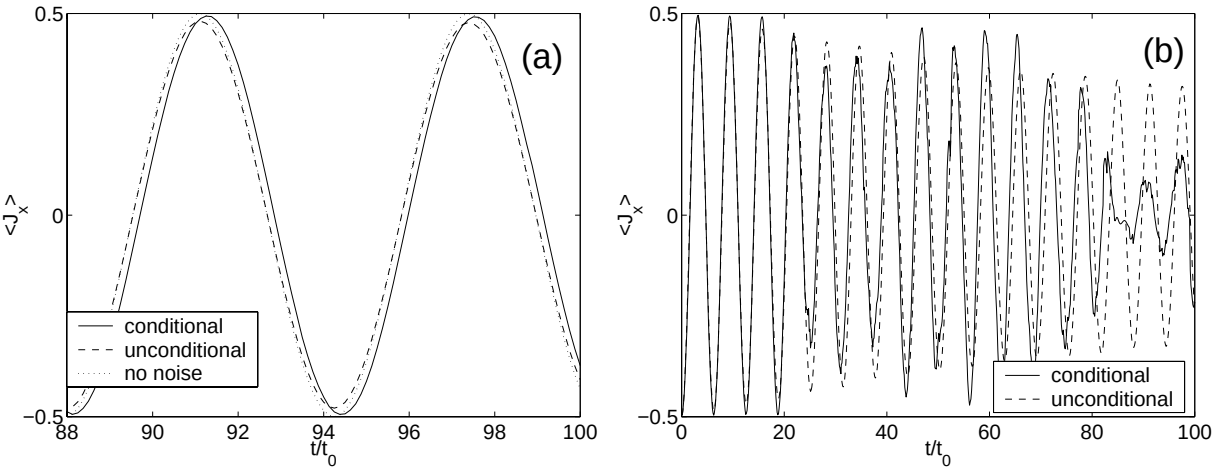

(2.86)) and is due to the phase kicks in individual trajectories. In Fig. 2.19(b), the increased noise ($\gamma = 100\Omega$) partially suppresses at times the conditional oscillations, leading to a faster decay of the unconditional dynamics.

In a noise-free potential, the presence of atoms collisions induces a collapse in the oscillations, followed at sometime later by revivals. This happens on a faster time scale for smaller numbers of atoms, as shown in Fig. 2.11. The collapses are due to the dephasing effect of the nonlinearity, while the revivals come from the granularity of small quantum systems, when all spectral components temporarily come back into phase. When a system is coupled to the environment, the spectral components will decohere, thereby preventing revivals.

We see just this thing happening to the double condensates in a noisy potential. Figure 2.20 shows that even when $\gamma = 10\Omega$, the resultant decoherence accelerates the collapse and suppresses the revival that was seen in Fig. 2.11. For a weak noise source, as in Figs. 2.20(a&b) where $\gamma/\Omega = 10$, the suppression of revivals is only partial, but for a larger noise source, as in Figs. 2.20(c&d) where $\gamma/\Omega = 100$, there is no hint of revivals.

Even though the mean evolution oscillates very little, the individual trajectories may at times tunnel vigorously. The longer-time simulations (Fig. 2.21) clearly illustrate this, where for $\gamma/\Omega = 100$ (in Fig. 2.21(b)), the conditional evolution suddenly revives near the

Figure 2.20: *Conditional (continuous line) and unconditional (dashed line) evolution of a 100-atom condensate in a noisy double-well potential, for different self-interaction strengths and well modulations. In (a) $\gamma/\Omega = 10$(a) and $\Theta = 0.9$, in (b) $\gamma/\Omega = 10$ and $\Theta = 2.0$, in (c) $\gamma/\Omega = 100$ and $\Theta = 0.9$, and in (d), $\gamma/\Omega = 100$ and $\Theta = 2.0$. The unconditional evolution is calculated from 100 trajectories. The time axis has been scaled by $t_0 = 1/\Omega$.*

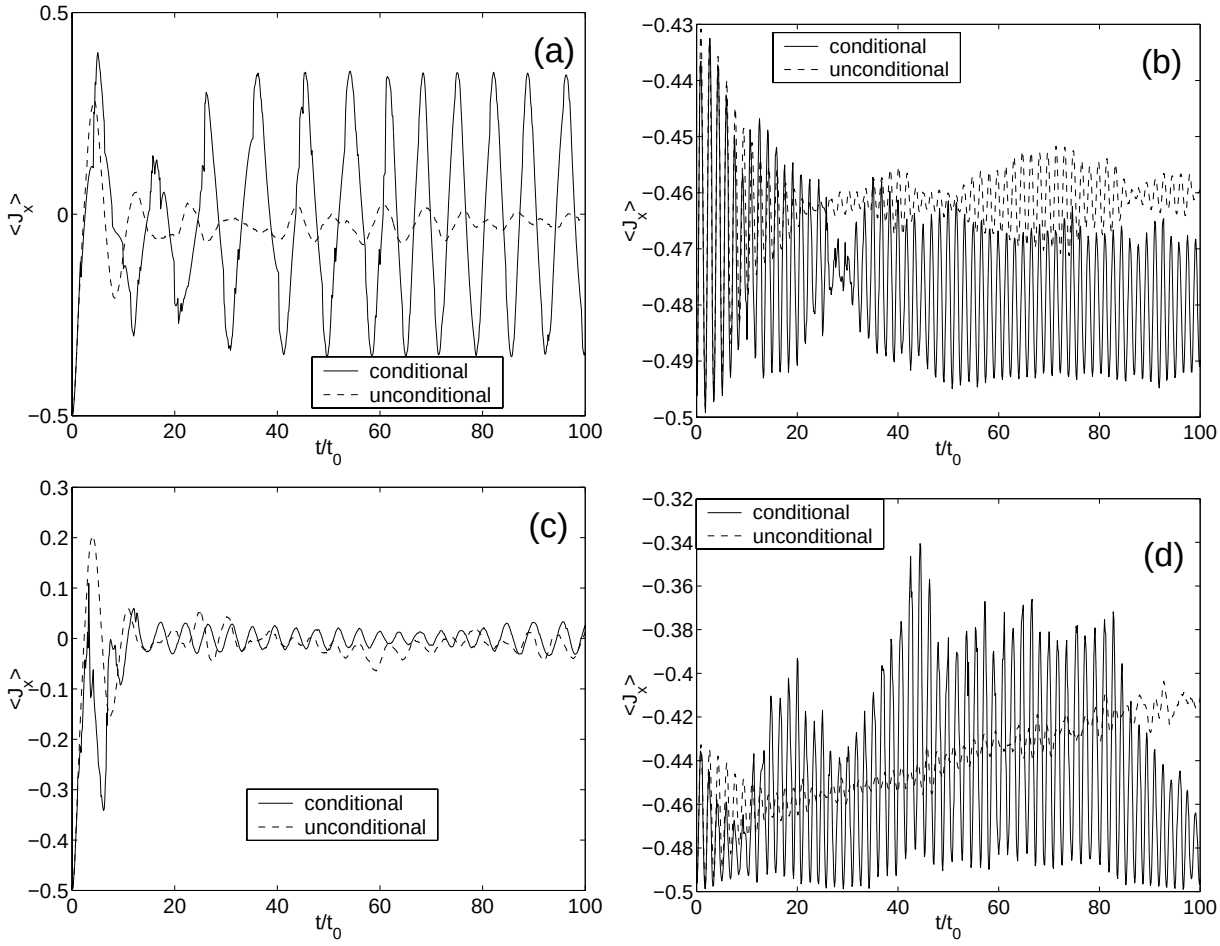

Figure 2.21: *Conditional (thin line) and unconditional (thick line) evolution of a 100-atom condensate in a noisy double-well potential, for* $\Theta = 0.9$ *(below critical). In (a),* $\gamma/\Omega = 10$ *and in (b),* $\gamma/\Omega = 100$*. The unconditional evolution is calculated from 100 trajectories. The time axis has been scaled by* $t_0 = 1/\Omega$*.*

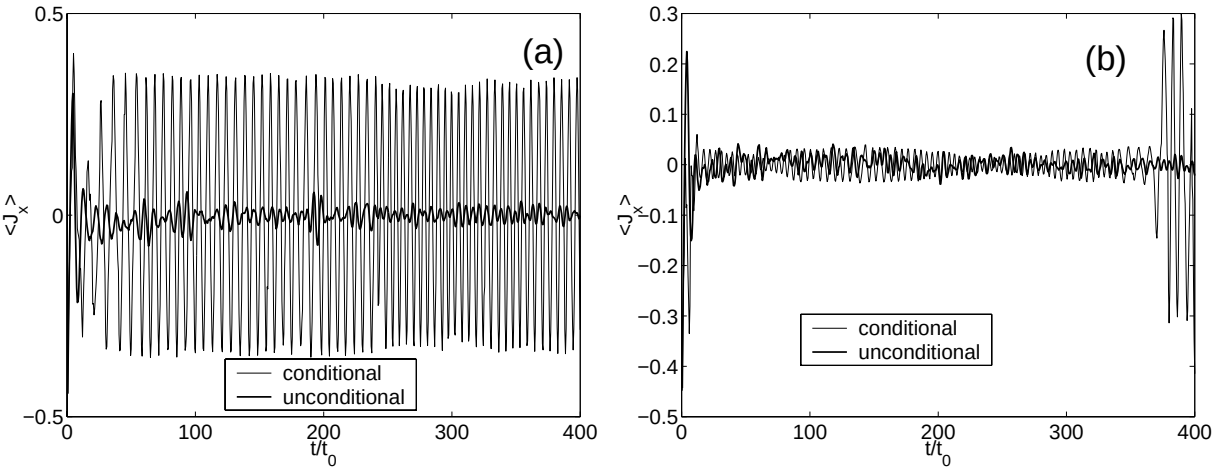

end of the simulation. Of course this conditional evolution has no meaning in the original physical situation of a condensate in a noisy potential - only the mean evolution has any correspondence. However the individual trajectories do have a physical interpretation as the system evolution conditioned on the results of a certain measurement process. The type of measurement model (and hence conditional evolution) is not unique for a given unconditional master equation (Eq. (2.85)). For example, the stochastic unravelling may be accomplished by a diffusive process, rather than this jump process, and it is to such a situation that we turn in Ch. 3.

Chapter 3

Homodyne measurements on a Bose-Einstein condensate

3.1 Symmetry-breaking measurements

This chapter describes a nondestructive measurement technique that monitors Josephson-like oscillations between the two components of a double Bose-Einstein condensate. The analysis is based on the system of two spatially-separated condensates that was introduced in Ch. 2. One of the condensates is placed in an optical cavity, which is strongly driven by a coherent optical field. The cavity output field is monitored using a homodyne detection scheme. The cavity field is well detuned from an atomic resonance, and experiences a dispersive phase shift proportional to the number of atoms in the cavity. Thus the coherent tunnelling oscillations in the atom distribution modulate the detected current. Even when the initial state is symmetric with respect to the two wells, back-action noise from the measurement induces Josephson-like oscillations; the measurement process itself establishes the phase.

The Bose condensates that have been produced in atom traps since 1995[3, 16, 35] contain well defined numbers of atoms, even when those numbers are very large $> 10^6$. For small numbers of atoms, as in the mesoscopic examples studied in this thesis, a number state is an appropriate description. How is this reconciled to the existence of a long-range order parameter, and its associated phase, as demonstrated in interference experiments[2, 4, 74]? For a multicomponent condensate, the total number of atoms may be definite, but there could be an uncertainty in how that number is distributed across

the different components. This uncertainty in the relative number implies that a relative phase difference may exist between the wave functions of any two components.

How does a coherent phase develop between, say, two number-state condensates that have been independently produced, or how does a phase difference develop between the two parts of a split condensate? To use the language of measurement, we may say that in order to detect a relative phase difference, we must couple the two components together. The measurement of phase induces, through the coupling, an uncertainty in the conjugate variable, which is the number of atoms. This leads the system to a state in which relative phase is more definite, which, in a self-consistent manner, becomes the phase that we measure. This process breaks the symmetry of having no phase information, and assigns a definite phase difference to the components, which varies randomly from one experiment or simulation to the next.

Many authors have discussed symmetry-breaking processes using double condensate models, for example by investigating the stability of the spatially symmetric mean-field ground state[138], the existence of nonsymmetric Hartree-Fock solutions[55], or symmetry-breaking in the processes leading to condensation[96]. However, this is mainly concerned with the breaking of spatial symmetry that occurs in the production of overlapping condensates, when the two condensates separate from one another, as with oil and water. The literature devoted to the symmetry-breaking processes that establish a relative phase[25, 71] has treated various measurement models designed to induce an interference pattern[30], which have been extended to include the presence of losses[159] or to be used as a phase standard[51], or to study subsequent phase evolution[94, 109, 133, 173, 175]. Most of the measurement models involve direct atom detection[85, 87, 95], although some continuous, nondestructive techniques have been proposed, including optical methods[88, 151] and a scheme for measuring the two-photon coherence between condensates in different hyperfine levels[153]. Some others deal with the phase manifested in coherent tunnelling, through destructive[91], or nondestructive[33, 152] techniques. In this thesis we concentrate on the Josephson oscillations that are induced in nondestructive continuous monitoring of the condensate.

The language of measurement is not necessary to describe how the phase is established. As Mermin[121, 120] has emphasised, quantum mechanics can be formulated entirely in terms of correlations, without recourse to models of measurement. That the conventional

Figure 3.1: *The homodyne detection scheme that monitors the tunnelling between two spatially separated condensates. One part of the condensate is contained in an optical cavity, the light in which is well detuned from any atomic resonance. The output light from the cavity is detected by balanced homodyne detection.*

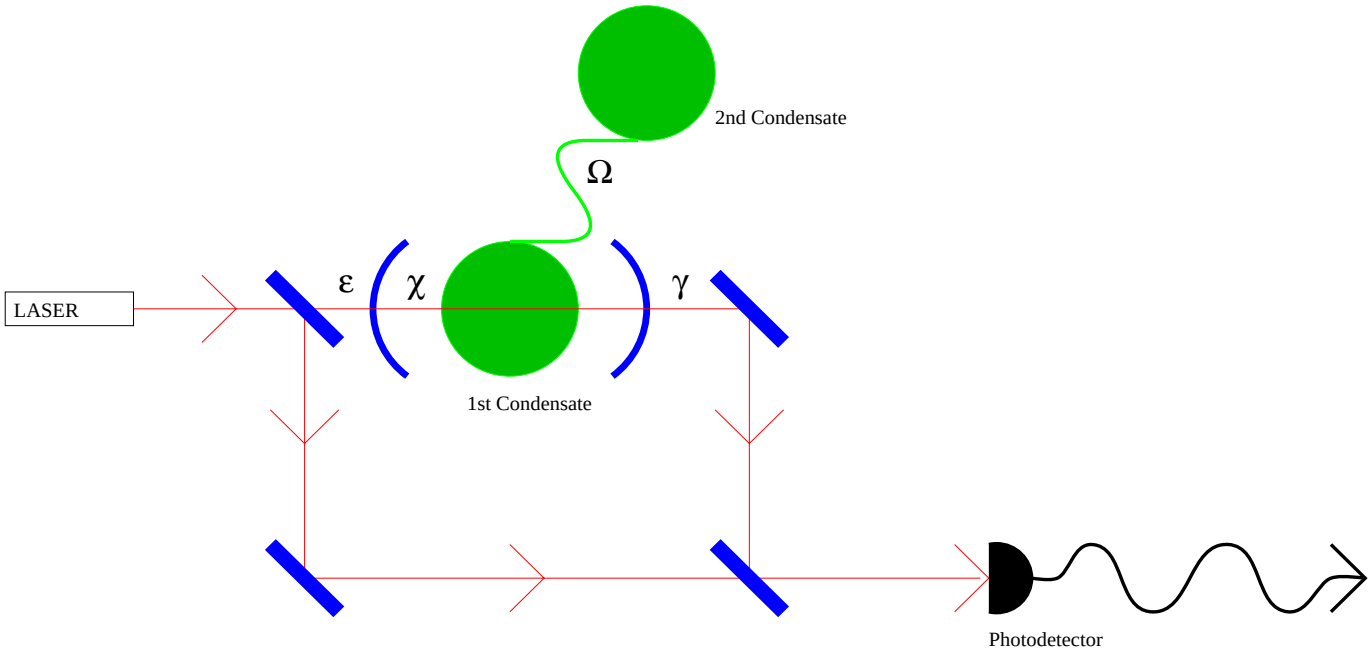

way of describing how quantum correlations develop and evolve is in terms of one system 'measuring' another is an accident of history, which, while providing an intuitive handle with which to grasp quantum mechanics, has often lead to confusion about the objective nature of the quantum world, particularly in popular accounts. The formulation of quantum mechanics in terms of developing correlations subsumes the measurement process as one particular type of correlation-inducing coupling, namely the interaction between a measurement apparatus and a sampled system. Thus while the system studied here is explicitly a measurement model, it provides insight into symmetry breaking in other situations as well, not necessarily so easily interpreted as measurement processes.

To investigate this symmetry-breaking process, we will use the double-well model introduced in Ch. 2, and once again use the two-mode Hamiltonian (Eq. (2.49)):

$$\hat{H}_2 = \hbar\Omega\hat{J}_z + 2\hbar\kappa\hat{J}_x^2. \tag{3.1}$$

3.2 Homodyne detection scheme

Figure 3.1 illustrates the system under investigation here. One of the wells of the double-well potential sits in an optical cavity. A coherent field strongly drives the cavity at the cavity frequency. We will assume that on the timescale of tunnelling oscillations, the cavity is heavily damped. The cavity field thus relaxes to the steady state on a much faster timescale than the condensate dynamics. This enables us to make an adiabatic elimination of the cavity dynamics. We can assume that the cavity field is far off resonance from any dipole transitions in the atomic species, so that the effect of the atoms is then entirely dispersive. The presence of the condensate shifts the phase of the cavity field by an amount proportional to the number of atoms in the cavity at any particular time. If the number of atoms in the cavity oscillates, so will the phase shift. Thus tunnelling of the condensate will be manifest as a modulated phase shift in the optical field exiting the cavity.

To detect this phase shift we consider a homodyne detection scheme. The optical cavity resides in one arm of an interferometer that combines the exiting light with a reference beam of the same frequency. The result falls on a photodetector, which records the photocurrent. If there is a difference in atom number between the two condensates, then coherent tunnelling can occur and the homodyne current will be modulated at the tunnelling frequency.

Assuming that the incoming light is detuned from any atomic resonance, the interaction Hamiltonian is

$$\hat{H}_I = -\int d^3r \hat{\psi}^\dagger(\mathbf{r})\hbar\mu g(\mathbf{r})\hat{a}^\dagger\hat{a}\hat{\psi}(\mathbf{r}), \tag{3.2}$$

where $\hat{a}$, $\hat{a}^\dagger$ are the cavity field operators, $g(\mathbf{r})$ is the intensity mode function and $\mu = g_d^2/4\Delta$ is the coupling strength, with dipole coupling constant g_d and optical detuning Δ.

Averaging over the optical mode function gives the interaction energy in terms of the condensate field operators c, $c^\dagger$:

$$\begin{aligned}\hat{H}_I &= -\hbar\chi\hat{a}^\dagger\hat{a}\hat{c}_1^\dagger\hat{c}_1 \\ &= -\hbar\frac{N}{2}\chi\hat{a}^\dagger\hat{a} - \hbar\chi\hat{a}^\dagger\hat{a}\hat{J}_x,\end{aligned} \tag{3.3}$$

where χ is the interaction strength. If the optical mode has a beam waist w, and a Gaussian profile $g(\mathbf{r}) = \cos^2(kz)\exp(-(x^2+y^2)/w^2)$ then the interaction strength is

$$\chi = \frac{\mu}{2\sqrt{2(r_0/w)^2+1}}. \tag{3.4}$$

For $N = 100$ atoms, $\chi > 10^{-3}s^{-1}$ should give detectable phase shifts (0.1 radians), and should be experimentally feasible. For example, in terms of the incident intensity I on the atom, the atomic linewidth γ_a, the total photon number N_P, and the saturation intensity I_s, the dipole coupling constant is[52]

$$g_d = \gamma_a \sqrt{\frac{I}{N_P I_s}}. \tag{3.5}$$

For a cavity of length l irradiated with light of frequency ω, the photon number is $N_P = Ilw^2/(\hbar\omega c)$. So the atom-light coupling strength becomes

$$\mu = \frac{\hbar\omega c\gamma_a^2}{4lw^2\Delta I_s}. \tag{3.6}$$

In the simulations given later in this chapter, the maximum measurement strength is $\chi \approx 10^3 s^{-1}$, which can be achieved by using the parameter values listed in Table 3.1, based on the $5S_{\frac{1}{2}} \longrightarrow 5P_{\frac{3}{2}}$ transition in Rubidium[52]. The narrow width of the intracavity field means that the power required to achieve the necessary coupling strengths is extremely small.

The cavity is driven by a strong coherent field of strength ϵ and strongly damped at the rate γ, and thus the cavity field is close to the coherent state $\alpha_0 = 2i\epsilon/\gamma$. The master equation for the whole system (cavity field plus condensate) is

$$\begin{aligned}\dot{\hat{\rho}}_{\rm tot} = -i\Omega\left[\hat{J}_z, \hat{\rho}_{\rm tot}\right] - i2\kappa\left[\hat{J}_x^2, \hat{\rho}_{\rm tot}\right] + i\chi\left[\hat{a}^\dagger\hat{a}\hat{J}_x, \hat{\rho}_{\rm tot}\right] - i(\delta - \frac{N\chi}{2})\left[\hat{a}^\dagger\hat{a}, \hat{\rho}_{\rm tot}\right] \\ - i\epsilon\left[\hat{a}^\dagger + \hat{a}, \hat{\rho}_{\rm tot}\right] + \frac{\gamma}{2}\left(2\hat{a}\hat{\rho}_{\rm tot}\hat{a}^\dagger - \hat{a}^\dagger\hat{a}\hat{\rho}_{\rm tot} - \hat{\rho}_{\rm tot}\hat{a}^\dagger\hat{a}\right),\end{aligned} \tag{3.7}$$

where the initial cavity detuning $\delta = N\chi/2$ is chosen to remove the N-dependent linear dispersion.

The optical field may now be adiabatically eliminated from the master equation [126, 181], under the assumption that the driving and damping terms dominate the coupling term. To do this, we first transform the master equation to a displacement picture using the displacement operator $\mathcal{D}(\alpha_0) = \exp(\alpha\hat{a}^\dagger - \alpha^*\hat{a})$ which creates a coherent state $\left|\alpha_0\right\rangle$ from the vacuum state:

$$\begin{aligned}\dot{\tilde{\rho}} &= \mathcal{D}^\dagger(\alpha_0)\dot{\hat{\rho}}_{tot}\mathcal{D}(\alpha_0) \\ &= \mathcal{S}\tilde{\rho} + i\chi\left[\left(\hat{a}^\dagger\hat{a} + \alpha_0^*\hat{a} + \alpha_0\hat{a}^\dagger + |\alpha_0|^2\right)\hat{J}_x, \tilde{\rho}\right] + \frac{\gamma}{2}\left(2\hat{a}\tilde{\rho}\hat{a}^\dagger - \hat{a}^\dagger\hat{a}\tilde{\rho} - \tilde{\rho}\hat{a}^\dagger\hat{a}\right),\end{aligned} \tag{3.8}$$

where $\mathcal{S}$ incorporates the condensate dynamics. For large damping γ, then

$$\left|\frac{\langle\mathcal{S}\rangle}{\gamma}\right| \sim \left|\frac{\chi|\alpha_0|\langle\hat{J}_x\rangle}{\gamma}\right| = \epsilon_0 \ll 1, \tag{3.9}$$

Table 3.1: *Fundamental and derived parameters of the intracavity system.*

Quantity	Value	Description
r_0	$10\mu m$	length scaling
w	$60\mu m$	beam width
l	$10cm$	cavity length
I_s	$17W/m^2$	saturation intensity
$\omega/2\pi$	$3.8 \times 10^{14}Hz$	optical frequency
$\gamma_a/2\pi$	$6MHz$	atomic linewidth
$\Delta/2\pi$	$300MHz$	optical detuning
P	$5.7 \times 10^{-9}W$	incident power
I	$3.2W/m^2$	intracavity intensity
N_P	15	photon number
g_d	$4.2 \times 10^6 s^{-1}$	dipole coupling constant
γ	$1.5 \times 10^9 s^{-1}$	cavity damping rate
ϵ	$4.1 \times 10^9 s^{-1}$	cavity driving
χ	$1.2 \times 10^3 s^{-1}$	coupling strength

and the displaced optical field will be close to the vacuum state. For the parameters given in Table 3.1, $\epsilon_0 \leq 1.5 \times 10^{-4}$, and it will be smaller for weaker coupling χ. The density matrix $\tilde{\rho}$ can then be expanded in powers of ϵ_0, up to second order:

$$\tilde{\rho} = \rho_0 |0\rangle_a\langle 0| + \rho_1 |1\rangle_a\langle 0| + \rho_1^\dagger |0\rangle_a\langle 1| + \rho_2 |1\rangle_a\langle 1| + \rho_{2'} |2\rangle_a\langle 0| + \rho_{2'}^\dagger |0\rangle_a\langle 2| + O(\epsilon^3). \tag{3.10}$$

Substituting this expansion into Eq. (3.8) and equating like terms gives

$$\dot{\rho}_0 = \mathcal{S}\rho_0 + \gamma\rho_2 + i\chi|\alpha_0|^2 \left[\hat{J}_x, \rho_0\right] - i\chi\alpha_0(\hat{J}_x\rho_1 + \rho_1^\dagger \hat{J}_x) \tag{3.11a}$$

$$\dot{\rho}_1 = \mathcal{S}\rho_1 - \frac{\gamma}{2}\rho_1 + i\chi|\alpha_0|^2 \left[\hat{J}_x, \rho_1\right] + i\chi\alpha_0(\hat{J}_x\rho_0 - \rho_2\hat{J}_x - \sqrt{2}\hat{J}_x\rho_{2'}) + i\chi\hat{J}_x\rho_1 \tag{3.11b}$$

$$\dot{\rho}_2 = \mathcal{S}\rho_2 - \gamma\rho_2 + i\chi|\alpha_0|^2 \left[\hat{J}_x, \rho_2\right] + i\chi\alpha_0(\hat{J}_x\rho_1^\dagger + \rho_1\hat{J}_x) + i\chi(\hat{J}_x\rho_2 - \rho_2\hat{J}_x) \tag{3.11c}$$

$$\dot{\rho}_{2'} = \mathcal{S}\rho_{2'} - \gamma\rho_{2'} + i\chi|\alpha_0|^2 \left[\hat{J}_x, \rho_{2'}\right] + i\sqrt{2}\chi\alpha_0\hat{J}_x\rho_1 + \sqrt{2}i\chi\hat{J}_x\rho_{2'}. \tag{3.11d}$$

We wish to trace over the field variables to get a reduced master equation for the atomic system alone:

$$\begin{aligned}\dot{\hat{\rho}} &= \mathrm{Tr}_{\mathrm{field}}\dot{\hat{\rho}}_{\mathrm{tot}} = \mathrm{Tr}_{\mathrm{field}}\dot{\tilde{\rho}} = \dot{\rho}_0 + \dot{\rho}_2 \\ &= \mathcal{S}(\rho_0 + \rho_2) + i\chi|\alpha_0|^2 \left[\hat{J}_x, \rho_0 + \rho_1\right] + i\chi\alpha_0 \left[\hat{J}_x, \rho_1^\dagger - \rho_1\right] + \gamma O(\epsilon_0^3).\end{aligned} \tag{3.12}$$

To eliminate ρ_1 from this expression, we can use Eq. (3.11b), noting that $|\alpha_0|\epsilon_0 \ll 1$ and that, for large damping, $\dot{\rho}_i \ll |\gamma\rho_i|$. From the leading order terms in Eq. (3.11b),

$$\rho_1 = \frac{2i\chi\alpha_0}{\gamma}\hat{J}_x\rho_0 + O(\epsilon_0^1). \tag{3.13}$$

Substituting this into Eq. (3.12) gives the master equation in terms of the atomic variables alone:

$$\dot{\hat{\rho}} = -i\Omega\left[\hat{J}_z, \hat{\rho}\right] - i2\kappa\left[\hat{J}_x^2, \hat{\rho}\right] + i\chi|\alpha_0|^2\left[\hat{J}_x, \hat{\rho}\right] - \frac{\Gamma}{2}\left[\hat{J}_x, \left[\hat{J}_x, \hat{\rho}\right]\right] + O(\epsilon_0^3), \tag{3.14}$$

where the measurement strength is $\Gamma = 16\chi^2\epsilon^2/\gamma^3$.

The double commutator represents a decoherence produced by photon number fluctuations in the optical field. It is a quantum measurement back-action term consistent with the interpretation that the optical field makes a measurement on the condensate. In fact this last term destroys coherence in the eigenbasis of $\hat{J}_x$ and thus should inhibit tunnelling oscillations. This is indeed true for the ensemble of measured systems described by the

master equation. However, as shown below, it is not true for a particular realisation of a single measurement run.

The ensemble-averaged effect of the measurement can be seen in the operator moment equations (for $\kappa = 0$):

$$\langle \dot{\hat{J}}_x \rangle = -\Omega \langle \hat{J}_y \rangle \tag{3.15a}$$

$$\langle \dot{\hat{J}}_y \rangle = \chi |\alpha_0|^2 \langle \hat{J}_z \rangle + \Omega \langle \hat{J}_x \rangle - \frac{\Gamma}{2} \langle \hat{J}_y \rangle \tag{3.15b}$$

$$\langle \dot{\hat{J}}_z \rangle = -\chi |\alpha_0|^2 \langle \hat{J}_y \rangle - \frac{\Gamma}{2} \langle \hat{J}_z \rangle. \tag{3.15c}$$

The terms with coefficient $\chi|\alpha_0|^2$ produce a precession around the x-axis, which tends to inhibit coherent tunnelling. The effect of these terms can be negated by adding a linear ramp, or tilt, to the double-well potential. The Γ terms cause a decay toward the origin, indicating decoherence, as expected. If the system begins in a number state with an equal number of atoms in each well, then no tunnelling will occur at all: these moments remain identically zero.

When the wells are tilted, so that the precession around the x-axis is suppressed, we can obtain equations for the second-order moments:

$$\langle \dot{\hat{J}}_x^2 \rangle = -\Omega \langle \hat{\Lambda} \rangle \tag{3.16a}$$

$$\langle \dot{\hat{J}}_y^2 \rangle = \Omega \langle \hat{\Lambda} \rangle + \Gamma(\langle \hat{J}_z^2 \rangle - \langle \hat{J}_y^2 \rangle) \tag{3.16b}$$

$$\langle \dot{\hat{J}}_z^2 \rangle = \Gamma(\langle \hat{J}_y^2 \rangle - \langle \hat{J}_z^2 \rangle) \tag{3.16c}$$

$$\langle \dot{\hat{\Lambda}} \rangle = 2\Omega(\langle \hat{J}_x^2 \rangle - \langle \hat{J}_y^2 \rangle) - \frac{\Gamma}{2} \langle \hat{\Lambda} \rangle. \tag{3.16d}$$

where $\hat{\Lambda} = \hat{J}_x \hat{J}_y + \hat{J}_y \hat{J}_x$.

This reveals that even when the system is started with an equal number of atoms in each well, the unconditional evolution of $\langle \hat{J}_x^2 \rangle$ and $\langle \hat{J}_y^2 \rangle$ exhibit oscillations initially; this number state has a hidden tunnelling phase. For long times, the amplitude of these oscillations decays due to Γ and the system approaches the fixed point $\langle \hat{J}_x^2 \rangle = \langle \hat{J}_y^2 \rangle = \langle \hat{J}_z^2 \rangle = \frac{1}{3} j(j+1)$. From this we see that the condensate has on average a definite initial phase (clearly seen in the second-order moments, but not the first order moments), which is determined by the initial state. In the simulations the initial state was chosen to be a eigenstate of $\hat{J}_x$, which is not the only state which gives an equal number of atoms in each well. Presumably in a real experiment, the initial state would be

$$|\psi(\tau)\rangle = e^{-i\tau \hat{J}_z} |j, 0\rangle_x, \tag{3.17}$$

where τ is a random variable uniformly distributed on the interval $[0, 2\pi]$. This then implies a random initial phase.

3.3 Stochastic trajectories

In quantum optics, a common technique deals with master equations describing open systems by numerically simulating stochastic realisations of quantum trajectories. We can choose the appropriate stochastic equations to correspond to a particular measurement model. Individual trajectories then correspond to particular runs of an experiment, in which relative phases may be evident, even though the unconditional behaviour (averaged over many paths) possesses phase symmetry. This method has already been used by several authors investigating the effect of measurement on the relative phase of binary condensates[91, 150, 151] and we have briefly considered such a scheme in Sec. 2.3.4. These differ from the approach we now consider in that the resultant stochastic process is a diffusive evolution rather than the jump process that occurs in the direct detection of atoms or individual photons.

The stochastic unravelling that we will use corresponds to the ideal limit of homodyne detection as described by Wiseman[179, 181]. The photocurrent comprises a series of photon-detection events. In the ideal limit, the rate of photon detection goes to infinity, as does the amplitude of the local oscillator, such that the back-action on the system remains finite. The conditional master equation (that is, the evolution conditioned on the measurement result) for the condensate and optical field undergoing homodyne detection is[179]

$$d\hat{\rho}_{\mathrm{tot},c} = \Bigg(-i\Omega\left[\hat{J}_z, \hat{\rho}_{\mathrm{tot},c}\right] - i2\kappa\left[\hat{J}_x^2, \hat{\rho}_{\mathrm{tot},c}\right] + i\chi\left[\hat{a}^\dagger\hat{a}\hat{J}_x, \hat{\rho}_{\mathrm{tot},c}\right] - i(\delta - \frac{N\chi}{2})\left[\hat{a}^\dagger\hat{a}, \hat{\rho}_{\mathrm{tot},c}\right] - i\epsilon\left[\hat{a}^\dagger + \hat{a}, \hat{\rho}_{\mathrm{tot},c}\right] + \gamma\mathcal{D}[\hat{a}]\rho_{\mathrm{tot},c}\Bigg)dt + \sqrt{\gamma}dW(t)\mathcal{H}[\hat{a}]\rho_{\mathrm{tot},c}, \quad (3.18)$$

where $dW(t)$ is the infinitesimal Weiner increment. In this Ito stochastic equation, $\hat{\rho}_{\mathrm{tot},c}$ is the density matrix that is conditioned on a particular realisation of the homodyne current up to time t. Wiseman's super-operators are defined as[179]

$$\mathcal{D}[\hat{a}]\hat{\rho} = \hat{a}\hat{\rho}\hat{a}^\dagger - \frac{1}{2}\left(\hat{a}^\dagger\hat{a}\hat{\rho} + \hat{\rho}\hat{a}^\dagger\hat{a}\right), \quad (3.19a)$$

$$\mathcal{H}[\hat{a}]\hat{\rho} = \hat{a}\hat{\rho} + \hat{\rho}\hat{a}^\dagger - \mathrm{Tr}\left(\hat{a}\hat{\rho} + \hat{\rho}\hat{a}^\dagger\right)\hat{\rho}. \quad (3.19b)$$

As with the unconditional evolution, we can adiabatically eliminate the cavity field variables from Eq. (3.18), by substituting in for the density operator the expansion Eq. (3.10). Tracing over the field variables gives

$$\begin{aligned}\dot{\hat{\rho}}_c &= \dot{\rho}_0 + \dot{\rho}_2 \\ &= \mathcal{S}(\rho_0+\rho_2) + i\chi|\alpha_0|^2\left[\hat{J}_x, \rho_0+\rho_1\right] + i\chi\alpha_0\left[\hat{J}_x, \rho_1^\dagger - \rho_1\right] \\ &+ \sqrt{\gamma}\frac{dW}{dt}\left(\rho_1+\rho_1^\dagger - (\rho_0+\rho_2)\mathrm{Tr}(\rho_1+\rho_1^\dagger)\right) + \gamma O(\epsilon_0^3). \end{aligned} \tag{3.20}$$

For $\gamma \sim \epsilon_0^{-2} \gg 1$, we can replace ρ_1 by Eq. (3.13) to give

$$\begin{aligned} d\hat{\rho}_c = -i\Omega\left[\hat{J}_z, \hat{\rho}_c\right]dt - i2\kappa\left[\hat{J}_x^2, \hat{\rho}_c\right]dt + \frac{\Gamma}{2}\left[\hat{J}_x, \left[\hat{J}_x, \hat{\rho}_c\right]\right]dt \\ + \sqrt{\Gamma}\left(\hat{J}_x\hat{\rho}_c + \hat{\rho}_c\hat{J}_x - 2\left\langle J_x\right\rangle_c\hat{\rho}_c\right)dW + dt\gamma O(\epsilon_0^3), \end{aligned} \tag{3.21}$$

where we have adjusted the initial cavity detuning δ and tilted the wells to remove unimportant terms. The adiabatic elimination in both the conditional and unconditional cases is equivalent to making the replacement $\hat{a} \longrightarrow \Gamma\hat{J}_x/\gamma$. Thus the environmental decoherence in the light field is transferred directly to a decoherence in the atomic operators, and constitutes the back action of the homodyne measurement on the condensate.

Just as in the unconditional evolution, we can derive equations of motion for the conditional moments from Eq. (3.21). Even when $\kappa = 0$, the stochastic terms in the equations always couple to higher order moments. To get a closed set of equations, we can factorise each third-order moment into a second-order moment multiplied by $\langle\hat{J}_x\rangle$. For an initial number state, we get the following closed set:

$$d\langle\hat{J}_x\rangle = -\Omega\langle\hat{J}_y\rangle dt + 2\sqrt{\Gamma}\left(\langle\hat{J}_x^2\rangle - \langle\hat{J}_x\rangle^2\right)dW \tag{3.22a}$$

$$d\langle\hat{J}_y\rangle = \left(\Omega\langle\hat{J}_x\rangle - \frac{\Gamma}{2}\langle\hat{J}_y\rangle\right)dt + 2\sqrt{\Gamma}\left(\frac{1}{2}\langle\hat{\Lambda}\rangle - \langle\hat{J}_x\rangle\langle\hat{J}_y\rangle\right)dW \tag{3.22b}$$

$$d\langle\hat{J}_z\rangle = -\frac{\Gamma}{2}\langle\hat{J}_z\rangle dt - 2\sqrt{\Gamma}\langle\hat{J}_x\rangle\langle\hat{J}_z\rangle dW \tag{3.22c}$$

$$d\langle\hat{J}_x^2\rangle = -\Omega\langle\hat{\Lambda}\rangle dt \tag{3.22d}$$

$$d\langle\hat{J}_y^2\rangle = \left(\Omega\langle\hat{\Lambda}\rangle - \Gamma\left(\langle\hat{J}_y^2\rangle - \langle\hat{J}_z^2\rangle\right)\right)dt \tag{3.22e}$$

$$d\langle\hat{J}_z^2\rangle = \Gamma\left(\langle\hat{J}_y^2\rangle - \langle\hat{J}_z^2\rangle\right)dt \tag{3.22f}$$

$$d\langle\hat{\Lambda}\rangle = \left(2\Omega(\langle\hat{J}_x^2\rangle - \langle\hat{J}_y^2\rangle) - \frac{\Gamma}{2}\langle\hat{\Lambda}\rangle\right)dt. \tag{3.22g}$$

Because the third-order correlations are now factorised, the second-order moments evolve deterministically. This means that the tunnelling oscillations do not show a slow phase

drift (as we shall see in the fully quantum results), and that they are also damped. However, for short times, these equations do reproduce all the dynamics seen in the quantum results.

From the conditional master equation, we can write down a stochastic Shrödinger equation that explicitly gives the conditional dependence on the measured current $I(t)$:

$$d\big|\tilde{\Psi}_c(t)\big\rangle = dt\left[-i\hat{H}_2 - \frac{\Gamma}{2}\hat{J}_x^2 + I(t)\hat{J}_x\right]\big|\tilde{\Psi}_c(t)\big\rangle, \tag{3.23a}$$

$$I(t) = 2\Gamma\big\langle\hat{J}_x\big\rangle_c + \sqrt{\Gamma}\xi(t), \tag{3.23b}$$

where $\big|\tilde{\Psi}_c(t)\big\rangle$ is the unnormalised ket describing the conditional state of the system, and where the stochastic term $\xi(t)$ has the correlations

$$\big\langle\xi(t)\big\rangle = 0 \tag{3.24a}$$

$$\big\langle\xi(t),\xi(t')\big\rangle = \delta(t-t'). \tag{3.24b}$$

Thus we can see how the system evolution is conditioned upon the measured current, and how oscillations in the particle number difference $\big\langle\hat{J}_x\big\rangle_c$ modulate the current.

For our purposes, it is more useful to consider the Shrödinger equation for the normalised ket that does not explicitly mention the detection current:

$$d\big|\Psi_c(t)\big\rangle = \left[-i\hat{H}_2dt - \frac{\Gamma}{2}\left(\hat{J}_x - \big\langle\hat{J}_x\big\rangle_c\right)^2 dt + \sqrt{\Gamma}\left(\hat{J}_x - \big\langle\hat{J}_x\big\rangle_c\right)dW\right]\big|\Psi_c(t)\big\rangle. \tag{3.25}$$

The terms in the equation due to the measurement depend on the quantity $\hat{J}_x - \big\langle\hat{J}_x\big\rangle_c$. This is minimal in semiclassical type trajectories for which $\big\langle\hat{J}_x^2\big\rangle_c$ factorises to $\big\langle\hat{J}_x\big\rangle_c^2$. Thus we may expect that for some range of values of χ, the stochastic measurement terms would drive the system towards an oscillating trajectory for which $\big\langle\hat{J}_x^2\big\rangle_c \simeq \big\langle\hat{J}_x\big\rangle_c^2$. The reduced uncertainty in position would lead to momentum fluctuations, which in turn could drive tunnelling oscillations.

3.4 Simulations

The results of the simulations of Eq. (3.25) are shown in Figs. 3.2 to 3.8. Time is plotted along the x-axis in units of $t_0 = 1/\Omega$. The strengths of the atom-atom collisions and the atom-field interaction were controlled by varying respectively the normalised variables $\Theta = \kappa N/\Omega$ and $\overline{\Gamma} = \Gamma N^2/\Omega$. The parameters stated in Table 3.1 give the range of measurement

strengths used in the simulations ($1.6\times10^{-3} < \overline{\Gamma} < 1.6\times10^{3}$) for $N = 100$ when the power of the optical field is varied. The mass of the particles is $m = 1.5\times10^{-25}kg$, corresponding to rubidium. In many respects, the simulation was similar to the quantum simulations in Ch. 2, except that at each time step, the conditional moment $\langle \hat{J}_x \rangle_c$ was calculated and incorporated into the effective Hamiltonian. The stochastic Weiner increment was implemented with Gaussian white noise whose strength was such as to produce the correct correlations.

The measured current gives the conditional dynamics of the the system. However, to present the conditional results we can plot $\langle \hat{J}_x \rangle_c$, which is proportional to the current without the noise (Eq. (3.23b)). For clarity, the other moments, namely $\langle \hat{J}_y \rangle_c$ and $\langle \hat{J}_z \rangle_c$, are not plotted in the figures. Except when Θ is very large, $\langle \hat{J}_y \rangle_c$ follows $\langle \hat{J}_x \rangle_c$, but with a $\frac{\pi}{2}$ phase difference, and $\langle \hat{J}_z \rangle_c$ remains at or close to zero.

The dynamics of the unmonitored system when started with all the condensate in one well have been shown in Fig. 2.11. When there are no atom-atom interactions ($\Theta = 0$), $\langle \hat{J}_x \rangle$ oscillates from $-\frac{1}{2}N$ to $+\frac{1}{2}N$. When the interactions are present but only weak, tunnelling still occurs, but the amplitude quickly collapses due to nonlinear dephasing. The collapse is followed some time later by small revivals. There is a critical strength of collisions ($\Theta = 1$) at which the tunnelling is suppressed. Above this value of Θ, the condensate is trapped in the well in which it started, with only very small oscillations occurring in $\langle \hat{J}_x \rangle$.

We expect to see similar behaviour in the current of the monitored system (Eq. (3.25)). When $\Theta = 0$, $\langle \hat{J}_x \rangle_c$ oscillates as before, for weak atom-light coupling (i.e. $\overline{\Gamma} \lesssim 16$). For stronger measurements, the resulting back action can be seen in the current. For long times, the amplitude of the tunnelling oscillations starts to fluctuate and a slow phase drift is evident. In the case when atom collisions are present, the effect of the measurements is to halt the collapse of the oscillations seen in the unmonitored system. The phase changes are also more pronounced. The effect of the critical value ($\Theta N = 1$) is seen in the suppression of the oscillations in the current above this value. Figure 3.2 shows the evolution of $\langle \hat{J}_x \rangle_c$ for values of Θ above and below the critical value.

If the system starts with an equal number of atoms in each well, then we can expect no coherent tunnelling in the absence of any detection apparatus. However, the presence of the field effects a measurement on the condensate system. This should establish a phase,

Figure 3.2: *Evolution of* $\langle \hat{J}_x \rangle_c$ *in the monitored system, for* $N = 100$ *atoms all initially in one well and* $\overline{\Gamma} = 16$. *In (a)* $\Theta = 0.5$ *and in (b)* $\Theta = 2.0$.

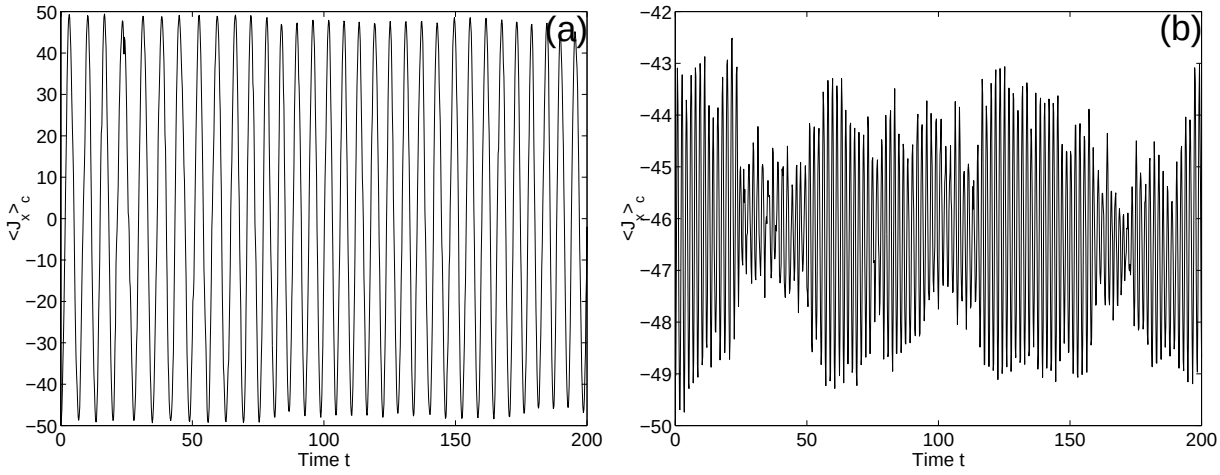

which can be detected by measuring the output current $I(t)$. The simulations of Eq. (3.25) show an oscillation in the current and, for the optimum interaction strength, this can be established in only a few tunnelling periods, for a small number of atoms. The results for the case where there are no atom collisions, ie $\Theta = 0$, are shown in Fig. 3.3, for various measurement strengths $\overline{\Gamma}$. The growth in oscillations occurs because, for large enough $\overline{\Gamma}$, $\langle \hat{J}_x \rangle_c^2$ is driven to match $\langle \hat{J}_x^2 \rangle_c$, which typically has large oscillations.

If, as in Fig. 3.3(a), the interaction strength is too small ($\overline{\Gamma} < 0.16$), then generally the fluctuations are not large enough to drive full tunnelling on the timescale shown; the current suffers small, rather irregular oscillations, with the borderline case of Fig. 3.3(b) only occasionally leading to full tunnelling oscillations. However even for large $\overline{\Gamma}$, when the oscillations in the current are established, such as in Fig. 3.3(c), they are not guaranteed to stay large in amplitude. This is because $\langle \hat{J}_z^2 \rangle_c$ undergoes what appears to be a random walk which, because of the Casimir invariant, directly affects the amplitude of the oscillations in $\langle \hat{J}_x^2 \rangle_c$ and $\langle \hat{J}_y^2 \rangle_c$. Consequently, since the measurement locks $\langle \hat{J}_x \rangle_c^2$ onto the orbit of $\langle \hat{J}_x^2 \rangle_c$, this changes the amplitude of the oscillations in the current. Because of the random nature of the orbit of $\langle \hat{J}_z^2 \rangle_c$, the tunnelling oscillations in the current over a certain time frame in a "good" run may be large, but in another with the same parameters the oscillations may be small and irregular in amplitude.

When the measurement is quite strong ($\overline{\Gamma} \simeq 1600$), as in Fig. 3.3(d), the tunnelling oscillations appear to be quite irregular. However, a Fourier transform of the data (Fig.

Figure 3.3: *Evolution of* $\langle \hat{J}_x \rangle_c$ *in the monitored system, for* $N = 100$ *atoms and* $\Theta = 0$. *In (a)* $\overline{\Gamma} = 1.6 \times 10^{-3}$, *in (b)* $\overline{\Gamma} = 0.16$, *in (c)* $\overline{\Gamma} = 16$, *and in (d)* $\overline{\Gamma} = 1600$.

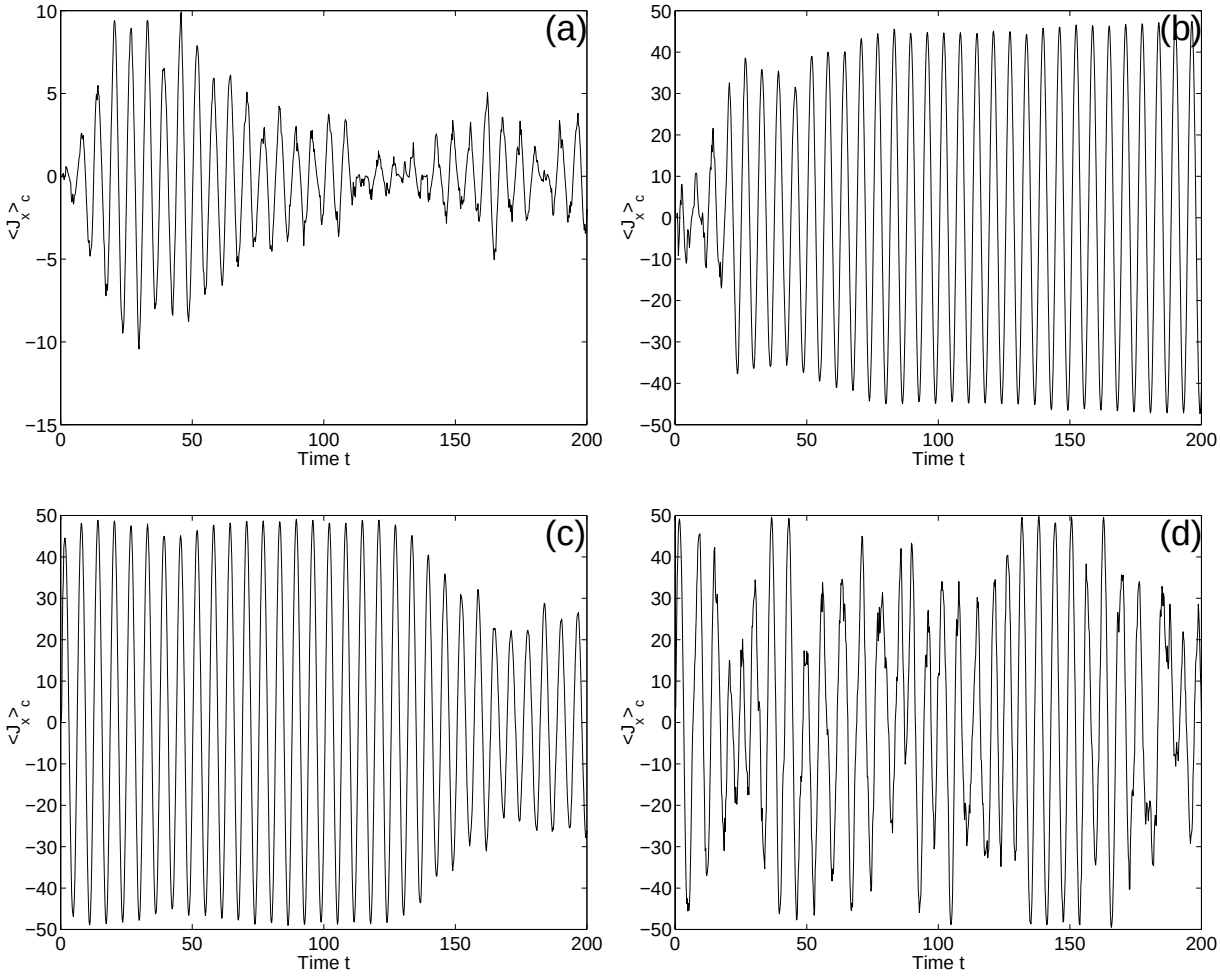

Figure 3.4: *Fourier transform of some of the tunnelling data in Figs 3.3 & 3.8. In (a)* $\overline{\Gamma} = 0.16$ *and* $\Theta = 0.0$*, in (b)* $\overline{\Gamma} = 1600$ *and* $\Theta = 0.0$*, in (c)* $\overline{\Gamma} = 0.16$ *and* $\Theta = 0.5$*, and in (d)* $\overline{\Gamma} = 0.16$ *and* $\Theta = 2.0$*.*

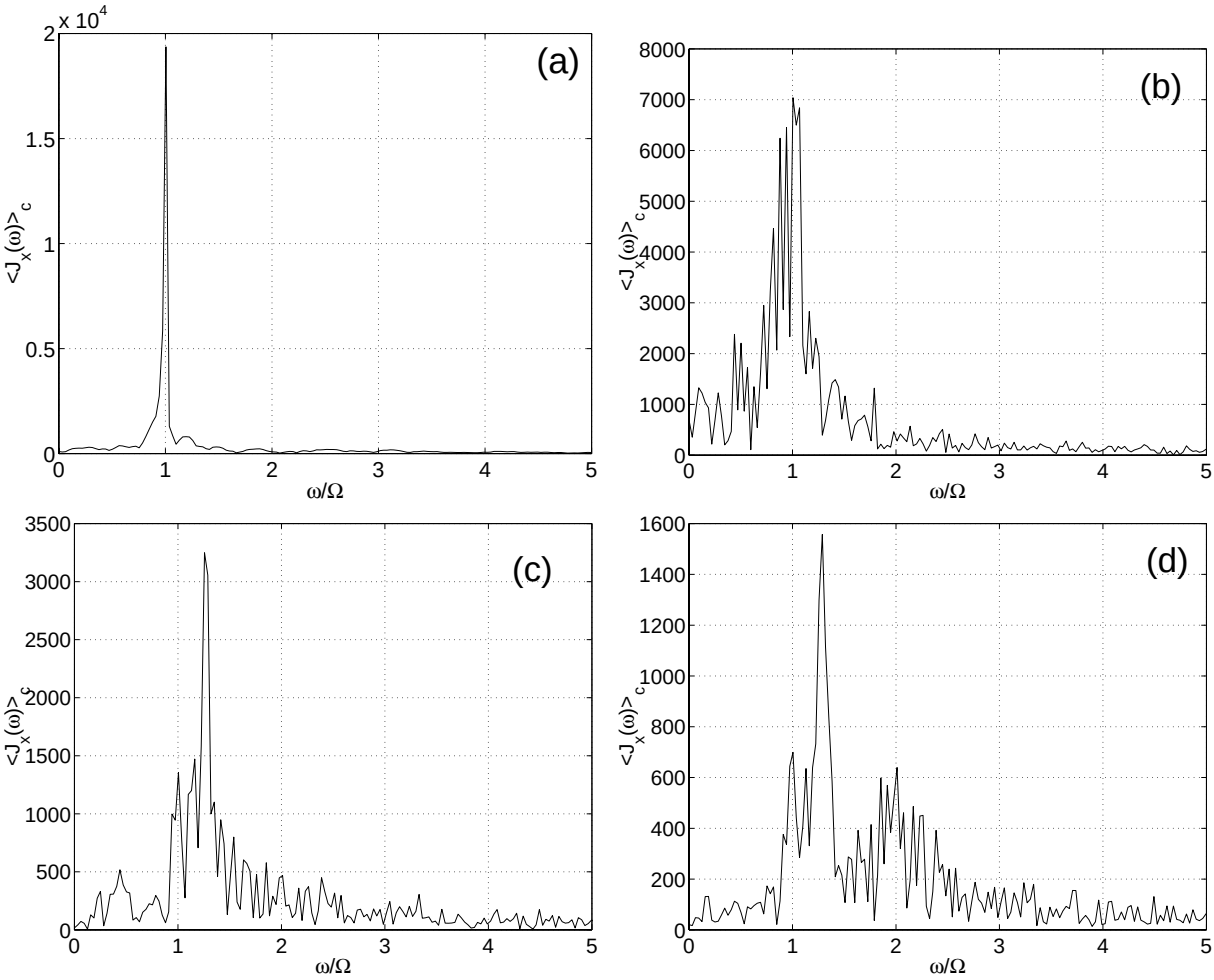

3.4(b)) picks out the tunnelling frequency Ω very strongly, so the fluctuations are mainly in the amplitude of oscillations, not in the phase. When the measurement strength is very large ($\overline{\Gamma} = 2.65 \times 10^4$), $\left\langle \hat{J}_x \right\rangle_c$ still indicates a tunnelling from one well to another, but the oscillations are no longer harmonic and appear quite random, both in frequency and amplitude.

The equations for the unconditional dynamics (Eqs. (3.15a) to (3.16d)) show a decay in the oscillations of $\left\langle \hat{J}_x^2 \right\rangle$ and $\left\langle \hat{J}_y^2 \right\rangle$ for long times, which increases with the measurement strength $\overline{\Gamma}$. Figure 3.5 shows the unconditional dynamics for two different measurement strengths. No such decay is seen in the individual trajectories, but rather there is a diffusion in the phase of the oscillation over long times which accounts for the decay in

Figure 3.5: *Unconditional evolution of second-order moments, for* $N = 100$ *atoms and* $\Theta = 0$*. In (a)* $\overline{\Gamma} = 16$ *and in (b)* $\overline{\Gamma} = 1600$

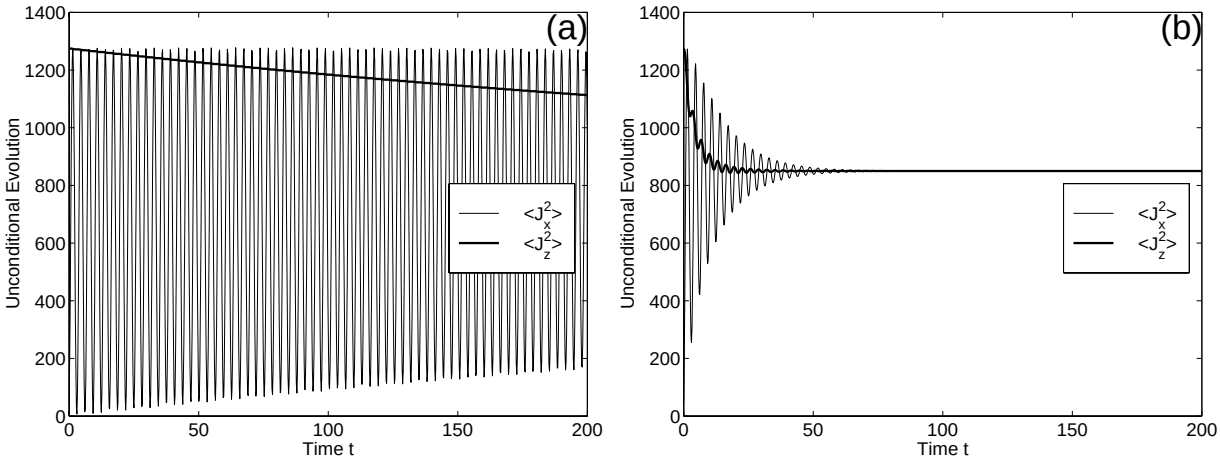

the mean evolution. This change in phase appears to be most rapid over the periods when the oscillations are small in amplitude and most likely to suffer random fluctuations.

Figures 3.6 and 3.7 show the approximate semiclassical dynamics given by Eq. (3.22). Since the second-order moments behave deterministically in these equations, phase diffusion will be inhibited and damping will occur for long times. However for short times or weak atom-light coupling, the results should be valid. The results for a weak coupling of $\overline{\Gamma} = 1.6 \times 10^{-3}$, as shown Fig. 3.6(a), reveal the build up of small tunnelling oscillations which vary in amplitude (similar to its quantum counterpart in Fig. 3.3(a)). A stronger measurement strength ($\overline{\Gamma} = 0.16$, as in Fig. 3.6(b)) leads to large regular oscillations, just as in the quantum case (Fig. 3.3(b)). Figure 3.7 gives results for a $N = 1000$ atom condensate for the same values of the measurement strength $\overline{\Gamma}$ as in Fig. 3.6. The relative amplitude of the tunnelling oscillations and the rate at which they develop are the same as for the smaller condensate. This justifies the use of $\overline{\Gamma}$, which contains a factor of N^2 in its definition, as the appropriate normalised measurement strength.

The presence of atom-atom interactions increases the phase diffusion, even for quite weak collisions ($\Theta \leq 0.1$). Figure 3.8 shows the evolution of $\langle \hat{J}_x \rangle_c$ for various atom-atom interaction strengths Θ, above and below the critical value. The amplitude is also more irregular, and the Fourier transform of the oscillations (Figs. 3.4(c&d)) no longer shows a clear peak at the expected tunnelling frequency, but a group of peaks, whose amplitudes and positions vary from one run to another, centered on the tunnelling frequency. In

Figure 3.6: *Approximate evolution of* $\langle \hat{J}_x \rangle_c$, *for* $N = 100$ *atoms and* $\Theta = 0$. *In (a)* $\overline{\Gamma} = 1.6 \times 10^{-3}$ *and in (b)* $\overline{\Gamma} = 0.16$. *The time axis has been normalised by* $t_0 = 1/\Omega$.

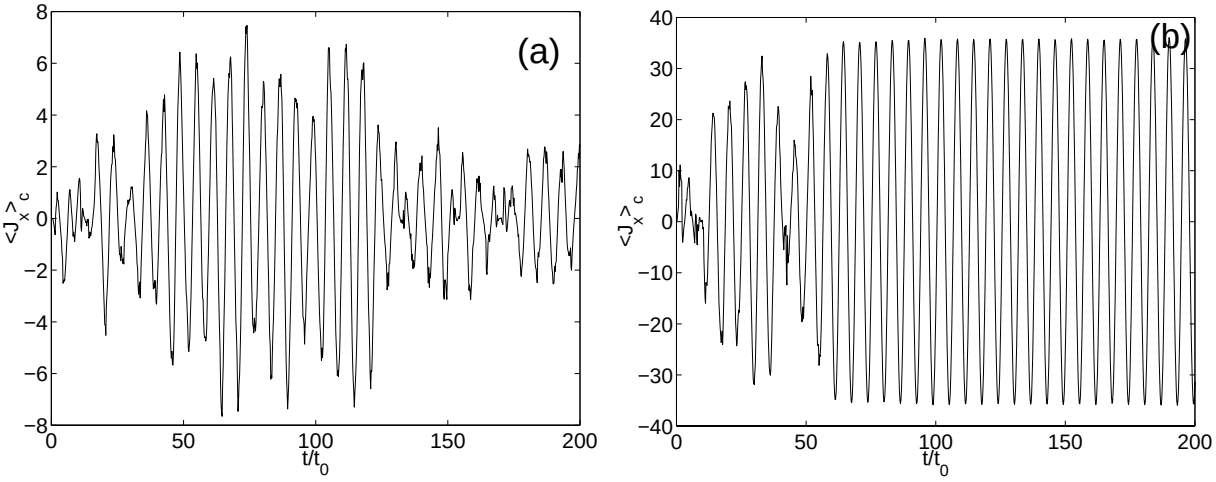

Figure 3.7: *Approximate evolution of* $\langle \hat{J}_x \rangle_c$, *for* $N = 1000$ *atoms and* $\Theta = 0$. *In (a)* $\overline{\Gamma} = 1.6 \times 10^{-3}$ *and in (b)* $\overline{\Gamma} = 0.16$. *The time axis has been normalised by* $t_0 = 1/\Omega$.

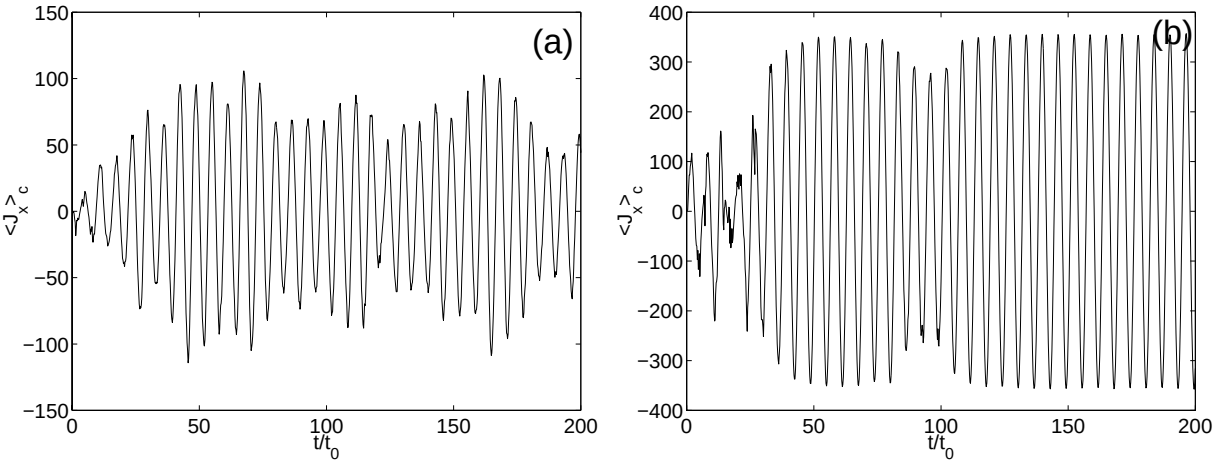

Fig. 3.8(b), $\Theta = 0.5$ which is close to the value of Θ calculated from the parameters given previously. Above the critical value of $\Theta = 1$, $\langle \hat{J}_x \rangle_c$ suffers small, very irregular oscillations around the origin (Fig. 3.8(c)). This is quite different to the behaviour of $\langle \hat{J}_x \rangle_c$ when the condensate was initially placed entirely in one well(Fig. 3.2(b)), in which case the condensate was trapped in the well it started in and the critical value of Θ marked quite a sharp boundary (or bifurcation) between two different types of behaviour. In this case where the condensate is distributed equally between the wells, the condensate is trapped in neither well, but remains across both, and the change in behaviour as the critical point is crossed is more continuous. As Θ increases past the critical point, we see a decrease in the overall amplitude of the tunnelling and in its regularity. However, the critical value of Θ is still quite meaningful in this case as an indication of when the strength of the atom collisions significantly suppresses the tunnelling. We note that the effects on self-trapping of coupling to an open system have also been studied in [152].

3.5 Before we move on

These simulations of the quantum dynamics show that, for an appropriate choice of measurement strength Γ, this homodyne detection scheme could well be suitable to detect the relative phase, in the form of Josephson-like tunnelling, between two condensates in a double-well potential. The dynamics of the measured current reflect the tunnelling of the condensate as well as the self-trapping effect caused by atom collisions. It also demonstrates quite vividly how a measurement can establish a (relative) phase in a system which initially exhibits no phase information.

For these very small condensates, the atom-number difference oscillates vigorously after only a few tunnelling periods. What happens for larger condensates in which quantum effects are less important? In the next chapter, we will discuss various attempts to build a semiclassical formulation of the monitored system, to see whether the back-action effects that are necessary to break the symmetry can be so described.

Figure 3.8: *Evolution of* $\langle \hat{J}_x \rangle_c$ *in the monitored system, for* $N = 100$ *atoms, and* $\overline{\Gamma} = 0.16$. *In (a)* $\Theta = 0.01$, *in (b)* $\Theta = 0.5$, *and in (c)* $\Theta = 2$.

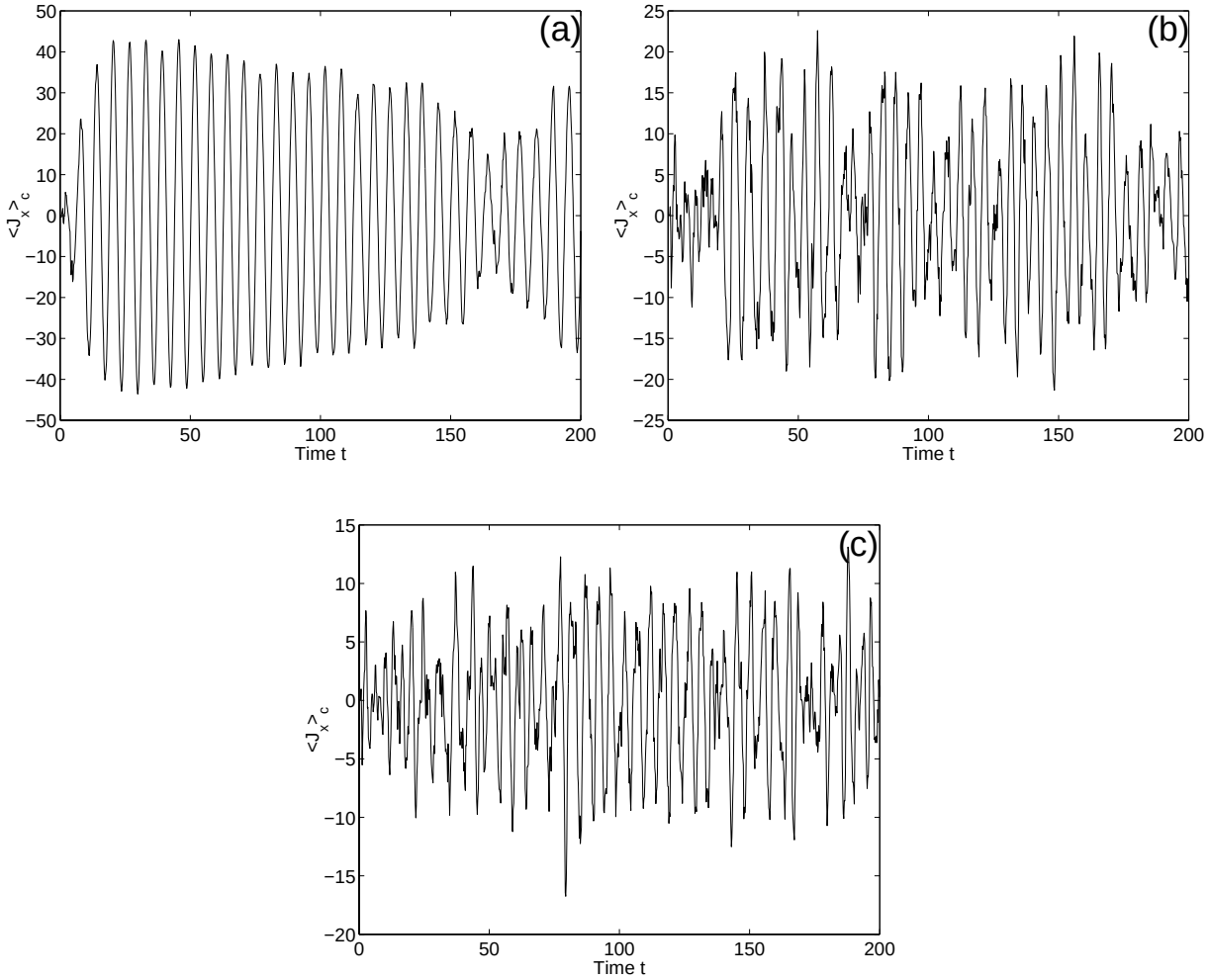

Chapter 4

Continuously monitored condensates: quasiprobability distributions

4.1 Introduction - conditional master equation

This chapter explores the different ways of describing the continuously monitored Bose condensate in terms of classical probability distributions. As in the rest of this thesis, our focus will be on providing quantum descriptions. Nevertheless we do mention in passing several semiclassical descriptions, whose analysis may lead to useful complimentary results. We shall follow two paths: The first involves a description in terms of classical random variables, which will include attempting a mean-field formulation of the problem. A detailed analysis in not attempted in this thesis, beyond stating the initial results and their implications. The second path makes use of quasiprobability distributions. We will exploit the Q function to study the dynamics on the Bloch sphere, and will also translate the system into phase-space variables via generalised Q and P distributions.

We begin with the conditional master equation (Eq. (3.21)) for the continuously measured double condensate:

$$d\hat{\rho}_c = -i\Omega\left[\hat{J}_z,\hat{\rho}_c\right]dt - i2\kappa\left[\hat{J}_x^2,\hat{\rho}_c\right]dt + \frac{\Gamma}{2}\left[\hat{J}_x,\left[\hat{J}_x,\hat{\rho}_c\right]\right]dt + \sqrt{\Gamma}\left(\hat{J}_x\hat{\rho}_c + \hat{\rho}_c\hat{J}_x - 2\left\langle\hat{J}_x\right\rangle_c\hat{\rho}_c\right)dW, \quad (4.1)$$

where $dW(t)$ is the infinitesimal Weiner increment and the decoherence is $\Gamma = 16\chi^2\epsilon^2/\gamma^3$. The optical field strength is ϵ and it is damped at the rate γ. The various couplings are: the measurement strength χ, the particle interaction strength κ, and the tunnelling

frequency Ω, which is given by the overlap between the local modes of each well. This Ito stochastic equation describes the state of the system conditioned on a particular history of measurement results[181, 179]. The value of the measured current, which depends on a classical random variable, feeds back into the master equation via $\langle \hat{J}_x \rangle_c$, resulting in a stochastic state matrix $\hat{\rho}_c$.

One 'classical' description is to write down equations of motion for diagonal elements $\rho_{m,m}$ of the state matrix in the number state basis:

$$\rho_{m,m}(t+dt) = \rho_{m,m}(t) + \frac{\Omega dt}{2}\Big(\sqrt{j(j+1)-m(m+1)}(\rho_{m,m+1}(t)+\rho_{m+1,m}(t)) - \sqrt{j(j+1)-m(m-1)}(\rho_{m,m-1}(t)+\rho_{m-1,m}(t))\Big) + 2\sqrt{\Gamma}dW\,(m-\overline{m})\,\rho_{m,m}(t), \quad (4.2)$$

where $\rho_{m,m} =_x \langle j,m|\hat{\rho}_c|j,m\rangle_x$ and $\overline{m} = \sum_m m\rho_{m,m}$. Now $|j,m\rangle_x$ are also the eigenstates of position, and so this equation gives the stochastic evolution of the conditional position distribution. Setting $\Omega = 0$ and identifying $x = 2q_0 m/N$ gives the closed equation

$$\rho_c(x,t+dt) = \rho_c(x,t) + \frac{\sqrt{\Gamma}N}{q_0}dW\,(x-\overline{x})\,\rho_c(x,t), \quad (4.3)$$

where $\rho_c(x) = \rho_{m,m}$. Thus without any tunnelling, the measurement process assigns a classical probability distribution to the variable x (as in [124]). This distribution is conditioned on previous imperfect measurement results and so is stochastic and nonlinear.

When the system exists in an eigenstate of position, the stochastic term in Eq. (4.3) disappears and the distribution is stationary. Thus for the measurement to induce back-action fluctuations, the off-diagonal coherences due to tunnelling must be present. These periodically induce an uncertainty in x as the state precesses around the $\hat{J}_z$ axis of the Bloch sphere, and it is at these times that measurement-induced fluctuations feed back into the conditional state.

4.2 Stochastic Gross-Pitaevskii equation

Continuing our quest to formulate a semiclassical description of the back-action effects of the measurement, we now derive a modified Gross-Pitaevskii (GP) equation from the stochastic Shrödinger equation (Eq. (3.25)):

$$d|\Psi_c(t)\rangle = \left[-i\hat{H}_2 dt - \frac{\Gamma}{2}\left(\hat{J}_x - \langle \hat{J}_x\rangle_c\right)^2 dt + \sqrt{\gamma}\left(\hat{J}_x - \langle \hat{J}_x\rangle_c\right)dW\right]|\Psi_c(t)\rangle \quad (4.4)$$

where, as in Ch. 2, $\hat{H}_2 = \Omega\hat{J}_z + 2\kappa\hat{J}_x^2$ and $\big|\Psi_c(t)\big\rangle$ describes the conditional state of the system. We use the measurement part of this equation to derive the terms needed to modify the GP equation. As in Sec. 2.2, we expand the state vector as

$$\big|\Psi_c(t)\big\rangle = \frac{1}{\sqrt{N!}}\left[\int d^3\mathbf{r}\Phi_c(\mathbf{r},t)\hat{\psi}^\dagger(\mathbf{r},0)\right]^N \big|0\big\rangle, \tag{4.5}$$

and then multiply Eq. (3.25) from the left by $\big\langle\Psi_c(t)\big|$. We must calculate terms like

$$\begin{aligned}\big\langle\Psi_c(t)\big|\hat{J}_x\big|\Psi_c(t)\big\rangle &= \frac{N}{2q_0}\big\langle\Psi_c(t)\big|\int dx\hat{\psi}^\dagger(x)x\hat{\psi}(x)\big|\Psi_c(t)\big\rangle \\ &= \frac{N^2}{2q_0}\int dx\Phi_c^*(x,t)\Phi_c(x,t)x \end{aligned}\tag{4.6a}$$

$$\begin{aligned}\big\langle\Psi_c(t)\big|\hat{J}_x^2\big|\Psi_c(t)\big\rangle &= \frac{N^2}{4q_0^2}\big\langle\Psi_c(t)\big|\int dx\hat{\psi}^\dagger(x)x^2\hat{\psi}(x)\big|\Psi_c(t)\big\rangle \\ &= \frac{N^3}{4q_0^2}\int dx\Phi_c^*(x,t)\Phi_c(x,t)x^2 \end{aligned}\tag{4.6b}$$

for the measurement terms in Eq. (3.25). For the other terms, we use the original many-body Hamiltonian (Eq. (2.1)) rather than the two-mode approximation $\hat{H}_2$. Minimising the integrand of the resultant expression gives

$$i\hbar\frac{\partial}{\partial t}\Phi_c(x,t) = \left[-\frac{\hbar^2}{2m}\nabla^2 + V(x) + V_R(x,t) + NU_0|\Phi_c(x,t)|^2\right]\Phi_c(x,t), \tag{4.7}$$

where $E[x] = \int dx\Phi_c^*(x,t)\Phi_c(x,t)x$ and where $V_R(x,t)$ is a time-dependent, stochastic potential:

$$V_R(x,t) = -\frac{N^2\Gamma}{8q_0^2}\left(x - E[x]\right)^2 + \frac{N\sqrt{\Gamma}}{2q_0}\left(x - E[x]\right)\frac{dW}{dt}, \tag{4.8}$$

which is quadratic in x. Since Eq. (4.7) is an Ito equation, the unconditional evolution is obtained by simply deleting the noise term, in which case, $V_R(x,t)$ reduces to an inverted parabola. This parabola would repel the distribution $\Phi(x,t)$ from the point $x = E[x]$, thus preventing the unconditional distribution to localise. In the conditional evolution, the stochastic contribution to the potential is large away from $x = E[x]$, which could possibly cause the distribution $\Phi_c(x,t)$ in individual trajectories to localise at different x values, or at least to remain compact around a mean that evolves in time.

Although not considered in this thesis, numerical integration of Eq. (4.7) should lead to similar behaviour as in the fully quantum simulations. In other words, for an initial distribution of an equal number of atoms in each well, the fluctuations induced by the measurement should drive tunnelling oscillations. The main distinguishing feature between

the quantum and semiclassical equations in the closed case was the collapse and revival sequence, but the homodyne measurement suppresses this in the open system. Hence there should be a good correspondence between the semiclassical and quantum systems. The mean-field approach has the advantage over the quantum two-mode approximation in that it is tractable and valid for large numbers of atoms.

4.3 Atomic Q function

Now we cease analysing the measurement process in terms of distributions that are explicitly defined as probabilities, and turn to distributions which in general may not qualify as true probabilities. Useful *quasi*probabilities can be derived by expanding the state in terms of an overcomplete basis set, such as the set of coherent states, rather than the orthogonal number-state basis set used in Eq. (4.3). The overcompleteness allows a diagonal expansion that results in a closed evolution equation for the distribution, and which contains all the effects of off-diagonal coherences. Thus the quantum state maps entirely onto the quasiprobability distribution.

4.3.1 Definition in terms of Bloch states

The numerical calculation of quasiprobabilities provides considerable insight into the dynamics on the Bloch sphere. The atomic Q function is defined as

$$Q(\mu) = \frac{\langle \mu | \rho_c | \mu \rangle}{\pi} \geq 0 \tag{4.9}$$

where $|\mu\rangle$ is the atomic coherent state, or Bloch state. Since $Q(\mu)$ is defined to be positive and normalised, it does qualify as a true probability distribution, however we do not need to interpret it as such for the present application. The Bloch states can be written in terms of the Dicke states as[6]

$$|\mu\rangle = \sum_{m=-j}^{j} \begin{pmatrix} 2j \\ m+j \end{pmatrix}^{\frac{1}{2}} \frac{\mu^{m+j}}{(1+|\mu|^2)^j} |j,m\rangle_z. \tag{4.10}$$

In terms of spherical coordinates, $\mu = e^{-i\phi}\tan(\theta/2)$ and

$$\begin{aligned} \langle \hat{J}_x \rangle &= \frac{N}{2}\sin\theta\cos\phi \\ \langle \hat{J}_y \rangle &= \frac{N}{2}\sin\theta\sin\phi \\ \langle \hat{J}_z \rangle &= -\frac{N}{2}\cos\theta. \end{aligned} \tag{4.11}$$

In this geometry, the maximal and minimal eigenstates of $\hat{J}_z$ are localised at the north ($\theta = \pi$) and south ($\theta = 0$) poles, respectively. The maximal and minimal eigenstates of $\hat{J}_x$ and $\hat{J}_y$ are localised around points that lie on the equator ($\theta = \pi/2$). So a number state with all the atoms in one well has a Q function centred at either $(\theta, \phi) = (\pi/2, 0)$ or $(\theta, \phi) = (\pi/2, \pi)$.

The Bloch states can be obtained by a rotation (θ, ϕ) around the sphere of the lowest-weight Dicke state $\big|j, -j\big\rangle_z$[6]:

$$\big|\mu\big\rangle = R_{\theta,\phi}\big|j, -j\big\rangle_z, \tag{4.12}$$

where

$$R_{\theta,\phi} = e^{\hat{J}_x \sin\phi - \hat{J}_y \cos\theta} = e^{\zeta \hat{J}_+ - \zeta^* \hat{J}_-}, \tag{4.13}$$

for $\zeta = \frac{1}{2}\theta \exp(-i\phi)$. The step operators $\hat{J}_+$ and J_- are the atomic equivalents of the annihilation and creation operators, in terms of which,

$$\hat{J}_x = \frac{1}{2}\left(\hat{J}_+ + \hat{J}_-\right), \tag{4.14a}$$

$$\hat{J}_y = \frac{i}{2}\left(\hat{J}_- - \hat{J}_+\right), \tag{4.14b}$$

$$\hat{J}_z = \frac{1}{2}\left[\hat{J}_+, \hat{J}_-\right]. \tag{4.14c}$$

Useful Bloch state relations include[110]: the inner product

$$\big\langle\lambda|\mu\big\rangle = \frac{(1 + \lambda^*\mu)^{2j}}{(1 + |\lambda|^2)^j\,(1 + |\mu|^2)^j}, \tag{4.15a}$$

the completeness identity

$$1 = \frac{2j+1}{\pi}\int d^2\mu \frac{\big|\mu\big\rangle\big\langle\mu\big|}{(1 + |\mu|^2)^2}, \tag{4.15b}$$

the matrix elements

$$\big\langle\lambda\big|\hat{J}_+\big|\mu\big\rangle = \frac{2j\lambda^*\,(1 + \lambda^*\mu)^{2j-1}}{(1 + |\lambda|^2)^j\,(1 + |\mu|^2)^j} = \Big(\big\langle\mu\big|\hat{J}_-\big|\lambda\big\rangle\Big)^*, \tag{4.15c}$$

and the integral

$$\frac{2j+1}{\pi}\int d^2\mu \frac{\mu^{*m}\mu^n}{(1 + |\mu|^2)^{2j+2}} = \frac{(2j-m)!m!}{(2j)!}\,\delta_{m,n} \quad 0 < m, n < 2j. \tag{4.15d}$$

4.3.2 Numerical simulations

Once the stochastic Schrödinger equation (Eq. (3.25)) has been used to calculate the conditional state as a function of time, the Q function can be calculated numerically from the definition of the Bloch state (Eq. (4.9)). The numerical simulations shown below were performed using the eigenstates of $\hat{J}_x$ as the basis set, whereas the Q function is defined in terms of the eigenstates of $\hat{J}_z$. To write the Q function in terms of the $\left|j,m\right\rangle_x$ states, we can use

$$\left|j,m\right\rangle_z = \sum_{m'} C^{j,m}_{m'} \left|j,m'\right\rangle_x, \tag{4.16}$$

the coefficients in which can be determined to within a phase factor from

$$C^{j,m}_{m'-1}\sqrt{j(j+1)-m(m'-1)} + C^{j,m}_{m'+1}\sqrt{j(j+1)-m(m'+1)} = 2C^{j,m}_{m'} \tag{4.17}$$

and the normalisation condition $\left|\sum C^{j,m}_{m'}\right|^2 = 1$.

Figures 4.1 to 4.5 contain stroboscopic contour plots of the Q function in polar coordinates (θ,ϕ), for the initial number state $\left|j,0\right\rangle_x$. This state corresponds to a band around the Bloch sphere that lies in the $\hat{J}_y - \hat{J}_z$ plane. Under the influence of the tunnelling term in $\hat{H}_2$, without measurement, this band spins around the $\hat{J}_z$ axis. As distinct from Sec. 2.2.1, the south pole of the Bloch sphere is at the bottom of the figure window ($\theta = 0$), but once again maximal occupation of one of the wells corresponds to a point at either the centre ($(\theta,\phi) = (\frac{\pi}{2},0)$) or the side edges ($(\theta,\phi) = (\frac{\pi}{2},\pm\pi)$). The strength of the measurement is given by the normalised quantity $\overline{\Gamma} = \Gamma N^2/\Omega$.

The collisionless case is shown in Figs. 4.1 and 4.2, for weak and strong measurement strengths respectively. In Fig. 4.1, the band on one side of the sphere grows at the expense of the other, until the distribution is localised in a semicircular band, precessing around the sphere in strong tunnelling oscillations. When the measurement is strong (Fig. 4.2), the localisation occurs much sooner, after which the Q function splits in twain in the J_z direction. The two components recombine and separate periodically, corresponding to growth and decline in the amplitude of the $\left\langle \hat{J}_x \right\rangle_c$ tunnelling oscillations. Occasionally, the components move over the poles of the sphere to recombine on the other side, causing a phase jump in the tunnelling oscillations.

Figures 4.3 to 4.5 show the effect of increasing collisional strength in the weak measurement regime. For $\Theta = 0.01$ (Fig. 4.3), the localised band twists slightly around its

Figure 4.1: *Contour plots of the atomic Q function in polar coordinates, with the initial state* $|j,0\rangle_x$*, for a weak measurement* ($\overline{\Gamma} = 0.16$) *and no atom collisions* ($\Theta = 0.00$). *The times of successive plots are separated approximately by the tunnelling period:* $t_n \simeq 2\pi n/\Omega$, *and are printed in units of* $t_0 = 1/\Omega$.

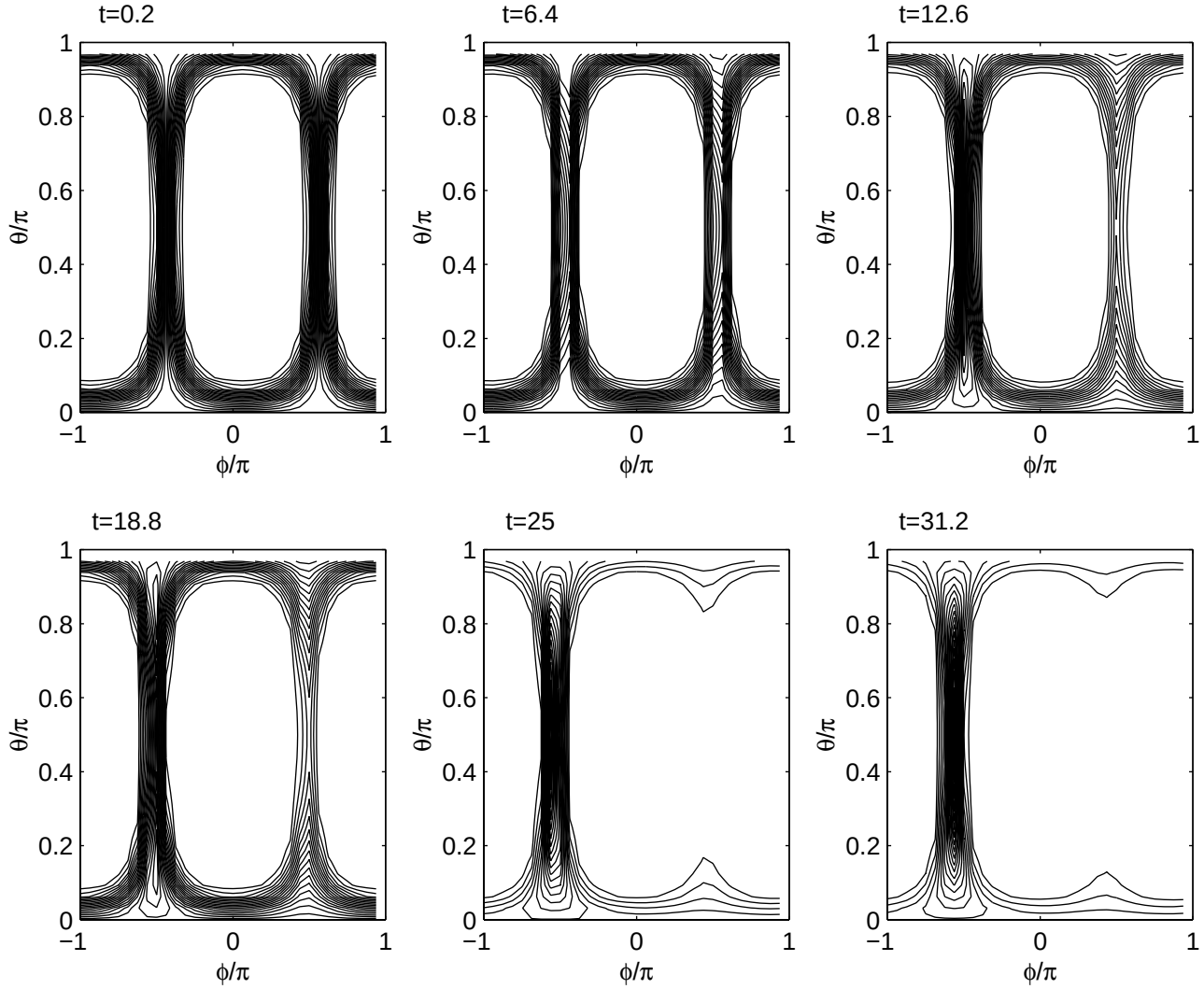

Figure 4.2: *Contour plots of the atomic Q function in polar coordinates, with the initial state* $|j,0\rangle_x$*, for a strong measurement (*$\overline{\Gamma} = 1600$*) and no atom collisions (*$\Theta = 0.00$*). The times of successive plots are separated approximately by the tunnelling period:* $t_n \simeq 2\pi n/\Omega$*, and are printed in units of* $t_0 = 1/\Omega$*.*

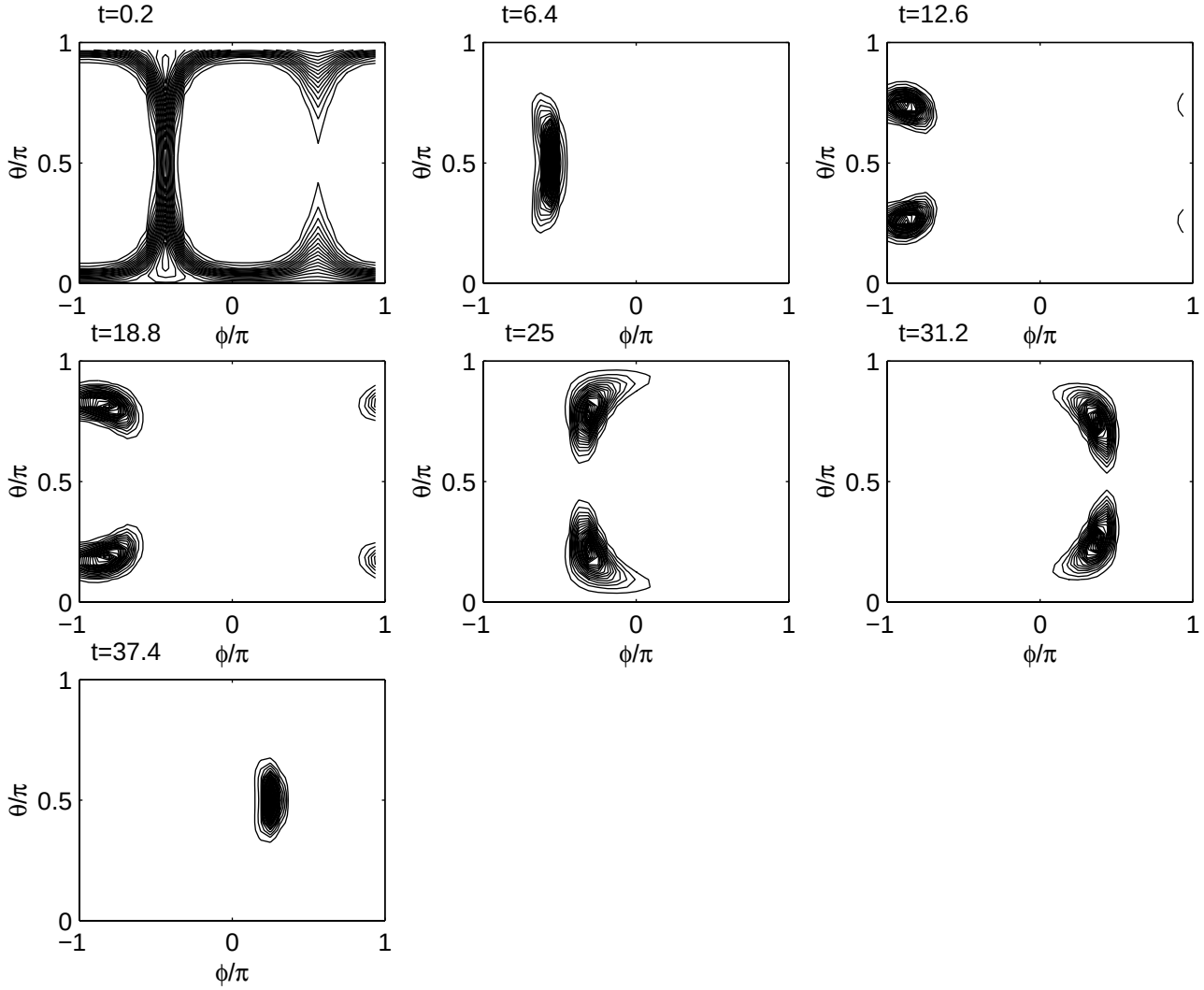

centre, but for $\Theta = 0.50$ (Fig. 4.4), the distribution shears drastically. Near the bottom of the Bloch sphere ($\theta = 0$), the rotation around the $\hat{J}_z$ axis is at the tunnelling frequency Ω, but near the top, it is greatly retarded. This is consistent with the semiclassical dynamical analysis in Sec. 2.2.1, which showed that the tunnelling motion of trajectories near the south of the Bloch sphere was more robust in the presence of collisions than trajectories near the top of the sphere. The resultant distribution lies almost parallel to the equator as it rotates around the $\hat{J}_z$ axis, its elongation smearing out any definite phase in the tunnelling oscillations. The zig-zag motion is due to the nonlinear twisting effect near the $\hat{J}_x$ poles.

When the atom collisions are above the critical strength, as in Fig. 4.5, no rotation around the vertical axis is evident. The band stays in place, but deforms and also expands near the base of the Bloch sphere. This is consistent with the suppression of tunnelling seen in the evolution of $\langle \hat{J}_x \rangle_c$.

To obtain a clearer insight into how the measurement feedback affects the Q distribution, we can evolve the system under the measurement part of the Schrödinger equation without the tunnelling or collisional terms present. Our previous initial state $|j, 0\rangle_x$ is stationary in this case, since it is an eigenstate of $\hat{J}_x$ and $\hat{J}_x^2$. So instead, we can begin with the same state but have it rotated $\pi/2$ around the sphere, i.e. $|j, 0\rangle_y$. This state is distributed around a great circle with J_y as its axis, as Fig. 4.6(a) shows. Under the influence of a weak measurement, the band on one side grows at the expense of the other, as in Fig. 4.6(b), until the Q function is located entirely on one side of the sphere. Which side this is varies from one run to another. After a longer time, or for a stronger measurement strength, the Q function separates into two compact distributions, equally spaced above and below the equator (Fig. 4.6(c)). These distributions then form into crescent shapes before eventually joining to form a circular band around the $\hat{J}_x$ axis (Fig. 4.6(d)).

This behaviour is an intuitive consequence of the conditional and nonlinear nature of the measured system. The presence of $\langle \hat{J}_x \rangle_c$ in Eq. (3.25), which conditions the evolution on past measurement results, induces the localisation evident in Figs. 4.6(b&c); an imperfect measurement partially collapses the wave function around the measurement value, thereby narrowing the distribution. The diffusive spread around the $\hat{J}_x$ axis seen in Fig. 4.6(d) betrays the presence of $\hat{J}_x^2$ in the stochastic Schrödinger equation, which generates this nonlinear precession.

Figure 4.3: Contour plots of the atomic Q function in polar coordinates, with the initial state $\left|j,0\right\rangle_x$, for a weak measurement ($\overline{\Gamma} = 0.16$) and weak interatomic interaction ($\Theta = 0.01$). The times of successive plots are separated approximately by the tunnelling period: $t_n \simeq 2\pi n/\Omega$, and are printed in units of $t_0 = 1/\Omega$.

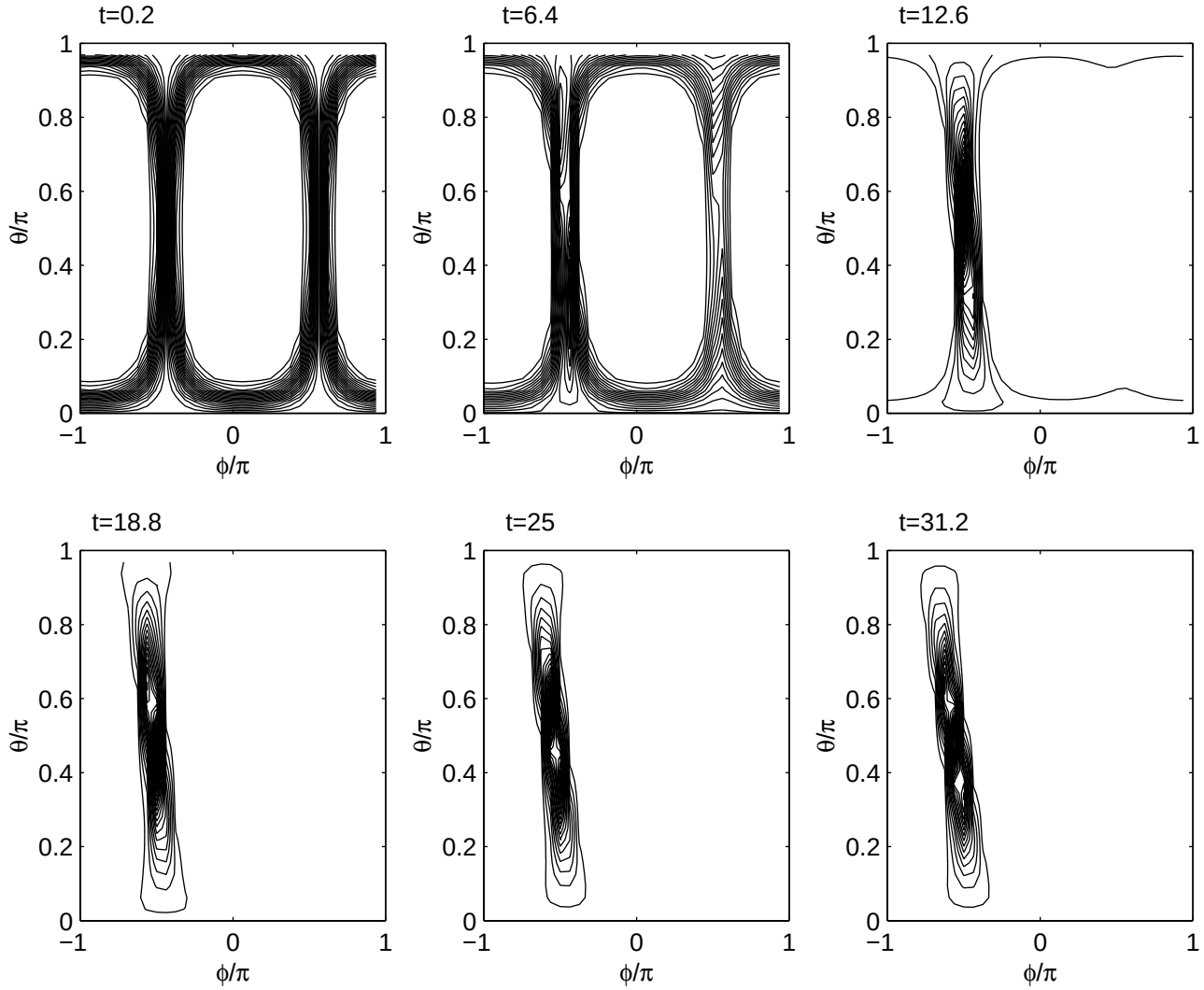

Figure 4.4: *Contour plots of the atomic Q function in polar coordinates, with the initial state* $|j,0\rangle_x$*, for a weak measurement* ($\overline{\Gamma} = 0.16$) *and strong interatomic interactions* ($\Theta = 0.50$). *The times of successive plots are separated approximately by the tunnelling period:* $t_n \simeq 2\pi n/\Omega$, *and are printed in units of* $t_0 = 1/\Omega$.

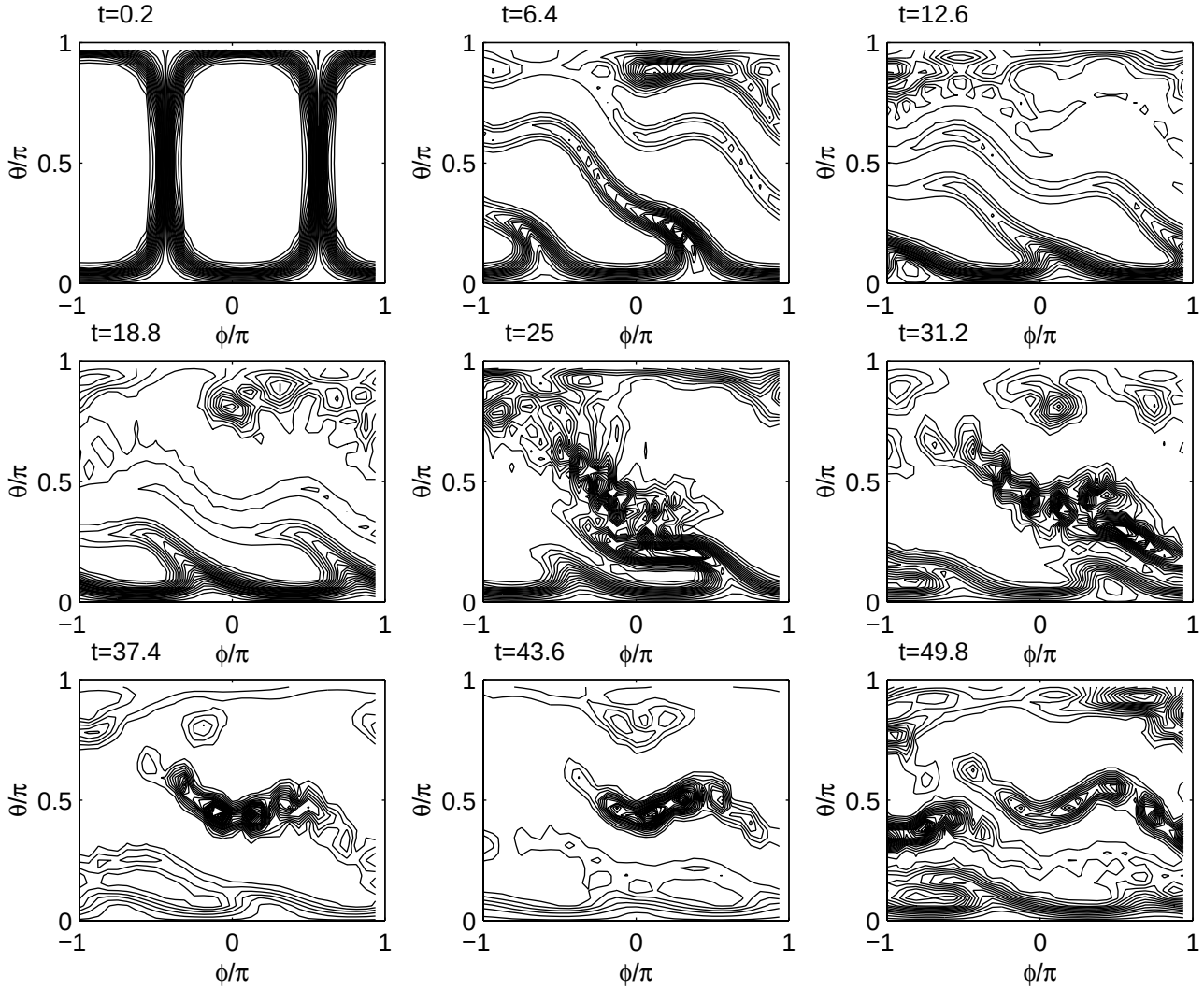

Figure 4.5: *Contour plots of the atomic Q function in polar coordinates, with the initial state* $|j,0\rangle_x$*, for a weak measurement* ($\overline{\Gamma} = 0.16$) *and very strong interatomic interactions* ($\Theta = 2.00$). *The times of successive plots are separated approximately by the tunnelling period:* $t_n \simeq 2\pi n/\Omega$, *and are printed in units of* $t_0 = 1/\Omega$.

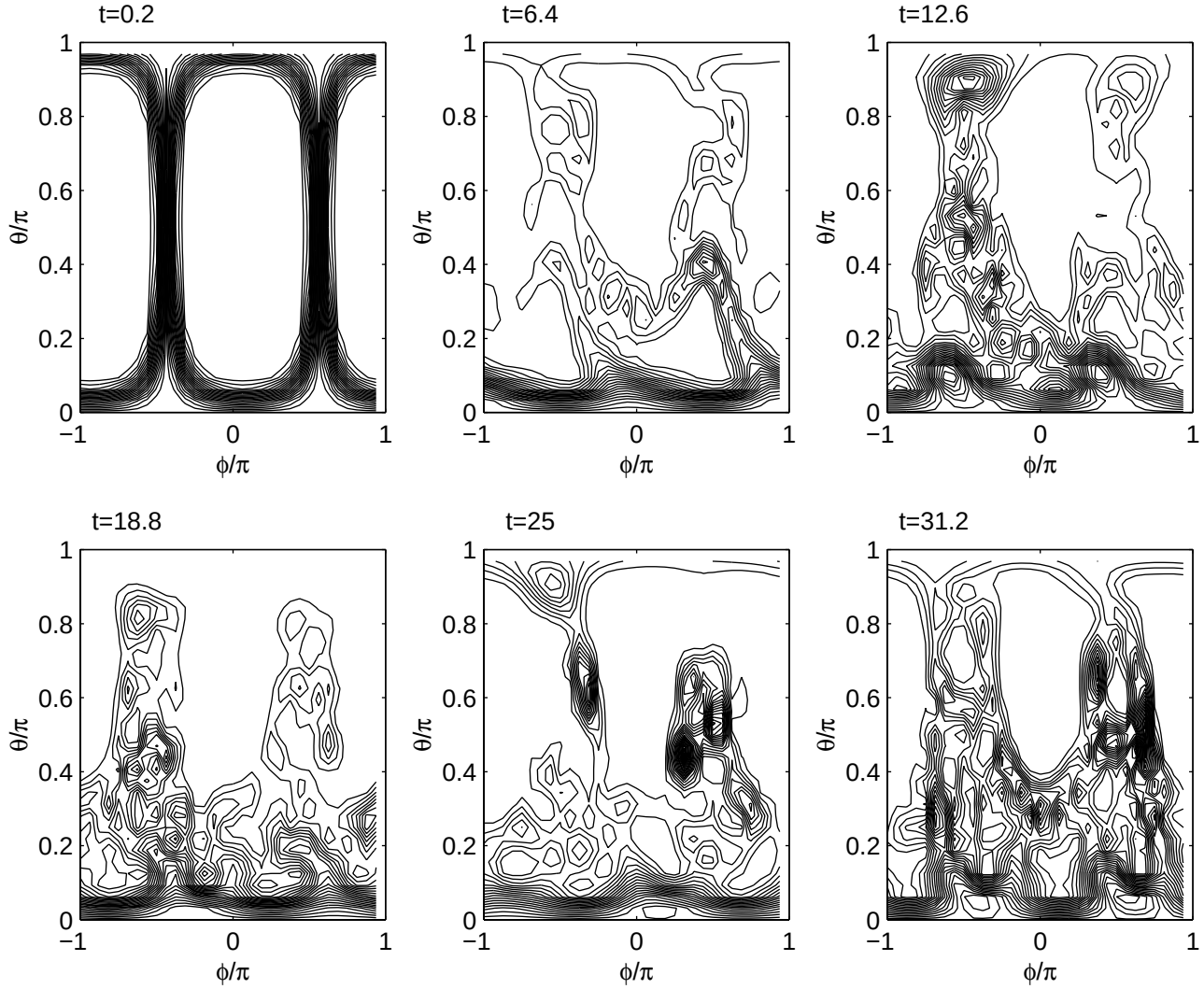

Figure 4.6: *Contour plots of the atomic Q function in polar coordinates, with the initial state* $|j,0\rangle_y$*, for various measurement strengths, and with no interatomic interactions (*$\Theta = 0.0$*) or tunnelling (*$\Omega = 0.0$*). The initial distribution is in (a), while (b), (c) and (d) are the contours at time* $t = 50s$ *for weak (*$\Gamma N^2 = .16s^{-1}$*), medium (*$\Gamma N^2 = 16s^{-1}$*) and strong (*$\Gamma N^2 = 1600s^{-1}$*) measurement strengths respectively.*

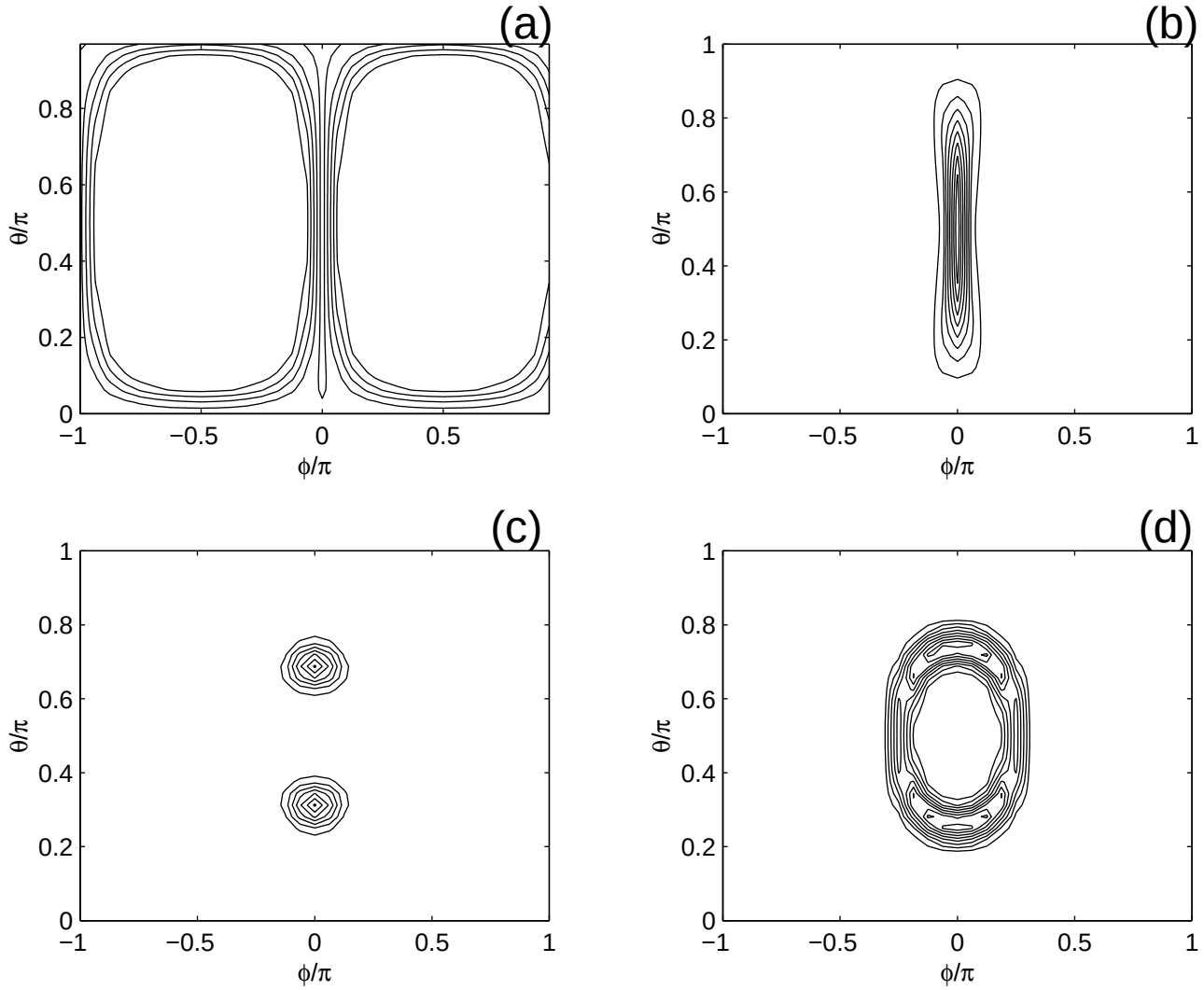

Figure 4.7: *Conditional dynamics of* $\langle \hat{J}_x \rangle_c$ *(continuous line) and* $\langle \hat{J}_z \rangle_c$ *(dashed line) when* $\Theta = 0$ *for different measurement strengths. In (a),* $\overline{\Gamma} = 16$ *and in (b),* $\overline{\Gamma} = 1600$*. The time axis is scaled by* $t_0 = 1/\Omega$*.*

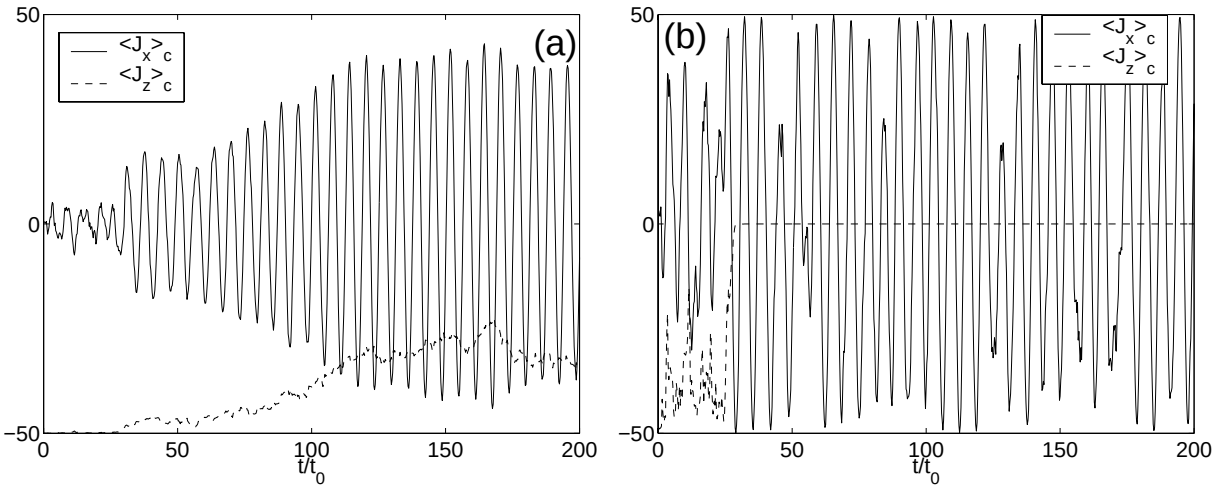

An alternative initial state

Thus far, in dealing with the monitored Bose condensate, we have been starting with the equal-weight number state $\left|j,0\right\rangle_x$, or its rotated cousin $\left|j,0\right\rangle_y$. But there are other initial states which generate the required symmetric spatial distribution of atoms. Starting with the system in the atomic coherent state $\left|j,-j\right\rangle_z$ gives the conditional dynamics shown in Figs. 4.7 and 4.8. This state is the ground state of the Hamiltonian $\hat{H}_2$ when the atomic collisions are very weak ($\Theta \ll 1$). Not only is it symmetric between the two wells, but it also contains no tunnelling-phase information, unlike the hidden phase in the number state $\left|j,0\right\rangle_x$. The tunnelling oscillations take longer to develop with the Bloch state, as the phase must first be established. For a medium interaction strength (Fig. 4.7(a)), oscillations of a definite phase are established by $t = 40t_0$ and these grow to be of a large amplitude by $t = 120t_0$. In a strong measurement (Fig. 4.7(b)), full oscillations appear at $t = 35t_0$ which persist, interrupted occasionally by jumps in the phase.

Figure 4.8 shows the effects of the atomic collisions on the monitored system starting in this state. For weak collisions ($\Theta = 0.01$), the dynamics appear unchanged (Fig. 4.8(a)): once again the measurement suppresses the collapses and revivals seen in the closed system. If we increase the collision strength (Figs. 4.8(b&c)), the period and amplitude decrease, just as they did for the semiclassical trajectories that started at $(x, y, z) = (0, \frac{1}{2}, 0)$. The period in Fig. 4.8(c) for $\Theta = 2$ is almost half the collisionless value, as it is in the semi-

Figure 4.8: *Conditional dynamics of* $\langle \hat{J}_x \rangle_c$ *(continuous line) and* $\langle \hat{J}_z \rangle_c$ *(dashed line) when* $\overline{\Gamma} = 16$ *for different atom-atom interaction strengths. In (a),* $\Theta = 0.01$*, in (b),* $\Theta = 0.50$*, and in (c),* $\Theta = 2.00$*. The time axis is scaled by* $t_0 = 1/\Omega$*.*

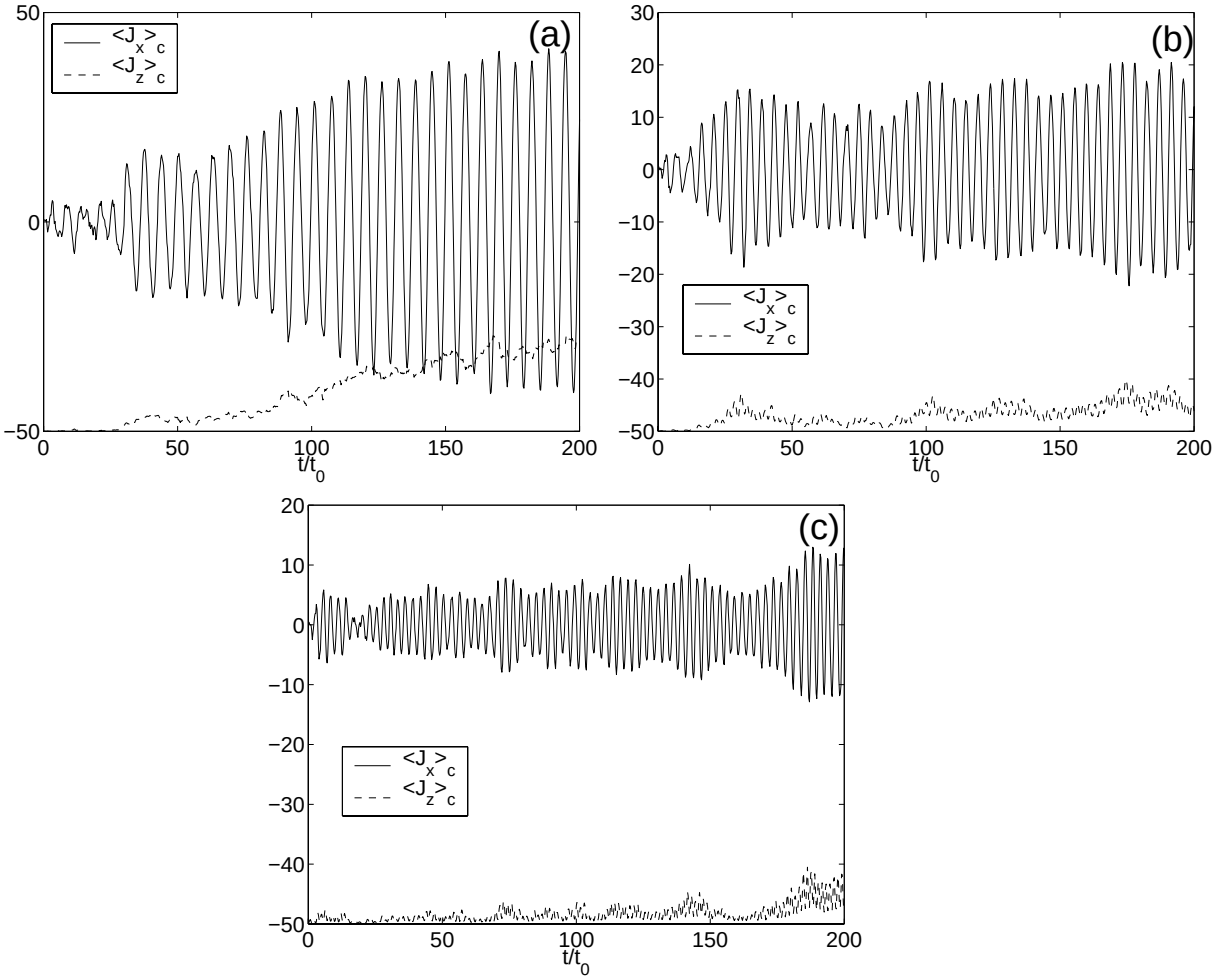

classical trajectory (Fig. 2.2(a)).

The atomic Q functions corresponding to these simulations appear in Figs. 4.9 to 4.11. In the collisionless case ($\Theta = 0$) for a measurement of strength of $\overline{\Gamma} = 16$ (Fig. 4.9), an asymmetric bulge in the distribution develops over time which precesses around the $\hat{J}_z$ axis. The distribution eventually moves away from the south pole of the sphere, while remaining compact, and this corresponds to the growth of tunnelling oscillations seen in Fig. 4.7(a). When the measurement strength is strong (Fig. 4.10), the distribution moves away from the south pole quickly, and then advances and retreats towards the equator, with frequent phase jumps. At about $t = 35t_0$, the Q function reaches the equator, at which point full tunnelling oscillations appear in Fig. 4.7(b). From this time on, the

distribution remains symmetric about the equator of the Bloch sphere, and its behaviour is similar to the previous strong measurement simulations with $\left|j,0\right\rangle_x$ as the initial state (Fig. 4.2): it periodically splits into two components which move apart, sometimes moving over the poles to come down along a different longitude, which corresponds to the phase jumps in the tunnelling oscillations.

When subcritical atom-atom interactions are included ($\Theta < 1$), the Q function evolution is very similar to the noninteracting case: the distribution gradually moves off the south pole of the Bloch sphere, remaining compact as it precesses around the $\hat{J}_z$ axis. For very strong self-interactions (as in Fig. 4.11, where $\Theta = 2.0$), the Q function develops the rotating asymmetries, but it never (up to time $t = 200t_0$) fully moves off the bottom of the sphere, leading only to oscillations of small amplitude.

4.4 Quasiprobability distributions using optical coherent states

The technique of mapping operator equations onto stochastic phase-space equations is common in quantum optics. Different phase-space representations are used to derive Fokker-Planck equations from the master equation. This technique is the basis of the second part of this thesis, in which quantum features are fully simulated by way of quasiprobability distributions. Here we apply the technique to the conditional master equation (Eq. (3.21)) to get a probabilistic semiclassical description.

Exactly what structure in Hilbert space is mapped onto the phase-space equations depends on what overcomplete set of states is used to represent $\hat{\rho}_c$. The most commonly used states are the coherent states $\left|\alpha\right\rangle$ of the boson field. They have the advantage of producing correspondences between the annihilation (and creation) operators and the phase-space variables that are simple in form[1]. The (conditional) Glauber-Sudarshan P function is defined by

$$\hat{\rho}_c = \int P(\alpha)\left|\alpha\right\rangle\left\langle\alpha\right| d^2\alpha, \tag{4.18}$$

[1]For an overview of the properties of coherent states and the phase-space representations constructed from them, see the fourth chapter of [62]

Figure 4.9: *Contour plots of the atomic Q function in polar coordinates, with the initial state* $|j,-j\rangle_z$*, for a medium strength measurement* ($\overline{\Gamma} = 16$) *and no atom collisions* ($\Theta = 0.00$). *The times of successive plots are separated approximately by the tunnelling period:* $t_n \simeq 2\pi n/\Omega$, *and are printed in units of* $t_0 = 1/\Omega$.

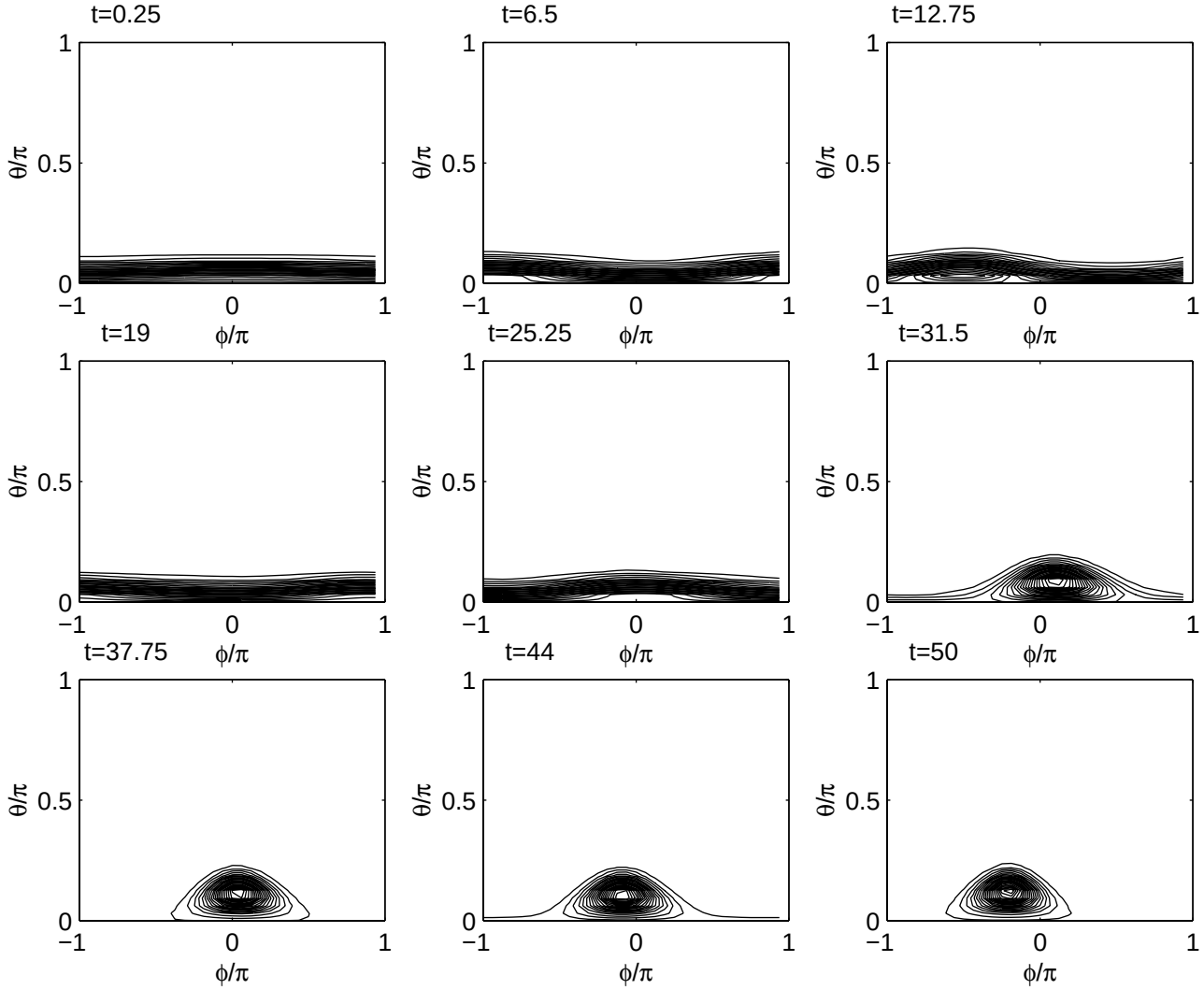

Figure 4.10: *Contour plots of the atomic Q function in polar coordinates, with the initial state* $\left|j,-j\right\rangle_z$*, for a strong measurement (*$\overline{\Gamma}=1600$*) and no atom collisions (*$\Theta=0.00$*). The times of successive plots are separated approximately by the tunnelling period:* $t_n \simeq 2\pi n/\Omega$*, and are printed in units of* $t_0 = 1/\Omega$*.*

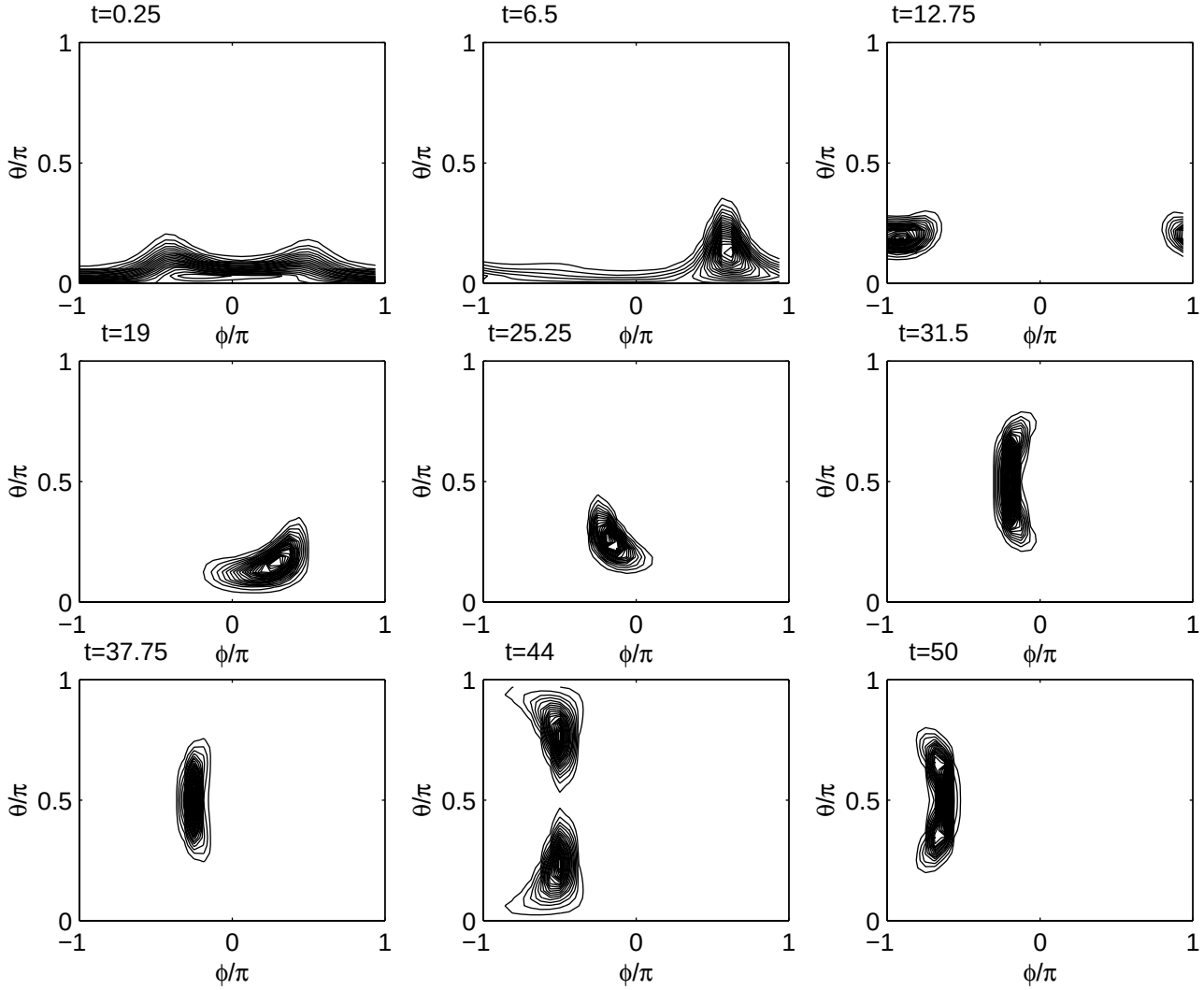

Figure 4.11: *Contour plots of the atomic Q function in polar coordinates, with the initial state* $|j,-j\rangle_z$*, for a medium strength measurement* ($\overline{\Gamma} = 0.16$) *and very strong interatomic interactions* ($\Theta = 2.0$). *The times of successive plots are separated approximately by half the tunnelling period:* $t_n \simeq \pi n/\Omega$, *and are printed in units of* $t_0 = 1/\Omega$.

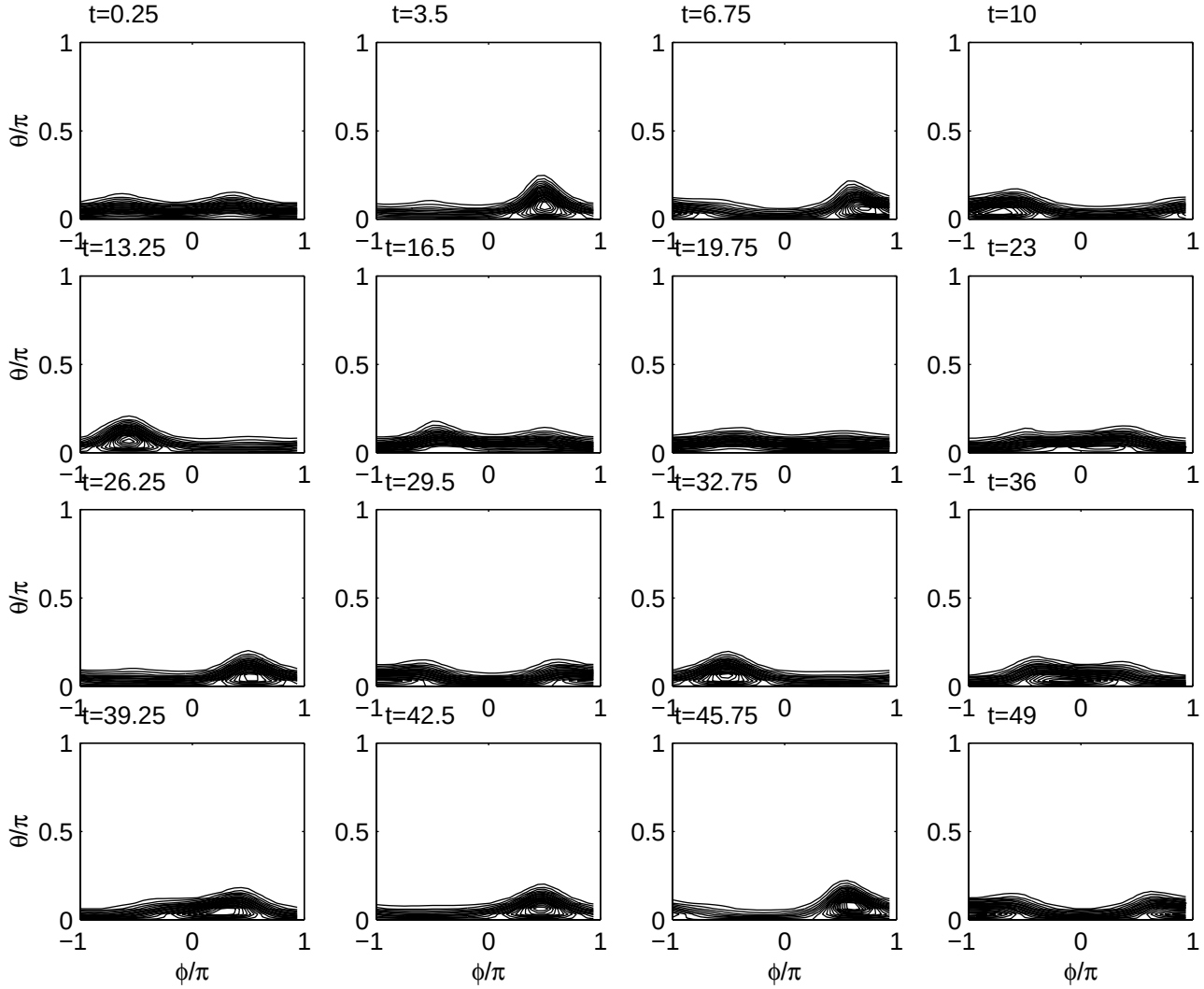

and leads to the operator correspondences[174]

$$\hat{c}\hat{\rho} \iff \alpha P(\alpha), \tag{4.19a}$$

$$\hat{c}^\dagger\hat{\rho} \iff \left(\alpha^* - \frac{\partial}{\partial\alpha}\right) P(\alpha), \tag{4.19b}$$

$$\hat{\rho}\hat{c} \iff \left(\alpha - \frac{\partial}{\partial\alpha^*}\right) P(\alpha), \tag{4.19c}$$

$$\hat{\rho}\hat{c}^\dagger \iff \alpha^* P(\alpha). \tag{4.19d}$$

Applying these operator correspondences to Eq. (3.21) results in

$$dP(t,\alpha,\alpha^*) = \Bigg[\sqrt{\Gamma}\left(|\alpha_2|^2 - |\alpha_1|^2 - \left\langle|\alpha_2|^2 - |\alpha_1|^2\right\rangle - \frac{1}{2}\left(\frac{\partial}{\partial\alpha_2}\alpha_2 - \frac{\partial}{\partial\alpha_1}\alpha_1 + \frac{\partial}{\partial\alpha_2^*}\alpha_2^* - \frac{\partial}{\partial\alpha_1^*}\alpha_1^*\right)\right) dW + dt\mathcal{L}_P + dt\mathcal{D}_P\Bigg] P, \tag{4.20a}$$

where the differential operators are

$$\mathcal{L}_P = \sum_{j=1,2}\frac{\partial}{\partial\alpha_j}\left(\frac{i\Omega}{2}\alpha_{3-j} + i\kappa\left(|\alpha_j|^2 - |\alpha_{3-j}|^2 + \frac{1}{2}\right)\alpha_j + \frac{\Gamma}{8}\alpha_j\right) + c.c. \tag{4.20b}$$

$$\mathcal{D}_P = \sum_{\mu,\nu=1}^{4}\frac{\partial^2}{\partial\alpha_\mu\partial\alpha_\nu}\left(\frac{-\Gamma D^\Gamma_{\mu\nu}}{8} - \frac{i\kappa D^\kappa_{\mu\nu}}{2}\right)\alpha_\mu\alpha_\nu, \tag{4.20c}$$

and where $\alpha_3 = \alpha_1^*$ and $\alpha_4 = \alpha_2^*$. The diffusion matrices are

$$\overline{D^\Gamma} = \begin{bmatrix} 1 & -1 & -1 & 1 \\ -1 & 1 & 1 & -1 \\ -1 & 1 & 1 & -1 \\ 1 & -1 & -1 & 1 \end{bmatrix}, \qquad \overline{D^\kappa} = \begin{bmatrix} 1 & 0 & -1 & 0 \\ 0 & -1 & 0 & 1 \\ -1 & 0 & 1 & 0 \\ 0 & 1 & 0 & -1 \end{bmatrix}. \tag{4.20d}$$

The first-derivative terms in Eq. (4.20a) govern the deterministic behaviour of the phase-space variables, causing a drift in the P distribution. The diffusive behaviour, due to the second-derivative terms $\mathcal{D}_P$, consists of a collisional contribution $\overline{D^\kappa}$ and a decoherence contribution $\overline{D^\Gamma}$.

One disadvantage of the P function is that it does not always exist for a given $\hat{\rho}_c$. An alternative representation uses the Wigner function, which does not have this limitation. The Wigner function is a Gaussian convolution over the P function:

$$G(\alpha) = \frac{2}{\pi}\int P(\beta)e^{-2|\beta-\alpha|^2}d^2\beta \tag{4.21}$$

and as such is better behaved and less singular than the P function. The Wigner operator correspondences are

$$\hat{c}\hat{\rho} \iff \left(\alpha + \frac{1}{2}\frac{\partial}{\partial\alpha^*}\right) G(\alpha), \tag{4.22a}$$

$$\hat{c}^\dagger\hat{\rho} \iff \left(\alpha^* - \frac{1}{2}\frac{\partial}{\partial\alpha}\right) G(\alpha), \tag{4.22b}$$

$$\hat{\rho}\hat{c} \iff \left(\alpha - \frac{1}{2}\frac{\partial}{\partial\alpha^*}\right) G(\alpha), \tag{4.22c}$$

$$\hat{\rho}\hat{c}^\dagger \iff \left(\alpha^* + \frac{1}{2}\frac{\partial}{\partial\alpha}\right) G(\alpha). \tag{4.22d}$$

The evolution equation for the Wigner distribution looks similar to that of the P distribution:

$$dG(t,\alpha,\alpha^*) = \left[\sqrt{\Gamma}\left(|\alpha_2|^2 - |\alpha_1|^2 - \left\langle|\alpha_2|^2 - |\alpha_1|^2\right\rangle - \frac{\partial^2}{\partial\alpha_2\partial\alpha_2^*} + \frac{\partial^2}{\partial\alpha_1\partial\alpha_1^*}\right) dW + dt\mathcal{L}_G + dt\mathcal{D}_G\right] G, \tag{4.23a}$$

where the differential operators are

$$\mathcal{L}_G = \sum_{j=1,2}\frac{\partial}{\partial\alpha_j}\left(\frac{i\Omega}{2}\alpha_{3-j} + i\kappa\left(|\alpha_j|^2 - |\alpha_{3-j}|^2\right)\alpha_j + \frac{\Gamma}{8}\alpha_j\right) + c.c. \tag{4.23b}$$

$$\mathcal{D}_G = \sum_{\mu,\nu=1}^{4}\frac{\partial^2}{\partial\alpha_\mu\partial\alpha_\nu}\frac{-\Gamma\alpha_\mu\alpha_\nu D^\Gamma_{\mu\nu}}{8}, \tag{4.23c}$$

except that there are higher-order derivative terms, which we have ignored. There is no diffusion due to atom collisions, but now the conditional part of the master equation (containing dW) contributes to the diffusion. There are other small differences in the drift terms as well.

The common disadvantage of the P and Wigner distributions is that both may go negative. This can occur when the diffusion matrix is not positive semidefinite; P and G cannot be regarded as true probability distributions. The Q function does not have this problem, since it is by definition positive:

$$Q(\alpha) = \frac{\left\langle\alpha\middle|\hat{\rho}_c\middle|\alpha\right\rangle}{\pi} \geq 0, \tag{4.24}$$

and it also exists for all $\hat{\rho}_c$. Using the operator correspondences

$$\hat{c}\hat{\rho} \iff \left(\alpha + \frac{\partial}{\partial \alpha^*}\right) Q(\alpha), \tag{4.25a}$$

$$\hat{c^\dagger}\hat{\rho} \iff \alpha^* Q(\alpha), \tag{4.25b}$$

$$\hat{\rho}\hat{c} \iff \alpha Q(\alpha), \tag{4.25c}$$

$$\hat{\rho}\hat{c}^\dagger \iff \left(\alpha^* + \frac{\partial}{\partial \alpha}\right) Q(\alpha), \tag{4.25d}$$

gives the Fokker-Planck equation:

$$dQ(t,\alpha,\alpha^*) = \Bigg[\sqrt{\Gamma}\left(|\alpha_2|^2 - |\alpha_1|^2 - \left\langle |\alpha_2|^2 - |\alpha_1|^2 \right\rangle + \frac{1}{2}\left(\frac{\partial}{\partial \alpha_2}\alpha_2 - \frac{\partial}{\partial \alpha_1}\alpha_1 + \frac{\partial}{\partial \alpha_2^*}\alpha_2^* - \frac{\partial}{\partial \alpha_1^*}\alpha_1^*\right)\right) dW + dt\mathcal{L}_Q + dt\mathcal{D}_Q\Bigg] Q, \tag{4.26a}$$

where differential operators for the Q function are

$$\mathcal{L}_Q = \sum_{j=1,2} \frac{\partial}{\partial \alpha_j}\left(\frac{i\Omega}{2}\alpha_{3-j} + i\kappa\left(|\alpha_j|^2 - |\alpha_{3-j}|^2 - \frac{1}{2}\right)\alpha_j + \frac{\Gamma}{8}\alpha_j\right) + c.c. \tag{4.26b}$$

$$\mathcal{D}_Q = \sum_{\mu,\nu=1}^{4} \frac{\partial^2}{\partial \alpha_\mu \partial \alpha_\nu}\left(\frac{-\Gamma D^\Gamma_{\mu\nu}}{8} + \frac{i\kappa D^\kappa_{\mu\nu}}{2}\right)\alpha_\mu \alpha_\nu. \tag{4.26c}$$

4.5 A semiclassical probability distribution

A comparison of the different Fokker-Planck equations for each of the three phase-space representations (Eqs. (4.20, 4.23 and 4.26) reveals certain differences. For example, the collisional diffusion matrix $\overline{D^\kappa}$ occurs with opposite sign in the P and Q equations and is absent in the Wigner equations. Likewise for the extra collision drift term $\frac{i}{2}\kappa\alpha_\mu$ and the conditional drift terms. This is because the moments derived from the three distributions (P, Q and Wigner) correspond to different orderings of operator products (normal, antinormal and symmetric ordering respectively), which is of course a characteristic of the quantum nature of the system. In the semiclassical limit, the ordering of terms should no longer matter, and so the differences between the three distributions should disappear in this limit.

Also, if the resultant distribution is to be a true classical probability distribution, then the diffusion matrix should be positive semidefinite - ensuring that the probability never goes negative. The conditional diffusion matrix in the Wigner equation is not positive semidefinite, and the collisional diffusion matrix in the P equation is negative semidefinite (since it is of opposite sign to that in the Q equation).

Fortunately, these two requirements for a semiclassical description are precisely satisfied in the limit of large atom number ($j \gg 1$), since in this limit all ordering-dependent terms, including the nonclassical diffusion terms, disappear. The result is a conditional probability distribution. It is conditioned upon the continuous, but imperfect, monitoring of the moment $\langle x \rangle = \langle |\alpha_2|^2 - |\alpha_1|^2 \rangle / 2$:

$$dF(t,\alpha,\alpha^*) = \left[\sqrt{\Gamma} \left(|\alpha_2|^2 - |\alpha_1|^2 - \langle |\alpha_2|^2 - |\alpha_1|^2 \rangle \right) dW + dt\mathcal{L} + dt\mathcal{D} \right] F, \tag{4.27a}$$

where the differential operators are

$$\begin{aligned} \mathcal{L}F &= \nabla_\alpha \cdot \mathbf{F_L} \\ &= \sum_{j=1,2} \frac{\partial}{\partial \alpha_j} \left(\frac{i\Omega}{2} \alpha_{3-j} + i\kappa \left(|\alpha_j|^2 - |\alpha_{3-j}|^2 \right) \alpha_j + \frac{\Gamma}{8} \alpha_j \right) F + c.c. \qquad (4.27b) \\ \mathcal{D} &= \sum_{\mu,\nu=1}^{4} \frac{\partial^2}{\partial \alpha_\mu \partial \alpha_\nu} \frac{-\Gamma \alpha_\mu \alpha_\nu D^\Gamma_{\mu\nu}}{8} \qquad (4.27c) \end{aligned}$$

and where, as before, the diffusion matrix is

$$\overline{D^\Gamma} = \begin{bmatrix} 1 & -1 & -1 & 1 \\ -1 & 1 & 1 & -1 \\ -1 & 1 & 1 & -1 \\ 1 & -1 & -1 & 1 \end{bmatrix}. \tag{4.27d}$$

That the diffusion matrix in $\mathcal{D}$ is positive semidefinite can be checked by rewriting it in terms of the real variables $x_i = \Re(\alpha_i)$, $y_i = \Im(\alpha_i)$. The result is

$$\sum_{\mu,\nu=1}^{4} \frac{\partial^2}{\partial \alpha_\mu \partial \alpha_\nu} \frac{-\Gamma \alpha_\mu \alpha_\nu D^\Gamma_{\mu\nu}}{8} = \sum_{\mu,\nu=1}^{4} \frac{\Gamma}{8} \frac{\partial^2}{\partial x_\mu \partial x_\nu} \begin{bmatrix} y_1^2 & -x_1 y_1 & -y_1 y_2 & x_2 y_1 \\ -x_1 y_1 & x_1^2 & x_1 y_2 & -x_1 x_2 \\ -y_1 y_2 & x_1 y_2 & y_2^2 & -x_2 y_2 \\ x_2 y_1 & -x_1 x_2 & -x_2 y_2 & x_2^2 \end{bmatrix}, \tag{4.28}$$

where $x_\mu = (x_1, y_1, x_2, y_2)_\mu$. For an arbitrary vector $\mathbf{h} = (h_1, h_2, h_3, h_4)'$,

$$\begin{aligned} \mathbf{h}' \begin{bmatrix} y_1^2 & -x_1 y_1 & -y_1 y_2 & x_2 y_1 \\ -x_1 y_1 & x_1^2 & x_1 y_2 & -x_1 x_2 \\ -y_1 y_2 & x_1 y_2 & y_2^2 & -x_2 y_2 \\ x_2 y_1 & -x_1 x_2 & -x_2 y_2 & x_2^2 \end{bmatrix} \mathbf{h} &= \mathbf{g}' \begin{bmatrix} 1 & -1 & -1 & 1 \\ -1 & 1 & 1 & -1 \\ -1 & 1 & 1 & -1 \\ 1 & -1 & -1 & 1 \end{bmatrix} \mathbf{g} \\ &= \frac{1}{2} \left((g_1 - g_2)^2 + (g_4 - g_3)^2 + (g_1 - g_2 + g_4 - g_3)^2 \right) \\ &\geq 0 \quad \forall \mathbf{g}, \end{aligned} \tag{4.29}$$

where $\mathbf{g} = (g1, g2, g3, g4)' = (y_1 h_1, x_1 h_2, y_2 h_3, x_2 h_4)'$. Thus the diffusion matrix is positive semidefinite.

Having generated a Fokker-Planck equation, we would then normally write down stochastic Langevin equations for the phase-space variables, so that numerical simulations can be performed. However the presence of the nonderivative term complicates matters, so instead we derive equations of motion for the conditional averages, which will be sufficient for our present purposes.

In the calculations of the evolution of the moment $\langle g(\alpha)\rangle$, the first-derivative terms in Eq. (4.27) become

$$\int d\alpha^4 g(\alpha) dt \mathcal{L} F = \int d\alpha^4 \mathbf{F_L} \cdot \nabla_\alpha g(\alpha), \tag{4.30}$$

and the contribution from the second-derivative terms is

$$\int d\alpha^4 g(\alpha) dt \mathcal{D} F = \sum_{\mu,\nu=1}^{4} \int d\alpha^4 \frac{-\Gamma \alpha_\mu \alpha_\nu D^{\Gamma}_{\mu\nu} dt}{8} \frac{\partial^2 g(\alpha)}{\partial \alpha_\mu \partial \alpha_\nu}, \tag{4.31}$$

where we have integrated by parts and ignored any surface terms. The resultant equations of motion for the conditional moments, up to second order, are

$$d\langle x\rangle = -\Omega\langle y\rangle dt + 2\sqrt{\Gamma}\left(\langle x^2\rangle - \langle x\rangle^2\right) dW \tag{4.32a}$$

$$d\langle y\rangle = \left(\Omega\langle x\rangle + 4\kappa\langle xz\rangle - \frac{\Gamma}{2}\langle y\rangle\right) dt + 2\sqrt{\Gamma}\left(\langle xy\rangle - \langle x\rangle\langle y\rangle\right) dW \tag{4.32b}$$

$$d\langle z\rangle = 4\left(\kappa\langle xy\rangle - \frac{\Gamma}{2}\langle z\rangle\right) dt + 2\sqrt{\Gamma}\left(\langle xz\rangle - \langle x\rangle\langle z\rangle\right) dW \tag{4.32c}$$

$$d\langle x^2\rangle = -2\Omega\langle xy\rangle dt + 2\sqrt{\Gamma}\left(\langle x^3\rangle - \langle x\rangle\langle x\rangle^2\right) dW \tag{4.32d}$$

$$d\langle y^2\rangle = \left(2\Omega\langle xy\rangle - 8\kappa\langle xyz\rangle - \Gamma\left(\langle y^2\rangle - \langle z^2\rangle\right)\right) dt + 2\sqrt{\Gamma}\left(\langle xy^2\rangle - \langle x\rangle\langle y\rangle^2\right) dW \tag{4.32e}$$

$$d\langle z^2\rangle = \left(8\kappa\langle xyz\rangle - \Gamma\left(\langle z^2\rangle - \langle y^2\rangle\right)\right) dt + 2\sqrt{\Gamma}\left(\langle xz^2\rangle - \langle x\rangle\langle z\rangle^2\right) dW \tag{4.32f}$$

$$d\langle xy\rangle = \left(\Omega(\langle x^2\rangle - \langle y^2\rangle) + 4\kappa\langle y^2 z\rangle - \frac{\Gamma}{2}\langle xy\rangle\right) dt + 2\sqrt{\Gamma}\left(\langle x^2 y\rangle - \langle x\rangle\langle xy\rangle\right) dW \tag{4.32g}$$

$$d\langle xz\rangle = \left(-\Omega\langle yz\rangle + 4\kappa\langle x^2 y\rangle - \frac{\Gamma}{2}\langle xz\rangle\right) dt + 2\sqrt{\Gamma}\left(\langle x^2 z\rangle - \langle x\rangle\langle xz\rangle\right) dW \tag{4.32h}$$

$$d\langle yz\rangle = \left(\Omega\langle xz\rangle + 4\kappa\left(\langle xy^2\rangle - \langle xz^2\rangle\right) - 2\Gamma\langle xz\rangle\right) dt + 2\sqrt{\Gamma}\left(\langle xyz\rangle - \langle x\rangle\langle yz\rangle\right) dW, \tag{4.32i}$$

where the variables x, y and z are as defined in Eq. (2.31). If the expectation of these equations is calculated, to get the unconditional equations, then they reduce to the equations

given in Ch. 3 that are derived from the unconditional master equation, except that now the objects within the averages $\langle ... \rangle$ commute. This is consistent with the idea that Eq. (4.27) provides a probabilistic semiclassical description, in which the nonclassical features of the distribution have been neglected, but which is not necessarily fully coherent.

As before, the equations couple to higher-order moments, through both the collision terms (containing κ) and the conditional terms (containing dW). If we factorise all the moments, then the stochastic terms disappear, and the moment equations reduce to the unconditional behaviour. Thus we cannot get a semiclassical description of the unconditional dynamics for the two mode system in this way. If we keep the second-order moments and factor third-order moments of the form $\langle \hat{J}_x \hat{A} \rangle \longrightarrow \langle \hat{J}_x \rangle \langle \hat{A} \rangle$ by choosing an appropriate initial state, then for $\kappa = 0$, we obtain a closed set of equations for the unconditional dynamics. If the initial distribution is Gaussian, the higher-order moments will initially factorise into first- and second-order moments, but they do not uncouple. Thus the subsequent evolution of the higher-order moments does not guarantee that the system will remain in a Gaussian distribution.

Although not a closed set, the unfactorised equations do provide some insight into how the back-action noise from the measurement induces a phase. If the system is started in a number state, then initially the only nonzero first- and second-order moments are

$$\langle \hat{J}_x \rangle = \frac{1}{2}(n_2 - n_1) \tag{4.33a}$$

$$\langle \hat{J}_y^2 \rangle = \langle \hat{J}_z^2 \rangle = \frac{1}{2} n_2 n_1. \tag{4.33b}$$

If at first there is an equal number of atoms in each well, then initially the only nonzero derivative is $d\langle \hat{J}_x \hat{J}_y \rangle = -N^2 \Omega dt/8$, which immediately induces fluctuations in $\langle \hat{J}_y \rangle$. This is consistent with the idea that it is the fluctuations in $\langle \hat{J}_y \rangle$ which drive the tunnelling oscillations. In other words, the measurement of position introduces an uncertainty into momentum, which then causes the oscillations.

4.6 Quasiprobability distributions using atomic coherent states

The system described by Eq. (3.21) cannot exist in a pure coherent state $|\alpha\rangle$, because these coherent states are not constrained to the Bloch sphere. In representing distributions constrained to lie on a sphere, the expansions derived in terms of these states will

be rather broad, leading to large sampling errors in any numerical simulation of the corresponding phase-space equations. A more natural set of states to work with is that of the atomic coherent states $|\mu\rangle$, defined in Sec. 4.3.1. Distribution functions defined in terms of these states are constrained to remain on the Bloch sphere. The disadvantage in using a quasiprobability distribution that better reflects the structure of the master equation, is that the governing equations are more complicated and not so amenable to simple analysis.

In order to obtain an equation for the atomic Q function, the following matrix elements are needed[148]:

$$\langle\mu|\rho\hat{J}_+|\mu\rangle = \frac{1}{(1+|\mu|^2)^{2j}}\frac{\partial}{\partial\mu}\mathcal{Q}(\mu) \tag{4.34a}$$

$$\langle\mu|\rho\hat{J}_-|\mu\rangle = \frac{1}{(1+|\mu|^2)^{2j}}\left(2j\mu-\mu^2\frac{\partial}{\partial\mu}\right)\mathcal{Q}(\mu), \tag{4.34b}$$

where

$$\mathcal{Q}(\mu) = \left(1+|\mu|^2\right)^{2j}\langle\mu|\rho|\mu\rangle. \tag{4.35}$$

We can transform the conditional master equation (Eq. (3.21)) into a differential equation for $\mathcal{Q}(\mu)$ using the correspondences:

$$\hat{\rho}_c\hat{J}_+ \iff \frac{\partial}{\partial\mu}\mathcal{Q}, \tag{4.36a}$$

$$\hat{\rho}_c\hat{J}_- \iff \left(2(j+1)\mu-\frac{\partial}{\partial\mu}\mu^2\right)\mathcal{Q}, \tag{4.36b}$$

$$\hat{\rho}_c\hat{J}_z \iff \left(\frac{\partial}{\partial\mu}\mu-(j+1)\right)\mathcal{Q}, \tag{4.36c}$$

as well as the conjugates of these.

The resultant equation is

$$d\mathcal{Q}(t,\mu,\mu^*) = \Bigg[\sqrt{\Gamma}dW\left((j+1)(\mu+\mu^*)+\frac{1}{2}\frac{\partial}{\partial\mu}\left(1-\mu^2\right)\right.$$
$$\left.+\frac{1}{2}\frac{\partial}{\partial\mu^*}\left(1-\mu^{*2}\right)-2\langle\hat{J}_x\rangle\right)+dt\left(\mathcal{S}+\mathcal{L}_\mathcal{Q}+\mathcal{D}_\mathcal{Q}\right)\Bigg]\mathcal{Q}, \tag{4.37a}$$

where the differential operators are

$$\mathcal{S} = \frac{1}{2}\Gamma\left((j+1)(2|\mu|^2-1)-(j+\frac{3}{2})(j+1)(\mu^2+\mu^{*2})\right) \tag{4.37b}$$

$$\mathcal{L}_{\mathcal{Q}} = \frac{\partial}{\partial\mu}\left(i\Omega\mu+2i\kappa(j+\frac{3}{2})\mu(1-\mu^2)+\frac{\Gamma}{2}(\mu^*(j+1)-\mu(j+\frac{3}{2}))(1-\mu^2)\right)+c.c. \tag{4.37c}$$

$$\mathcal{D}_{\mathcal{Q}} = \sum_{j,k=1,2}(1+\mu_j^2)(1+\mu_k^2)\left(\frac{i\kappa}{2}D^{\kappa}_{jk}-\frac{\Gamma}{8}D^{\Gamma}_{jk}\right), \tag{4.37d}$$

and where $\mu_1=\mu$ and $\mu_2=\mu^*$. The diffusion matrices are

$$\overline{D^{\kappa}}=\begin{bmatrix}1 & 0\\ 0 & -1\end{bmatrix}, \qquad \overline{D^{\Gamma}}=\begin{bmatrix}1 & -1\\ -1 & 1\end{bmatrix}. \tag{4.37e}$$

In terms of Bloch states, the expectation value of an operator $\hat{\Lambda}$ is

$$\langle\hat{\Lambda}\rangle = Tr\left(\hat{\Lambda}\rho\right)=\frac{2j+1}{\pi}\int d^2\lambda\frac{\langle\lambda|\hat{\Lambda}\rho|\lambda\rangle}{(1+|\lambda|^2)^2}, \tag{4.38}$$

which for $\hat{J}_x$, we can write in terms of $\mathcal{Q}$ as

$$\begin{aligned}\langle\hat{J}_x\rangle &= \frac{(2j+1)(j+1)}{\pi}\int d^2\lambda\frac{(\lambda+\lambda^*)\,\mathcal{Q}(\lambda)}{(1+|\lambda|^2)^{3+2j}}\\ &= E\left[\frac{\lambda+\lambda^*}{(1+|\lambda|^2)}\right].\end{aligned} \tag{4.39}$$

The equation for $\mathcal{Q}$ bears some resemblance to that for the coherent-state Q function. For example, both the interatomic interactions and the atom-light coupling lead to diffusion terms. However, the atom-light coupling produces considerably more complex zeroth- and first-order terms. Nevertheless, this phase-space representation is much more compact than before since the dynamics are constrained to lie on a sphere, and phase-space dimensionality is reduced by half. Both of these factors would make numerical simulation with the atomic $\mathcal{Q}$ function simpler than with the ordinary Q function.

As for the coherent-state case, we may try to find the semiclassical limit of Eq. (4.37), in order to find a true probability distribution for which the calculated moments do not depend on operator ordering. One way is to take the limit $j \gg 1$, which simplifies some of the constants in front of zeroth- and first-order terms, but does not remove the $\overline{D^{\kappa}}$ diffusion term as it does in Eq. (4.27). This is because the size of μ is not constrained in such a limit.

Another way of generating a semiclassical distribution function would be to use an atomic P function[136], compare the result with Eq. (4.37) and remove discrepant terms.

This completes our exploration of alternative ways to analyse a condensate undergoing a homodyne measurement scheme. The numerical calculations of the Q functions in Sec. 4.3.2 complement the simulations of Ch. 3, while other sections have paved the way for a semiclassical analysis. These kinds of quasiprobability distributions will be used again in the second part of the thesis to map quantum equations of motion onto stochastic complex-number equations, for numerical simulations of multimode systems.

Chapter 5

Weak force detection using a double Bose-Einstein condensate

5.1 Introduction

We shall conclude this part of the thesis by studying a possible application of the Bose-Einstein condensate in precision measurement. Tentative steps have been taken in this direction already, with the realisation of a Bose-Einstein atomic clock in the laboratory, based on persistent tunnelling oscillations between two coupled condensates[3, 16, 35]. Although inspired by this attempt, this chapter, as the title suggests, deals not with precision clocks, but with precision force measurements. Although the scheme presented here uses tunnelling oscillations, the essence of the measurement lies in generating quantum entanglement in this mesoscopic system. The use of maximal quantum entanglement of a large number of particles has been suggested before[13, 86], in the context of making a frequency-standard measurement with an array of two-level or spin-half systems[178, 177], such as cold, trapped ions[13, 86]. Here we shall apply these ideas to the Bose condensate, and find an improvement in precision that is proportional to the number of atoms N in the condensate.

5.2 Two-mode system

We consider the case where a condensate has formed in a quartic double-well potential, and use the two-mode Hamiltonian introduced as Eq. (2.49):

$$\hat{H}_2 = \hbar\Omega\hat{J}_z + 2\hbar\kappa\hat{J}_x^2. \tag{5.1}$$

The commutation relations for these operators are

$$\left[\hat{J}_i, \hat{J}_j\right] = i\epsilon_{ijk}\hat{J}_k \tag{5.2}$$

where ϵ_{ijk} allows cyclic permutations of $i, j, k \in \{x, y, z\}$.

The operator $\hat{J}_x$ gives the condensate particle-number difference between the two wells, $\hat{J}_y$ corresponds to the momentum induced by tunnelling, and $\hat{J}_z$ is the difference in occupation between the upper and lower energy eigenstates of the potential. The splitting between these levels is given by Ω, which is the tunnelling frequency, and κ corresponds to the strength of the interparticle hard-sphere interactions.

As discussed in Ch. 2, the two-mode approximation is valid in the regime where the overlap between the single-particle ground-state modes of each well is small and where the many-body effects do not affect significantly the properties of these modes. These conditions lead to[33, 125]

$$\frac{\Omega}{\omega_0} \ll 1, \qquad N \ll \frac{r_0}{|a|}, \tag{5.3}$$

where a is the scattering length which determines the strength of the two-atom collisions and where $r_0 = \sqrt{\hbar/2m\omega_0}$ characterizes the size of the wells.

5.3 Measurement scheme

As Fig. 5.1 shows, the detection of the weak force proceeds in several stages. The first step is to prepare the initial state of the system in a quantum state which can optimise the precision of the measurement. With this in mind, we consider the weak tunnelling limit $\Omega \ll \kappa N$. In this case, the ground state of the Hamiltonian (Eq. (2.49)) for attractive interactions ($\kappa < 0$) is a superposition of the extremal eigenstates of the operator $\hat{J}_x$[31, 68, 77, 162]:

$$\left|E\right\rangle = \frac{1}{\sqrt{2}}\left(\left|j, -j\right\rangle_x + \left|j, j\right\rangle_x\right). \tag{5.4}$$

Figure 5.1: *Outline of the measurement scheme. The stages are: (a) preparation of the superposition state, (b) interaction with the weak force for time τ, (c) a $\frac{\pi}{2}$ rotation caused by tunnelling, and (d) a homodyne measurement of the number of atoms in one well.*

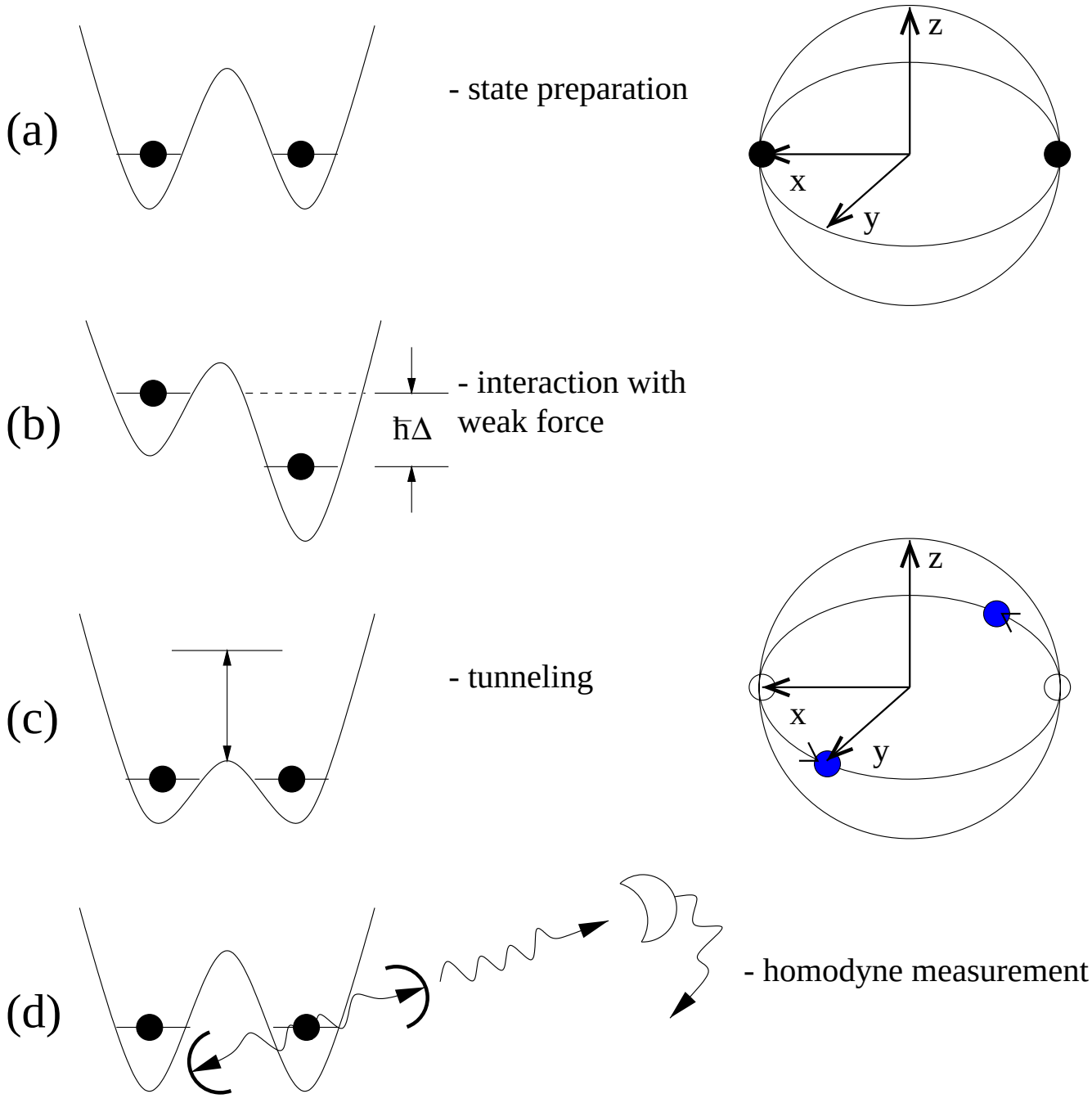

We will see that with such an initial state the precision of the measurement can be controlled by the total number of atoms in the condensate. This state is easily represented on the Bloch sphere (Fig. 5.1(a)) by two diametrically opposed points on the equator. A method for preparing such a state has been proposed in [31] for overlapping two-species condensates, through control of the analogous Josephson coupling term. In principle, the two species of this superposition state could be coherently transfered to spatially separated wells in order to produce the state we require here.

The second step in the measurement process, after having achieved the ground state described by Eq. (5.4), and before the tunnelling is turned on, is to allow the weak force to act for a certain time τ. This force may be due to a varying gravitational field, for example, and has the effect of adding a linear ramp to the potential:

$$\hat{H_F} = \hbar\Delta\hat{J}_x, \tag{5.5}$$

where Δ is the frequency shift induced by the weak force (see Fig. 5.1(b)) and $j = N/2$. The initial ground state (Eq. (5.4)) then evolves into the superposition:

$$\big|\Psi(\tau)\big\rangle = \frac{1}{\sqrt{2}}\left(e^{i\Delta j\tau}\big|j,-j\big\rangle_x + e^{-i\Delta j\tau}\big|j,j\big\rangle_x\right). \tag{5.6}$$

The state now contains the phase shift induced by the weak force. This phase shift is "amplified" $2j$ times the single-particle value due to the specially prepared initial state.

The next step involves a technique analogous to Ramsey interferometry. In order to detect the induced phase shift, we rotate the state (Eq. (5.6)) around the Bloch sphere by 90^0. Such a rotation can be achieved by turning on the tunnelling between the two wells of the trap for a time $t_{\frac{\pi}{2}} = \pi/(2\Omega)$. If the interatomic interaction is strong, the rotation operation will be affected by the nonlinear term in Eq. (2.49), which will distort the final state from the y-axis on the Bloch sphere and affect the precision of the measurement. To avoid this, we could use a Feshbach resonance[89, 164] to suppress the collisions. The state is then rotated to

$$\big|\Psi(\tau + t_{\pi/2})\big\rangle = \frac{1}{\sqrt{2}}\left(e^{i\Delta j\tau}\big|j,-j\big\rangle_y + e^{-i\Delta j\tau}\big|j,j\big\rangle_y\right). \tag{5.7}$$

Finally, a number measurement can be performed on one of the condensates. This corresponds to a projection onto the $\hat{J}_x$ eigenstates. The resultant probability distribution is

$$P_x(m) = \frac{1}{2}\left|e^{i\Delta\tau j}{}_x\!\big\langle j,m|j,-j\big\rangle_y + e^{-i\Delta\tau j}{}_x\!\big\langle j,m|j,j\big\rangle_y\right|^2. \tag{5.8}$$

Now the inner product of the J_x and J_y eigenstates will be a binomial function of m peaked around $m = 0$, with

$$ {}_x\langle j, m|j, -j\rangle_y = e^{-im\pi}\, {}_x\langle j, m|j, j\rangle_y. \tag{5.9} $$

This leads to

$$ \begin{aligned} P_x(m) &= 2\cos^2(\Delta j\tau + m\pi/2)\left|{}_x\langle j, m|j, j\rangle_y\right|^2 && (5.10)\\ &= \begin{cases} 2\cos^2\Delta j\tau\left|{}_x\langle j, m|j, j\rangle_y\right|^2 & m \text{ even} \\ 2\sin^2\Delta j\tau\left|{}_x\langle j, m|j, j\rangle_y\right|^2 & m \text{ odd} \end{cases}, && (5.11) \end{aligned} $$

which describes how the output fringes are shifted by the presence of the force Δ. In the absence of the force, all the odd fringes are absent, but for $\Delta \neq 0$, the probability that a particular measurement will fall on an odd fringe is

$$ Pr\{m \text{ odd}\} = \sin^2\Delta j\tau \simeq (\Delta j\tau)^2 \tag{5.12} $$

for small Δ.

Note that Eq. (5.11) is only correct when j is an integer (i.e. an even number of atoms). For half-integral values of j, Eq. (5.10) becomes

$$ P_x(m) = 2\left(1 + (-1)^n \sin(2\Delta j\tau)\right)\left|{}_x\langle j, m|j, j\rangle_y\right|^2, \tag{5.13} $$

where $n = m + \frac{1}{2}$, an integer. In the absence of the force, odd and even fringes are equally probable, but for $\Delta \neq 0$, the odd fringes reduce and the even fringes grow:

$$ Pr\{n \text{ odd}\} \simeq \frac{1}{2} - \Delta j\tau \tag{5.14} $$

for small Δ. This does not offer the same advantage as Eq. (5.12), because the probability does not grow from zero, and the change is only linear in the size of the force.

5.4 Measurement readout

The measurement of atom number is effected through the homodyne scheme[33] illustrated in Fig. 3.1. The condensate is placed in an optical cavity, which at the time of the readout stage of the measurement contains a light field which is highly driven and damped. The optical field is thus in a coherent state with amplitude α_0. It is also detuned from any atomic resonance so that the condensate merely imposes a phase shift on the light. This

can be detected by measuring the quadrature components of the field. For a dispersive interaction that acts on a timescale t_I over which the dynamics of the condensate itself is negligible,

$$\hat{H}_I = \hbar\chi \hat{J}_x a^\dagger a, \tag{5.15}$$

where χ is the measurement strength and $a^\dagger$, a are the light field creation and annihilation operators. The quadrature components $\hat{X} = a^\dagger + a$ and $\hat{Y} = i(a^\dagger - a)$ then execute simple harmonic motion:

$$\hat{X}(t_I) = \cos(\chi t_I \hat{J}_x)\hat{X}(0) + \sin(\chi t_I \hat{J}_x)\hat{Y}(0) \tag{5.16a}$$

$$\hat{Y}(t_I) = \cos(\chi t_I \hat{J}_x)\hat{Y}(0) - \sin(\chi t_I \hat{J}_x)\hat{X}(0). \tag{5.16b}$$

After t_I, the light field is rapidly damped out and the resulting photocurrent is integrated in order to measure $\hat{X}$. If all the light is emptied from the cavity, then the distribution of the integrated photocurrent for $\hat{X}$ is the true distribution of $\hat{X}$[180, 181]. In terms of the Wigner function G, this is given by the marginal distribution:

$$p(x) = \frac{1}{4}\int_{-\infty}^{\infty} dy G(x, y), \tag{5.17}$$

where $x = \alpha^* + \alpha$ and $y = i(\alpha^* - \alpha)$.

To calculate the Wigner function of the optical field, we must first find its reduced density operator. Assuming that field is initially in the coherent state α_0, then with the condensate state described by $\hat{\rho}_c$,

$$\begin{aligned}
\hat{\rho}_{\text{field}} &= \text{Tr}_{\text{cond}}\{\hat{\rho}\} = \text{Tr}_{\text{cond}}\left\{e^{-i\chi t_I \hat{J}_x \hat{a}\hat{a}^\dagger}\hat{\rho}_c|\alpha_0\rangle\langle\alpha_0|e^{i\chi t_I \hat{J}_x \hat{a}\hat{a}^\dagger}\right\} \\
&= \sum_{m=-j}^{j}\langle j,m|e^{-i\chi t_I \hat{J}_x \hat{a}\hat{a}^\dagger}\hat{\rho}_c|\alpha_0\rangle\langle\alpha_0|e^{i\chi t_I \hat{J}_x \hat{a}\hat{a}^\dagger}|j,m\rangle \\
&= \sum_{m=-j}^{j} P_x(m)|\alpha'_m\rangle\langle\alpha'_m|
\end{aligned} \tag{5.18}$$

where $\alpha'_m = \alpha_0 e^{-i\chi t_I m}$ and where $P_x(m)$ is the probability of measuring the condensate in state $|j,m\rangle$, as defined in Eq. (5.10). The Wigner characteristic function is then

$$\begin{aligned}
\chi_W(\lambda,\lambda^*) &= \text{Tr}_{\text{field}}\left\{\hat{\rho}_{\text{field}} e^{\lambda\hat{a}^\dagger - \lambda\hat{a}}\right\} \\
&= \sum_{m=-j}^{j} P_x(m)\chi_W^{\alpha'_m}(\lambda,\lambda^*),
\end{aligned} \tag{5.19}$$

where $\chi_W^{\alpha'_m}$ is the characteristic function for the coherent state $|\alpha'_m\rangle$. Due to the linearity of the Fourier transform, the Wigner function will thus be a sum of Gaussians, weighted by the atom number distribution of the condensate:

$$G(\alpha, \alpha^*) = \frac{2}{\pi} \sum_{m=-j}^{j} P_x(m) e^{-2|\alpha - \alpha'_m|^2} \tag{5.20}$$

For convenience, we set the initial conditions of the light field such that $x(0) = 0$, i.e. $\alpha_0 = \frac{i}{2} y(0)$. This gives

$$G(x, y) = \frac{2}{\pi} \sum_{m=-j}^{j} P_x(m) e^{-\frac{1}{2}(x - y(0)\sin\chi t_I m)^2 - \frac{1}{2}(y - y(0)\cos\chi t_I m)^2}. \tag{5.21}$$

After integration, the marginal distribution becomes

$$p(x) = \frac{1}{\sqrt{2\pi}} \sum_{m=-j}^{j} P_x(m) e^{-\frac{1}{2}(x - y(0)\sin\chi t_I m)^2}. \tag{5.22}$$

Thus each m value is mapped onto a Gaussian at position $y(0)\sin\chi t_I m$ with width equal to one. This is illustrated in Fig. 5.2. To be able to distinguish without ambiguity different m values in the output, there should be at least 4 standard deviations between the means of adjacent Gaussians. The resultant condition on the atom-light coupling is then

$$\chi t_I > \frac{4}{|y(0)|} = \frac{2}{|\alpha_0|} \tag{5.23}$$

and

$$\chi t_I \ll \frac{1}{N}. \tag{5.24}$$

If the fringes close to $m = 0$ only are needed, then this last condition may be relaxed considerably to a condition which merely prevents aliasing:

$$\chi t_I < \frac{\pi}{N}. \tag{5.25}$$

Nevertheless, there is a limit on the size of the induced phase shift.

The analysis above assumes perfect detector efficiencies and an infinite time of integration so that all the light is removed from the cavity. The results can be generalised to hold when this is not the case[[179],p63]. For a detector efficiency of η_∞ and a total integration time of T, then the distribution for the integrated photocurrent is

$$p(x) = \frac{1}{\sqrt{2\pi\eta}} \sum_{m=-j}^{j} P_x(m) e^{-\frac{1}{2}(x - \eta y(0)\sin\chi t_I m)^2/\eta}, \tag{5.26}$$

Figure 5.2: *The probability distribution resulting from the homodyne measurement. The fringes corresponding to adjacent m values can be distinguished if the coherent amplitude of the light field α_0 is large enough.*

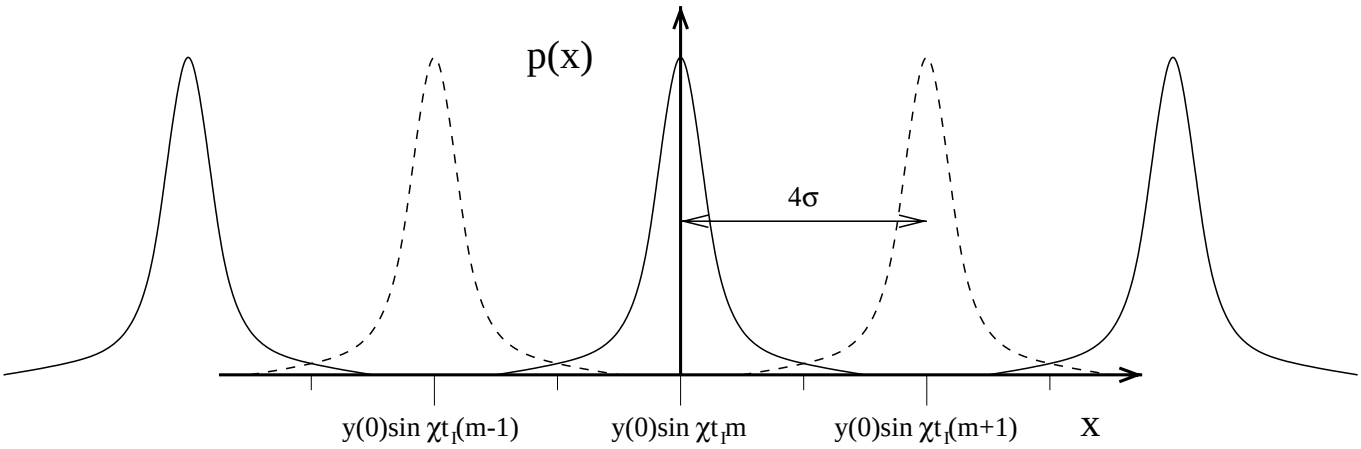

where $\eta = \eta_\infty \left(1 - e^{-\gamma T}\right)$ and γ is the damping rate of the cavity. The lower bound on the atom-light coupling becomes

$$\chi t_I > \frac{4}{\sqrt{\eta}|y(0)|} = \frac{2}{\sqrt{\eta}|\alpha_0|}. \tag{5.27}$$

Thus the effects of detector inefficiencies and a low damping rate can be overcome by starting with a large coherent state amplitude in the cavity. For example, with a detector efficiency of $\eta_\infty = .5$ and cavity parameters as given in table 3.1, then for $\gamma T \gg 1$, the lower limit on the interaction time is

$$t_I > 4.3 \times 10^{-4} s, \tag{5.28}$$

which is quite small. For a typical damping rate of $\gamma = 1.5 \times 10^9 s^{-1}$, the required damping time T is also small.

5.5 Phase errors and phase diffusion

Interatomic collisions are necessary to produce the initial superposition of condensates in the first stage of the scheme, but their effect on subsequent stages of the measurement scheme is unwanted. A Feshbach resonance[89] could be used to tune the collisional term to zero. However, this technique may be unfeasible[164], so we will now discuss briefly the

effect of the nonlinearity, and other sources of phase error on the different stages of the scheme.

As well as the diffusive effect of collisions, there are also the effects of decoherence to consider. These could be due to external perturbations of the trapping potential or, if the optical field is present, to fluctuations in the condensate momentum from the atom-field coupling. The overall effect of the nonlinearity, external perturbations and the back action on the condensate may be seen in the following master equation, in which the dynamics of the optical field have been adiabatically eliminated[126]:

$$\dot{\hat{\rho}}_p \;=\; -i2\kappa[\hat{J}_x^2,\hat{\rho}_p] \;+\; i\chi|\alpha|^2[\hat{J}_x,\hat{\rho}_p] \;-\; \frac{2\chi^2|\alpha|^2}{\gamma}[\hat{J}_x,[\hat{J}_x,\hat{\rho}_p]] \;-\; \frac{\sigma^2}{2}[\hat{J}_x,[\hat{J}_x,\hat{\rho}_p]], \quad (5.29)$$

where σ is the size of the external perturbations. This master equation can be generated from the random Hamiltonian

$$\hat{H}_{\rm Ito} = \hbar\left(\chi|\alpha|^2+\sigma'\xi\right)\hat{J}_x + \hbar\left(2\kappa - \frac{i}{2}\sigma'^2\right)\hat{J}_x^2 \quad (5.30)$$

where $\sigma' = \sigma + (2\chi|\alpha|)/(\sqrt{\gamma})$ and $\xi = dW/dt$ is delta-correlated white noise. This Hamiltonian can generate stochastic differential equations that are to be interpreted in the Ito sense[1]. So that ordinary calculus may be used, we use the Stratonovich form:

$$\hat{H}_{\rm Str} = \hbar\sigma'\xi\hat{J}_x + \hbar 2\kappa\hat{J}_x^2. \quad (5.31)$$

We have removed the linear deterministic term since it can be negated by tilting the two wells in proportion to the intensity of the light field.

In the detection part of the scheme (stage 2), $\hat{H}_{\rm Str}$ will induce an extra self-phase change in the components of the superposition state:

$$\phi_\pm = \pm\Delta j\tau \pm \sigma' jW(\tau) + 2\kappa j^2\tau, \quad (5.32)$$

where $W(\tau)$ is the Wiener process. Since the self-phase change due to the nonlinearity is the same for both components, there is no net effect on the output probability distribution (Eq. (5.10)). The overall phase shift in the fringes is therefore

$$\phi = \Delta j\tau + \sigma' jW(\tau). \quad (5.33)$$

Thus the phase shift suffers a random walk, with mean $\overline{\phi}(\tau) = \Delta j\tau$ and standard deviation $\sigma_\phi(\tau) = \sigma' j\sqrt{\tau}$. This phase uncertainty could be reduced by isolating the trapping

[1] See Appendix A

apparatus from mechanical vibrations and stray electromagnetic fields, and also by only turning on the cavity field when required in the third stage. If the cavity field must be on during the detection stage, the resultant phase error is

$$\sigma_\phi(\tau) = \frac{2\chi|\alpha|}{\sqrt{\gamma}} j\sqrt{\tau} = \frac{2\chi|\alpha|}{\sqrt{\gamma\tau}\Delta}\overline{\phi}(\tau). \tag{5.34}$$

The relative error may be minimised by increasing the detection time τ or decreasing the strength of the interaction with the optical field. For typical parameters (as used above), with $j = 50$ and $\tau = 160ms$, the phase error is $\sigma_\phi = 0.08$ *rad*, which could be a major restriction on the sensitivity of the measurement. This highlights the advantage of switching on the cavity field only when it is needed, especially when the waiting time involved is very small $\sim 1/\gamma \simeq 10^{-9}s$.

In the third stage, the constraints of the two-mode approximation limit the size of the interwell coupling. Even if the atomic collisions are only weak compared to the tunnelling term, the nonlinear term will cause a collapse (through dephasing) in any tunnelling oscillations, as shown in Fig. 2.11. However, this should not occur before there is time for at least one quarter of an oscillation (a $\frac{\pi}{2}$ pulse) to occur. If the self-interactions are stronger, then they will induce a nonlinear rotation around the $\hat{J}_x$ axis and a diffusion in the distribution on the Bloch sphere. The effect of the extra rotation may be negated by adjusting the time of the pulse so that the final state lies in the $\hat{J}_y - \hat{J}_z$ plane. The effect of the diffusion can not be so removed, and may wash out the interference fringes. The decoherence part of the Hamiltonian will induce a random rotation around the $\hat{J}_x$ axis, which will also reduce the visibility of the fringes.

Finally, there is the last stage of the measurement wherein the condensate interacts with the cavity field. Without tunnelling, the collisions and the decoherence will have no direct effect on the state of the light field, since terms involving only $\hat{J}_x$ in the Hamiltonian do not affect the x-distribution. This can be seen from the reduced density operator for the cavity field:

$$\begin{aligned}
\hat{\rho}_{\text{field}} &= \text{Tr}_{\text{cond}}\left\{e^{-i\chi t_I \hat{J}_x \hat{a}\hat{a}^\dagger - i\sigma'\xi\hat{J}_x - i2\kappa\hat{J}_x^2}\hat{\rho}_c|\alpha_0\rangle\langle\alpha_0|e^{i\chi t_I \hat{J}_x \hat{a}\hat{a}^\dagger + i\sigma'\xi\hat{J}_x + i2\kappa\hat{J}_x^2}\right\} \\
&= \sum_{m=-j}^{j}\langle j,m|e^{-i\chi t_I m\hat{a}\hat{a}^\dagger - i\sigma'\xi m - i2\kappa m^2}\hat{\rho}_c|\alpha_0\rangle\langle\alpha_0|e^{i\chi t_I m\hat{a}\hat{a}^\dagger + i\sigma'\xi m + i2\kappa m^2}|j,m\rangle \\
&= \sum_{m=-j}^{j} P_x(m)|\alpha'_m\rangle\langle\alpha'_m|,
\end{aligned} \tag{5.35}$$

which is unaffected by $\hat{H}_{\rm Str}$.

If the Ω is not exactly zero then, for a strong atom-light interaction, a back action may develop over time which will induce tunnelling[33] through momentum fluctuations. This would directly affect the phase of the cavity field, and it also may open a way for the atom-atom interaction to have an effect. In order to prevent this, the interwell coupling must be suppressed by switching on a high barrier, either magnetic or with a far detuned laser pulse.

5.6 Mean-field limit

The scheme outlined above depended on starting in a state which was a quantum superposition of two condensates and on the resulting entanglement. For comparison, we will analyse the mean-field analogue to discover which features of this scheme remain in the absence of quantum entanglement.

In the mean-field limit, the system is described by a Gross-Pitaevskii (GP) equation[106, 154, 185]:

$$i\hbar\dot{\Phi}(x,t) = \left(-\frac{\hbar^2}{2M}\frac{\partial^2}{\partial x^2} + Rx + V(x) + U_0 N|\Phi(x,t)|^2\right)\Phi(x,t), \tag{5.36}$$

where M is the atomic mass, the constant R is the gradient of the force and U_0 is the strength of the interparticle interactions. Suppose that the interatomic collisions are negligible. Then, when the overlap between the wells is small, we may expand the mean field in terms of the local wave functions of each well:

$$\Phi(x,t) = b_1(t)e^{-iE_0t/\hbar}u_1(x) + b_2(t)e^{-iE_0t/\hbar}u_2(x), \tag{5.37}$$

where

$$u_j(x) = \frac{1}{(2\pi r_0)^{\frac{1}{4}}}e^{(x-(-1)^j q_0)^2/4r_0^2}, \quad r_0 = \sqrt{\frac{\hbar}{2M\omega_0}}, \tag{5.38}$$

and

$$b_j(t) = \int u_j^*(x)\Phi(x,t)dx. \tag{5.39}$$

The ground-state energy of each of the local modes is $E_0 = \hbar(\nu+\omega_0)/2$, as in Ch. 2. The GP equation (Eq. (5.36)), then generates the following equations of motion:

$$\dot{b}_j(t) = \frac{(-1)^{j+1}iRq_0}{\hbar}b_j(t) + \frac{i\Omega}{2}b_{3-j}(t). \tag{5.40}$$

As before the force acts for a time τ and then the tunnelling for a time $t_{\frac{\pi}{2}}$:

$$b_j(\tau + t_{\pi/2}) = e^{(-1)^{j+1}iRq_0\tau/\hbar}b_j(0)\cos\frac{\Omega t_{\pi/2}}{2} + ie^{(-1)^j iRq_0\tau/\hbar}b_{3-j}(0)\sin\frac{\Omega t_{\pi/2}}{2}. \quad (5.41)$$

Suppose we start off with an equal occupation in each well, such that $b_1(0) = b_2(0) = \frac{1}{\sqrt{2}}$. Then the mean population difference is shifted by the presence of the weak force:

$$\begin{aligned}\langle m\rangle &= \frac{N}{2}\left(|b_2(\tau+t_{\pi/2})|^2 - |b_1(\tau+t_{\pi/2})|^2\right)\\ &= -\frac{N}{2}\sin\frac{2Rq_0\tau}{\hbar}\\ &= -\frac{N}{2}\sin\Delta\tau. \end{aligned} \quad (5.42)$$

This did not occur in the previous quantum treatment, in which $\langle m\rangle \equiv 0$. Even when the system is simply in a number state (not a superposition) with an equal number of atoms in each well, i.e. $|j,0\rangle_x$, the mean population difference is unaffected by the presence of the force. This demonstrates that, as a classical treatment, the mean field situation cannot be regarded as the large number limit of a quantum number state.

5.7 Coherent states

In quantum optics, it is the minimum uncertainty coherent state $|\alpha\rangle$ which is most like a mean field with amplitude α. The analogue in our case is the atomic coherent state, or Bloch state, first introduced in Sec. 4.3.1:

$$|\beta\rangle = \sum_m \begin{pmatrix} 2j \\ m+j \end{pmatrix} \frac{\beta^{m+j}}{(1+|\beta|^2)^j}|j,m\rangle_z, \quad (5.43)$$

where β can be described in terms of the angular coordinates of a point on the sphere $\beta = \tan\theta e^{i\psi}$.

Suppose the system starts in the state given by $\beta = 0$, which is symmetric with respect to the two wells. This state is also the ground state $|j,-j\rangle_z$ of the system when $\Omega \gg |\kappa|N$. Hence the coherence between the two condensates has been well established through tunnelling. To work out the mean population difference, we can use the Heisenberg equations of motion. Under the weak-force Hamiltonian $\hat{H}_F$ (Eq. (5.5)), the annihilation

and creation operators for the local modes obey

$$\dot{\hat{c}}_j = \tfrac{(-1)^{j+1}i\Delta}{2}\hat{c}_j \tag{5.44a}$$

$$\dot{\hat{c}}_j^\dagger = \tfrac{(-1)^{j}i\Delta}{2}\hat{c}_j^\dagger, \tag{5.44b}$$

and under the tunnelling Hamiltonian (Eq. (2.49) with $\kappa = 0$),

$$\ddot{\hat{c}}_j = -\tfrac{\Omega^2}{4}\hat{c}_j \tag{5.45a}$$

$$\ddot{\hat{c}}_j^\dagger = -\tfrac{\Omega^2}{4}\hat{c}_j^\dagger. \tag{5.45b}$$

As we have done before, we let the force to act for a time τ and then the tunnelling for a time $t_{\frac{\pi}{2}}$. After time $t = \tau + t_{\frac{\pi}{2}}$, the operators in the Heisenberg picture become

$$\hat{c}_j(t) = \tfrac{1}{2}\left(e^{(-1)^{j+1}i\Delta\tau/2}\hat{c}_j(0) + ie^{(-1)^{j}i\Delta\tau/2}\hat{c}_{3-j}(0)\right) \tag{5.46a}$$

$$\hat{c}_j^\dagger(t) = \tfrac{1}{2}\left(e^{(-1)^{j}i\Delta\tau/2}\hat{c}_j^\dagger(0) - ie^{(-1)^{j+1}i\Delta\tau/2}\hat{c}_{3-j}^\dagger(0)\right). \tag{5.46b}$$

These are the quantised equivalent of the equations for the semiclassical mode populations (Eq. (5.40)). They can be rewritten using the identities $\hat{c}_2^\dagger\hat{c}_1 = \hat{J}_z - i\hat{J}_y$ and $\hat{c}_2\hat{c}_1^\dagger = \hat{J}_z + i\hat{J}_y$, to become

$$\hat{J}_x(t) = \sin(\Delta\tau)\hat{J}_z(0) + \cos(\Delta\tau)\hat{J}_y(0). \tag{5.47}$$

Therefore, the mean population difference for an initial state of $\left|j, \pm j\right\rangle_z$ is

$$\left\langle m\right\rangle = \left\langle \hat{J}_x(t)\right\rangle = \pm\frac{N}{2}\sin(\Delta\tau), \tag{5.48}$$

which gives a greatest change in $\left\langle m\right\rangle$ of any Bloch state. For the ground state $\left|j, -j\right\rangle_z$ the difference in occupation between the two wells is as given above in the mean-field approach (Eq. (5.42)). Figure 5.3 shows the change in $\left\langle m\right\rangle$ for a general Bloch state (ϕ,θ) as the initial state. The case shown is for $N = 10$ and $\tau\Delta = 0.1$, but the shape is independent of N.

It may seem better to use this Bloch state as the initial state, since it could be easier to generate than the superposition state in Eq. (5.4), and the sign of the weak force may be determined from the measurement of $\left\langle m\right\rangle$. However, the size of the induced phase change given Eq. (5.42) is *not* amplified by j. In other words, the macroscopic occupation of a single condensed state is not fully utilised.

A comparison of the relative uncertainty in either case clearly demonstrates this point. In the first case, where the superposition state is used, the phase is inferred from the

Figure 5.3: *The shift in the mean population difference for an initial Bloch state, as a function of the Bloch-state parameters* (θ, ϕ). *The condensate contains 100 atoms and has been subjected to a phase shift of* $\tau\Delta = 0.1$.

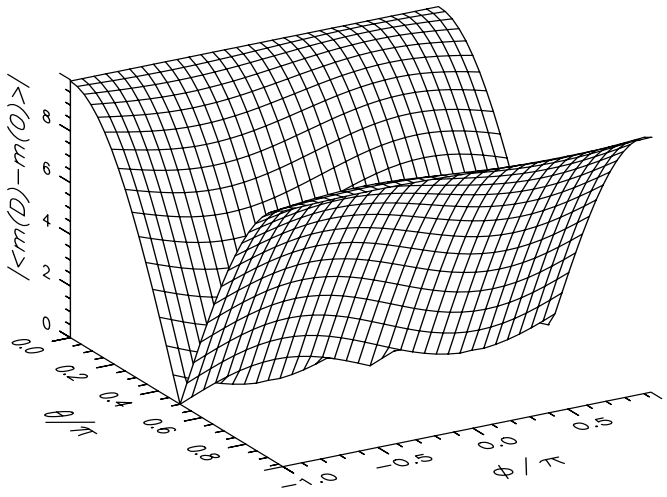

proportion of detection events falling on odd fringes (Eq. (5.12)). The uncertainty in this binomial distribution with probability $P = \sin^2 \Delta j\tau$ is

$$\delta P = \sqrt{\frac{P(1-P)}{N_D}}, \tag{5.49}$$

where N_D is the number of detection events. The relative uncertainty in the phase is thus

$$\frac{\delta\phi}{\phi} = \frac{1}{\phi}\left|\frac{dP}{d\phi}\right|^{-1} \delta P = \frac{1}{\Delta\tau N\sqrt{N_D}}. \tag{5.50}$$

When the initial state is the Bloch coherent state $\left|j, -j\right\rangle$, the uncertainty in the mean of the distribution is

$$\delta\langle m\rangle = \sqrt{\frac{\langle m^2\rangle - \langle m\rangle^2}{N_D}}. \tag{5.51}$$

This gives a relative uncertainty in ϕ of

$$\frac{\delta\phi}{\phi} = \frac{1}{\phi}\left|\frac{d\langle m\rangle}{d\phi}\right|^{-1} \delta\langle m\rangle = \frac{1}{\Delta\tau\sqrt{NN_D}}. \tag{5.52}$$

Thus the precision of the measurement grows in proportion to the number of condensed atoms when the entangled state (Eq. (5.4)) is used, but only as the square root of the

number of atoms when the coherent state $\left|j,-j\right\rangle$ is used. This demonstrates the advantage of using quantum entanglement of two macroscopically distinct states in order to make a highly sensitive force detector.

5.8 Implementation

If the weak force in question is gravity, then, with the parameters quoted above, the size of the induced phase shift is

$$\frac{\phi}{g} = \frac{jM\tau q_0}{\hbar} \simeq 2.4 \times 10^4 rad \,\text{per}\, g, \tag{5.53}$$

where $q_0 = 15\mu m$ and $M = 10^{-26}$ (for lithium). While this is small compared to the phase shift that atom interferometric techniques[98, 142, 186] can obtain ($\simeq 3 \times 10^6 rad$ per g), improvements can be made. The size of the phase shift may be increased by using more atoms, by separating the wells further, or by allowing a longer time τ for the interaction. The number of atoms could be increased by up to 10 times without invalidating the two-mode approximation. The two wells need to remain close during the preparation of the initial state and during tunnelling, but could be separated and brought together again during the weak force interaction. The time of the interaction is limited by mechanical vibration, but if two gravimeters were being used as a gradiometer to cancel the effect of common motion, the interaction time could be extended.

For a force such as gravity, which acts continuously on the condensate through all stages of the scheme, its size will not be related to the phase shift in the manner described in Sec. 5.3. However, this method will be able to detect the presence of such forces, and if the trapping field is appropriately biased, deviations from an expected value could be detected. The size of the force could then be gleaned from the size of the magnetic field needed to produce a null measurement.

A variation on the scheme would be able to detect the change in the atomic scattering length a due to a Feshbach resonance[89]. Suppose a Feshbach resonance were to be induced in the condensate in well 2, through the application of a magnetic field bias B. The scattering length changes by[127]

$$a = a_0 \left(1 - \frac{\Delta_{\mathrm{FR}}}{B - B_0}\right), \tag{5.54}$$

where $\Delta_{\rm FR}$ describes the width of resonance at $B = B_0$. The Hamiltonian must then include the term:

$$\begin{aligned}\hat{H}_{\rm FR} &= \kappa_2 {c_2^\dagger}^2 {c_2}^2 \\ &= \kappa_2 \left(\frac{N}{2} \left(\frac{N}{2} - 1 \right) + (N-1)\, \hat{J}_x + \hat{J}_x^2 \right), \end{aligned} \tag{5.55}$$

where $\kappa_2 = 2\pi\hbar\Delta/(mV_{eff}(B_0 - B))$. The terms proportional to N and N^2 only produce constant energy shifts and may be ignored, to give

$$\hat{H}_{\rm FR} = \kappa_2 \left((N-1)\, \hat{J}_x + \hat{J}_x^2 \right). \tag{5.56}$$

If, instead of allowing the system to interact with a weak force, we induce this Feshbach resonance for time τ on the superposition state $\left|E\right\rangle$ (Eq. (5.4)), the output phase is shifted in the manner described in Sec. 5.3, but by the amount

$$\phi_{\rm FR} = \frac{\kappa_2 N}{2}(N-1)\tau. \tag{5.57}$$

5.9 Les adieux

Throughout the first section of this thesis, we have been using the two-mode system as a vehicle to study the quantum and semiclassical properties of small Bose-Einstein condensates. We have viewed it as an isolated quantum system and also as a quantum system coupled to the environment, to see how certain exquisite quantum phenomena survive under measurement. We have even used it to suggest a practical use for Bose-Einstein condensates. But now it is time to farewell our trusted friend, and with it, many of the analytic methods that the two-mode approximation enabled. In the second section of the thesis, we are flung into new territory. We shall harness the engine of multimode quantum simulations to take us into higher dimensions and greatly expanded Hilbert spaces.

Part II

Quantum evolution of a Bose gas during evaporative cooling

Chapter 6

Quantum effects in optical fibre communications systems

6.1 Multimode simulations

The second part of this thesis studies the multimode quantum dynamics governed by the nonrelativistic boson Hamiltonian Eq. (2.1). Before we attempt a three-dimensional calculation of Bose condensation, we first consider a simpler problem: the propagation of light through optical fibres in nonlinear regimes. Like the system of dilute atomic vapour in traps, this simpler system consists of a gas of interacting bosons. However, in this case, the gas is restricted to one spatial dimension and since the gas consists of photons, the interparticle interactions are very weak. Both of these factors make the system a natural choice to be studied via the techniques developed in quantum optics. In particular, several authors[22, 23, 24, 32, 44, 45, 47, 48, 50, 157] have applied phase-space techniques derived from the standard quantum optical quasiprobabilities. This treatment assumes that the fibre contains a strong coherent field (a quantum soliton) which is perturbed by quantum noise effects that correspond to diffusion terms in the quasiprobability equations.

6.2 Model

Unlike the interparticle interactions in the atomic gas, interactions between the photons in a fibre cannot be approximated as hard sphere collisions. This is because the photon interactions are mediated through the dielectric material constituting the fibre. The coupling to the dialectric introduces frequency-dependent and time-delayed behaviour.

The complete Hamiltonian and its derivation have been given in the literature[22, 24, 42, 44, 45, 47, 172, 188]; we will only go over the salient points here. The starting point is a Lagrangian that generates classical Maxwell's equations for a one-dimensional dielectric waveguide, and that gives a Hamiltonian corresponding to the dielectric energy[43]:

$$\mathcal{W} = \int \left[\frac{1}{2\mu} B^2 + \int_{t_0}^{t} E(t') \dot{D}(t') dt' \right] dV, \tag{6.1}$$

where the electric field E gives the polarisation response of the dialectric to an incident electric displacement D. The field variables are then quantised by introducing equal-time commutators between the canonical coordinates and their conjugate momenta. The Lagrangian must produce both the correct energy and Maxwell's equations, otherwise the conjugate momenta will contain an arbitrary scaling, leading to incorrect commutation relations[42].

To the resultant Hamiltonian must be added couplings to linear gain, absorption and phonon reservoirs[23]. The phonon field consists of thermal and spontaneous excitations in the displacement of atoms from their mean locations in the dielectric lattice. The phonon-photon coupling induces Raman transitions and scattering from acoustic waves (the Brillouin effect) resulting in extra noise sources and an additional contribution to the nonlinearity. The initial state of phonons is thermal, with $n_{th}(\omega) = [\exp(\hbar\omega/kT) - 1]^{-1}$.

We can introduce the photon-density operator $\hat{\Psi}(t, x)$ as the annihilation operator for the linear quasi-particle excitations of the coupled electromagnetic and polarisation fields traveling through the fibre[45]. The non-zero equal-time commutations relations for these Bose operators are

$$\left[\hat{\Psi}(x), \hat{\Psi}^\dagger(x') \right] = \delta(x - x'). \tag{6.2}$$

In terms of these operators, the Hamiltonian in the interaction picture and within the rotating wave approximation for a single polarisation is[43, 45]

$$\begin{aligned} \hat{H}_P(t) = \int_{-\infty}^{\infty} dx \frac{\hbar}{2} \Bigg[& iv \left(\nabla \hat{\Psi}^\dagger \hat{\Psi} - \hat{\Psi}^\dagger \nabla \hat{\Psi} \right) + \omega'' \nabla \hat{\Psi}^\dagger \nabla \hat{\Psi} - \chi_e \hat{\Psi}^\dagger \hat{\Psi}^\dagger \hat{\Psi} \hat{\Psi} \\ & + 2 \int_0^\infty d\omega \left[\hat{\Psi}^\dagger \hat{\Psi} r(\omega) \left(\hat{A}(x, \omega) + \hat{A}^\dagger(x, \omega) \right) + \omega \hat{A}(x, \omega) \hat{A}^\dagger(x, \omega) \right] \Bigg], \end{aligned} \tag{6.3}$$

where v and ω'' are the group velocity and dispersion relation, respectively, at the carrier frequency, which has wave number $k = k_c$. These can be written in terms of the wave-

number dependence of the angular frequency ω:

$$v = \left.\frac{\partial\omega}{\partial k}\right|_{k=k_c}, \qquad \omega'' = \left.\frac{\partial^2\omega}{\partial k^2}\right|_{k=k_c}. \tag{6.4}$$

The nonlinear term in Eq. (6.3) arises from the intensity dependent refractive index $n = n_0 + In_2$. It is often called the $\chi^{(3)}$ effect, so named because it arises from the third-order term in the expansion of the polarisation field in terms of the electric field[1]. The coefficient of the electronic nonlinearity is defined as

$$\chi_e = \frac{\hbar(1-f)n_2\omega_c^2 v^2}{\mathcal{A}c}, \tag{6.5}$$

where ω_c is the carrier frequency, $\mathcal{A}$ is the effective cross-sectional area of the traveling mode, and f is the fraction of the nonlinearity due to the Raman gain:

$$\begin{aligned} f &= \frac{\chi_R}{\chi_e} = \frac{2}{\chi_e}\int_0^\infty dt \int_0^\infty d\omega r^2(\omega)\sin(\omega t) \\ &\simeq 0.2, \end{aligned} \tag{6.6}$$

where the numerical value for f has been determined from a detailed fit to the experimentally measured Raman gain spectrum, details of which will be given later.

In the last term of Eq. (6.3), the atomic vibrations within the silica structure of the fibre are modelled as a continuum of localised oscillators, and are coupled to the radiation modes by a Raman transition with a frequency-dependent strength of $r(\omega)$. The atomic displacement is proportional to $\hat{A}+\hat{A}^\dagger$, where the phonon annihilation and creation operators, $\hat{A}$ and $\hat{A}^\dagger$, have the commutation relations

$$\left[\hat{A}(x,\omega), \hat{A}^\dagger(x',\omega')\right] = \delta(x-x')\delta(\omega-\omega'). \tag{6.7}$$

The frequency dependence of the coupling $r(\omega)$ has been determined empirically through measurements of the Raman gain spectrum[23].

Even though it has reduced dimensionality and lacks any spatially modulated terms, the fibre Hamiltonian Eq. (6.3) contains some complications not present in the atom optics Hamiltonian Eq. (2.1): it contains terms describing a finite group velocity and the Raman interaction. However, in a propagating frame of reference that moves with the radiation field, the group velocity terms disappear in the Heisenberg equations of motion. Also, once we have integrated over the phonon reservoirs, the Raman terms contribute only an extra time-delayed nonlinearity and thermal noise sources to the equations of motion.

6.3 Phase-space methods

To generate numerical equations for simulation, operator representation theory, which was introduced in Sec. 4.4, can be used. A generalised form of Eq. (4.18), known as the positive-P representation, produces exact results[24, 44], while a truncated Wigner representation[22, 23, 47] gives approximate results. We will apply the Wigner technique to Eq. (6.3) because it is simpler, and for large mode occupations, its results are accurate. First, we expand the field operators in terms of operators for the free-field modes:

$$\hat{a}_k(t) = \frac{1}{\sqrt{2\pi}} \int_{L/2}^{L/2} dx \hat{\Psi}(t,x) e^{-i(k-k_c)x - i\omega_c t} \tag{6.8}$$

Applying the operator correspondences in Eq. (4.22) to the master equation for the reduced density operator $\hat{\rho}_a$ in which the phonon modes have been traced over, namely

$$\dot{\hat{\rho}}_a = \mathrm{Tr}_A \dot{\hat{\rho}} = \mathrm{Tr}_A \frac{1}{i\hbar} \left[\hat{H}_P, \hat{\rho} \right], \tag{6.9}$$

gives an equation for the Wigner function $G(t, \alpha_k, \alpha_k^*)$ that contains third- and fourth-order derivative terms. For a large photon number, we may neglect these higher-order terms. The resultant Fokker-Planck equation can be converted into an equivalent Ito stochastic equation for the phase-space variable

$$\Psi(t,x) = \frac{1}{\sqrt{2\pi}L} \sum_k e^{i(k-k_c)x + i\omega_c t} \alpha_k. \tag{6.10}$$

and its conjugate.

Standard custom in fibre optics applications[128, 132] involves using the propagative reference frame with the normalised variables: $\tau = (t - x/v)/t_0$ and $\zeta = x/x_0$, where $t_0 \sim 1ps$ is a typical pulse duration and $x_0 = t_0^2/|k''| \sim 1km$ for dispersion shifted fibre. This change of variables is useful only when second-order derivatives involving ζ can be neglected, which occurs for $vt_0/x_0 \ll 1$. For typical values of the parameters used in the simulations, the inequality is satisfied ($vt_0 \sim 10^{-4}m$).

6.4 Modified nonlinear Shrödinger equation

The resultant equation, which includes gain and loss, is a Raman-modified nonlinear Schrödinger (NLS) equation [158] with stochastic noise terms:

$$\frac{\partial}{\partial\zeta}\phi(\tau,\zeta) = \Gamma_G + \Big[\frac{\alpha}{2} \pm \frac{i}{2}\frac{\partial^2}{\partial\tau^2} + i\int_{-\infty}^{\tau} d\tau' h(\tau-\tau')\phi^*(\tau',\zeta)\phi(\tau',\zeta) + i\Gamma_R(\tau,\zeta)\Big]\phi(\tau,\zeta), \tag{6.11}$$

where $\alpha = \alpha^G - \alpha^A$ is the net dimensionless intensity gain and $\phi = \Psi\sqrt{vt_0/\overline{n}}$ is a dimensionless photon field amplitude. The photon flux is $|\phi|^2\overline{n}/t_0$, where $\overline{n} = |k''|\mathcal{A}c/(n_2\hbar\omega_c^2 t_0)$ is of the order the number of photons in a pulse of width t_0. The positive sign in front of the second-derivative term applies for anomalous dispersion ($k'' < 0$), which occurs for longer wavelengths, and the negative sign applies for normal dispersion ($k'' > 0$).

The causal nonlinear response function $h(\tau)$ is normalised so that $\int h(\tau)d\tau = 1$, and it includes both electronic and Raman nonlinearities:

$$h(\tau) = h_e(\tau) + h_R(\tau) = \frac{\overline{n}x_0}{v^2}\left(\chi_e\delta(\tau) + 2H(\tau)\int_0^{\infty} r^2(\nu/t_0)\sin(\nu\tau)d\nu\right), \tag{6.12}$$

where $H(\tau)$ is the Heaviside step function and where the frequency-dependent coupling $r(\nu/t_0)$ is as defined in Eq. (6.3). The Raman response function $h_R(\tau)$ causes effects like the soliton self-frequency shift[69]. The Raman gain, whose spectrum has been extensively measured[40, 166, 167], can be modelled as a sum of n Lorentzians. This gives a response function of the form

$$h_R(\tau) = H(\tau)\sum_{j=0}^{n} F_j\delta_j e^{-\delta_j\tau}\sin(\nu_j\tau), \tag{6.13}$$

where the F_j are the Lorentzian strengths, the δ_j are the widths (corresponding to damping), and the ν_j are the centre frequencies, all in normalised units. The $j = 0$ Lorentzian models the Brillouin contribution to the response function. The values for an $n = 10$ fit are given in Table 6.1.

The initial conditions must include complex quantum vacuum fluctuations, in order to correctly represent operator fields. For coherent inputs, the fields are correlated as

$$\big\langle\Delta\phi(\tau,0)\Delta\phi^*(\tau',0)\big\rangle = \frac{1}{2\overline{n}}\delta(\tau-\tau'). \tag{6.14}$$

Fibre loss and the presence of a gain medium each contribute spontaneous-emission noise. The complex gain/absorption noise enters the NLS equation through an additive stochastic

Table 6.1: *Fitting parameters for the 11-Lorentzian model of the Raman gain spectrum $h_R(\omega)$. All frequencies are in terahertz.*

j	F_j	ν_j	δ_j
0	0.16	0.005	0.005
1	-0.3545	0.3341	8.0078
2	1.2874	26.1129	46.6540
3	-1.4763	32.7138	33.0592
4	1.0422	40.4917	30.2293
5	-0.4520	45.4704	23.6997
6	0.1623	93.0111	2.1382
7	1.3446	99.1746	26.7883
8	-0.8401	100.274	13.8984
9	-0.5613	114.6250	33.9373
10	0.0906	151.4672	8.3649

term Γ_G, whose correlations are defined by

$$\left\langle \Gamma_G(\nu,\zeta)\Gamma_G^*(\nu',\zeta')\right\rangle = \frac{(\alpha_G+\alpha_A)}{2\overline{n}}\delta(\zeta-\zeta')\delta(\nu+\nu'), \tag{6.15}$$

where $\Gamma_G(\nu,\zeta)$ is the Fourier transform of the noise source:

$$\Gamma_G(\nu,\zeta) = \frac{1}{\sqrt{2\pi}}\int_{-\infty}^{\infty} d\tau \Gamma_G(\tau,\zeta)e^{i\nu\tau}. \tag{6.16}$$

Similarly, the real Raman noise, which appears as a multiplicative stochastic variable Γ_R, has correlations

$$\left\langle \Gamma_R(\nu,\zeta)\Gamma_R(\nu',\zeta')\right\rangle = \frac{1}{\overline{n}}\delta(\zeta-\zeta')\delta(\nu+\nu')\left[n_{th}(\nu)+\frac{1}{2}\right]\alpha_R(\nu), \tag{6.17}$$

where the dimensionless gain function is $\alpha_R(\nu) = \alpha_R(\omega\tau_0) = \sqrt{8\pi}|\Im\{h_R(\nu)\}|$, and the thermal Bose distribution is given by $n_{th}(\nu) = [\exp(\hbar\nu/kT\tau_0)-1]^{-1}$. Thus the Raman noise is strongly temperature dependent, but it also contains a spontaneous component which provides vacuum fluctuations even at $T=0$.

Equations (6.11-6.17) can be discretised and, without any further approximation, can be numerically simulated using a split-step Fourier integration routine. These equations include all the currently known noise sources that are significant in soliton propagation,

including effects like the soliton self-frequency shift. Guided acoustic wave Brillouin scattering [9, 158, 157] noise sources are included in the Raman gain function. These have little effect on the position of an isolated soliton, but are important for long-range soliton collision effects[38, 161] that occur in pulse-trains. As an example of this numerical technique, calculations of the uncertainty in arrival times of propagating solitons will be presented in Sec. 6.7. What makes calculations using Eqs. (6.11-6.17) tractable is that all the noise sources have been scaled by a factor of $\overline{n}$ in the denominator. This physically means that there are many bosons in each mode, and it allows the stochastic terms to be treated as a perturbation around the deterministic, or coherent, behaviour. In the simulations of evaporative cooling in Ch. 7, which use the same numerical technique, we cannot assume that there are many particles per modes. This demands greater computing resources than do the soliton calculations, and also pushes the currently known phase-space techniques to the very limit of their validity.

6.5 Perturbation theory

We now proceed to derive the approximate effects of noise on soliton jitter. The results of this analysis are summarised in the next section, with this section being for those who are eager for a taste of soliton perturbation theory[48, 79, 97, 99, 102, 171].

In order to simplify the calculation, we firstly assume that gain and loss in the fibre balance exactly so that $\alpha = 0$. This requires that the amplifier sections in the fibre are sufficiently close together ($\sim x_0$ or less) so that the soliton can propagate without distortion[129].

Secondly, we assume that the Raman nonlinear response function is instantaneous on the timescale of the soliton width. This is equivalent to assuming that the phonon modes are heavily damped, ie $\delta_j \ll 1$ and means that the Raman coupling leads to only incoherent scattering of the propagating radiation. Equation (6.11) then reduces to

$$\frac{\partial}{\partial\zeta}\phi(\tau,\zeta) = \Gamma_G + \left[\pm\frac{i}{2}\frac{\partial^2}{\partial\tau^2} + i\phi^*(\tau,\zeta)\phi(\tau,\zeta) + i\Gamma_R(\tau,\zeta)\right]\phi(\tau,\zeta). \tag{6.18}$$

In the absence of the noise sources, these equations have stationary solutions in the form of bright (+) or dark (−) solitons. Solitons are solitary waves in which the effects of dispersion are balanced by nonlinear effects, to produce a stationary pulse that is robust in the presence of perturbations.

6.5.1 Bright solitons

The stationary soliton of Eq. (6.18) for anomalous dispersion is:

$$\phi_s(\tau,\zeta) = A\mathrm{sech}(\mathrm{A}\tau - \mathrm{q}(\zeta))\mathrm{e}^{\mathrm{iV}\tau+\mathrm{i}\theta(\zeta)}, \tag{6.19}$$

where $\partial q/\partial\zeta = VA$ and $\partial\theta/\partial\zeta = (A^2 - V^2)/2$, with amplitude A and velocity V. Following the method presented in [79, 97], we treat the effects of the noise terms as perturbations around a soliton solution whose parameters vary slowly with ζ:

$$\phi(\tau,\zeta) = \overline{\phi}(\tau,\zeta) + \Delta\phi(\tau,\zeta), \tag{6.20}$$

where

$$\overline{\phi}(\tau,\zeta) = A(\zeta)\mathrm{sech}(A(\zeta)\tau - q(\zeta))e^{iV(\zeta)\tau+i\theta(\zeta)} \tag{6.21}$$

for a bright soliton. Substituting Eq. (6.20) into Eq. (6.18) gives the following linearised equation (first order in $\Delta\phi(\tau,\zeta)$):

$$\frac{\partial}{\partial\zeta}\Delta\phi(\tau,\zeta) \;=\; \left[\pm\frac{i}{2}\frac{\partial^2}{\partial\tau^2} + i2\overline{\phi}^*(\tau,\zeta)\overline{\phi}(\tau,\zeta)\right]\Delta\phi(\tau,\zeta) \;+\; i\overline{\phi}(\tau,\zeta)^2\Delta\phi^*(\tau,\zeta) \;+\; s(\tau,\zeta), \tag{6.22}$$

where the noise source have been grouped together in

$$s(\tau,\zeta) = \Gamma_G + i\Gamma_R(\tau,\zeta)\overline{\phi}(\tau,\zeta). \tag{6.23}$$

Now we wish to determine the evolution of these soliton parameters as a function of propagation distance ζ. To do this, we expand the perturbation in terms of the soliton parameters plus a continuum term:

$$\begin{aligned}\Delta\phi(\tau,\zeta) &= \sum_i \frac{\partial\overline{\phi}(\tau,\zeta)}{\partial P_i}\Delta P_i + \Delta\phi_c(\tau,\zeta) \\ &= \sum_i f_{P_i}\Delta P_i + \Delta\phi_c(\tau,\zeta),\end{aligned} \tag{6.24}$$

where $P_i \in \{V, q, A, \theta\}$. The projection functions for each parameter are

$$f_A = \left(\frac{1}{A} - \tau\tanh(A\tau - q)\right)\overline{\phi}, \tag{6.25a}$$

$$f_q = \tanh(A\tau - q)\overline{\phi}, \tag{6.25b}$$

$$f_V = i\tau\overline{\phi}, \tag{6.25c}$$

$$f_\theta = i\overline{\phi}. \tag{6.25d}$$

In order to select out the evolution of particular parameters, we need to use the adjoint functions $\underline{f_{P_i}}$ that obey the orthogonality condition

$$\Re\left\{\int_{-\infty}^{\infty} d\tau f_{P_i}\underline{f_{P_j}}^*\right\} = \delta_{i,j}. \tag{6.26}$$

Appropriate adjoint functions are

$$\underline{f_A} = \overline{\phi}, \tag{6.27a}$$
$$\underline{f_q} = \tau\overline{\phi}, \tag{6.27b}$$
$$\underline{f_V} = i\tanh(A\tau - q)\overline{\phi}, \tag{6.27c}$$
$$\underline{f_\theta} = i\tau\tanh(A\tau - q)\overline{\phi}. \tag{6.27d}$$

Substituting the Taylor expansion (Eq. (6.24)) into the linearised equation (Eq. (6.22)) and using the adjoint functions to project out particular parameters shows that the growth of fluctuations in the fundamental soliton parameters is governed by

$$\frac{\partial}{\partial\zeta}\Delta q(\zeta) = A\Delta V(\zeta) + S_q(\zeta), \tag{6.28a}$$
$$\frac{\partial}{\partial\zeta}\Delta V(\zeta) = S_V(\zeta), \tag{6.28b}$$

where we have taken the unperturbed velocity to be zero: $\mathrm{V} = 0$. The stochastic terms are defined as

$$S_{P_i}(\zeta) = \Re\left\{\int_{-\infty}^{\infty} d\tau \underline{f_p}^*(\zeta)s(\tau,\zeta)\right\}. \tag{6.29}$$

We wish to find the growth of fluctuations in position $q(\zeta)$. Because the position depends on the soliton frequency V, as seen from Eq. (6.19), the contributions arising from both S_q and S_V must be considered. Firstly,

$$\begin{aligned} S_q(\zeta) &= \Re\left\{\int_{-\infty}^{\infty} d\tau A\tau\mathrm{sech}(\mathrm{A}\tau - \mathrm{q})\mathrm{e}^{-\mathrm{i}\mathrm{V}\tau-\mathrm{i}\theta}\left(\Gamma_\mathrm{G} + \mathrm{i}\Gamma_\mathrm{R}\mathrm{Asech}(\mathrm{A}\tau-\mathrm{q})\mathrm{e}^{\mathrm{i}\mathrm{V}\tau+\mathrm{i}\theta}\right)\right\} \\ &= \int_{-\infty}^{\infty} d\tau A\tau\mathrm{sech}(\mathrm{A}\tau-\mathrm{q})\Re\{\mathrm{e}^{-\mathrm{i}\mathrm{V}\tau-\mathrm{i}\theta}\Gamma_\mathrm{G}\}, \end{aligned} \tag{6.30}$$

and

$$\begin{aligned} S_V(\zeta) &= \Re\left\{\int_{-\infty}^{\infty} d\tau A\tau(-i)\mathrm{sech}(\mathrm{A}\tau-\mathrm{q})\tanh(\mathrm{A}\tau-\mathrm{q})\mathrm{e}^{-\mathrm{i}\mathrm{V}\tau-\mathrm{i}\theta}\left(\Gamma_\mathrm{G} + \mathrm{i}\Gamma_\mathrm{R}\mathrm{Asech}(\mathrm{A}\tau-\mathrm{q})\mathrm{e}^{\mathrm{i}\mathrm{V}\tau+\mathrm{i}\theta}\right)\right\} \\ &= \int_{-\infty}^{\infty} d\tau A\tau\mathrm{sech}(\mathrm{A}\tau-\mathrm{q})\tanh(\mathrm{A}\tau-\mathrm{q})\left(\mathrm{Asech}(\mathrm{A}\tau-\mathrm{q})\Gamma_\mathrm{R} + \Im\{\mathrm{e}^{-\mathrm{i}\mathrm{V}\tau-\mathrm{i}\theta}\Gamma_\mathrm{G}\}\right). \end{aligned} \tag{6.31}$$

From this we can calculate the growth of the fluctuations in velocity:

$$\begin{aligned}\Delta V(\zeta) &= \Delta V(0) + \int_0^\zeta d\zeta' S_V(\zeta') \\ &= \Re\left\{\int_{-\infty}^{\infty} \Delta\phi(\tau,\zeta)\underline{f_V}^* d\tau\right\} + \int_0^\zeta d\zeta' S_V(\zeta'). \end{aligned} \tag{6.32}$$

Using the various noise correlations from Eqs. (6.14,6.15,6.17), the correlations in the velocity fluctuations can be calculated:

$$\begin{aligned}\left\langle \Delta V(\zeta)\Delta V^*(\zeta')\right\rangle &= \left\langle \Delta V(0)\Delta V^*(0)\right\rangle + \int_0^\zeta\int_0^{\zeta'} d\zeta'' d\zeta''' \left\langle S_V(\zeta'')S_V^*(\zeta''')\right\rangle \\ &= \frac{A}{6\overline{n}} + \left(\frac{\alpha_G A}{3\overline{n}} + \frac{2A^2\mathcal{I}(t_0)}{\overline{n}}\right)\zeta \qquad \zeta<\zeta', \end{aligned} \tag{6.33}$$

where the overlap integral $\mathcal{I}(t_0)$ is defined as

$$\mathcal{I}(t_0) = \int_{-\infty}^{\infty}\int_{-\infty}^{\infty} d\tau d\tau' \tanh(\tau)\mathrm{sech}^2(\tau)\tanh(\tau')\mathrm{sech}^2(\tau')\tilde{\mathcal{F}}(\tau/A-\tau/A'). \tag{6.34}$$

Here $\tilde{\mathcal{F}}(\tau)$ is the inverse Fourier transform of the fluorescence $\mathcal{F}(\nu) = \frac{1}{2}(n_{th}(\nu)+\frac{1}{2})\alpha_R(\nu)$.

The correlations in position fluctuations correspond to the jitter in arrival times, because we have chosen a propagative reference frame. The jitter therefore feeds off position fluctuations as well as noise entering through the velocity:

$$\begin{aligned}\left\langle \Delta q(\zeta)\Delta q*(\zeta')\right\rangle = \left\langle \Delta q(0)\Delta q*(0)\right\rangle + \int_0^\zeta\int_0^{\zeta'} d\zeta'' d\zeta'''\Big(A^2\left\langle \Delta V(\zeta'')\Delta V^*(\zeta''')\right\rangle \\ + \left\langle S_q(\zeta'')S_q^*(\zeta''')\right\rangle\Big) \qquad \zeta<\zeta'. \end{aligned} \tag{6.35}$$

Thus the timing jitter is

$$\begin{aligned}\left\langle(\Delta\tau(\zeta))^2\right\rangle &= \left\langle \Delta q(\zeta)\Delta q*(\zeta)\right\rangle \\ &= \frac{\pi^2}{24\overline{n}} + \frac{\pi^2\alpha_G}{12\overline{n}}\zeta + \frac{A^3}{6\overline{n}}\zeta^2 + \left(\frac{\alpha_G A^3}{9\overline{n}} + \frac{2A^4\mathcal{I}(t_0)}{3\overline{n}}\right)\zeta^3, \end{aligned} \tag{6.36}$$

which contains cubic terms due to the gain and Raman couplings, and also slower growing terms due to the initial vacuum fluctuations and amplifier noise.

An alternative method that is often used[70, 102, 171] for deriving the timing jitter exploits conserved quantities in the NLS equation. The relevant quantities are the energy W and momentum I:

$$W = \int_{-\infty}^{\infty} d\tau|\phi|^2 = 2A \tag{6.37a}$$

$$I = \Im\left\{\int_{-\infty}^{\infty} d\tau\phi^*\phi_\tau\right\} = 2AV, \tag{6.37b}$$

for a bright soliton solution (Eq. (6.19)). To obtain the fluctuations in velocity, we can differentiate both sides of Eq. (6.37) and substitute in for $d\phi/d\zeta$ from Eq. (6.18) to get

$$\frac{dA}{d\zeta} = \Re\left\{\int_{-\infty}^{\infty} d\tau \phi^* s\right\} \tag{6.38a}$$

$$V\frac{dA}{d\zeta} + A\frac{dV}{d\zeta} = -\Im\left\{\int_{-\infty}^{\infty} d\tau \phi_\tau^* s\right\}. \tag{6.38b}$$

Combining these two equations and integrating gives

$$\Delta V(\zeta) = \Delta V(0) + \Re\left\{\int_0^\zeta d\zeta' \int_{-\infty}^{\infty} d\tau(-i)A\tau\,\tanh(A\tau)\mathrm{sech}(\mathrm{A}\tau)\mathrm{e}^{-\mathrm{iV}\tau-\mathrm{i}\theta}\mathrm{s}(\tau,\zeta')\right\}, \tag{6.39}$$

which is the same as Eq. (6.32) and which can be used to obtain the leading order terms in the timing jitter.

6.5.2 Dark solitons

Fibres in the normal dispersion regime can support dark soliton solutions, so called since they correspond to a dip in the background intensity[78]:

$$\phi_t(\tau,\zeta) = E\sqrt{1-A^2\mathrm{sech}^2(\mathrm{EA}\tau-\mathrm{q}(\zeta))}e^{i\theta(\zeta)}e^{i\sigma(\zeta,\tau)}, \tag{6.40a}$$

$$\sigma(\zeta,\tau) = \arcsin\left(\frac{A\tanh(EA\tau-q(\zeta))}{\sqrt{1-A^2\mathrm{sech}^2(\mathrm{EA}\tau-\mathrm{q}(\zeta))}}\right), \tag{6.40b}$$

where $d\theta/d\zeta = E^2$, $dq/d\zeta = A\sqrt{1-A^2}E^2$ and E is the amplitude of the background field. The size of the intensity dip at the centre of the soliton is given by A, with the intensity going to zero in a black $\tanh(\tau)$ soliton, for which $A = 1$. Dark solitons are classed as topological solitons, because they connect two background pulses of different phase. The total phase difference between the boundaries is $\psi = 2\arcsin(A)$.

The nonvanishing boundary conditions of the dark pulse complicate the perturbation calculation of jitter variance. In order to use the conservation laws to calculate the growth in fluctuations, the constants of motion must be regularised so that their variational derivatives vanish at the boundary[102, 171]. The regularised momentum is $I_{\mathrm{reg}} = I - \psi$, which enables the leading order terms in the jitter growth to be calculated in the same manner as given above. We may rewrite the dark soliton solution as

$$\phi_t(\tau,\zeta) = Ee^{i\theta(\zeta)}\left(\sqrt{1-A^2} + Ai\tanh(EA\tau-q(\zeta))\right), \tag{6.41}$$

which is a simpler form for calculating the τ derivatives. The resulting expression for the jitter growth for a black soliton ($A = 1$) is

$$\left\langle (\Delta\tau(\zeta))^2 \right\rangle = \frac{1}{12\overline{n}}\zeta^2 + \left(\frac{\alpha_G}{18\overline{n}} + \frac{\mathcal{I}(t_0)}{6\overline{n}} \right) \zeta^3. \tag{6.42}$$

where the overlap integral $\mathcal{I}(t_0)$ is as defined in Eq. (6.34). As in the anomalous dispersion regime, the vacuum fluctuations contribute to quadratic growth in the jitter variance, and gain and Raman fluctuations contribute to cubic growth. However, the size of the jitter is smaller than that in the bright soliton case, for the same propagation distance ζ. The contribution from the vacuum and gain terms is one half and the contribution from the Raman term is one quarter of that in Eq. (6.36), giving dark solitons some advantage over their bright cousins.

6.6 Summary of noise scaling properties

In summary, there are three different sources of noise in the soliton, all of which must be taken into account for small pulse widths. These noise sources contribute to fluctuations in the velocity parameter, which lead to quadratic or cubic growth in the timing-jitter variance for single-pulse propagation. The noise sources also produce other effects, such as those effected through soliton interactions, but we will not consider these here.

The initial vacuum fluctuations cause diffusion in position which is important for small propagation distances. For bright solitons this is given by[48]

$$\left\langle (\Delta\tau(\zeta))^2 \right\rangle_I = \frac{\pi^2}{24\overline{n}} + \frac{1}{6\overline{n}}\zeta^2 \qquad \text{(bright)}. \tag{6.43a}$$

For purposes of comparison, note that $\overline{N} = 2\overline{n}$ is the mean photon number for a sech(τ) soliton. Numerical calculations confirmed that for tanh(τ) dark solitons, the variance was about one half the bright-soliton value, as predicted by the analysis in Sec. 6.5.2:

$$\left\langle (\Delta\tau(\zeta))^2 \right\rangle_I = \frac{\pi^2}{48\overline{n}} + \frac{1}{12\overline{n}}\zeta^2 \qquad \text{(dark)}. \tag{6.43b}$$

This shot-noise effect, which occurs without amplification, is simply due to the initial quantum-mechanical uncertainty in the position and momentum of the soliton. Because of the Heisenberg uncertainty principle, the soliton momentum and position cannot be specified exactly. This effect dominates the Gordon-Haus effect over propagation distances

less than a gain length. However, for short pulses, this distance can still correspond to many dispersion lengths, thus generating large position jitter.

As is well known, the noise due to gain and loss in the fibre produces the Gordon-Haus effect, which is currently considered the major limiting factor in any long-distance soliton-based communications system using relatively long ($> 10ps$) pulses. Amplification with mean intensity gain α^G, chosen to compensate fibre loss, produces a diffusion (or jitter) in position. Unless other measures are taken, for sufficiently small amplifier spacing[129] and at large distances this is given by[70, 76, 102]

$$\left\langle (\Delta\tau(\zeta))^2 \right\rangle_{GH} \simeq \frac{\alpha^G}{9\overline{n}}\zeta^3 \qquad \text{(bright)}, \tag{6.44a}$$

$$\left\langle (\Delta\tau(\zeta))^2 \right\rangle_{GH} \simeq \frac{\alpha^G}{18\overline{n}}\zeta^3 \qquad \text{(dark)}, \tag{6.44b}$$

in which the linearly growing terms have been neglected.

Another effect of the amplifier noise is to introduce an extra noise term via the fluctuations in the Raman-induced soliton self-frequency shift. This term scales as the fifth power of distance and hence will become important for long propagation distances. This combined effect of spontaneous emission noise and the Raman intrapulse scattering has been dealt with by a number of authors[7, 123, 134, 182]. Equation (6.11) models this accurately, since it includes the delayed Raman nonlinearity, and the effect would be seen in numerical simulations carried out over long propagation distances.

A lesser known effect is the fluctuations in velocity that arise from the Raman phase-noise term Γ_R in Eq. (6.11). Like the Gordon-Haus effect, this Raman noise generates a cubic growth in jitter variance:

$$\left\langle (\Delta\tau(\zeta))^2 \right\rangle_{R} = \frac{2\mathcal{I}(t_0)}{3\overline{n}}\zeta^3 \qquad \text{(bright)}, \tag{6.45a}$$

$$\left\langle (\Delta\tau(\zeta))^2 \right\rangle_{R} = \frac{\mathcal{I}(t_0)}{6\overline{n}}\zeta^3 \qquad \text{(dark)}. \tag{6.45b}$$

where $\mathcal{I}(t_0)$ is the integral defined in Eq. (6.34) that indicates the spectral overlap between the pulse spectrum and the Raman fluorescence. The mean-square Raman-induced timing jitter has a cubic growth in both cases, but the dark soliton variance is one quarter of that of the bright soliton.

The magnitude of this Raman jitter can be found by evaluating $\mathcal{I}(t_0)$ numerically, or else using an analytic approximation. An accurate model of the Raman gain, on which $\mathcal{I}(t_0)$ depends, requires a multi-Lorentzian fit to the experimentally measured spectrum. A

Figure 6.1: *Spectra of (a) the Raman gain $|\Im\{h_R(\omega)\}|$ and (b) fluorescence function $\mathcal{F}(\omega)$ for the 11-Lorentzian model (continuous lines) and the single-Lorentzian model (dashed lines), for a temperature of $T = 300K$. Figure (b) also shows the spectrum of a $t_0 = 1ps$ soliton.*

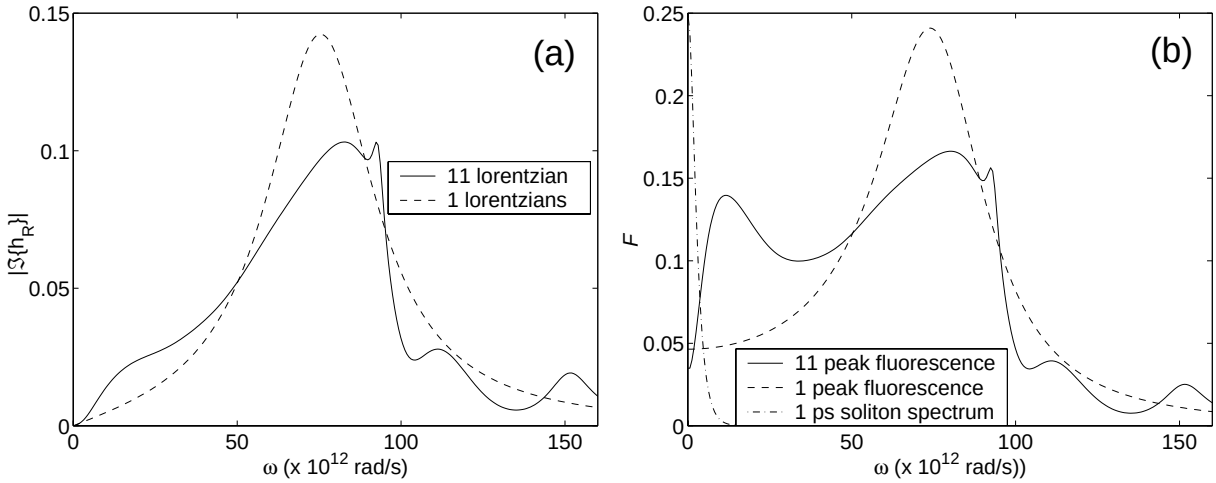

fit with 11 Lorentzians was used in the numerical simulations, however a single-Lorentzian model[105, 187] can suffice for approximate calculations; both models are shown in Fig. 6.1(a). For the single-Lorentzian model, the fluorescence spectrum is approximately flat at low frequencies:

$$\begin{aligned}\mathcal{F}(\nu) &= \sqrt{2\pi}\left(n_{th}(\nu)+\frac{1}{2}\right)|\Im\{h_R(\nu)\}| \\ &\simeq \frac{2F_1\nu_1\delta_1^2 k_B T}{(\nu_1^2+\delta_1^2)^2\hbar} = \mathcal{F}(0), \end{aligned} \tag{6.46}$$

which greatly simplifies the Raman correlations. As Fig. 6.1(b) indicates, the spectral overlap of $\mathcal{F}(\nu)$ with a $t_0 = 1ps$ soliton occurs in this low-frequency region. Thus the white-noise approximation for the Raman correlations is good for solitons of this pulse width and larger. For smaller pulse widths, not only is the Raman contribution to the noise larger due to the greater overlap, but the coloured nature of the correlations must be taken into account.

In the single-Lorentzian model, $\mathcal{I}(t_0 \to \infty) \simeq \frac{4}{15}\mathcal{F}(0)$, which gives

$$\left\langle(\Delta t(x))^2\right\rangle_R \simeq \frac{8|k''|^2 n_2\hbar\omega_0^2\mathcal{F}(0)}{45\mathcal{A}ct_0^3}x^3 = \frac{8t_0^2\mathcal{F}(0)}{45\overline{n}}\left(\frac{x}{x_0}\right)^3 \quad \text{(bright)}, \tag{6.47a}$$

$$\left\langle(\Delta t(x))^2\right\rangle_R \simeq \frac{2|k''|^2 n_2\hbar\omega_0^2\mathcal{F}(0)}{45\mathcal{A}ct_0^3}x^3 = \frac{2t_0^2\mathcal{F}(0)}{45\overline{n}}\left(\frac{x}{x_0}\right)^3 \quad \text{(dark)}. \tag{6.47b}$$

At a temperature of $300K$, $\mathcal{F}(0) = 4.6\times10^{-2}$ when a single Lorentzian centred at 12 THz with fitting parameters $F_1 = 0.7263$, $\delta_1 = 20\times10^{12}t_0$ and $\nu_1 = 75.4\times10^{12}t_0$ is used.

Figure 6.2: *Timing jitter in $t_0 = 500fs$ bright (a) and dark (b) solitons due to initial quantum fluctuations (circles), Gordon-Haus effect (crosses) and Raman noise (plus signs). The asterisks give the total jitter and the continuous line gives the approximate analytic results for the Raman jitter.*

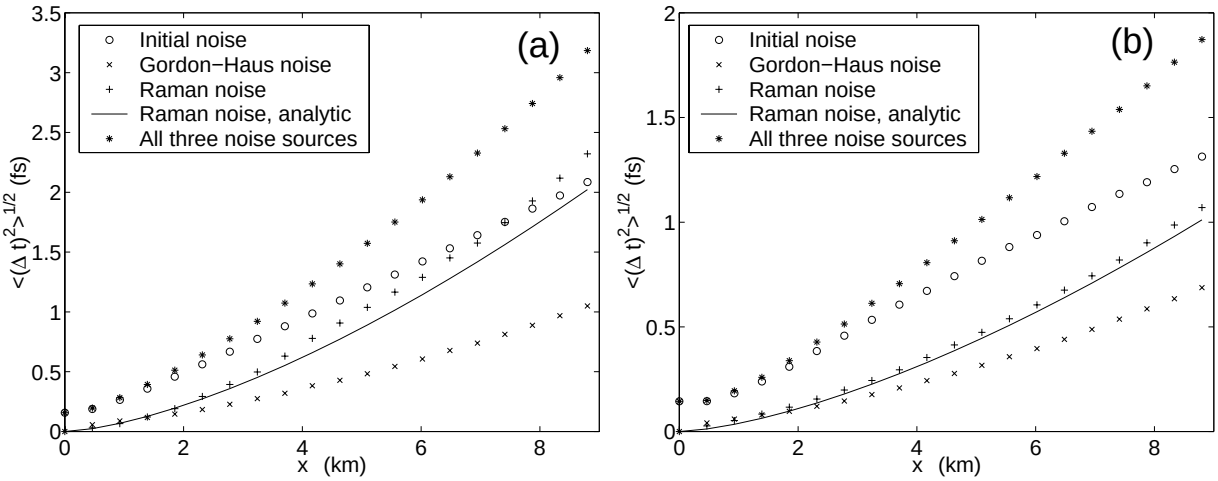

6.7 Numerical results

More precise numerical results for $t_0 = 500fs$ bright and dark solitons are shown in Figs. 6.2(a) and 6.2(b), respectively. The gain and photon number were chosen to be $g = 0.2dB/km$ and $\overline{n} = 4\times10^6$, with $x_0 = 440m$. These values are based on $\mathcal{A} = 40[\mu m]^2$, $k'' = 0.57[ps]^2/km$, and $n_2 = 2.6 \times 10^{-20}[m]^2/W$ for a dispersion-shifted fibre[119, 130, 131]. These numerical calculations used the multiple-Lorentzian model of the Raman response function shown in Fig. 6.1(b), which accurately represents the detailed experimental response function. The initial conditions consist of a coherent laser pulse injected into the fibre. In the Wigner representation, this minimum uncertainty state leads to the initial vacuum fluctuations. We take the initial pulse shape in the anomalous dispersion regime to be a fundamental bright soliton, with $A = 1$ and $V = \theta = q = 0$. Such a soliton can be experimentally realised with a sufficiently intense pulse, which will reshape into a soliton or soliton train. The nonsoliton part of the wave will disperse and any extra solitons will move away at different velocities from the fundamental soliton. The numerical simulation in the normal dispersion regime used two black solitons of opposite phase chirp ($A = \pm1$), so that the field amplitude at either boundary was the same. This phase matching ensured the stability of the numerical algorithm, which assumes periodic boundary conditions.

The position jitter at a given propagation time was calculated by combining the wave-

form with a phase-matched local oscillator pulse that had a linear chirp in amplitude, and integrating the result to give the soliton position. This homodyne measurement involves symmetrically ordered products, so the Wigner representation will give the correct statistics. The variance in soliton position was then calculated from a sample of 1000 trajectories. For this small distance of propagation ($\simeq 10km$), the jitter variance due to the initial noise is twice the Gordon-Haus jitter, but for larger distances, the cubic effects are expected to dominate.

For these short pulses, the Raman jitter dominates the Gordon-Haus jitter (by a factor of two in the bright soliton case) and will continue to do so even for long propagation distances. For short propagation distances, the Gordon-Haus effect is not exactly cubic, because of neglected terms in the perturbation expansion, which give a linear (as opposed to cubic) growth in the jitter variance. However, there are no such terms in the Raman case. The analytic Raman results are also shown in the figures, which show that the approximate formula given in Eq. (6.47) gives a reasonable fit to the numerical data even for these subpicosecond pulses. Using this approximate formula, the relative size of the two effects scales as

$$\frac{\left\langle (\Delta t(x))^2 \right\rangle_R}{\langle (\Delta t(x))^2 \rangle_{GH}} = \frac{6\mathcal{I}(t_0)|k''|}{g{t_0}^2} = \frac{6\mathcal{I}(t_0)}{gx_0} \simeq \frac{8\mathcal{F}(0)}{5gx_0} \qquad \text{(bright)}, \tag{6.48a}$$

$$\frac{\left\langle (\Delta t(x))^2 \right\rangle_R}{\langle (\Delta t(x))^2 \rangle_{GH}} = \frac{3\mathcal{I}(t_0)|k''|}{g{t_0}^2} = \frac{3\mathcal{I}(t_0)}{gx_0} \simeq \frac{4\mathcal{F}(0)}{5gx_0} \qquad \text{(dark)}, \tag{6.48b}$$

where the gain in unnormalised units (chosen to balance the fibre loss of $0.2dB/km$) is $g = \alpha^G/x_0 = 4.6\times10^{-5}m^{-1}$. This equation shows why experiments to date[119, 130, 131], which have used longer pulses ($t_0 > 1ps$) and dispersion-shifted fibre, have not detected the Raman-noise contribution to the jitter. The Raman jitter exceeds the Gordon-Haus jitter for bright solitons with periods $x_0 < 1.5km$. Dark solitons, on the other hand, have an enhanced resistance to the Raman noise, which means that a shorter period is needed before the Raman jitter will become important.

The total jitter, which corresponds to the realistic case where all three noise sources are active, is also shown in Fig. 6.2, and, in the bright soliton case, is about a factor of three larger than the ordinary Gordon-Haus effect, over the propagation distance shown. The physical origin of these quantum noise sources cannot easily be suppressed. The initial vacuum-induced timing jitter is caused by the shot-noise variance in the soliton guiding frequency. The physical origin of the Raman jitter is in frequency shifts due to soliton

phase modulation by the ever-present phonon fields in the fibre medium.

Thus we have seen how the Wigner representation can be used to simulate the quantum dynamics of an interacting bosonic system. The phase-space techniques are particularly suited to this problem for several reasons: the initial state is coherent, the boson self-interactions are relatively weak, and there are many particles per mode. All of these characteristics allow a tractable calculation without recourse to any semiclassical approximations. The use of soliton solutions in this one-dimensional system means that the initial pulse shape is preserved, with the various quantum noise sources varying only the soliton parameters. The pulse then remains coherent indefinitely, maintaining a compact distribution in phase space. In contrast to this situation, in Ch. 7 we turn to a system which has none of these characteristics: the initial state is not coherent, the phase-space distribution is not guaranteed to remain compact and the quantum effects are very large.

Chapter 7

Quantum simulations of evaporatively cooled Bose-Einstein condensates

7.1 Introduction

7.1.1 Important issues

We now undertake to study the quantum dynamics governed by the atom-optics Hamiltonian (Eq. (2.1)) without recourse to the two-mode approximation. Our tools are the quantum optics phase-space techniques introduced in Ch. 6. In the quantum soliton calculations, the initial state is taken to be the coherent output of a laser; in other words a coherent state. However, the precise state of a Bose condensate in an atom trap is currently unknown, as it forms by a dynamical evaporative cooling process, in which particle interactions play a vital role. Also the condensate may never reach equilibrium during its lifetime. Thus to determine the properties of the condensate state, one must study its formation via the cooling process.

The Bose-Einstein condensate that has been produced with trapped atomic samples of neutral atoms[3, 16, 35] is often described as the atomic equivalent to laser light. Condensates are certainly matter waves characterised by what is called the off-diagonal long-range order parameter. Precise measurements of the momentum spread in recent experiments[165] have shown that the long-range order extends over the entire length of the condensate. Other interference and diffraction experiments[2, 4, 74] have also confirmed the existence of this long-range coherence. But this does not mean that the condensate exists in a coherent state, for which it would have to possess coherence of all orders at all

length scales. In fact the presence of interparticle interactions means that the atom density should be anticorrelated at short distances. There have been indirect local measurements that demonstrate the existence of some forms of higher-order coherence[18, 26, 84, 122], but a complete description or confirmation of all the coherence properties of the condensate is not yet available. Indeed, it has been pointed out[135] that these experiments do not measure the true second-order correlation function, and that anticorrelation effects due to interatomic repulsion extend over longer distances than the scattering length a_0. Thus a lack of second-order coherence over short length scales should be measurable in the laboratory.

Possession of coherence implies the existence of a phase. Can a phase be ascribed to a condensate in isolation or only in relation to other condensates? Such issues were addressed in Ch. 3, in the context of measurements of relative phase. There it was shown that even if a condensate in isolation was in a number state, interaction with a second condensate induced a relative phase, thus breaking the symmetry. In contrast, in other condensed-matter systems, such as superfluids and superconductors, which contain many more particles (by a factor of 10^{20} or more), the symmetry-breaking processes occur during the formation of the order parameter when quantum fluctuations are important. During the early stages of order-parameter formation, the condensed part of the system is small and subject to quantum fluctuations. As Bose stimulation populates the condensate, these fluctuations freeze out, to become macroscopic properties of an essentially classical system. In the case of condensates in atom traps, if and how the symmetry breaks during the formation remains an open question. Is there sufficient decoherence that the environment can couple to the condensate order parameter and break the symmetry, or are these condensates closer to number states, in which phase remains undetermined until an actual measurement or other intervention? This process of symmetry breaking has much wider implications than for Bose-condensed systems; it aids the understanding of cosmological evolution and the formation of structure in the early universe[81, 104, 190, 191].

To address important issues such as these about the nature of the condensate, a quantum mechanical simulation of the evaporative cooling process that leads to condensation must be undertaken. The final ground state of this many-body system is the result of a quantum dynamical process which is far from thermal equilibrium. This problem has been approached by many authors using various approximate methods. But to provide a

benchmark for these treatments, and to precisely determine coherence properties, all the quantum effects must be included without approximation.

7.1.2 Evaporative cooling

The production of atomic Bose condensates in recent years has relied upon the development of efficient atom trapping and cooling techniques. In particular, it is the amazing success of evaporative cooling techniques that has enabled condensation in atom traps. Atom evaporation cools far below recoil limit of laser cooling and reduces the temperature by many orders of magnitude without diluting the gas. In this process, the gas is loaded into a magnetic or magneto-optical trap, perhaps at first undergoing some laser cooling[145]. The gas will approximately obey a Bose-Einstein distribution. Atoms in the high-temperature tail of the distribution have enough energy to escape from the trap, and do so taking away more than the average energy per atom. The remaining atoms rethermalise through elastic interatomic collisions, thereby repopulating the upper levels. The temperature is thus lowered, and there is always a supply of hot atoms which can take away more energy.

The evaporative cooling procedure was first developed to cool hydrogen atoms[41, 82] in attempts to produce Bose condensation, but was more successfully applied to alkali-metal gases[37, 103, 143], leading to condensation in rubidium (^{87}Rb)[3] sodium (^{23}Na)[35], and lithium (^{7}Na)[16]. These alkali gases have a larger effective scattering cross section for elastic collisions and so rethermalise at the faster rate necessary to overcome atom loss processes, such as three-body recombination. Evaporative cooling is now a common procedure, with Bose condensates being produced in approximately twenty laboratories worldwide at the time of writing, mainly in ^{87}Rb and including one in hydrogen[59].

This chapter presents the results of using phase-space methods to directly simulate the quantum dynamics of evaporatively cooled condensates. The method enables calculation of the time evolution of system properties. We will review the results for several physical situations, which reveal interesting transient behaviours and also evidence for the spontaneous formation of additional structures, including the evidence for vortices as reported in [46]. This thesis does not attempt to provide conclusive answers to all the issues raised above or to completely characterise the condensate ground state, but rather it summarises the progress that has been made using phase-space techniques. These first attempts of such multimode quantum calculations constitute only the first steps of a comprehensive

investigation into the quantum dynamics of Bose condensates. The methods used here can and must be further developed. Hence we will also discuss the limitations of the method and also possible ways in which it may be improved to extend the results presented here.

In Sec. 7.2 we will overview different approaches to tackling this problem and introduce the phase-space techniques that will be used. Section 7.3 gives the details of the positive-P and Wigner methods, and also describes the physical system modelled in the simulations. Details of the numerical technique are given in Sec. 7.4, as well as the computational constraints that are placed on the range of physical situations that can be modelled. The largest section of this chapter (Sec. 7.5) contains the numerical results, and the thesis concludes in Sec. 7.6 with a discussion of possible future directions.

7.2 Quantum simulations

Many calculations of cooling dynamics have treated the cooling process classically[17, 36, 101], often using the classical transport equation for either a truncated Boltzmann distribution[8] or the more accurate truncated Bose distribution[183, 184]. This leads to the question of how to handle the transition to the final quantum-dominated condensate. It is often assumed to be a canonical ensemble at a temperature estimated from the classical theory with the final ensemble behaviour calculated from the mean-field Gross-Pitaevskii (GP) equation[11, 34, 96, 141]. Mean-field theory can only give semiclassical results, although some authors have included quantum corrections to the mean-field ground state[15, 146, 189] to account for nonclassical features. Others have developed quantum kinetic theories, either through quantum corrections[175] to the GP equations or directly from a master equation[64, 65, 66, 83, 92, 93]. These master-equation approaches are derived in the weak-interaction limit in which the condensate states are taken to be low-lying eigenstates of the trapping potential, populated from a thermal reservoir of excited atoms. The theory of Gardiner et al[63] enables a quantitative prediction of condensate growth that agrees well with experiment. In an alternative approach, Stoof[168] has derived a Fokker-Planck equation for a Wigner function, which can be used to describe the kinetic, coherent and transition regimes of evaporative cooling, for the limits of both weak and strong coupling. All of these quantum approaches make assumptions about how the states evolve in order to achieve tractable calculations of measurable properties.

However, small atom traps are neither in the thermodynamic limit, nor necessarily in a steady state. A first-principles theory is required as a benchmark, for comparisons of these previous approximations. Computing the physics of quantum many-body systems is a notoriously difficult problem; quantum mechanical objects reside in Hilbert space, the dimension of which grows exponentially with the number of particles. Thus even specifying the initial conditions precisely becomes prohibitive for large numbers of particles; a problem which lead Feynman[58] to say:

> Can a quantum system be probabilistically simulated by a classical (probabilistic, I'd assume) universal computer? ...If you take the computer to be the classical kind I've described so far, ... and there're no changes in any laws, and there's no hocus-pocus, the answer is certainly, No![58]

However, the arguments that Feynman propounds to support this claim are not so conclusive. Quantum Monte Carlo (QMC) methods, for example, allow the simulation of quantum systems, albeit in imaginary time. Ceperley[29] revises Feynman's conclusions to prohibit only dynamical calculations in real time:

> The only way around this argument is to give up the possibility of simulating general quantum dynamics and to stick to what is experimentally measurable; arbitrary initial conditions cannot be realised in the laboratory anyway.[29]

The initial conditions are not necessarily the problem. A system may begin in a classical-like state, which requires few numbers to specify, but evolve nonclassical correlations and other quantum features over time. This is precisely what happens in the evaporative cooling of gases: the initial state is at a high temperature and described well by classical distributions; as energy is removed from the system, the gas approaches a critical regime in which quantum effects become important. Moreover, since the number of particles is relatively small, the condensate may never reach equilibrium, thus requiring dynamical simulations to calculate measurable quantities.

Quantum Monte Carlo (QMC) theories[28, 29] can be used to obtain first-principles calculations of thermodynamic quantities even for very strong particle interactions[73], but cannot be applied practically to transient, nonequilibrium situations. They are applicable to the study of superfluidity and other condensed matter phenomena, which occur in isotropic systems in the thermodynamic limit. The extension of QMC methods into the

(real) time domain to allow dynamical calculations has not yet been achieved, although progress to this end has been made with coherent-state operator expansions[21].

Any simulation of evaporative cooling must include all the relevant modes for the trapped atoms, up to the energy levels required for hot atoms to escape. The three-dimensional calculations presented here include more than 3×10^4 relevant modes, with up to 1.0×10^4 atoms present. The quantum state vector therefore has over 10^{40000} components. Keeping track of all these components and calculating the evolution matrix to perform quantum number-state calculations in the time domain is an enormous computational problem, as Feynman emphasised.

But we have seen in Ch. 6 how a many-body multimode quantum system can be simulated, using the phase-space methods that have already proved successful in laser theory[67, 111, 169]. These techniques can handle large numbers of particles, but can also systematically treat departures from classical behaviour. For example, generalised phase-space representations were used to correctly predict quadrature squeezed quantum soliton dynamics in optical fibres[24, 50], which as we saw in Ch. 6 are described by nearly identical quantum equations (Eq. (6.3)) to those used in atom-atom interaction studies[163]. The coherent-state (positive-P) phase-space equations are exactly equivalent to the relevant quantum equations, provided that phase-space boundary terms[1] vanish. They have the advantage that they are computationally tractable for the large Hilbert spaces typical of Bose condensation experiments. Techniques of this sort may provide a way of extending QMC methods[28, 29] into the time domain.

7.3 Phase-space equations

The model that we will use includes the usual nonrelativistic Hamiltonian for neutral atoms, in a trap $V(\mathbf{x})$, interacting via a potential $U(\mathbf{x})$, in $d = 2$ or $d = 3$ dimensions:

$$\hat{H} = \int d^d\mathbf{x}\Bigg[\frac{\hbar^2}{2m}\nabla\hat{\psi}^\dagger(\mathbf{x})\nabla\hat{\psi}(\mathbf{x}) + V(\mathbf{x})\hat{\psi}^\dagger(\mathbf{x})\hat{\psi}(\mathbf{x}) + \hat{\psi}^\dagger(\mathbf{x})\hat{R}(\mathbf{x}) + \hat{\psi}(\mathbf{x})\hat{R}^\dagger(\mathbf{x}) + \frac{1}{2}\int d^d\mathbf{y}U(\mathbf{x}-\mathbf{y})\hat{\psi}^\dagger(\mathbf{x})\hat{\psi}^\dagger(\mathbf{y})\hat{\psi}(\mathbf{y})\hat{\psi}(\mathbf{x})\Bigg]. \quad (7.1)$$

Where $\hat{\psi}^\dagger$ and $\hat{\psi}$ are the bosonic many-body creation and annihilation operators for atoms at position $\mathbf{x}$. Here $\hat{R}(\mathbf{x})$ represents a localised absorber that removes the neutral atoms;

[1] A careful treatment of this problem of boundary terms appears in [60]. See also [163].

for example, via collisions with foreign atoms, or at the location of the 'RF-scalpel' resonance, which is used to accelerate evaporative cooling[17]. We expand $\hat{\psi}$ using free-field modes with a momentum cutoff $k_{\max}$:

$$\hat{\psi}(t,x) = \frac{1}{\sqrt{(2\pi)^3 V}} \sum_{|\mathbf{k}|\leq k_{\max}} e^{i\mathbf{k}\cdot\mathbf{x}} \hat{a}_k(t). \tag{7.2}$$

Provided that $k_{\max} \ll a_0^{-1}$, where a_0 is the s-wave scattering length, $U(\mathbf{x}-\mathbf{y})$ can be replaced by the renormalised pseudopotential $U_0\delta^d(\mathbf{x}-\mathbf{y})$, where $U_0 = 4\pi a_0\hbar^2/m$ in three dimensions[107]. In two dimensions, U_0 is defined similarly but with a factor ξ_0 in the denominator, which corresponds to the effective spatial extent of the condensate in the third direction. This factor is of the order of the lattice spacing in the simulation, and is chosen to be equal to x_0, the scaling length.

7.3.1 Positive-P technique

The resulting quantum time evolution for the density matrix $\hat{\rho}$ can be solved by expanding into a coherent-state basis, and then transforming to an equivalent set of equations for the coherent state amplitudes. In the positive-P representation[60], $\hat{\rho}$ is expanded into off-diagonal coherent state projection operators:

$$\hat{\rho} = \int P(\psi_1,\psi_2) \frac{|\psi_1\rangle\langle\psi_2|}{\langle\psi_2|\psi_1\rangle} \mathcal{D}\psi_1 \mathcal{D}\psi_2, \tag{7.3}$$

where ψ_1 and ψ_2 are the coherent-state amplitudes, and $\mathcal{D}\psi_1$ and $\mathcal{D}\psi_2$ are the functional integration measures. $P(\psi_1,\psi_2)$ is a positive distribution function which exists for all density matrices. When the boundary terms in the integration vanish, P is governed by a Fokker-Planck equation which can be converted to Langevin equations[2] describing stochastic trajectories for the phase-space variables.

The phase-space equations can be expressed as two coupled complex stochastic partial differential equations for ψ_1 and ψ_2:

$$i\hbar\frac{\partial}{\partial t}\psi_j(t,\mathbf{x}) = \Big[\frac{-\hbar^2}{2m}\nabla^2 + V(t,\mathbf{x}) + U_0\psi_j(t,\mathbf{x})\psi^*_{3-j}(t,\mathbf{x}) + \sqrt{i\hbar U_0}\xi_j(t,\mathbf{x}) - \frac{i\hbar}{2}\Gamma(t,\mathbf{x})\Big]\psi_j(t,\mathbf{x}), \tag{7.4}$$

[2] See Appendix A.

where $j \in \{1, 2\}$. These equations can be simulated numerically[176] in one, two or three transverse dimensions, with either attractive or repulsive potentials. Several different evaporation procedures are possible. These involve implementing different spatial profiles for the trapping potential and the modulated absorption. The time dependence of these potentials can also vary for the different schemes. We shall choose from these forms:

$$V_1(t, \mathbf{x}) = V_{\max}(t)\Sigma_{j=1}^{d}[\sin(\pi x_j/L_j)]^2\,, \tag{7.5a}$$

$$V_2(t, \mathbf{x}) = V_{\max}(t)\Sigma_{j=1}^{d}\left(2x_j/L_j\right)^2\,, \tag{7.5b}$$

$$V_3(t, \mathbf{x}) = V_{\max}(t)\sqrt[4]{\Sigma_{j=1}^{d}\left(2x_j/L_j\right)^8}\,. \tag{7.5c}$$

Here $V_{\max}(t) = V_0(t)(1 - \alpha\ \min\{t, t_{\max}\})$, where α is typically the inverse of the total simulation time. The trap width is L_j in the j-th direction, so that $-L_j/2 \le x_j \le L_j/2$. These forms correspond to the potential height being swept downwards linearly in time, thus successively removing cooler and cooler subpopulations of atoms. The sinusoidal shape of the V_1 is chosen so that the trap is harmonic near the centre of the trap and smoothly approaches a maximum near the edge. Figures 7.1(a) and 7.1(b) show a two-dimensional cross section of V_1 and V_3 respectively.

The corresponding absorption profiles $\Gamma_i(\mathbf{x})$ are

$$\Gamma_1(\mathbf{x}) = \Gamma_{\max}\Sigma_{j=1}^{d}[\sin(\pi x_j/L_j)]^{50}\,, \tag{7.6a}$$

$$\Gamma_2(\mathbf{x}) = \Gamma_{\max}\Sigma_{j=1}^{d}\left(2x_j/L_j\right)^{50}\,, \tag{7.6b}$$

$$\Gamma_3(\mathbf{x}) = \Gamma_{\max}\sqrt[4]{\Sigma_{j=1}^{d}\left(2x_j/L_j\right)^{200}}\,. \tag{7.6c}$$

For this situation, atoms are absorbed when they reach regions of large $\Gamma(\mathbf{x})$, located near the trap edges. Γ_1 and Γ_3 are illustrated in Figs. 7.1 (c&d).

An alternative strategy, which perhaps better reflects the procedure followed in current experiments, is to keep the trapping potential constant and gradually bring in the absorption profile toward the centre of the trap. This corresponds to the radio-frequency (RF) scalpel, or 'circle of death', tuned to flip the spin of the atoms and thus transfer them from a trapped to an untrapped state. For the nonsinusoidal potentials, the scalpels in the simulations are

$$\Gamma_i(t, \mathbf{x}) = \Gamma_{\max}e^{-50(r_i(\mathbf{x})-(1-\alpha(t))L/2)^2}, \qquad r \in \{2, 3\}, \tag{7.7a}$$

$$r_2(\mathbf{x}) = \sqrt{\Sigma_{j=1}^{d}\left(2x_j/L_j\right)^2}, \tag{7.7b}$$

$$r_3(\mathbf{x}) = \sqrt[8]{\Sigma_{j=1}^{d}\left(2x_j/L_j\right)^8}, \tag{7.7c}$$

Figure 7.1: *Two-dimensional cross sections of the potential and absorption profiles. The sinusoidal trap V_1 and the quadratic trap V_3 are shown in (a) and (b) respectively, while the corresponding absorption profiles are shown in (c) and (d).*

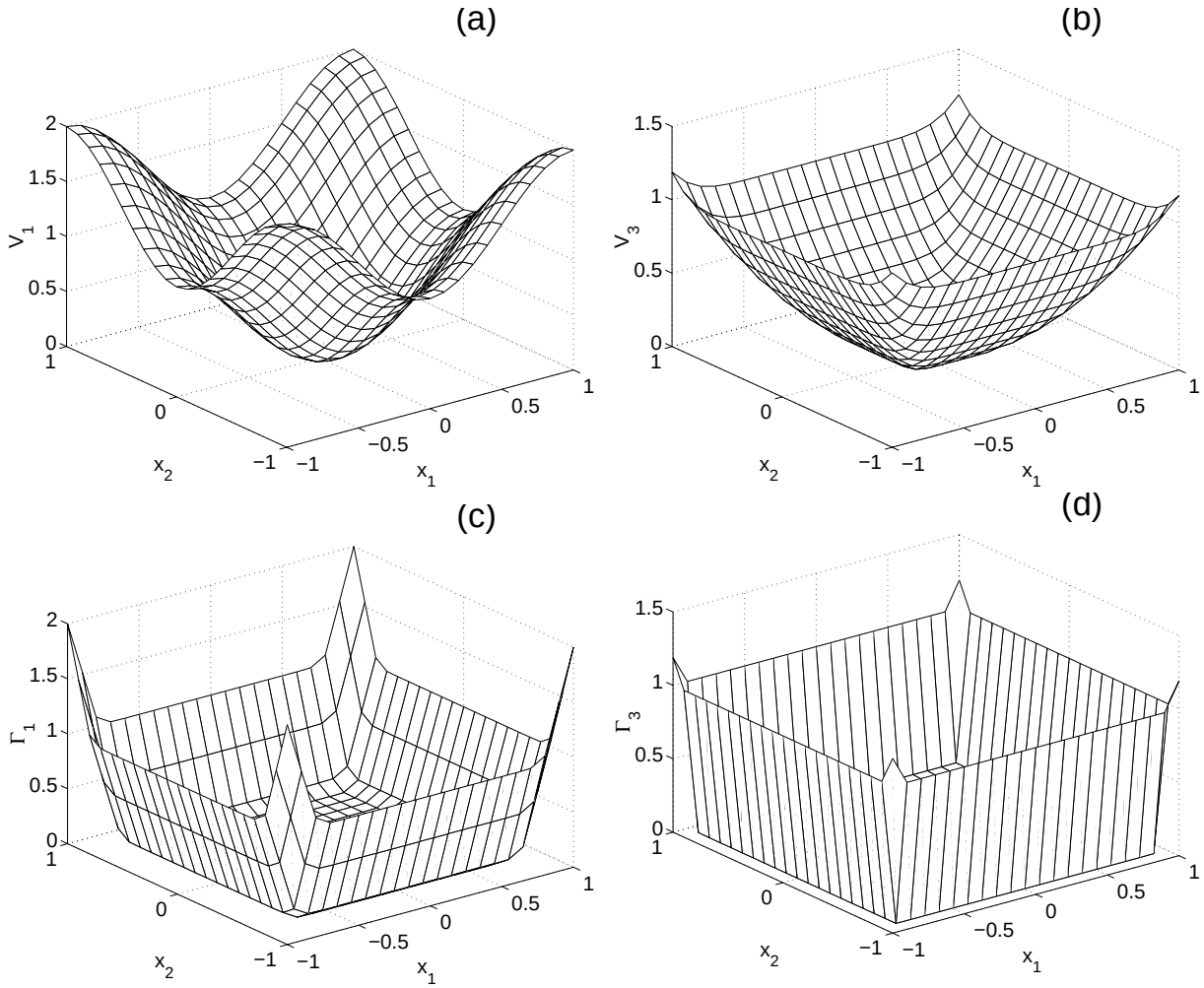

where $\alpha(t) = \alpha \min\{t, t_{\max}\}$ and $L = \min\{L_j\}$. The advantage of this method is that the spatial density of atoms is kept high, which aids the thermalisation necessary for evaporative cooling.

In deterministic limit, the positive-P equations (Eq. (7.4)) correspond precisely to the well-known Gross-Pitaevskii (GP) equation, with the addition of a coefficient $\Gamma(\mathbf{x})$ for the absorption of atoms by the reservoirs. Quantum effects come from the spontaneous collision terms ξ_j, which are real Gaussian stochastic fields, with correlations:

$$\left\langle \xi_1(s,\mathbf{x})\xi_2(t,\mathbf{y})\right\rangle = \delta_{ij}\delta(s-t)\delta^d(\mathbf{x}-\mathbf{y})\,. \tag{7.8}$$

Unlike the Wigner equation for phase-space evolution (Eq. (6.11)), no explicit vacuum noise in the initial conditions is required. This is because the positive-P variables correspond to normally ordered operator products, in which vacuum contributions do not explicitly appear. The quantum correlations that can be calculated include $n(\mathbf{k}) = \left\langle \psi_1(\mathbf{k})\psi_2^*(\mathbf{k})\right\rangle$, which gives the observed momentum distribution.

7.3.2 Wigner technique

An alternative strategy to generate phase-space equations is to use the Wigner function, as in Ch. 6. The Wigner technique allows the direct calculation of symmetrically ordered products, in which a vacuum contribution explicitly appears. The disadvantage of using the Wigner function is that it is not guaranteed to be positive, with higher-order terms appearing in the Fokker-Planck equation. Once these terms have been removed, the Wigner function is constrained to be positive and Langevin equations can be generated. Thus the Wigner technique is not exact, and may produce incorrect results at long times, especially for low occupation numbers. However, it does provide a good check on the positive-P results.

With the higher-order terms removed, the resultant phase-space evolution is given by

$$i\hbar\frac{\partial}{\partial t}\psi(t,\mathbf{x}) = \left[\frac{-\hbar^2}{2m}\nabla^2 + V(t,\mathbf{x}) - \frac{i\hbar}{2}\Gamma(t,\mathbf{x}) + U_0\psi(t,\mathbf{x})\psi^*(t,\mathbf{x})\right]\psi(t,\mathbf{x}) + \frac{i\hbar}{\sqrt{2}}\sqrt{\Gamma(\mathbf{x})}\xi(t,\mathbf{x})\,, \tag{7.9}$$

where $\xi(t,\mathbf{x})$ is a complex delta-correlated stochastic field:

$$\left\langle \xi(s,\mathbf{x})\xi^*(t,\mathbf{y})\right\rangle = \delta(s-t)\delta^d(\mathbf{x}-\mathbf{y})\,. \tag{7.10}$$

We have now only one phase-space equation in which the quantum effects enter as vacuum fluctuations in the initial conditions:

$$\left\langle \Delta\psi(0,\mathbf{x})\Delta\psi^*(0,\mathbf{y})\right\rangle = \frac{1}{2}\delta^d(\mathbf{x}-\mathbf{y})\,. \tag{7.11}$$

The effect of the stochastic field $\xi(t,\mathbf{x})$ is to maintain the vacuum noise that would otherwise be damped by the absorption term.

Unless otherwise indicated, all results and figures in this chapter pertain to the positive-P calculations.

7.4 Computational method

In order to generate numerical solutions to the phase-space equations, scaled variables can be introduced: $\tau = t/t_0$, $\mathbf{z} = \mathbf{x}/x_0$, $a_j = \psi_j x_0^{d/2}$ and $\zeta_j = \xi_j t_0^{1/2} x_0^{d/2}$. The positive-$P$ equations, in scaled form, become

$$\frac{\partial}{\partial\tau}a_j(\tau,\mathbf{z}) = \left[\frac{i}{2}\nabla^2 - iu_0 a_j(\tau,\mathbf{z})a^*_{3-j}(\tau,\mathbf{z}) - iv(\tau,\mathbf{z}) - \gamma(\tau,\mathbf{z}) - i\sqrt{iu_0}\xi_j(t,\mathbf{z})\right]a_j(\tau,\mathbf{z})\,, \tag{7.12}$$

where $v(\mathbf{z}) = t_0 V(\mathbf{x})/\hbar$, $\gamma(\mathbf{z}) = t_0\gamma(\mathbf{x})/2$ and $u_0 = U_0 t_0/(\hbar x_0^d)$. Here x_0 is set to $x_0 = (\hbar t_0/m)^{1/2}$.

In the simulations, these equations were discretised and propagated forward using a split-step Fourier method on a transverse lattice z_i of l^d sites. For most of the simulations, $l = 32$. The deterministic dispersion and potential/absorption terms in Eq. (7.12) were incorporated into exponential propagators, $U_{k-\mathrm{prop}}(k_i,\Delta\tau_k)$ and $U_{x-\mathrm{prop}}(z_i,\Delta\tau_k)$ respectively, with the dispersion term applied in Fourier space. The nonlinear and stochastic contribution to the increment $\Delta a_{\mathrm{NL}}(a(z_i,\tau_k),\Delta\tau_k)$ were applied in co-ordinate space using an iterative semi-implicit method, which ensures stability and convergence for stiff nonlinear equations with stochastic terms[49]. In this algorithm, the field value at τ_{k+1} is

calculated from $a(\tau_k)$ according to

$$
\begin{aligned}
a^{(a)} &= U_{k-\mathrm{prop}}(\Delta\tau_k/2)a(\tau_k) && \text{(7.13a)}\\
a^{(0)} &= U_{x-\mathrm{prop}}(\Delta\tau_k/2)a^{(a)}(\tau_k) && \text{(7.13b)}\\
&\cdots \\
a^{(m)} &= a^{(0)} + \frac{1}{2}\Delta a_{\mathrm{NL}}(a^{(m-1)}, \Delta\tau_k) && \text{(7.13c)}\\
&\cdots \\
a^{(b)} &= U_{x-\mathrm{prop}}(\Delta\tau_k/2)\left(a^{(m)} + \frac{1}{2}\Delta a_{\mathrm{NL}}(a^{(m)}, \Delta\tau_k)\right) && \text{(7.13d)}\\
a(\tau_{k+1}) &= U_{k-\mathrm{prop}}(\Delta\tau_k/2)\Delta a^{(b)} && \text{(7.13e)}\\
& && \text{(7.13f)}
\end{aligned}
$$

where the transverse dependence (on z_i, k_i) has been suppressed.

The stochastic equations (Eqs. (7.4) and (7.9)) derived from a Fokker-Planck equation are to be interpreted in the Ito sense, with the increments evaluated at the beginning of the time interval. An implicit integration method, such as used here, implements a Stratonovich equation. However, the only difference between the two equations in this case is a phase factor. This does not affect intensity moments, which are the quantities of interest.

An adaptive time-step routine was used, in which the time step was sensitive to the size of the nonlinear contribution to the increment. Hence the time step generally increased as atoms were lost out of the trap. The minimum time step was typically $\sim t_0/1000$, with all calculations being repeated at half the time step (and noise sampled from the same process with twice the resolution[176]), to check numerical convergence.

The Fourier method used here implies periodic boundary conditions, which are not part of the physical situation being modelled. The spatially modulated absorption must be large enough near the boundary to prevent any part of the fields a_j from reaching the edge and reappearing on the other side of the simulation window. A sinc filter was also incorporated into the $U_{k-\mathrm{prop}}$ to remove any high frequency components caused by mismatch near the boundary.

7.4.1 Constraints and limitations

In practical computations, it is necessary to consider rather small traps. This is because the numerical lattice spacing used to sample the stochastic fields in x-space must be of order $\Delta x = 1/k_{\max}$, where $k_{\max}$ is the largest ordinary momentum considered in the problem. However, the value of the corresponding kinetic energy, $E_K = (\hbar k_{\max})^2/2m$, must be large enough to allow energetic atoms to escape over the potential barrier of the trap; otherwise no cooling can take place. This sets an upper bound on the lattice spacing and hence on the maximum trap size, which depends on the number of lattice points that can be computed.

The available lattice sizes used here were 32^3 points in three dimensions and 64^2 points in two dimensions. With this limit, and parameter values similar to those used in the experiments, the available trap sizes that can be treated are of the order of micron dimensions. These are smaller than those used currently, although traps of this type are quite feasible. The other possibility within the constraints is to use a trap which is of larger dimensions but lower in potential height. For this type of trap, which was simulated here, the width was $L_j = 10\mu m$, with a maximum potential height of $V_{\max}/k_B = 1.9 \times 10^{-7} K$, and an initial temperature of $T_0 = 2.4 \times 10^{-7} K$.

A further limitation is that the initial density must be such that $\langle n(k) \rangle \lesssim 1$; otherwise the gas would already be Bose condensed, with many particles in particular modes. This places a limit on the number of atoms which can simulated, if we assume an initially noncondensed grand canonical ensemble of (approximately) noninteracting atoms. There were initially around 500 atoms in the two-dimensional simulations presented here, and $10,000$ in the three-dimensional case. These correspond to atomic densities of $n_0 = 5.0 \times 10^{12}/m^2$ and $n_0 = 1.0 \times 10^{19}/m^3$ respectively.

However not all the lattice points that atoms can occupy are contained within the trap. Necessarily, some of the lattice points correspond to untrapped sites. The proportion of lattice sites that lie within the trap depends on the trapping potential. For the sinusoidal trap in three dimensions, up to half the sites lie outside the trap, a result of embedding an approximately spherical potential within a cubic lattice structure. The nonspherical trap V_3 defined in Eq. (7.5) overcomes this problem and confines more atoms. But in this case the larger nonlinear terms, coupled with the stochastic terms, drive large excursions into phase space at long times. This causes the fields a_j to vary significantly from one trajectory

to the next, thus increasing the sampling error in the calculations of the moments. The numerical algorithm may still converge, although the rapidly changing fields at long times do preclude fast simulations.

The underlying problem here is with the phase-space representation. Highly nonclassical states are not well represented by the coherent states by which the positive-P expansion is defined: off-diagonal elements, where ψ_1 differs from ψ_2, become large and the state can no longer be mapped onto a compact region of phase space. In fact, for longer times the distribution may not vanish at the phase-space boundaries, leading to a breakdown of the positive-P method. Other basis states may be used for the expansion, but the resulting phase-space equations will not be so simple as Eq. (7.4), if they exist at all. The upshot is that for the positive-P technique to give a tractable numerical problem, relatively weakly interacting atoms must be considered, with scattering lengths much less than the usual s-wave scattering lengths for the alkali-metal atoms. A consequence of the weak nonlinearity is that, as revealed in the simulations, the dominant mechanism of condensate growth is spontaneous emission into the ground state, rather than the stimulated emission as found in other studies[63].

7.5 Numerical results

For the small-trap parameters used in the simulations, the effect of the stochastic terms on the dynamics is very large. In fact the quantum fluctuations that these stochastic terms introduce are much larger than the initial thermal fluctuations, such that the initial features of the distribution do not persist. This means that the choice of the initial state of the system is not critical, and also that in order to determine properties of the final quantum ground state of the system, the stochastic terms are vital. To illustrate this, we can remove the quantum noise terms, so that the simulations are of the GP equation, with initial conditions corresponding to a thermal state. For our parameters, these simulations did not show strong Bose condensation effects, in contrast to the fully quantum-mechanical simulations. This demonstrates the highly nonclassical nature of the early stages of Bose condensation, in which spontaneous transitions to the lowest energy states clearly play an important role.

For the simulations shown in the figures, $a_0 = 0.6nm$ and the mass, corresponding

Table 7.1: *Unnormalised and normalised parameters for the evaporated system.*

Quantity	Value	Description
a_0	$0.60nm$	s-wave scattering length
m	$1.45 \times 10^{-25}kg$	atomic mass
$U_0^{(3)}$	$5.8 \times 10^{-52}Jm^3$	particle-interaction strength
L_j	$10\mu m$	trap width
T_0	$2.4 \times 10^{-7}K$	initial temperature
μ/k_B	$1.4 \times 10^{-7}K$	initial chemical potential
$V_{\max}/k_B$	$1.93 \times 10^{-7}K$	initial potential height
$\Gamma_{\max}$	$1.27 \times 10^4 s^{-1}$	atomic damping rate
t_0	$0.79ms$	time scale factor
x_0	$0.76\mu m$	length scale factor
k_0	$1.32 \times 10^6 m^{-1}$	wave-number scale factor
$k_{\max}$	$1.6 \times 10^6 m^{-1}$	maximum wave number
$v_{\max}$	20	normalised initial potential height
$\gamma_{\max}$	5	normalised damping rate
u_0	0.01	normalised interaction strength
α	0.01	ramping rate

to rubidium, is $m = 1.5 \times 10^{-25} kg$, with the other parameters as in Table 7.1. These parameters correspond to relatively weakly interacting atoms, in order to reduce the sampling error, discussed above, which increases rapidly with longer times and larger coupling constants. All results are plotted in normalised units, with space scaled by $x_0 = 0.76\mu m$, and time scaled by $t_0 = 0.79ms$.

7.5.1 Evolution of momentum distribution

Figure 7.2 shows individual trajectories for the evolution of the stochastic fields using the sinusoidal profiles for the potential (V_1) and absorption (Γ_1). The trajectories correspond to (the real part of) the product $n(k) = a_1(k)a_2^*(k)$, which when averaged gives the observed momentum distribution. Figure 7.2(a) shows the result of including the nonlinear term, but without the noise terms, which corresponds to a solution of the GP equation. The final momentum distribution is small, with no evidence of condensation, and is almost identical to the case where there are no atom interactions at all. This contrasts with the case shown in Figs. 7.2(b&c), which contains all noise terms and shows a final atom density that is quite narrow and tall, with a width corresponding to a temperature below the critical temperature for condensation. The peak final momentum state population is much greater than one and also greater than that of the initial conditions. Thus it appears that spontaneous emission into what will be the condensate mode is much more important, for these parameters and over this timescale, than the stimulated effect due to the nonlinear term.

This condensation effect is more pronounced in the three-dimensional case (Fig. 7.2(b&c)) than in two dimensions (Fig. 7.2(d)), showing that the evaporative cooling process is more efficient with the extra degree of freedom and the greater number of atoms that are present.

As is usual in quantum mechanics, only the ensemble averages of the simulations have an operational meaning. Thus, while individual stochastic realisations have a definite coherent phase, these phases are different for distinct stochastic realisations; the ensemble average has no absolute phase information. The average evolution of a two-dimensional condensate is shown in Fig. 7.3(a). Since this is an ensemble average, it corresponds to the measurable momentum distribution. In this case, the condensate is only weakly occupied.

Figure 7.3(b) shows the average over several three-dimensional trajectories. The final peak momentum density is a lot lower than in individual paths. Since the condensate does

Figure 7.2: *Single-trajectory simulations of a three-dimensional Bose condensate, showing the atom density $n(k)$ Fourier space versus time. Time has been normalised by $t_0 = 0.79ms$ and momentum by $k_0 = 1.32 \times 10^6 m^{-1}$. The evolution in time of $n(k)$ along one dimension is shown in (a) (b) and (d), while (c) gives a two-dimensional cross section at time $t = 100t_0$. In (a), the stochastic terms are absent to give a solution to the GP equation, while (b) and (c) show the results of the full $+P$ equations. For comparison, (d) shows the result for a two-dimensional simulation.*

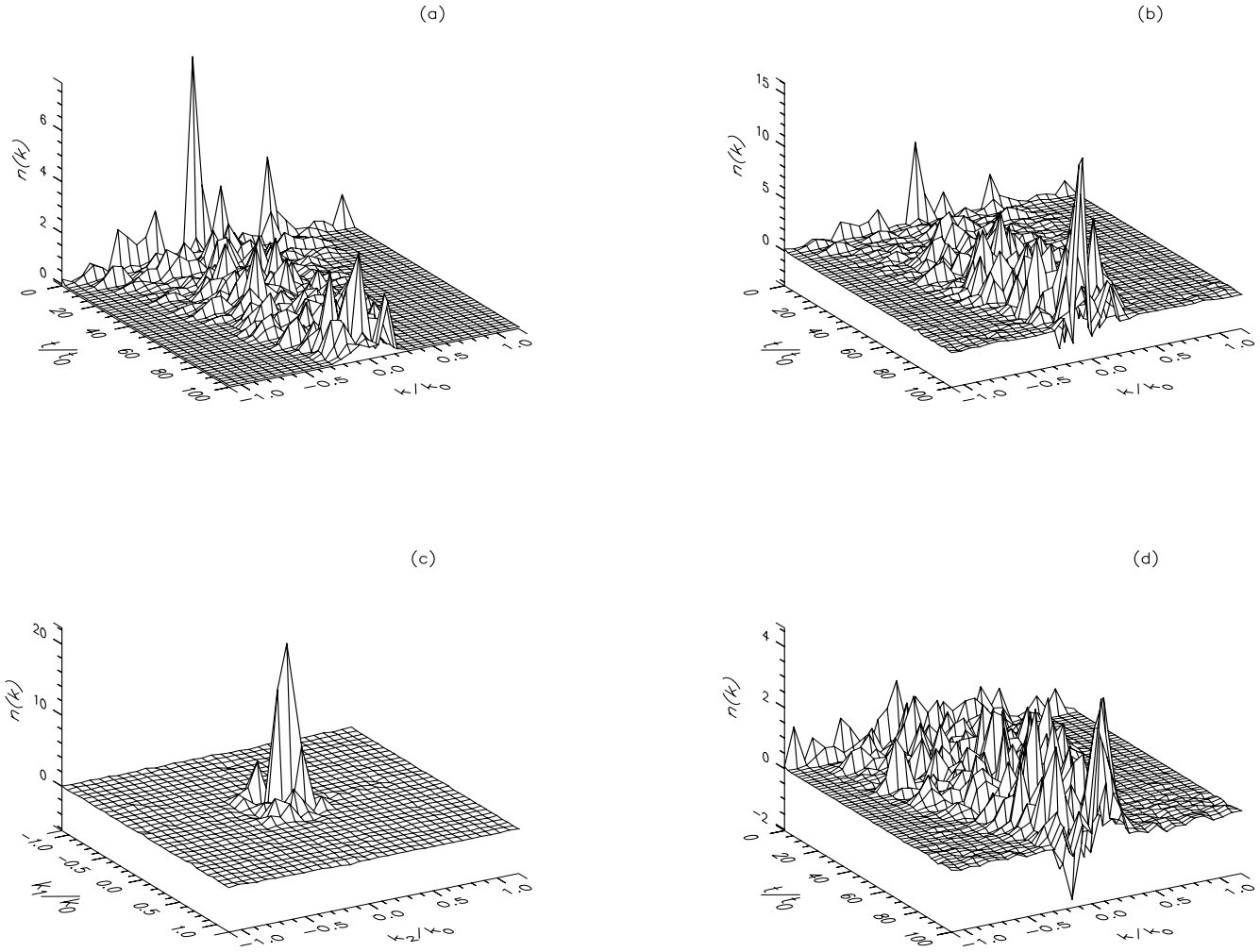

Figure 7.3: *Simulation of (a) a two-dimensional and (b) a three-dimensional Bose condensate, showing the ensemble average (55 paths and 15 paths, respectively) atom density* $\langle n(k) \rangle$ *along one dimension in Fourier space versus time. Time has been normalised by* $t_0 = 0.79ms$ *and momentum by* $k_0 = 1.32 \times 10^6 m^{-1}$.

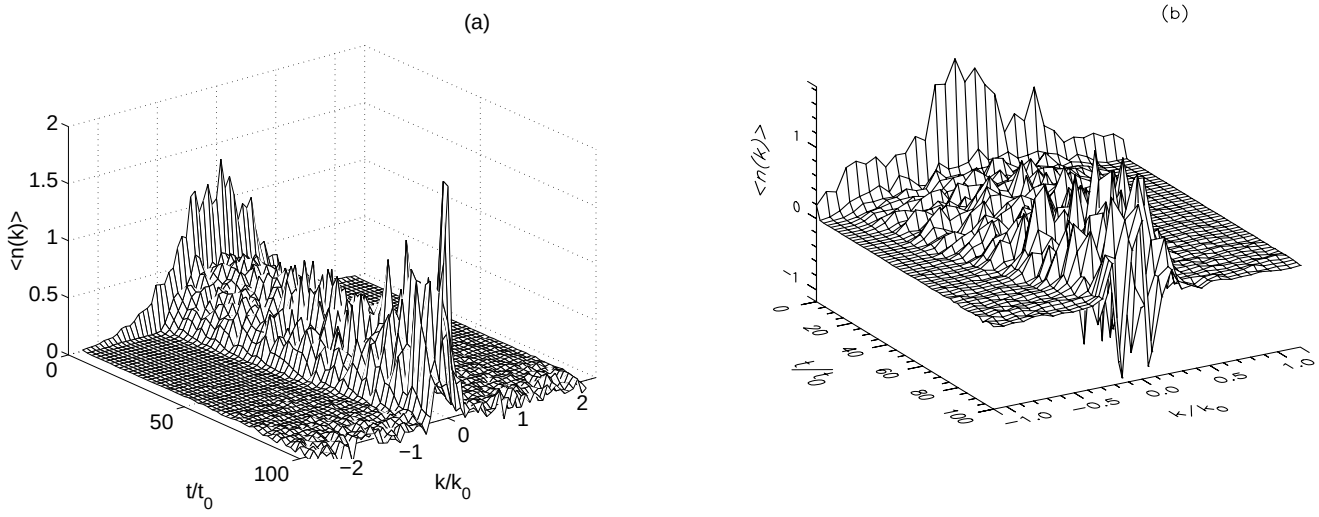

not have to form in the ground state, the Bose-condensed peaks that occur at different momentum values in single runs are averaged out in the overall ensemble. This effect is particularly pronounced in three dimensions, with the extra degree of freedom. A more useful indication of condensation is given by the following measure of phase-space confinement:

$$\mathcal{C} = \frac{\int d^3k \langle \psi_1(\mathbf{k}) \psi_1(\mathbf{k}) \psi_2^*(\mathbf{k}) \psi_2^*(\mathbf{k}) \rangle}{\left(\int d^3k \langle \psi_1(\mathbf{k}) \psi_2^*(\mathbf{k}) \rangle \right)^2 x_0^3}. \tag{7.14}$$

This higher-order correlation function is the quantum analogue of the participation ratio defined by Hall[75]. It offers an advantage over the variance in that for a multipeaked distribution, it is largely insensitive to the relative positions of the peaks. For example, with a one-dimensional distribution comprised of a sum of nonoverlapping Gaussians

$$P(x) = \sum_i A_i e^{-\frac{(x-x_i)^2}{2\sigma_i^2}}, \tag{7.15}$$

the unnormalised $\mathcal{C}$ parameter

$$\tilde{\mathcal{C}} = \frac{\int dx P^2(x)}{\left(\int dx P(x) \right)^2} \simeq \frac{\sum_i A_i^2 \sigma_i}{2\sqrt{\pi} \left(\sum_i A_i \sigma_i \right)^2}, \tag{7.16}$$

does not depend on x_i, to leading order, whereas the variance does:

$$\sigma_P^2 = \frac{\sum_{i,j} A_i A_j \sigma_i \sigma_j (\sigma_i^2 + x_i^2 - x_i x_j)}{\left(\sum_i A_i \sigma_i \right)^2}. \tag{7.17}$$

Figure 7.4: *Simulation of a three-dimensional Bose condensate, showing the ensemble average evolution of the confinement parameter $\mathcal{C}$. The continuous line is calculated from the positive-P equations (69 paths) and the dashed line from the Wigner equation (60 paths). The dotted line is the GP result (22 paths). The time axis has been normalised by $t_0 = 0.79ms$.*

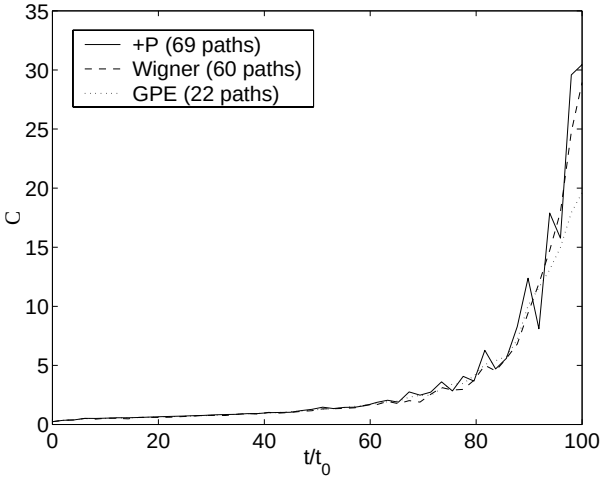

Figure (7.4) shows the evolution of $\mathcal{C}$ calculated from 69 runs of the three-dimensional simulation. The sharp rise near $t = 100t_0$ is a strong indication of condensation occurring at this point. On the same figure, we also see the GP result, which does not show such a sharp increase.

7.5.2 Wigner results

In the Wigner representation, products like $\langle aa^* \rangle$ do not directly correspond to normally ordered operator products such as the atom density. Calculations of aa^* from individual trajectories in themselves reveal little information about the evolving state: because the occupation number of each mode is small ($\langle n(k) \rangle \lesssim 1$) initially, the vacuum noise in each mode is relatively large, and it is only when the average is taken that the signal emerges from the noise. Thus only ensemble average results are shown here.

Figure 7.4 shows the evolution of the $\mathcal{C}$ parameter, which is calculated in the Wigner representation by:

$$\mathcal{C} = \frac{\int d^3k \left(\langle \psi(\mathbf{k})\psi(\mathbf{k})\psi^*(\mathbf{k})\psi^*(\mathbf{k}) \rangle - 2\langle \psi(\mathbf{k})\psi^*(\mathbf{k}) \rangle + \frac{1}{2} \right)}{\left(\int d^3k \langle \psi(\mathbf{k})\psi^*(\mathbf{k}) \rangle - \frac{1}{2} \right)^2 x_0^3}. \tag{7.18}$$

A comparison of the two results shown in Fig. 7.4 confirms that using the positive-P and Wigner techniques gives the same physical results. The difference between the two

curves is well accounted for by the statistical error that arises from using a finite number of trajectories in the ensemble averages.

7.5.3 Angular momentum and vortices

For the finite-size condensates in atom traps, just as the final ground state is not expected to be precisely the zero momentum eigenstate, so too such condensates are not constrained to fall into the $L = 0$ angular momentum eigenstate. Individual atoms in the initial distribution have arbitrary angular momenta, as do escaping atoms. Central limit theorem arguments show that the variance in angular momentum will scale approximately as $\langle \hat{L}^2 \rangle \propto N$. Thus we can expect that each trapped condensate should have angular momentum, unless constrained by the trap geometry. The angular momentum can be carried either by quasiparticles or vortices[108, 140]. A j-th order vortex has momentum $L = j\hbar N/m$ and therefore cannot form spontaneously in the thermodynamic limit of large N. However, recent work [5] has suggested that a vortex may form spontaneously when a condensate is quenched suddenly below the critical temperature. For small condensates, a spontaneous $j = \pm 1$ vortex may be quite likely, even without this rapid quench.

Vortices may also form as collective excitations of the mean field in response to external perturbations[39, 53, 112, 113, 160]. Proposals in the literature for imparting angular momentum to the condensate include: stirring the condensate with a detuned laser beam or some other narrow potential[20]; coherent coupling, via Raman transitions, to a laser pulse of nonzero angular momentum[115, 116, 117]; inducing a topological phase through the Aharonov-Casher effect[144] by inserting a conducting wire through a central hole in the condensate; and by rotating the trap above a critical frequency Ω_c[19]. Here we shall consider the possibility of vortices forming spontaneously in the condensate through the process of evaporative cooling, without external intervention. The quantised circular motion evident in the dynamical calculations presented here may only be transitive, and may not persist in the final condensed state. Stability studies[147, 149] have shown that vortices cannot persist within a stationary condensate that occupies a simply connected region of space, because of the relatively large vortex core[57]. Unless the condensate is rotating at a rate greater than the critical frequency Ω_c, the vortex core will migrate to the edge of the condensate and vanish[56]. The vortex can also be forced to remain by pinning it with a narrow detuned laser beam[90], or some feature of the trap geometry,

such as in a toroidal trap.

Experimental investigation of vortex states in condensates not only requires the generation of vortices, but also their detection, which is not a trivial task: the dip in density that characterises the vortex core may be smaller than what can be resolved by available imaging techniques. Also, a vortex core may form along any direction in a three-dimensional geometry. Instead of searching an intensity variation due the vortex core, one may observe the interference pattern between two overlapping condensates. A phase slip in the fringes would reveal the presence of a vortex core in either of the condensates[12, 170].

At the time of writing, vortices have only recently been created and detected in the laboratory, in an experiment in which the problems of producing, stabilising and detecting vortices are overcome by using a two-component condensate[118]. In this experiment, vortices were created by coherently coupling the two components by a circulating laser beam. The components are distinguished by an internal state, with the component containing the vortex forming a ring around the other component; the interior condensate can be used to pin the vortex core of the rotating component. An interferogram constructed by coherent transfer between the two components measures the phase variation around the ring and hence its angular momentum.

The angular momentum of a condensate is a quantitative measure of the presence of vortices, and it is now an experimentally accessible quantity. Thus in the numerical simulations presented here, vortices are detected by searching for macroscopic occupation of particular angular momentum modes: we transform the spatial lattice into a lattice which uses the angular momentum eigenstates as a basis set. The two-dimensional results are obtained by integrating the spatial profile over orthogonal modes with corresponding field operators $\hat{\Psi}_{jn}$:

$$\hat{\Psi}_{jn} = \int_V d^d x \hat{\psi}(\mathbf{x}) R_n(r(\mathbf{x})) Y_j(\theta(\mathbf{x}), \phi(\mathbf{x})), \tag{7.19}$$

which have the commutation relations

$$\left[\hat{\Psi}_{jn}, \hat{\Psi}^\dagger_{j'n'}\right] = \delta_{n,n'}\delta_{j,j'}. \tag{7.20}$$

The appropriate radial modes in a two-dimensional geometry that extends to $r_{\max}$ can be

written in terms of the Jacobi polynomials $P_n^{(\alpha,\beta)}$ as:

$$\begin{aligned} R_n(r) &= \frac{\sqrt{2(n+1)}}{r_{\max}} P_n^{(1,0)}\Big(1-\frac{2r}{r_{\max}}\Big) \\ &= (-1)^n \frac{\sqrt{2(n+1)}}{r_{\max}} \sum_{l=0}^{n} \binom{n+1}{l} \binom{n}{n-l} \left(\frac{r}{r_{\max}}\right)^{n-l} \left(\frac{2r}{r_{\max}}-1\right) \end{aligned} \quad (7.21)$$

and the spherical harmonics reduce to[108]

$$Y_j(\theta) = \frac{1}{\sqrt{2\pi}} e^{i\theta j}. \quad (7.22)$$

The angular momentum distribution is then given by a summation over the radial modes:

$$\langle n(j)\rangle = \sum_{n,n'} \left\langle \hat{\Psi}^\dagger_{jn} \hat{\Psi}_{jn'} \right\rangle = \sum_{n} \left\langle \hat{\Psi}^\dagger_{jn} \hat{\Psi}_{jn} \right\rangle + \sum_{n\neq n'} \left\langle \hat{\Psi}^\dagger_{jn} \hat{\Psi}_{jn'} \right\rangle. \quad (7.23)$$

In the simulations, we shall neglect the off-diagonal coherences and calculate only the first term in Eq. (7.23). The angular momentum distribution for individual trajectories shows large occupation in particular angular modes, different for each run. This indicates that vortices with different momenta appear each time. For example, in the trajectory shown in Fig. 7.5, a vortex with $j = -1$ appears at about one quarter of the way through the simulation, and persists until the end. A less stable vortex with $j = -6$ also forms, but this decays near the end of the simulation. The maximum occupation of the $j = -1$ vortex is around $n(j) = 20$, owing to relatively small initial atom numbers in this two-dimensional trap simulation. The ensemble average of the angular momentum distribution, shown in Fig. 7.6, reveals quite a broad range of final angular momentum; this is consistent with the existence of vortices.

7.5.4 Other trap geometries and cooling schemes

All the simulations hereto presented have used the sinusoidal potential and absorption, with the height of the potential swept downwards in time. We now consider some alternative evaporation procedures.

Figure 7.7 shows the evolution of a single three-dimensional trajectory using the trap profiles V_3 and Γ_3 (defined in Eqs. (7.5c) and (7.6c), respectively), designed for the maximum initial retention of atoms. This geometry is effective in that in the first few time steps shown in the figure, up to three times more atoms are retained. This has the advantage of increasing the rate of the thermalising collisions, and should therefore aid the

Figure 7.5: *Angular momentum distribution $n(j)$, during the condensation of a two-dimensional Bose gas. The time axis has been normalised by $t_0 = 0.79ms$.*

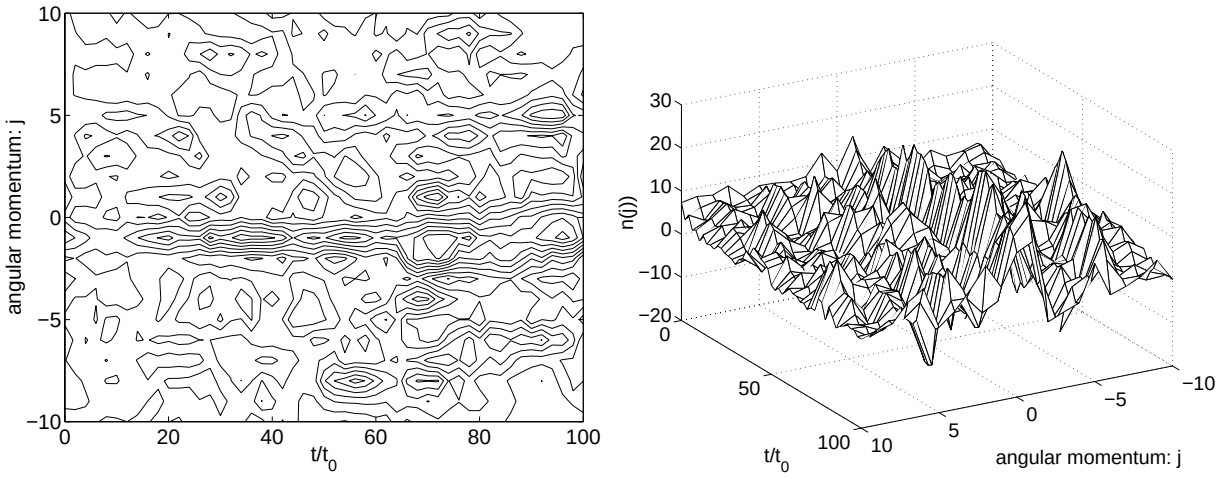

Figure 7.6: *Ensemble average of the angular momentum distribution $\langle n(j) \rangle$, during the condensation of a two-dimensional Bose condensate (40 paths). The time axis has been normalised by $t_0 = 0.79ms$.*

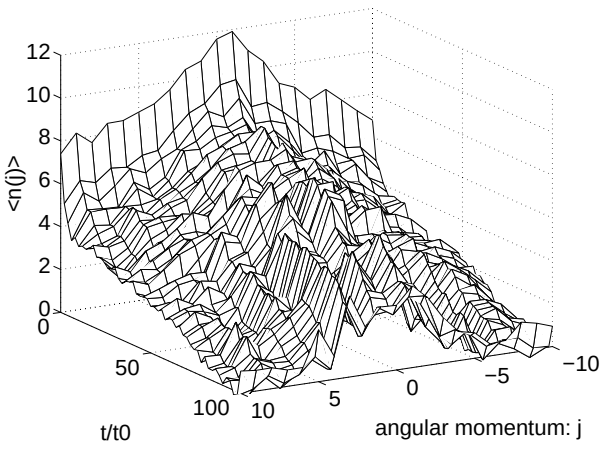

Figure 7.7: *Single-trajectory calculation of (a) the atom density $n(k)$ and (b) the total number of atoms of a three-dimensional Bose condensate in a trap defined by V_3 and Γ_3. Time has been normalised by $t_0 = 0.79ms$ and momentum by $k_0 = 1.32 \times 10^6 m^{-1}$.*

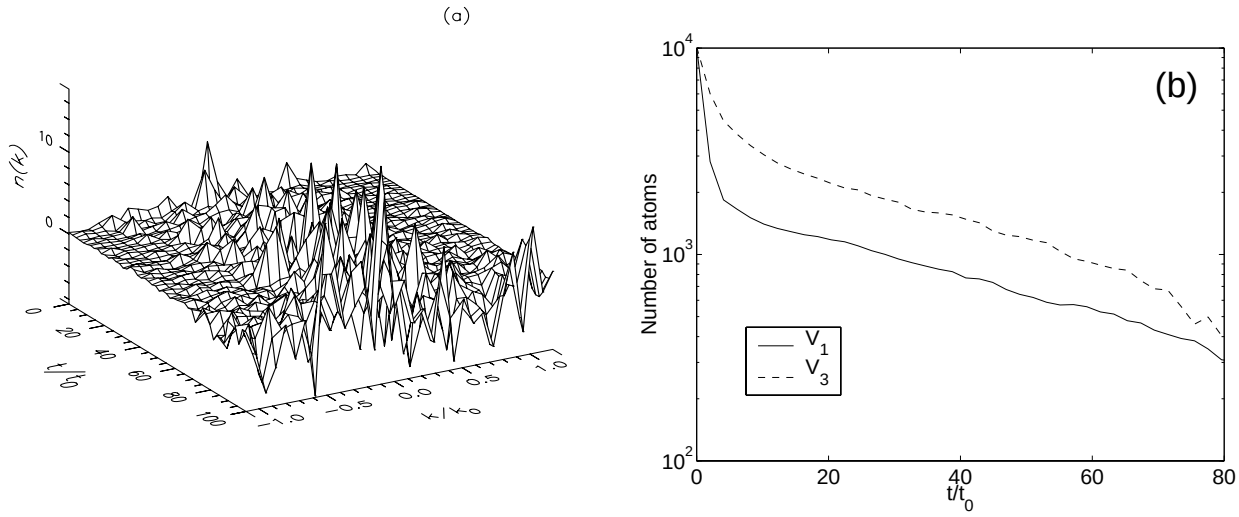

onset of condensation, but it does lead to problems with the simulation technique. As the negative-going peaks indicate, large phase-space excursions start to develop at $t = 100t_0$. These excursions strain the numerical algorithm, thereby requiring more simulation time to control numerical error. Also, because of the larger statistical error, the ensemble must contain many more members to give a meaningful average result.

These phase-space excursions are known to develop with the positive-P technique when the size of the damping relative to the nonlinearity is small. The damping in this case is only present at the edges of the x-domain and is thus not able to curb the growth of the excursions, which occurs throughout the whole domain where the nonlinearity is large. This effect is diminished when the region of damping expands over time towards the centre of the trap, as in the implementation of the RF-scalpel. It is this situation that we now consider.

Figure 7.8 shows the evolution of a single trajectory in both k and x space for a three-dimensional simulation in which V_3 is kept constant and Γ_3 implemented as the scalpel. Apart from the different tapping potential with normalised height $v = 47.0$ and the different evaporation procedure with ramping rate $\alpha = 0.007$, all parameters are the same as the previous three-dimensional case (shown in Figs. 7.2(b&c)). As in the previous case, the hottest atoms (which are progressively less energetic) are removed over time.

Figure 7.8: *Single-trajectory calculation of the atom density (a) in Fourier space $n(k)$ and (b) in coordinate space $n(x)$ for a three-dimensional Bose condensate undergoing an 'RF-scalpel' evaporation. Time has been normalised by $t_0 = 0.79ms$, momentum by $k_0 = 1.32 \times 10^6 m^{-1}$ and position by $x_0 = 0.76\mu m$.*

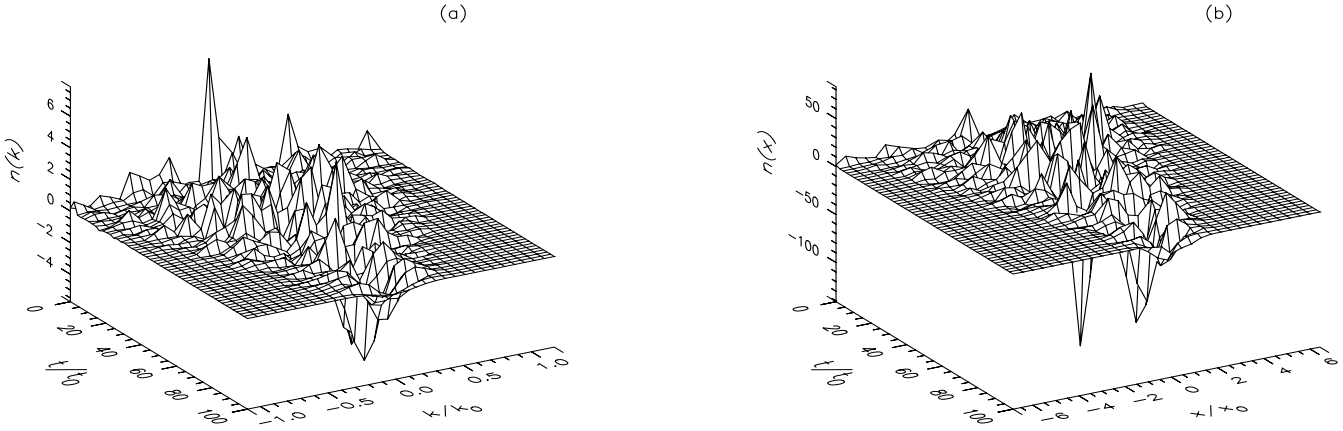

Unlike the previous case, the effect of the scalpel cutting into the spatial distribution can be seen, to produce a final distribution which occupies a small volume. Also unlike the previous case, there are no large peaks in the final k-distribution, but rather the final distribution is small and smooth[3]. One reason for this small peak momentum density is that since the final x-distribution is now much narrower, the k-distribution must be correspondingly larger if the distribution is transform limited. The waveforms must at least obey Heisenberg's uncertainty principle for the x and k variables:

$$\Delta x \Delta k \geq \frac{1}{2}. \tag{7.24}$$

Equality corresponds to transform limited, or minimum uncertainty, distributions. In the simulation shown, $\Delta x \Delta k \simeq 0.53$, which is very close to being transform limited. As this limit is approached, the occupied volume in k-space can no longer be compressed, leading to a high loss rate through the higher k-modes which are now damped.

Thus the simulation has resulted in (almost) the lowest energy configuration for the given spatial confinement. What is not occurring is a large occupation of this state, since

[3]That the final 'intensity' $a_1 a_2^*$ is negative shows that the system is not in a coherent state, but rather a superposition of coherent states.

Figure 7.9: *A three-dimensional GP calculation with strongly interacting atoms, showing the time evolution of the atom density in (a) Fourier space and (b) coordinate space. Time has been normalised by* $t_0 = 0.79ms$*, momentum by* $k_0 = 1.32 \times 10^6 m^{-1}$ *and position by* $x_0 = 0.76\mu m$*.*

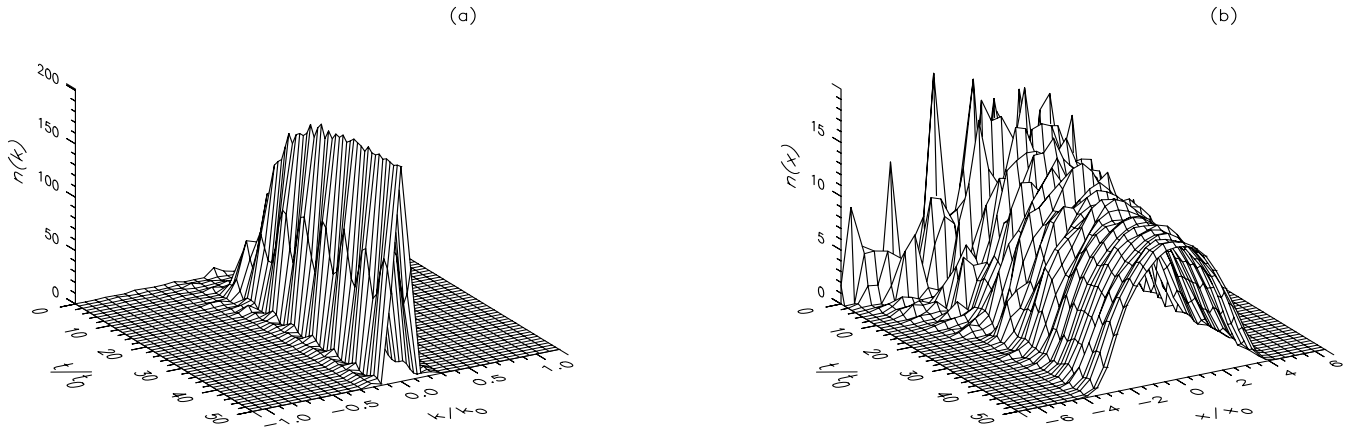

the total number of atoms finally is very small, due to the greater damping. Of course the absorbing scalpel can be reversed or turned off before it cuts into the minimum uncertainty state. But when that happens, the distribution spreads out again in both x and k space. This does not occur when the stochastic terms in the simulation are turned off, and so may be regarded as a spontaneous quantum heating effect, due perhaps to anticorrelations in the atoms' positions. Since the nonlinear (mean-field) term is quite small in these simulations, there is no bosonic-stimulation incentive to stay in the minimum uncertainty state.

Gross-Pitaevskii simulations indicate that a condensate might form in this situation if the interaction strength were much stronger. It is an indication only, because for these parameters a mean-field treatment, in which spontaneous correlation effects are neglected, is not physically justified. Figure 7.9 gives the GP results for atoms with a scattering length of $60nm$. A macroscopic occupation of the minimum uncertainty state occurs early in the simulation, which persists after the scalpel is turned off at $t = 40$. Whether the Bose stimulation evident in this situation would overcome the quantum heating effect is uncertain without carrying out the fully quantum calculation.

Truncating the noise terms in the positive-P equation like this in order to produce the GP equation cannot be justified for a first-principles calculation. The GP equation may be

regarded as the limit of the positive-P or Wigner equations when there are many particles per mode. In this limit, the physical situation being simulated has changed, from one in which begins in an uncondensed state with on average less than one atom per mode, to one which starts in an already condensed state with many atoms distributed among a few modes. So instead of modelling evaporative cooling from an uncondensed to an condensed state, the simulation models the relaxation of a condensate in some form of excited state (not a canonical ensemble in this case) to a zero-temperature ground state. This resembles the simulations presented in [114].

Neglecting the noise terms in the phase-space equations (Eq. (7.4)) constrains a system that begins in a coherent state (or a mixture of coherent states) to remain so. If the assumption of many particles per mode is *not* made, then this fully coherent description is inconsistent with the usual formulation of the GP equation, which does take into account certain atom correlations. This is because a state which is diagonal in a coherent state expansion cannot include any atom correlations. However it may be possible to derive phase-space equations using an expansion in which atom correlations are included in the basis. With such equations, atom correlations effects may still be retained even if the noise terms are neglected.

7.6 Conclusions

In summary, in this chapter we have demonstrated a three-dimensional real-time quantum dynamical simulation of Bose condensation with mesoscopic numbers of interacting atoms on a large lattice. Sampling errors and lattice size restrictions impose strong limitations on these simulations. The main limitation preventing a description of current experiments is the weak nonlinearity required by the method. Also, the possible appearance of boundary terms in the positive-P distribution prohibits simulations over long times. The results show evidence for highly nonclassical behaviour in a first principles simulation of condensate formation. For certain situations, the simulations reveal a unique form of condensate which, as distinct from current experiments, has a relatively low atom density. The main mechanism of condensate formation here would seem to be a spontaneous emission into the condensate mode rather than bosonic stimulation. The final state in these cases, for which there is no canonical condensate, is far from thermal equilibrium. Spontaneous

vortex formation in small evaporatively cooled condensates is also observed.

Simulations of the now traditional form of evaporative cooling (using the RF scalpel and maintaining a high density) appear intractable with this method. This is due to the large size of the stochastic terms, which must be included to treat accurately the interatomic collisions. Removing the stochastic terms results in mean-field simulations that show considerable differences with the first-principles quantum calculations for these parameters. The quantum simulations show that the phase-space distribution becomes quite broad, indicating that the corresponding quantum state evolves into superpositions of distant coherent states. Calculations of higher-order correlations also suggest that the condensate is far from being in a coherent state. Thus the customary phase-space representations, which involve coherent-state expansions, are not the natural choice with which to treat this problem.

7.6.1 Future directions

We shall conclude this thesis with a discussion of a possible way forward. As we saw in Sec. 4.6, other phase-space techniques besides those involving coherent states are possible. Any overcomplete set of states could be used to generate an appropriate expansion, although the utility of such a basis in generating phase-space equations is another matter. With the initial choice of candidates so large, some physical insight can be helpful to find prospective basis sets.

The Bogolubov transformation[107, 137], used to describe perturbations to the mean field, is similar to a squeezing transformation. So perhaps squeezed states provide a closer fit to the true ground state, in which case an expansion of the density operator in terms of squeezed states[27, 155, 156] might produce more compact realisations in phase space.

As an illustration of how squeezing enters the picture once we move beyond coherent states, consider a weakly interacting condensate occupying a single mode of the trapping potential. The annihilation operator for this mode can be expanded around a coherent state:

$$\hat{a} = \alpha + \delta\hat{a}. \tag{7.25}$$

The condensate will occupy the state which minimises the free energy[140]:

$$\hat{F} = (E_0 - \mu)\hat{a}^\dagger\hat{a} + \hbar\kappa\hat{a}^\dagger\hat{a}^\dagger\hat{a}\hat{a}, \tag{7.26}$$

where μ is the chemical potential, which can be written in terms of the coherent amplitude $\alpha = |\alpha|e^{i\theta}$ as $\mu = E_0 + 2\hbar\kappa|\alpha|^2$. Substituting the expansion for $\hat{a}$ into Eq. (7.26) and retaining terms quadratic in $\delta\hat{a}$ gives

$$\begin{aligned}\hat{F} &\simeq \hbar\kappa\left(-|\alpha|^4 + |\alpha|^2(e^{2i\theta}\delta\hat{a}^\dagger\delta\hat{a}^\dagger + 2\delta\hat{a}^\dagger\delta\hat{a} + e^{-2i\theta}\delta\hat{a}\delta\hat{a}\right) \\ &= \hbar\kappa\left(-|\alpha|^4 + |\alpha|^2(\hat{X}^2 - 1)\right), \end{aligned} \tag{7.27}$$

where the quadrature operators have been defined as

$$\hat{X} = \delta\hat{a}e^{-i\theta} + \delta\hat{a}^\dagger e^{i\theta} \tag{7.28a}$$

$$\hat{Y} = -i\delta\left(\hat{a}e^{-i\theta} - i\delta\hat{a}^\dagger e^{i\theta}\right). \tag{7.28b}$$

Thus Eq. (7.27) shows that minimising the free energy minimises the fluctuations in the $\hat{X}$ quadrature, and hence maximises the fluctuations in the $\hat{Y}$ quadrature. Now the number variance is

$$\begin{aligned}\Delta n^2 &= \left\langle(\hat{a}^\dagger\hat{a})^2\right\rangle - \left\langle\hat{a}^\dagger\hat{a}\right\rangle^2 \\ &= |\alpha|^2\left(\left\langle X^2\right\rangle - \left\langle X\right\rangle^2 + O\Big(\frac{\langle X\rangle^3}{|\alpha|}\Big)\right), \end{aligned} \tag{7.29}$$

which means that with minimised fluctuations in the $\hat{X}$ quadrature, the ground state is amplitude squeezed.

Appendix B overviews the properties of squeezed states and suggests how suitable phase-space representations can be generated from them. As these preliminary investigations show, the price to pay for going beyond coherent states is a higher-dimensional phase space and an increase in complexity. Generalisation of the phase-space representations involves extra parameters (the squeezing parameter ξ in this case), which must be either chosen *a priori* or evolved through simulation to obtain a more compact phase-space representation. There are a myriad of possible choices for the type of representation, each with a large parameter space. No comprehensive survey of representations has been undertaken, so the future in this direction is open. The work presented in this thesis is only a tentative beginning; but perhaps a seed has been sown that will one day reap a harvest of powerful multimode quantum dynamical simulation techniques.

Appendix A

Stochastic calculus in outline

This appendix states some results needed to deal with random terms in differential equations. Proofs of these statements are in [61], with further explanation in [22].

A.1 The Fokker-Planck equation

Consider a system of stochastic variables $\mathbf{x}$, distributed according to a probability distribution $P(\mathbf{x}, t)$. In many cases, the time evolution of $P(\mathbf{x}, t)$ is governed by the Fokker-Planck (FP) equation:

$$\frac{\partial}{\partial t}P = -\sum_i \frac{\partial}{\partial x_i}A_i(\mathbf{x}, t)P + \frac{1}{2}\sum_{ij}\frac{\partial}{\partial x_i}\frac{\partial}{\partial x_j}\left[\mathbf{B}(\mathbf{x}, t)\mathbf{B}^T(\mathbf{x}, t)\right]_{ij}P \tag{A.1}$$

where $\mathbf{A}$ is vector and $\mathbf{B}$ is a matrix. The first-order derivative terms in Eq. (A.1), known as drift terms, govern the deterministic evolution of $\mathbf{x}$, while the second-order derivative terms govern the stochastic or diffusive behaviour of $\mathbf{x}$.

An explicit expression for the evolution of individual trajectories of $\mathbf{x}(t)$ is possible with the Wiener increment dW:

$$dx_i(t) = A_i(\mathbf{x}, t)dt + \sum_j B_{ij}(\mathbf{x}, t)dW_j(t) \tag{A.2}$$

which should be interpreted according to the Ito calculus.

A.2 The Wiener process

The well known Wiener process $W(t)$ is governed by a FP equation in which the drift term is zero and the diffusion coefficient is equal to one. Its random trajectories are

continuous but not differentiable. The probability distribution P governing W spreads out with increasing time, until as $t \to \infty$, $P \to 0$ everywhere. We define the Wiener increment as:

$$dW(t) = W(t+dt) - W(t), \tag{A.3}$$

which has the following expectation values

$$E[dW] = 0 \tag{A.4a}$$

$$E[dW(t)^2] = dt \tag{A.4b}$$

$$E[dW(t)^{2+n}] = 0 \qquad n > 2 \tag{A.4c}$$

$$E[dW(t)dW(t')] = 0. \tag{A.4d}$$

Any process with white-noise correlations:

$$\left\langle \xi(t)\xi(t') \right\rangle = \delta(t-t'), \tag{A.5}$$

can be written in terms of the Wiener process as

$$\xi(t) = \frac{dW(t)}{dt}. \tag{A.6}$$

A.3 Ito and Stratonovich stochastic calculi

An Ito stochastic equation of the form

$$dx_i(t) = A_i(\mathbf{x},t)dt + \sum_j B_{ij}(\mathbf{x},t)dW_j \tag{A.7}$$

is equivalent to the Stratonovich equation

$$dx_i(t) = \left(A_i(\mathbf{x},t) - \frac{1}{2}\sum_{kj} B_{kj}(\mathbf{x},t)\frac{\partial}{\partial x_k}B_{ij}(\mathbf{x},t) \right) dt + \sum_j B_{ij}(\mathbf{x},t)dW_j. \tag{A.8}$$

In other words, Eq. (A.7) when interpreted according to the rules of Ito calculus gives the same solution as Eq. (A.8) when interpreted according to the rules of Stratonovich calculus.

The two versions of stochastic calculus arise from different ways of defining the integral of a stochastic variable. The Ito integral evaluates the terms in the Riemann sum at the beginning of the time interval, and thus corresponds to an explicit integration procedure,

while the Stratonovich calculus is equivalent to evaluating the increment at the centre of the time interval, which corresponds to an implicit algorithm.

The Stratonovich calculus has the simplicity of conforming to the rules of standard calculus, and the noise terms of Stratonovich equations can be regarded as the ideal limit of physical processes. However there is a mathematical convenience to the Ito calculus because at any particular time t, the dependent variable $x(t)$ is independent of the stochastic increment $dW(t)$; standard calculus rules can be adapted by keeping terms that are second order in the differential dx and by using the results of Eq. (A.4).

Appendix B

Quasiprobability distributions using squeezed-state expansions

As the numerical results from Ch. 7 indicate, the use of the coherent-state positive-P representation in evaporative cooling simulations leads to phase-space excursions when the atoms are strongly interacting. Large phase-space excursions indicate that the positive-P function is diffusing rapidly and that it may be developing finite boundary terms, leading to the breakdown of the method.

These phase-space excursions arise because the system is evolving in a state which is not compactly described by a coherent-state expansion. Moments such as the Fourier atom density $n(k) = a_1(k)a_2^*(k)$ becoming negative in single trajectories indicates that the state description requires superpositions of coherent states.

As a possible alternative basis set for phase-space representations, we now consider the set of squeezed states.

B.1 Squeezed states

A general squeezed state for a singe mode is defined as:

$$\big|\xi,\alpha\big\rangle = D(\alpha)S(\xi)\big|0\big\rangle, \tag{B.1}$$

in which the vacuum state is squeezed by $S(\xi)$ and then displaced by $D(\alpha)$. The squeezing and displacement operators are defined respectively as

$$S(\xi) = e^{\frac{1}{2}(\xi^*\hat{a}^2 - \xi\hat{a}^{\dagger 2})} \tag{B.2a}$$

$$D(\alpha) = e^{\alpha\hat{a}^\dagger - \alpha^*\hat{a}}, \tag{B.2b}$$

where the coherent amplitude is $\alpha = |\alpha|e^{i\theta}$. The squeezing parameter ξ is complex, with $|\xi| = r$ describing the amount of squeezing and $\arg(\xi) = \phi$ giving the direction in the complex plane. Setting $\phi = 2\theta$ specifies squeezing along the axis of the coherent displacement, ie amplitude squeezing, since for a squeezed state with quadratures as defined in Eq. (7.28),

$$\begin{aligned}\left\langle(\Delta\hat{X})^2\right\rangle &= \left\langle\hat{X}^2\right\rangle - \left\langle\hat{X}\right\rangle^2 \\ &= \cosh(2r) - \sinh(2r)\cos(\phi - 2\theta) \\ &= \frac{e^{2r}}{2}(1 - \cos(\phi - 2\theta)) + \frac{e^{-2r}}{2}(1 + \cos(\phi - 2\theta)),\end{aligned} \tag{B.3}$$

where

$$\mu = \cosh(r) \tag{B.4a}$$

$$\nu = e^{i\phi}\sinh(r). \tag{B.4b}$$

So the $\hat{X}$ quadrature in Eq. (B.3) is minimised when $\phi = 2\theta$ and maximised when $\phi = 2\theta + \pi$.

The squeezed state can also be produced by displacing the vacuum and then squeezing the resultant state[174]:

$$\left|\xi, \alpha\right\rangle = S(\xi)D(\beta(\alpha, \xi))\left|0\right\rangle, \tag{B.5}$$

where $\beta(\alpha, \xi) = \mu\alpha + \nu\alpha^*$. This leads to the interpretation of the squeezed state as a coherent state $\left|\beta\right\rangle$ of the 'antisqueezed' operator

$$\begin{aligned}\hat{b} &= S(\xi)\hat{a}S^\dagger(\xi) \\ &= \mu\hat{a} + \nu\hat{a}^\dagger.\end{aligned} \tag{B.6}$$

With respect to $\hat{b}$, $\left|\beta\right\rangle$ has all the usual coherent state properties, such as

$$\hat{b}^\dagger = \left(\frac{\beta^*}{2} + \frac{\partial}{\partial\beta}\right)\left|\beta\right\rangle \tag{B.7a}$$

$$\hat{b} = \left(\frac{\beta}{2} - \frac{\partial}{\partial\beta^*}\right)\left|\beta\right\rangle = \beta\left|\beta\right\rangle, \tag{B.7b}$$

which are the identities needed to form the operator correspondences for a P function.

B.2 Squeezed-state P functions

We define the squeezed-state P function P_ξ via the expansion

$$\begin{aligned}\hat{\rho} &= \int d\alpha d\alpha^* P_\xi(\alpha,\alpha^*)\big|\alpha,\xi\big\rangle\big\langle\alpha,\xi\big| \\ &= \int d\beta d\beta^* P(\beta,\beta^*)\big|\beta\big\rangle\big\langle\beta\big| \end{aligned} \tag{B.8}$$

for the system density operator $\hat{\rho}$.

Operator correspondences for $\hat{a}$ and $\hat{a}^\dagger$ can be found by expressing these operators in terms of $\hat{b}$ and $\hat{b}^\dagger$ and then using the usual P function operator correspondences. Proceeding thus we arrive at:

$$\hat{a}\hat{\rho} \iff \left(\alpha + \nu\frac{\partial}{\partial\beta}\right) P_\xi \tag{B.9a}$$

$$\hat{a}^\dagger\hat{\rho} \iff \left(\alpha^* - \mu\frac{\partial}{\partial\beta}\right) P_\xi \tag{B.9b}$$

$$\hat{\rho}\hat{a}^\dagger \iff \left(\alpha^* + \nu\frac{\partial}{\partial\beta^*}\right) P_\xi \tag{B.9c}$$

$$\hat{\rho}\hat{a} \iff \left(\alpha - \mu\frac{\partial}{\partial\beta^*}\right) P_\xi. \tag{B.9d}$$

These reduce to the usual coherent-state P function correspondences when $\nu \to 0$ and $\mu \to 1$. When we are not in this limit, then extra derivative terms appear in the correspondences, leading to diffusion terms as well as drift terms in the evolution equation for P_ξ from the linear terms in the master equation, and higher-order derivatives from the nonlinear terms. For example, the evolution equation for an anharmonic oscillator (Eq. (7.26)) is

$$\begin{aligned}\frac{\partial P_\xi}{\partial t} = E_0\left[-\frac{\partial}{\partial\alpha}\alpha + \frac{\partial}{\partial\alpha^*}\alpha^* - \frac{\partial^2}{\partial\beta^2}\mu\nu + \frac{\partial^2}{\partial\beta^{*2}}\mu\nu^*\right] P_\xi \\ + \hbar\kappa\left[-2\frac{\partial}{\partial\alpha}|\alpha|^2\alpha + 2\frac{\partial}{\partial\alpha^*}|\alpha|^2\alpha^* + \mathcal{D}_\xi(\alpha,\alpha^*)\right] P_\xi,\end{aligned} \tag{B.10}$$

where $\mathcal{D}_\xi$ contains diffusions terms as well as third- and fourth-order derivate terms, which must be truncated before Langevin equations can be generated for α and α^*. As in the Wigner technique, the final phase-space equations are then approximate.

A more fundamental problem with this squeezed-state P function is that the squeezing parameter ξ is constant and not part of the evolving dynamics. For this representation to be of any advantage, we would need to know *a priori* the value of the squeezing parameter

ξ_m that would minimise the spread in phase space. But not only do we not know this optimum value, we also have no guarantee that it exists as a constant independent of the system dynamics. In fact, we would expect the optimum value ξ_m to be correlated to α (for the single-mode case the phase of ξ_m must be such as to minimise the amplitude fluctuations). So we need a phase-space representation in which ξ is a variable:

$$\hat{\rho} = \int d\alpha d\alpha^* d\xi d\xi^* P(\alpha,\alpha^*,\xi,\xi^*)\big|\alpha,\xi\big\rangle\big\langle\alpha,\xi\big| \tag{B.11}$$

To obtain evolution equations for ξ, we need to rewrite the effect of the creation and annihilations on the squeezed state in terms of partial derivatives with respect to ξ, in the manner of Eq. (B.7). To prevent any higher order derivative terms from appearing in the evolution equation for the P distribution, we need direct operator correspondences for $\hat{a}^2$ and $\hat{a}^{\dagger 2}$. One may consider doing this via the squeezing operator $S(\xi,\xi^*)$. The simplest way to differentiate this operator (because $\left[\hat{a}^2,\hat{a}^{\dagger 2}\right]$ does not commute with $\hat{a}^2$ or $\hat{a}^{\dagger 2}$) appears to be

$$\begin{aligned}\mathcal{L}(\xi,\xi^*)S(\xi,\xi^*) &= \left(\xi^*\frac{\partial}{\partial\xi^*}+\xi\frac{\partial}{\partial\xi}\right)S(\xi,\xi^*)\\ &= \frac{1}{2}\left(\xi^*\hat{a}^2-\xi\hat{a}^{\dagger 2}\right)S(\xi,\xi^*),\end{aligned} \tag{B.12}$$

which is not useful, since we cannot generate operator correspondences separately for $\hat{a}^2$ and $\hat{a}^{\dagger 2}$. The exponent of $S(\xi,\xi^*)$ can be factored to find $\frac{\partial}{\partial\xi}S$ and $\frac{\partial}{\partial\xi^*}S$ using results like[156]

$$e^{\xi^*\hat{A}-\xi\hat{A}^\dagger} = e^{-\xi\hat{A}^\dagger}e^{-\ln\cosh r\hat{B}}e^{\xi^*\hat{A}}, \tag{B.13}$$

where $\hat{A}=\frac{1}{2}\hat{a}^2$ and $\hat{B}=\hat{a}^\dagger\hat{a}+\frac{1}{2}$. But this does not appear to lead to anything more useful.

Alternatively the phase of ξ can be locked into that of α to ensure an expansion in amplitude-squeezed states:

$$\hat{\rho} = \int d\alpha d\alpha^* dr P(\alpha,\alpha^*,r)\big|\alpha,r\big\rangle\big\langle\alpha,r\big|. \tag{B.14}$$

This reduces the phase-space dimensionality, but has complications of its own: since $S(\xi,\xi^*)\longrightarrow S(\alpha,\alpha^*,r)$, the correspondences for $\hat{a}$ and $\hat{a}^\dagger$ must be rederived.

Thus there are many ways in which generalised phase-space representations could be generated. However, finding one which gives exact phase-space equations (regardless of whether these give improved statistics) is not a trivial matter, without having the simplicity of coherent states.

Bibliography

[1] Agrawal, G. P. *Nonlinear Fiber Optics*, second ed. Academic Press, 1995.

[2] Anderson, B. P., and Kasevich, M. A. Macroscopic quantum interference from atomic tunnel arrays. *Science 282* (Nov. 1998), 1686–1689.

[3] Anderson, M. H., Ensher, J. R., Matthews, M. R., Weiman, C. E., and Cornell, E. A. Observations of Bose-Einstein condensation in a dilute atomic vapor. *Science 269*, 5221 (July 14 1995), 198–201.

[4] Andrews, M. R., Townsend, C. G., and Ketterle, W. Observation of interference between two Bose condensates. *Science 275*, 5300 (Jan. 31 1997), 637.

[5] Anglin, J. R., and Zurek, W. H. Vortices in the wake of rapid Bose-Einstein condensation. *Physical Review Letters 83*, 9 (Aug. 30 1999), 1707–1710.

[6] Arecchi, F. T., Courtens, E., Gilmore, R., and Thomas, H. Atomic coherent states in quantum optics. *Physical Review A 6*, 6 (Dec. 1972), 2211–2236.

[7] Baboiu, D.-M., Mihalache, D., and Panoiu, N.-C. Combined influence of amplifier noise and intrapulse Raman scattering on the bit-rate limit of optical fiber communication systems. *Optics Letters 20*, 18 (Sept. 18 1995), 1865–1867.

[8] Berg-Sørensen, K. Kinetics for evaporative cooling of a trapped gas. *Physical Review A 55*, 1 (Feb. 1997), 1281–1287.

[9] Bergman, K., Haus, H. A., and Shirasaki, M. *Applied Physics B 55*, 3 (Sept. 1 1992), 242.

[10] Bernstein, L., Eilbeck, J. C., and Scott, A. C. The quantum theory of local modes in a coupled system of nonlinear oscillators. *Nonlinearity 3* (1990), 293–323.

[11] Bijlsma, M., and Stoof, H. T. C. Variational approach to the dilute Bose gas. *Physical Review A 55*, 1 (Jan. 1997), 498–512.

[12] Bolda, E., and Walls, D. F. Detection of vorticity in Bose-Einstein condensed gases by matter-wave interference. *Physical Review Letters 81*, 25 (Dec. 21 1998), 5477–5480.

[13] Bollinger, J. J., Itano, W. M., Wineland, D. J., and Heinzen, D. J. Optimal frequency measurements with maximally correlated states. *Physical Review A 54*, 6 (Dec. 1996), R4649–R4652.

[14] Bose, S. Plancks gesetz und lichtquantenhypothese. *Zeitschrift für Physik 26* (1924), 178–181.

[15] Braaten, E., and Nieto, A. Quantum corrections to the ground state of a trapped Bose-Einstein condensate. *Physical Review B 56*, 22 (Dec. 1997), 14745–14765.

[16] Bradley, C. C., Sackett, C. A., Tollett, J. J., and Hulet, R. G. Evidence of Bose-Einstein condensation in an atomic gas with attractive interactions. *Physical Review Letters 75*, 9 (Aug. 28 1995), 1687–1690.

[17] Burnett, K. Bose-Einstein condensation with evaporatively cooled atoms. *Contemporary Physics 37*, 1 (Jan. 1 1996), 1–14.

[18] Burt, E. A., Ghrist, R. W., Myatt, C. J., Holland, M. J., Cornell, E. A., and Wieman, C. E. Coherence, correlations, and collisions: What one learns about Bose-Einstein condensates from their decay. *Physical Review Letters 79*, 3 (July 1997), 337–340.

[19] Butts, D. A., and Rokhsar, D. S. Predicted signatures of rotating Bose-Einstein condensates. *Nature 397* (Jan. 28 1999), 327–329.

[20] Caradoc-Davies, B. M., Ballagh, R. J., and Burnett, K. Coherent dynamics of vortex formation in trapped Bose-Einstein condensates. *Physical Review Letters 83*, 5 (Aug. 2 1999), 895–898.

[21] Caratzoulas, S., and Pechukas, P. Phase space path integrals in monte carlo quantum dynamics. *Journal of Chemical Physics 104*, 16 (Apr. 22 1996), 6265.

[22] Carter, S. J. Quantum theory of nonlinear fiber optics: Phase-space representations. *Physical Review A 51*, 4 (Apr. 1995), 3274–3301.

[23] Carter, S. J., and Drummond, P. D. Squeezed quantum solitons and Raman noise. *Physical Review Letters 67*, 27 (Dec. 30 1991), 3757–3760.

[24] Carter, S. J., Drummond, P. D., Reid, M. D., and Shelby, R. M. Squeezing of quantum solitons. *Physical Review Letters 58*, 18 (May 4 1987), 1841–1844.

[25] Castin, Y., and Dalibard, J. Relative phase of two Bose-Einstein condensates. *Physical Review A 55*, 6 (June 1997), 4330–4337.

[26] Castin, Y., and Dum, R. Bose-Einstein condensates in time-dependent traps. *Physical Review Letters 77*, 27 (Dec. 1996), 5315–5319.

[27] Caves, C. M., and Schumaker, B. L. New fomalism for two-photon quantum optics. I. quadrature phases and squeezed states. *Physical Review A 31*, 5 (May 1985), 3068–3092.

[28] Ceperley, D. M. Path integrals in the theory of condensed helium. *Reviews of Modern Physics 67*, 2 (Apr. 2 1995), 279–335.

[29] Ceperley, D. M. Microscopic simulations in physics. *Reviews of Modern Physics 71*, 2 (Mar. 1 1999), S438–S443.

[30] Cirac, J. I., Gardiner, C. W., Naraschewski, M., and Zoller, P. Continuous observation of interference fringes from Bose condensates. *Physical Review A 54*, 5 (Nov. 1996), R3714–R3717.

[31] Cirac, J. I., Lewenstein, M., Mølmer, K., and Zoller, P. Quantum superposition states of Bose-Einstein condensates. *Physical Review A 57*, 2 (Feb. 1998), 1208–1218.

[32] Corney, J. F., Drummond, P. D., and Liebman, A. Quantum noise limits to terabaud communications. *Optics Communications 140* (Aug. 1 1997), 211–215.

[33] Corney, J. F., and Milburn, G. J. Homodyne measurements on a Bose-Einstein condensate. *Physical Review A 58*, 3 (Sept. 1998), 2399–2406.

[34] Damle, K., Majumdar, S. N., and Sachdev, S. Phase ordering kinetics of the Bose gas. *Physical Review A 54*, 6 (Dec. 1996), 5037–5041.

[35] Davis, K. B., Mewes, M.-O., Andrews, M. R., van Druten, N. J., Durfee, D. S., Kurn, D. M., and Ketterle, W. Bose-Einstein condensation in a gas of sodium atoms. *Physical Review Letters 75*, 22 (Nov. 27 1995), 3969–3973.

[36] Davis, K. B., Mewes, M.-O., and Ketterle, W. An analytical model for evaporative cooling of atoms. *Applied Physics B 60*, 2/3 (Feb. 1 1995), 155–159.

[37] Davis, K. B., Mewes, M.-O., and Ketterle, W. Evaporative cooling of sodium atoms. *Physical Review Letters 74*, 26 (June 26 1995), 5202–5205.

[38] Dianov, E. M., Luchnikov, A. V., Pilipetskii, A. N., and Prokhorov, A. M. Long-range interaction of picosecond solitons through excitation of acoustic waves in optical fibers. *Applied Physics B 54* (1992), 175–180.

[39] Dodd, R. J., Burnett, K., Edwards, M., and Clark, C. W. Excitation spectroscopy of vortex states in dilute Bose-Einstein condensed gases. *Physical Review A 56*, 1 (July 1997), 587–590.

[40] Dougherty, D. J., Kartner, F. X., Haus, H. A., and Ippen, E. P. Measurement of the Raman gain spectrum of optical fibres. *Optics Letters 20*, 1 (Jan. 1 1995), 31–33.

[41] Doyle, J. M., Sandberg, J. C., and Yu, I. A. Evaporative cooling of atomic hydrogen: Theory of cooling and progress towards the Bose-Einstein transition. *Physica B 194/195* (Feb. 1 1994), 13.

[42] Drummond, P. D. Electromagnetic quantization in dispersive inhomogeneous nonlinear dielectrics. *Physical Review A 42* (1990), 6845.

[43] Drummond, P. D. Quantum theory of nonlinear optics. Lecture notes for the Nordic Summer School in Nonlinear Optics, 1997.

[44] Drummond, P. D., and Carter, S. J. Quantum-field theory of squeezing in solitons. *Journal of the Optical Society of America B 4*, 10 (Oct. 1987), 1565–1573.

[45] Drummond, P. D., Carter, S. J., and Shelby, R. M. Time dependence of quantum fluctuations in solitons. *Optics Letters 14*, 7 (Apr. 1 1989), 373–375.

[46] Drummond, P. D., and Corney, J. F. Quantum dynamics of evaporatively cooled Bose-Einstein condensates. *Physical Review A 60*, 4 (Oct. 1999), R2661–2664.

[47] Drummond, P. D., and Hardman, A. D. Simulation of quantum effects in Raman-active waveguides. *Europhysics Letters 21*, 3 (Jan. 20 1993), 279–284.

[48] Drummond, P. D., and Man, W. Quantum noise in reversible soliton logic. *Optics Communications 105* (1994), 99–103.

[49] Drummond, P. D., and Mortimer, I. K. Computer simulations of multiplicative stochastic differential equations. *Journal Of Computational Physics 93* (1991), 144.

[50] Drummond, P. D., Shelby, R. M., Friberg, S. R., and Yamamoto, Y. Quantum solitons in optical fibres. *Nature 365* (Sept. 23 1993), 307–313.

[51] Dunningham, J. A., and Burnett, K. Phase standard for Bose-Einstein condensates. *Physical Review Letters 82*, 19 (May 10 1999), 3729–3733.

[52] Dyrting, S. Observation of nonlinear resonances in laser cooled rubidium. Jan. 6 1996.

[53] Edwards, M., Dodd, R. J., Clark, C. W., Ruprecht, P. A., and Burnett, K. Properties of a Bose-Einstein condensate in an anisotropic harmonic potential. *Physical Review A 53*, 4 (Apr. 1 1996), R1950–1953.

[54] Einstein, A. Quantentheorie des einatomigen idealen gases: Zweite abhandlung. *Sitzungber. Preuss. Akad. Wiss. 1925* (Jan. 1925), 3–14.

[55] Esry, B. D., and Greene, C. H. Spontaneous spatial symmetry breaking in two-component Bose-Einstein condensates. *Physical Review A 59*, 2 (Feb. 1999), 1457–1460.

[56] Feder, D. L., Clark, C. W., and Schneider, B. I. Vortex stability of interacting Bose-Einstein condensates confined in anisotropic harmonic traps. *Physical Review Letters 82*, 25 (June 21 1999), 4956–4959.

[57] Fetter, A. L. Vortex stability in a trapped Bose condensate. *Journal of Low Temperature Physics 113*, 3–4 (1998), 189–194.

[58] Feynman, R. P. Simulating physics with computers. *International Journal of Theoretical Physics 21*, 6–7 (1982), 467–489.

[59] Fried, D. G., Killian, T. C., Willmann, L., huis, D. L., Moss, S. C., Kleppner, D., and Greytak, T. J. Bose-Einstein condensation of atomic hydrogen. *Physical Review Letters 81*, 18 (Nov. 1998), 3811–3814.

[60] Gardiner, A. G. C. W., and Drummond, P. D. Positive P representation: Application and validity. *Physical Review A 55*, 4 (Apr. 1997), 3014–3032.

[61] Gardiner, C. W. *Handbook of stochastic methods for physics, chemistry, and the natural sciences*, vol. 13 of *Springer series in synergetics*. Springer-Verlag, Berlin, New York, 1983.

[62] Gardiner, C. W. *Quantum Noise*. Springer, Berlin, 1991.

[63] Gardiner, C. W., Lee, M. D., Ballagh, R. J., Davis, M. J., and Zoller, P. Quantum kinetic theory of condensate growth: comparison of experiment and theory. *Physical Review Letters 81*, 24 (Dec. 14 1999), 5266–5269.

[64] Gardiner, C. W., and Zoller, P. Quantum kinetic theory: A quantum kinetic master equation for condensation of a weakly interacting Bose gas without a trapping potential. *Physical Review A 55*, 4 (Apr. 1997), 2902–2921.

[65] Gardiner, C. W., and Zoller, P. Quantum kinetic theory. III. quantum kinetic master equation for strongly condensed trapped systems. *Physical Review A 58*, 1 (July 1998), 536–556.

[66] Gardiner, C. W., Zoller, P., Ballagh, R. J., and Davis, M. J. Kinetics of Bose-Einstein condensation in a trap. *Physical Review Letters 79*, 10 (Sept. 8 1997), 1793–1796.

[67] Glauber, R. J. The quantum theory of optical coherence. *Physical Review 130*, 6 (June 1963), 2529–2539.

[68] Gordon, D., and Savage, C. M. Excitation spectrum and instability of a two-species Bose-Einstein condensate. *Physical Review A 58*, 2 (Aug. 1998), 1440–1444.

[69] Gordon, J. P. *Optics Letters 11*, 10 (Oct. 1986), 662–664.

[70] Gordon, J. P., and Haus, H. A. Random walk of coherently amplified solitons in optical fiber transmission. *Optics Letters 11*, 10 (Oct. 1986), 665–667.

[71] Graham, R., Wong, T., Collett, M. J., Tan, S. M., and Walls, D. F. Phase preparation by atom counting of Bose-Einstein condensates in mixed states. *Physical Review A 57*, 1 (Jan. 1998), 493–502.

[72] Griffin, A., Snoke, D. W., and Stringari, S. *Bose-Einstein condensation.* Cambridge University Press, Cambridge, 1995.

[73] Grüter, P., Ceperley, D., and Laloë, F. Critical temperature of Bose-Einstein condensation of hard-sphere gases. *Physical Review Letters 79*, 19 (Nov. 10 1997), 3549–3552.

[74] Hall, D. S., Matthews, M. R., Wieman, C. E., and Cornell, E. A. Measurements of relative phase in two-component Bose-Einstein condensates. *Physical Review Letters 81*, 8 (Aug. 24 1998), 1543–1546.

[75] Hall, M. J. W. Universal geometric approach to uncertainty, entropy, and information. *Physical Review A 59*, 4 (Apr. 1 1999), 2602–2615.

[76] Hamaide, J., Emplit, P., and Haelterman, M. Dark-soliton jitter in amplified optical transmission systems. *Optics Letters 16*, 20 (Oct. 1991), 1578–1580.

[77] Harris, D. J., Wiseman, H. M., and Milburn, G. J. Unpublished, 1998.

[78] Hasegawa, A., and Tappert, F. Transmission of stationary nonlinear optical pulses in dispersive dielectric fibres. II. normal dispersion. *Applied Physics 23*, 4 (Aug. 1973), 171–172.

[79] Haus, H. A., and Wong, W. S. Solitons in optical communications. *Reviews of Modern Physics 68*, 2 (Apr. 1996), 423–444.

[80] Hecht, C. E. The possible superfluid behaviour of hydrogen atom gases and liquids. *Physica 25*, 10 (Oct. 1959), 1159–1161.

[81] Hendry, P. C., Lawson, N. S., Lee, R. A. M., McCliktoch, P. V. E., and Williams, C. D. H. Generation of defects in superfluid ^{4}He as an analogue of the formation of cosmic strings. *Nature 368* (Mar. 24 1994), 315–317.

[82] Hess, H. F. Evaporative cooling of magnetically trapped and compressed spin-polariz ed hydrogen. *Physical Review B 34*, 5 (Sept. 1986), 3476–3479.

[83] Holland, M., Williams, J., and Cooper, J. Bose-Einstein condensation: Kinetic evolution obtained from simulated trajectories. *Physical Review A 55*, 5 (May 1997), 3670–3677.

[84] Holland, M. J., Jin, D. S., Chiofalo, M. L., and Cooper, J. Emergence of interaction effects in Bose-Einstein condensation. *Physical Review Letters 78*, 20 (May 1997), 3801–3805.

[85] Horak, P., and Barnett, S. M. Creation of coherence in Bose-Einstein condensates by atom detection. *Journal of Physics B 32* (July 28 1999), 3421–3436.

[86] Huelga, S. F., Macchiavello, C., Pellizzari, T., Ekert, A. K., Plenio, M. B., and Cirac, J. I. Improvement of frequency standards with quantum entanglement. *Physical Review Letters 79*, 20 (Nov. 17 1997), 3865–3868.

[87] III, J. H. M., and Das, K. K. Visibility limit in multiparticle eigenstates of definite relative phase. *Physical Review A 59*, 3 (Mar. 1999), 2213–2215.

[88] Imamoğlu, A., and Kennedy, T. A. B. Optical measurements of the condensate phase. *Physical Review A 55*, 2 (Feb. 1997), R849–R852.

[89] Inouye, S., Andrews, M. R., Stenger, J., Miesner, H.-J., Stamper-Kurn, D. M., and Ketterle, W. Observations of Feshbach resonances in a Bose-Einstein condensate. *Nature 392* (Mar. 12 1998), 151–154.

[90] Isoshima, T., and Machida, K. Vortex stabilization in Bose-Einstein condensate of alkali-metal atom gas. *Physical Review A 59*, 3 (Mar. 1999), 2203–2212.

[91] Jack, M. W., Collett, M. J., and Walls, D. F. Coherent quantum tunneling between two Bose-Einstein condensates. *Physical Review A 54*, 6 (Dec. 1996), R4625–R4628.

[92] Jaksch, D., Gardiner, C. W., Gheri, K. M., and Zoller, P. Quantum kinetic theory. IV. intensity and amplitude fluctuations of a Bose-Einstein condensate at finite temperature including trap loss. *Physical Review A 58*, 2 (Aug. 1998), 1450–1464.

[93] Jaksch, D., Gardiner, C. W., and Zoller, P. Quantum kinetic theory. II. simulation of the quantum Boltzmann master equation. *Physical Review A 56*, 1 (July 1997), 575–586.

[94] Javanainen, J., and Wilkens, M. Phase and phase diffusion of a split Bose-Einstein condensate. *Physical Review Letters 78*, 25 (June 23 1997), 4675–4678.

[95] Javanainen, J., and Yoo, S. M. Quantum phase of a Bose-Einstein condensate with an arbitrary number of atoms. *Physical Review Letters 76*, 2 (Jan. 8 1996), 161–164.

[96] Kagan, Y., and Svistunov, B. V. Evolution of correlation properties and appearance of broken symmetry in the process of Bose-Einstein condensation. *Physical Review Letters 79*, 18 (Nov. 3 1997), 3331–3334.

[97] Kartner, F. X., Dougherty, D. J., Haus, H. A., and Ippen, E. P. Raman noise and soliton squeezing. *Journal of the Optical Society of America B 11*, 7 (July 1994), 1267–1276.

[98] Kasevich, M., and Chu, S. Atomic interferometry using stimulated Raman transitions. *Physical Review Letters 67*, 2 (July 8 1991), 181–184.

[99] Kaup, D. J. Perturbation theory for solitons in optical fibers. *Physical Review A 42*, 9 (Nov. 1990), 5689–5694.

[100] Ketterle, W., and van Druten, N. J. Bose-Einstein condensation of a finite number of particles trapped in one or three dimensions. *Physical Review A 54*, 1 (July 1996), 656–660.

[101] Ketterle, W., and van Druten, N. J. Evaporative cooling of trapped atoms. *Advances in atomic, molecular, and optical physics 37* (1996), 181–236.

[102] Kivshar, Y. S., Haelterman, M., Emplit, P., and Hamaide, J. P. Gordan-Haus effect on dark solitons. *Optics Letters 19*, 1 (Jan. 1994), 19.

[103] Kokkelmans, S. J. J. M. F., Verhaar, B. J., and Gibble, K. Prospects for Bose-Einstein condensation in cesium. *Physical Review Letters 81*, 5 (Aug. 1998), 951–954.

[104] Laguna, P., and Zurek, W. H. Density of kinks after a quench: When symmetry breaks, how big are the pieces? *Physical Review Letters 78*, 13 (Mar. 31 1997), 2519–2522.

[105] Lai, Y., and Yu, S.-S. General quantum theory of nonlinear optical-pulse propagation. *Physical Review A 51*, 1 (Jan. 1995), 817–829.

[106] Landau, L. D., and Lifshitz, E. M. *Statistical physics*, third ed., vol. 5 of *Course of theoretical physics*. Pergamon Press, 1980, pp. 85–118.

[107] Landau, L. D., and Lifshitz, E. M. *Statistical physics, Part 1*, third ed., vol. 5 of *Course of theoretical physics*. Pergamon Press, 1980.

[108] Landau, L. D., and Lifshitz, E. M. *Statistical Physics, Part 2*, second ed., vol. 9 of *Course of theoretical physics*. Pergamon Press, 1980.

[109] Law, C. K., Pu, H., Bigelow, N. P., and Eberly, J. H. Quantum phase diffusion of a two-component dilute Bose-Einstein condensate. *Physical Review A 58*, 1 (July 1998), 531–535.

[110] Lawande, S. V. In *Stochastic processes - fomalism and applications* (1983), vol. 184 of *Lecture notes in physics*, Springer-Verlag, pp. 256–268.

[111] Louisell, W. H. *Quantum statistical properties of radiation*. Wiley classics library. Wiley, 1973.

[112] Lundh, E., Pethick, C. J., and Smith, H. Zero-temperature properties of a trapped Bose-condensed gas: Beyond the Thomas-Fermi approximation. *Physical Review A 55*, 3 (Mar. 1997), 2126–2131.

[113] Lundh, E., Pethick, C. J., and Smith, H. Vortices in Bose-Einstein condensed atomic clouds. *Physical Review A 58*, 6 (Dec. 1998), 4816–4823.

[114] Marshall, R. J., New, G. H. C., Burnett, K., and Choi, S. Exciting, cooling, and vortex trapping in a Bose-condensed gas. *Physical Review A 59*, 3 (Mar. 1999), 2085.

[115] Marzlin, K.-P., and Zhang, W. Laser induced rotation of a trapped Bose-Einstein condensate. *Physical Review A 57*, 5 (May 1998), 3801–3804.

[116] Marzlin, K.-P., and Zhang, W. Quantized circular motion of a trapped Bose-Einstein condensate: Coherent rotation and vortices. *Physical Review A 57*, 6 (June 1998), 4761–4769.

[117] Marzlin, K.-P., Zhang, W., and Wright, E. M. Vortex coupler for atomic Bose-Einstein condensates. *Physical Review Letters 79*, 24 (Dec. 15 1997), 4728–4731.

[118] Matthews, M. R., Anderson, B. P., Haljan, P. C., Hall, D. S., Weiman, C. E., and Cornell, E. A. Vortices in a Bose-Einstein condensate. *cond-mat 9908209* (Aug. 23 1999).

[119] Mecozzi, A., Midrio, M., and Romagnoli, M. Timing jitter in soliton transmission with sliding filters. *Optics Letters 21*, 6 (Mar. 15 1996), 402–404.

[120] Mermin, N. D. Nonlocal character of quantum theory? *American journal of physics 66*, 10 (1998), 920.

[121] Mermin, N. D. What is quantum mechanics trying to tell us? *American journal of physics 66*, 9 (1998), 753.

[122] Mewes, M.-O., Andrews, M. R., van Druten, N. J., Kurn, D. M., Durfee, D. S., and Ketterle, W. Bose-Einstein condensation in a tightly confining DC magnetic trap. *Physical Review Letters 77*, 3 (July 1996), 416–419.

[123] Mihalache, D., Crasovan, L.-C., Panoiu, N.-C., Moldoveanu, F., and Baboiu, D.-M. Timing jitter of femtosecond solitons in monomode optical fibers. *Optical Engineering 35*, 6 (June 1996), 1611–1615.

[124] Milburn, G. J. Classical and quantum conditional statistical dynamics. *Journal of Quantum and Semiclassical Optics 8* (1996), 269–276.

[125] Milburn, G. J., Corney, J. F., Wright, E. M., and Walls, D. F. Quantum dynamics of an atomic Bose-Einstein condensate in a double-well potential. *Physical Review A 55*, 6 (June 1997), 4318–4324.

[126] Milburn, G. J., Jacobs, K., and Walls, D. F. Quantum-limited measurements with the atomic force microscope. *Physical Review A 50*, 6 (Dec. 1996), 5256–5263.

[127] Moerdijk, A. J., Verhaar, B. J., and Axelsson, A. Resonances in ultracold collisions of ^{6}Li, ^{7}Li, and ^{23}Na. *Physical Review A 51*, 6 (June 1995), 4852–4861.

[128] Mollenauer, L. F. *Philosophical Transactions of the Royal Society of London A 315* (1985), 435.

[129] Mollenauer, L. F., Gordon, J. P., and Islam, M. N. Soliton propagation in long fibers with periodically compensated loss. *IEEE Journal of Quantum Electronics 22*, 1 (Jan. 1986), 157–173.

[130] Mollenauer, L. F., Mamyshev, P. V., and Neubelt, M. J. Measurement of timing jitter in filter-guided soliton transmission at 10gbits/s and achievement of 375gbits/s-mm, error free, at 12.5 and 15gbits/s. *Optics Letters 19*, 10 (May 15 1994), 704–706.

[131] Mollenauer, L. F., Neubelt, M. J., Evangelides, S. G., Gordon, J. P., Simpson, J. R., and Cohen, L. G. Experimental study of soliton transmission over more than 10000km in dispersion-shifted fiber. *Optics Letters 15*, 21 (Nov. 1 1990), 1203–1205.

[132] Mollenauer, L. F., Stolen, R. H., and Gordon, J. P. Experimental observation of picosecond pulse narrowing and solitons in optical fibers. *Physical Review Letters 45* (Sept. 1980), 1095–1097.

[133] Mølmer, K. Phase collapse and excitations in Bose-Einstein condensates. *Physical Review A 58*, 1 (July 1998), 566–575.

[134] Moores, J. D., Wong, W. S., and Haus, H. A. Stability and timing maintenance in soliton transmission and storage rings. *Optics Communications 113* (Dec. 15 1994), 153–175.

[135] Naraschewski, M., and Glauber, R. J. Spatial coherence and density correlations of trapped Bose gases. *Physical Review A 59*, 6 (June 1999), 4595–4607.

[136] Narducci, L. M., Bowden, C. M., Bluemel, V., Garrazana, G. P., and Tuft, R. A. Multitime-correlation functions and the atomic coherent-state representation. *Physical Review A 11*, 3 (Mar. 1975), 973–980.

[137] Navez, P. Macroscopic squeezing in a Bose-Einstein condensate. *Modern Physics Letters B 12*, 18 (Aug. 10 1998), 705.

[138] Öhberg, P. Stablity properties of the two-component Bose-Einstein condensate. *Physical Review A 59*, 1 (Jan. 1999), 634–638.

[139] Pais, A. *Subtle is the Lord....* Oxford University Press, Oxford, 1982.

[140] Parkins, A. S., and Walls, D. F. The physics of trapped dilute-gas Bose-Einstein condensates. *Physics Reports 303*, 1 (Sept. 1998), 1.

[141] Pérez-García, V. M., Michinel, H., Cirac, J. I., and Lewenstein, M. Dynamics of Bose-Einstein condensates: Variational solutions of the Gross-Pitaevskii equations. *Physical Review A 56*, 2 (Aug. 1997), 1424–1432.

[142] Peters, A., Chung, K. Y., and Chu, S. Atom interferometry applied: Measuring gravity with ultra hight precision. In *IV Conference on Optics and Interferometry with Atoms* (St. Johns College, Oxford, July 21–23 1997).

[143] Petrich, W., Anderson, M. H., Ensher, J. R., and Cornell, E. A. Evaporative cooling of rubidium atoms in a magnetic trap. In *Fourteenth International Conference on Atomic Physics (ICAP XIV)* (1994), p. 7.

[144] Petrosyan, K. F., and You, L. Topological phases and circulating states of Bose-Einstein condensates. *Physical Review A 59*, 1 (Jan. 1999), 639–642.

[145] Phillips, W. D. Laser cooling and trapping of neutral atoms. *Reviews of Modern Physics 70*, 3 (July 1998), 721–741.

[146] Plimak, L. I., and Walls, D. F. Nonclassical spatial and momentum distributions in a Bose-condensed gas. *Physical Review A 54*, 1 (July 1996), 652–655.

[147] Pu, H., Law, C. K., Eberly, J. H., and Bigelow, N. P. Coherent disintegration and stability of vorticies in trapped Bose condensates. *Physical Review A 59*, 2 (Feb. 1999), 1533–1537.

[148] Puri, R. R., and Lawande, S. V. Exact thermodynamic behaviour of a collective atomic system in an external field. *Physica A 101* (1980), 599–612.

[149] Rokhsar, D. S. Vortex stability and persistent currents in trapped Bose gases. *Physical Review Letters 79*, 12 (Sept. 22 1997), 2164–2167.

[150] Ruostekoski, J., Collett, M. J., Graham, R., and Wall, D. F. Macroscopic superpositions of Bose-Einstein condensates. *Physical Review A 57*, 1 (Jan. 1998), 511–517.

[151] Ruostekoski, J., and Walls, D. F. Nondestructive optical measurement of relative phase between two Bose-Einstein condensates. *Physical Review A 56*, 4 (Oct. 1997), 2996–3006.

[152] Ruostekoski, J., and Walls, D. F. Bose-Einstein condensate in a double-well potential as an open quantum system. *Physical Review A 58*, 1 (July 1998), R50–R53.

[153] Ruostekoski, J., and Walls, D. F. Measurement scheme for relative phase diffusion between two Bose-Einstein condensates. *Physical Review A 59*, 4 (Apr. 1999), 2571–2574.

[154] Ruprecht, P. A., Holland, M. J., Burnett, K., and Edwards, M. Time-dependent solution of the nonlinear Schrödinger equation for Bose-condensed trapped neutral atoms. *Physical Review A 51*, 6 (June 1995), 4704–4711.

[155] Schumaker, B. L., and Caves, C. M. A new fomalism for two-photon optics. In *Rochester conference proceedings* (1983), pp. 743–750.

[156] Schumaker, B. L., and Caves, C. M. New fomalism for two-photon quantum optics. II. mathematical foundation and compact notation. *Physical Review A 31*, 5 (May 1985), 3093–3111.

[157] Shelby, R. M., Drummond, P. D., and Carter, S. J. Phase-noise scaling in quantum soliton propagation. *Physical Review A 42*, 5 (Sept. 1990), 2966–2796.

[158] Shelby, R. M., Levenson, M. D., and Bayer, P. W. *Physical Review B 31* (1985), 5244.

[159] Sinatra, A., and Castin, Y. Phase dynamics of Bose-Einstein condensates: Losses versus revivals. *The European Physical Journal D 4* (1998), 247–260.

[160] Sinha, S. Semiclassical analysis of collective excitations in Bose-Einstein condensate. *Physical Review A 55*, 6 (June 1997), 4325–4329.

[161] Smith, K., and Mollenauer, L. F. Experimental observation of soliton interaction over long fiber paths: discovery of a long-range interaction. *Optics Letters 14* (1989), 1284–1286.

[162] Steel, M. J., and Collett, M. J. Quantum state of two trapped Bose-Einstein condensates with a josephson coupling. *Physical Review A 57*, 4 (Apr. 1998), 2920–2930.

[163] Steel, M. J., Olsen, M. K., Plimak, L. I., Drummond, P. D., Tan, S. M., Collett, M. J., Walls, D. F., and Graham, R. Dynamical quantum noise in trapped Bose-Einstein condensates. *Physical Review A 58*, 6 (Dec. 1998), 4824–4835.

[164] Stenger, J., Inouye, S., Andrews, M. R., Miesner, H.-J., Stamper-Kurn, D. M., and Ketterle, W. Strongly enhanced inelastic collisions in a Bose-Einstein condensate near Feshbach resonances. *Physical Review Letters 82*, 12 (Mar. 22 1999), 2422–2425.

[165] Stenger, J., Inouye, S., Chikkatur, A. P., Stamper-Kurn, D. M., Pritchard, D. E., and Ketterle, W. Bragg spectroscopy of a Bose-Einstein condensate. *Physical Review Letters 82*, 23 (June 1999), 4569–4573.

[166] Stolen, R. H., Gordon, J. P., Tomlinson, W. J., and Haus, H. A. Raman response function of Silica-core fibers. *Journal of the Optical Society of America B 6*, 6 (June 1989), 1159–1166.

[167] Stolen, R. H., Lee, C., and Jain, R. K. Developement of the stimulated Raman spectrum in single-mode Silica fibers. *Journal of the Optical Society of America B 1*, 4 (Aug. 1984), 652–657.

[168] Stoof, H. T. C. Coherent versus incoherent dynamics during Bose-Einstein condensation in atomic gases. *Journal of Low Temperature Physics 114*, 1–2 (1999), 11–108.

[169] Sudarshan, E. C. G. Equivalence of semiclassical and quantum mechanical descriptions of statistical light beams. *Physical Review Letters 10*, 7 (Apr. 1 1963), 277–279.

[170] Tempere, J., and Devreese, J. T. Fringe pattern of interfering Bose-Einstein condensates with a vortex. *Solid State Communications 108*, 12 (1998), 993–997.

[171] Uzunov, I. M., and Gerdjikov, V. S. Self-frequency shift of dark solitons in optical fibers. *Physical Review A 47*, 2 (Feb. 1993), 1582–1585.

[172] von Foerster, T., and Glauber, R. J. Quantum theory of light propagation in amplifying media. *Physical Review A 3*, 4 (Apr. 1971), 1484–1511.

[173] Wallis, H., Röhrl, A., Naraschewski, M., and Schenzle, A. Phase-space dynamics of Bose condensates: Interference versus interaction. *Physical Review A 55*, 3 (Mar. 1997), 2109–2119.

[174] Walls, D. F., and Milburn, G. J. *Quantum Optics*. Springer-Verlag, Berlin, 1994.

[175] Walser, R., Williams, J., Cooper, J., and Holland, M. Quantum kinetic theory for a condensed bosonic gas. *Physical Review A 59*, 5 (May 1999), 3878–3889.

[176] Werner, M. J., and Drummond, P. D. Robust algorithms for solving stochastic partial differential equations. *Journal of Computational Physics 132*, 2 (Apr. 1997), 312–326.

[177] Wineland, D. J., Bollinger, J. J., Itano, W. M., and Heinzen, D. J. Squeezed atomic states and projection noise in spectroscopy. *Physical Review A 50*, 1 (July 1994), 67–87.

[178] Wineland, D. J., Bollinger, J. J., Itano, W. M., Moore, F. L., and Heinzen, D. J. Spin squeezing and reduced quantum noise in spectroscopy. *Physical Review A 46*, 11 (Dec. 1992), R6797–R6800.

[179] Wiseman, H. M. *Quantum trajectories and feedback*. PhD thesis, The University of Queensland, 1994.

[180] Wiseman, H. M. SU(2) distribution functions and measurement of the fluorescence of a two-level atom. *Jornal of Quantum and Semiclassical Optics 7* (1995), 569–584.

[181] Wiseman, H. M., and Milburn, G. J. Quantum theory of field-quadrature measurements. *Physical Review A 47*, 1 (Jan. 1993), 642–662.

[182] Wood, D. Constraints on the bit rates in direct detection optical communication systems using linear or soliton pulses. *Journal of Lightwave Technology 8*, 7 (July 1990), 1097–1106.

[183] Wu, H., Armondo, E., and Foot, C. J. Dynamics of evaporative cooling for Bose-Einstein condensation. *Physical Review A 56*, 1 (July 1997), 560–569.

[184] Yamashita, M., Koashi, M., and Imoto, N. Quantum kinetic theory for evaporative cooling of trapped atoms: Growth of Bose-Einstein condensate. *Physical Review A 59*, 3 (Mar. 1999), 2243–2249.

[185] Yoon, B., and Negele, J. W. Time-dependent Hartree approximation for a one-dimensional system of bosons with attractive δ-function interactions. *Physical Review A 16*, 4 (Oct. 1977), 1451–1457.

[186] Young, B., Kasevich, M., and Chu, S. Precision atom interferometry with light pulses. In *Atom interferometry* (1997), P. R. Bernan, Ed., Academic Press, pp. 363–405.

[187] Yu, S.-S., and Lai, Y. Impacts of self-Raman effect and third-order dispersion on pulse squeezed state generation using optical fibres. *Journal of the Optical Society of America B 12*, 12 (Dec. 01 1995), 2340.

[188] Yurke, B., and Potasek, M. J. Solution to the initial value problem for the quantum nonlinear Schrödinger equation. *Journal of the Optical Society of America B 6*, 6 (June 1989), 1227–1238.

[189] Ziegler, K., and Shukla, A. Bose-Einstein condensation in a trap: The case of a dense condensate. *Physical Review A 56*, 2 (Aug. 1997), 1438–1442.

[190] Zurek, W. H. Cosmological experiments in superfluid helium? *Nature 317* (Oct. 10 1985), 505–508.

[191] Zurek, W. H. Cosmological experiments in condensed matter systems. *Physics Reports 276* (1996), 177–221.

. . . but this book is already too long, and I fear lest I should seem to catch at an opportunity of airing my little smattering of science more childishly than profitably.

-St. Augustine, from 'The City of God', Book 11.